On quantum transport in flat-band materials

Oriekhov, D.

Citation

Oriekhov, D. (2023, October 4). *On quantum transport in flat-band materials*. *Casimir PhD Series*. Retrieved from https://hdl.handle.net/1887/3642874

On quantum transport in flat-band materials

Proefschrift

ter verkrijging van
de graad van doctor aan de Universiteit Leiden,
op gezag van rector magnificus prof. dr. ir. H. Bijl,
volgens besluit van het college voor promoties
te verdedigen op woensdag 4 oktober 2023
klokke 13.45 uur

door

Dmytro Oleksandrovich Oriekhov

geboren te Kyiv, Oekraïne
in 1996

Promotores:	Prof. dr. C. W. J. Beenakker
	Prof. dr. I. Adagideli (Sabanci University, Istanbul)
Promotiecommissie:	Prof. dr. J. Aarts
	Dr. L. Fritz (Universiteit Utrecht)
	Dr. E. Greplová (Technische Universiteit Delft)
	Prof. dr. K. E. Schalm
	Prof. dr. ir. H. J. W. Zandvliet (Universiteit Twente)

The cover shows an artistic representation of some results presented in this thesis: the dynamical gap generation in a flat-band material on the front cover, the spectral functions of a bilayer dice lattice on the back cover; the background shows the dice lattice itself, as a platform that hosts these physical effects. The cover is a digital painting made by Oleg Mykhailov, cousin of the author of the thesis.

To my family.

Contents

Chapter 1

Introduction

1.1 Preface

This thesis is devoted to the study of the role of flat bands in transport and interacting properties of atomically-thin materials.

Flat band is defined as a part of Bloch band with macroscopically large region of momentum space with nearly constant dispersion. Why the flat bands are so important? The answer is given by considerations coming from classical physics (mechanics, electrodynamics). The equations of motion for a single particle in external potential U are captured by the Lagrangian function $L = T - U$ or Hamiltonian $H = T + U$ with T being a kinetic energy. The definition of flat band says that T is approximately constant in some parameter range - region in momentum space. Adjusting the energy level to this constant level $\tilde{T} = T - T_0$, we find that $\tilde{L} = \tilde{T} - U \approx U$. This means that the physics of a particle are determined solely by an external potential. Such situation in not typical for classical physics. The clear consequence of this estimation appears in quantum systems: even weak potential or interactions inside the system lead to instability of the initial ground state and re-configuration. In the modern experiments the investigation of possible new ground states in a flat band systems is a young topic which appeared just 5 years ago with a discovery of magic angle twisted bilayer graphene [1]. Nevertheless, the enormous attention led to appearance of many thousands of papers with number of intriguing results. The most prominent examples are discoveries of superconductivity and Mott insulating states in magic angle twisted bilayer [1] and trilayer [2], superconducting states in Bernal bilayer [3] and ABC trilayer graphene

[4], and Kagome metals [5].

In this thesis several theoretical predictions for the new ground states in flat band systems are discussed. One might ask why the ground state of flat band systems is so hard to calculate? The reason is that the presence of flat band enhances the role of *all* interactions. Thus, a very rigorous symmetry analysis and precise estimation of each of interaction constants is required to build a phase diagram and understand which phase dominates. In the Chapter 2 the strong enhancement of RKKY spin-spin interactions is predicted. For the case when the screened Coulomb interaction is present, the possibility of formation of excitonic gap with intervalley-polarized order is discussed in Chapter 3. These results can be viewed as a building blocks for future theory of phase diagram in flat band materials. Based on experiments like [1, 6] it is expected that one would have the competition between all these correlated states, and as an example the final ground state might have unconventional type of superconductivity. Also the high controllability in experiments with 2D materials might allow to tune and select which of interactions will be dominating in particular setup. Other main chapters of this thesis are devoted to the study of the role of flat bands in a non-interacting case. Such situation is typical for realizations of flat band materials in artificial systems such as STM-type experiments with electronic lattices [7], optical lattice realizations [8] or superlattice structures in organic chemical frameworks [9, 10].

1.2 Examples of simple tight-binding models with flat bands

Next, let us introduce the particular examples of flat band models studied in this thesis. The main idea behind these lattices is that they have simple geometry and the tight-binding description gives simple Hamiltonians that can be analyzed with analytical and numerical methods. The two lattices, dice and Lieb, discussed below are examples of bipartite lattices where connection between two different sublattices is made only via hopping parameters to third sublattice.

1.2.1 Dice lattice and $\alpha - \mathcal{T}_3$ model

The dice (also called $\mathcal{T}_3$) lattice is probably historically the first tight-binding model with flat bands. It was firstly studied by B. Sutherland

Figure 1.1. The dice (also called $\mathcal{T}_3$) lattice whose red points display atoms of the A sublattice, blue points describe the B sublattice, and the green points define the C sublattice. The vectors $\boldsymbol{a}_1 = (\sqrt{3}, 0)d$ and $\boldsymbol{a}_2 = (\sqrt{3}/2, 3/2)d$ are the basis vectors of the C sublattice. The nearest neighbor hopping parameters between hub (C) and rim (A, B) atoms are t_1 and t_2.

in 1986 [11] as an example where localization of wave functions happens due to local topology. The $\alpha - \mathcal{T}_3$ model describes quasiparticles in two dimensions on the dice lattice schematically shown in Fig.1.1, where d denotes the distance between neighbor atoms. This lattice has a unit cell with three different lattice sites whose two sites (A, C) like in graphene form a honeycomb lattice with hopping amplitude $t_{AC} = t_1$ and additional B sites at the center of each hexagon are connected to the C sites with hopping amplitude $t_{BC} = t_2$. The C atoms are called hub centers, while A and B are rim sites, and electrons hop between rim and hub atoms only. Two hopping parameters t_1 and t_2 are not equal, in general, and the dice model corresponds to the limit $t_1 = t_2$. The lattice structure and basis vectors $\mathbf{a}_1 = (\sqrt{3}, 0)d$, $\mathbf{a}_2 = (\sqrt{3}/2, 3/2)d$ are shown on Fig.1.1. Since there are three atoms per unit cell, the wave functions can be written in terms of 3-component vectors with elements assigned to each sublattice. This leads to the so-called pseudospin $S = 1$ description.

The tight-binding equations are [12]:

$$\varepsilon \Psi_C(\boldsymbol{r}) = -t_1 \sum_j \Psi_A(\boldsymbol{r} + \boldsymbol{\delta}_j^A) - t_2 \sum_j \Psi_B(\boldsymbol{r} - \boldsymbol{\delta}_j^A),$$

$$\varepsilon \Psi_A(\boldsymbol{r}) = -t_1 \sum_j \Psi_C(\boldsymbol{r} - \boldsymbol{\delta}_j^A),$$

$$\varepsilon \Psi_B(\boldsymbol{r}) = -t_2 \sum_j \Psi_C(\boldsymbol{r} + \boldsymbol{\delta}_j^A), \tag{1.1}$$

where the vectors δ_j^A connect nearest neighbor atoms C to atoms A:

$$\boldsymbol{\delta}_1^A = \frac{\mathbf{a}_1 + \mathbf{a}_2}{3}, \ \boldsymbol{\delta}_2^A = \frac{\mathbf{a}_3 - \mathbf{a}_1}{3}, \ \boldsymbol{\delta}_3^A = -\frac{\mathbf{a}_2 + \mathbf{a}_3}{3} \quad \text{with} \quad \mathbf{a}_3 = \mathbf{a}_2 - \mathbf{a}_1. \tag{1.2}$$

The corresponding tight-binding Hamiltonian in momentum space reads [13]

$$H_0(\boldsymbol{k}) = \begin{pmatrix} 0 & f_{\boldsymbol{k}} \cos\Theta & 0 \\ f_{\boldsymbol{k}}^* \cos\Theta & 0 & f_{\boldsymbol{k}} \sin\Theta \\ 0 & f_{\boldsymbol{k}}^* \sin\Theta & 0 \end{pmatrix}, \quad \alpha \equiv \tan\Theta = \frac{t_2}{t_1},$$

$$f_{\boldsymbol{k}} = -\sqrt{t_1^2 + t_2^2}\,(1 + e^{-ik a_2} + e^{-ik a_3}), \tag{1.3}$$

and acts on three-component wave functions with the following order of components $\Psi^T = (\Psi_A, \Psi_C, \Psi_B)$. As was noted in Introduction, the angle Θ can be used to interpolate between graphene and dice model. Thus, our results can be compared with graphene literature by taking limit $\Theta \to 0$ or $\Theta \to \frac{\pi}{2}$.

It is easy to derive the energy spectrum of the above Hamiltonian, which is qualitatively the same for any α and consists of three bands: the zero-energy flat band, $\varepsilon_0(\mathbf{k}) = 0$, whose existence is protected by the particle-hole symmetry, and two dispersive bands

$$\varepsilon_{\pm}(\mathbf{k}) = \pm|f_k| = \pm\sqrt{t_1^2 + t_2^2}\Big[3 + 2(\cos(\boldsymbol{a}_1\boldsymbol{k}) + \cos(\boldsymbol{a}_2\boldsymbol{k}) + \cos(\boldsymbol{a}_3\boldsymbol{k}))\Big]^{1/2}. \tag{1.4}$$

The eigenvectors in the whole Brillouin zone (BZ) are given by Eq.(2) in [13] (gapless case) and by Eq.(5) in [14] (gapped case). For dispersionless band the wave function is localized on atoms of sublattices A, B while it is zero on hub atoms C. The presence of a completely flat band with zero energy is perhaps one of the remarkable properties of the $\alpha - \mathcal{T}_3$ lattice model.

There are six values of momentum for which $f_{\boldsymbol{k}} = 0$ and all three bands intersect. They are situated at corners of the hexagonal Brillouin zone. The two inequivalent points, for example, are

$$\boldsymbol{K} = \frac{2\pi}{d}\left(\frac{\sqrt{3}}{9}, \frac{1}{3}\right), \quad \boldsymbol{K}' = \frac{2\pi}{d}\left(-\frac{\sqrt{3}}{9}, \frac{1}{3}\right). \tag{1.5}$$

For momenta near the K-points, $\boldsymbol{k} = \boldsymbol{K}(\boldsymbol{K}') + \tilde{\boldsymbol{k}}$, we find that $f_{\boldsymbol{k}}$ is linear in $\tilde{\boldsymbol{k}}$, i.e., $f_{\boldsymbol{k}} = \hbar v_F(\xi \tilde{k}_x - i\tilde{k}_y)$ with valley index $\xi = \pm$, where $v_F = 3td/2\hbar$ is the Fermi velocity, and in what follows we omit for the simplicity of notation the tilde over momentum. As for lattice parameters we take their numerical values the same as in graphene. Hence, in the linear order to momentum deviations from the K and K' points, the low-energy Hamiltonian describes massless pseudospin-1 fermions [12, 13] which for equal hoppings, $\Theta = \pi/4$, is given by the scalar product of momentum and the spin-1 matrices:

$$H_\xi(\mathbf{k}) = \hbar v_F \left(\xi S_x k_x + S_y k_y \right),$$

$$S_x = \frac{1}{\sqrt{2}} \begin{pmatrix} 0 & 1 & 0 \\ 1 & 0 & 1 \\ 0 & 1 & 0 \end{pmatrix}, \quad S_y = \frac{1}{\sqrt{2}} \begin{pmatrix} 0 & -i & 0 \\ i & 0 & -i \\ 0 & i & 0 \end{pmatrix} \tag{1.6}$$

where $\mathbf{k} = \mathbf{q} - \mathbf{K}_\xi$ is the wave vector measured relative to the Dirac points located at $\mathbf{K}_\xi = \xi 4\pi/(3\sqrt{3}a)\{1, 0\}$, corresponding to K ($\xi = +$) and K' ($\xi = -$) points, and $v_F = 3ta/(\sqrt{2}\hbar)$ is the Fermi velocity. This Hamiltonian reminds a Dirac-type Hamiltonian (relativistic dispersion) but now for spin-1 particles. Such effective Hamiltonians, that do not occur for elementary particles in high-energy physics, attracted much attention in the last years [15].

The $\mathcal{T}_3$ lattice was experimentally realized in Josephson arrays [16, 17] as well as in a network made of metallic wires tailored in a high mobility two-dimensional electron gas [18], and its optical realization by laser beams was proposed in Ref.[19]. The atomic-scale realization of dice lattice is missing because of the complexity of hopping structure (the hoppings between neighboring A and B sublattices should be strongly suppressed).

1.2.2   Lieb lattice

The Lieb lattice is schematically shown in Fig.1.2. It was studied by E. H. Lieb in 1989 [20] in connection with specific properties of Heisenberg spin model on it. This lattice consists of three square sublattices, with atoms placed in the corners and in the middle of each side of big squares forming a line-centered-square lattice. The tight-binding equations describing this lattice are very similar to Eq.(1.1), the only difference comes from the orientation of vectors connecting nearest neighbors δ_j. The tight-binding

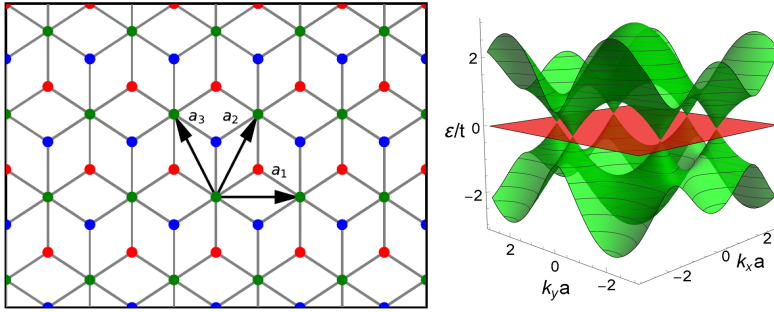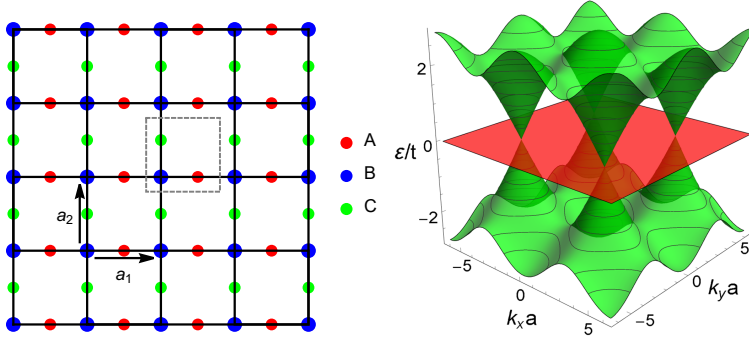**Figure 1.2.** The Lieb lattice whose red points display atoms of the A sublattice, blue points describe the B sublattice, and the green points define the C sublattice. The vectors $\boldsymbol{a}_1 = (1, 0)a$ and $\boldsymbol{a}_2 = (0, 1)a$ are the basis vectors of the B sublattice. The nearest neighbor hopping parameters between hub (B) and rim (A, C) atoms are t_1 and t_2.

Hamiltonian was described in Ref.[21]:

$$H_0 = \begin{pmatrix} 0 & -2t\cos(k_x a/2) & 0 \\ -2t\cos(k_x a/2) & 0 & -2t\cos(k_y a/2) \\ 0 & -2t\cos(k_y a/2) & 0 \end{pmatrix} \quad (1.7)$$

Notably, the dispersion contains only single Dirac cone inside first Brillouin zone (see Fig.1.2). This Hamiltonian reduces to the following low-energy model near the center of BZ $k_{x,y} = \frac{\pi}{a} + q_{x,y}$:

$$H_{Lieb} = \begin{pmatrix} 0 & v_F q_x & 0 \\ v_F q_x & 0 & v_F q_y \\ 0 & v_F q_y & 0 \end{pmatrix}. \quad (1.8)$$

The energy dispersions defined by this Hamiltonian are given by three bands, one is flat band and the other two are dispersive bands (see Fig.4.4c):

$$\varepsilon_0 = 0, \ \varepsilon_\pm = \pm 2t\sqrt{\cos^2(k_x a/2) + \cos^2(k_y a/2)}. \quad (1.9)$$

The notable property of both dice and Lieb lattices in that flat band is placed at charge-neutrality point. Below we discuss the structure of wave functions in flat band in real space.

The experimental realization of Lieb lattice on atomic scale was made with the help of STM technique that creates an electronic lattice on surface of substrate [7].
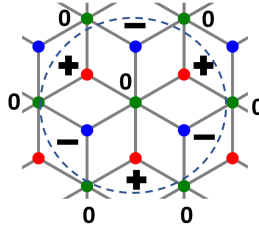
Figure 1.3. The configuration of flat band state wave function that is localized around one of the hub sites. While the components of the wave function on a hub (green C) sites are zeros, the sign-alternating components on A and B sites compose a localized state.

1.2.3 Structure of flat band wave functions on a lattice

The main feature of the models described above in the presence of exactly flat band at the charge-neutrality point in the spectrum. it is easy to find flat band solutions in momentum space from tight-binding Hamiltonian. But the question arises - how such states are organized on a lattice? The answer on this question was the historical motivation that attracted attention to these lattices [11, 20] well before the first atomically-thin material was experimentally realized [22].

Let us look on tight-binding equations (1.1). The flat band placed at zero energy results in three equations:

$$0 = -t_1 \sum_j \Psi_A(\boldsymbol{r} + \boldsymbol{\delta}_j^A) - t_2 \sum_j \Psi_B(\boldsymbol{r} - \boldsymbol{\delta}_j^A),$$

$$0 = -t_1 \sum_j \Psi_C(\boldsymbol{r} - \boldsymbol{\delta}_j^A), \quad 0 = -t_2 \sum_j \Psi_C(\boldsymbol{r} + \boldsymbol{\delta}_j^A). \tag{1.10}$$

The two last equations are equivalent and give the same solution $\Psi_C(\boldsymbol{r}) = 0$. The first equation gives algebraic relation on components of wave function on A and B sublattices, that can be easily satisfied by choosing the sign structures of the components according to the Fig.1.3. For example, all B-components are equal to $\Psi_B = -t_1/t_2\Psi_A$. The state shown in Fig.1.3 is localized around one of the sublattice C sites. For each site one can build correspond state, thus having the high degeneracy of such flat band of the order of number of atoms in the sample. The experiments [16–18] have confirmed the existence of novel localization effects, which arise due to the presence of flat band in the spectrum of $\mathcal{T}_3$ lattice.

1.3   Beyond exactly flat bands: high-order van Hove singularities

In experiments with atomically-thin crystals it is typical to have not exactly flat bands due to different next nearest neighbor hopping terms, role of substrates and similar effects [1, 23]. The general concept that captures relatively "flat" parts of band in a dispersion are called saddle points. The corresponding pronounced divergent peaks in density of states are called van Hove singularities. The original concept was studied by L. van Hove in 1953 [24]. Recently, a generalization of the concept, called high-order van Hove singularities, was introduced by Liang Fu group [25]. The difference between these concepts is the following:

1) The term "flat bands" in this Thesis is used to describe bands that have constant dispersion, thus representing mathematically precise flatness of the band. The corresponding density of states has a Dirac delta-function peak;

2) the usual van Hove singularities correspond to momentum-dependent dispersion $\varepsilon(k_x, k_y) \sim k_x^2 - k_y^2$ and give logarithmically-divergent density of states;

3) the high-order van Hove singularities give power law divergent density of states.

All such features in the band structure are expected to produce strongly correlated states (superconductivity, etc) at corresponding doping due to high density of states and small group velocity of quasiparticles [26–28]. However, some observable signatures might be different and the Sixth Chapter 6 studies such differences for orbital susceptibility. The classification of high-order van Hove singularities was given in Refs.[29, 30], and the field of discovering materials with them only starts its growing.

1.4   Zero energy modes: Majorana zero modes and Andreev bound states

When the flat band is placed close to charge-neutrality point in the system the whole reach physical picture coming from flat bands becomes easily accessible for experimental studies. In addition to discussion of possible physical effects related to the flat bands in 2D crystals, this thesis also contains several results related to another type of states placed

near charge-neutrality point: Majorana zero modes and Andreeev bound states.

In the past decades the great attention was given to a possibility of making topologically protected quantum qubit. One of the key possibilities was to use so-called Majorana zero modes - a collective excitations in superconductors that are bound to zero energy (charge neutrality point) and are non-Abelian anions.

However, they are typically mimicked by another non-topological modes placed at or around charge neutrality point - Andreeev bound states. Such bound states appear in Josephson junctions. In this case mimicking means that the expected observable signatures of Majorana zero modes are nearly exactly reproduced by Andreev bound states.

Modern experimental state of this is the following: there are devised that host Majorana modes, however their manufacturing is related to enormously complicated process of reducing disorder [31]. Still a next generation of experiments is required to make Majorana zero modes accessible for quantum computing.

In this thesis chapters 7 and 8 are devoted to Majorana zero modes and the signatures mimicked by Andreev bound states.

1.5   About this thesis

Below follows the brief description of chapter contents:

1.5.1   Chapter 2

The Second chapter is devoted to the study of spin-spin interaction between two impurities placed on a 2D dice lattice. Such interaction is mediated by the electrons of a lattice. It is called Ruderman-Kittel-Kasuya-Yoshida [32–34] spin-spin interaction. The RKKY interaction was calculated using the effective low-energy theory that works close to charge-neutrality point and captures flat band and Dirac cones. The standard approximation of RKKY interaction which uses non-interacting Green's function of the electrons was used. The main results concerning the role of flat band are the following: the RKKY interaction between two impurities is strongly enhanced and diverges as inverse temperature when chemical potential placed at flat band level. At the same time enhancement is finite but large when the chemical potential is close to flat band

level. Such picture holds only for certain positions of impurities related to the localization of flat band wave functions. Apart from that, the description of the RKKY interaction for arbitrary temperatures and positions of chemical potential are given in terms of exact analytic expressions.

Apart from that, the chapter contains important mathematical results for the physics of RKKY interaction in graphene. The interaction integrals are calculated in the most general fashion with both finite temperature and chemical potential taken into account. The exact analytic expressions obtained there allow one to analyze dependencies on physical parameters and relative positions of impurities on different sublattices as well as obtain short exponentially-precise asymptotic expressions.

1.5.2   Chapter 3

In the Third Chapter the role of flat band in dynamical generation of excitonic gap is studied. Excitons are bound states of electron and holes tied by an attractive Coulomb interaction. The excitonic gap in the spectrum appears when it is energetically favorable to create excitons out of electrons and holes that have energies close to charge-neutrality point. Experimentally and theoretically it was found that the excitonic gap is generated in multilayer graphene (see Refs.[35–44]) and the more softer dispersion is - the larger gap is generated. Such picture is in agreement with simple considerations about the role of kinetic and potential energies discussed in the Preface (1.1) of this Introduction.

As the flat bands represent the most soft type of kinetic energy, it is expected that the dynamical excitonic gap generation should be favorable. In the Chapter 3 several possible gap parameters for dice lattice are studied that satisfy symmetries and correspond to different pairings in sublattice spaces. It is shown that among several possible scenarios one dominates as energetically more favorable. The excitonic gap in such case has an intervalley type (pairing happens for quasiparticles from different valleys). For the formation of corresponding order parameter (excitonic gap) the flat band plays a role of catalyst. Similarly to chemical reactions, where the catalyst does not disappear during reaction but helps it to proceed more efficiently, the excitonic gap formation splits flat band into two but leaves both of them perfectly flat. But, the flat band enormously enhances the energy gap size. These predictions suggest that such mechanism might compete with superconductivity in flat band systems and dominate in their transport properties at intermediate temperatures

leading to insulating state.

In addition, it is important to underline that the type of excitonic gap that is favorable due to flat band catalysis has particular type of symmetry. In other words, not every type of excitonic order parameter is enhanced in the presence of flat band. The studies of such valley-mixing order parameters in more complicated systems such as twisted bilayer graphene are very active ongoing topic [45, 46].

1.5.3   Chapter 4

In the Fourth Chapter of this thesis the role of flat bands in the optical properties of dice and Lieb lattices was analyzed. For this purpose a zitterbewegung method, firstly introduced by J. Cserti et.al. [47], was generalized to be used for different effective models.

The calculation of optical conductivity is based on a Kubo formula for linear response. However, for most typical models the analytical calculations quickly become very complicated and the full integration cannot be performed. The idea behind zitterbewegung method is to convert part of calculation complexity into solution of differential equations - Heisenberg equations of motion. For particles with positive and negative energy bands in spectrum such equations predict a trembling motion, zitterbewegung (firstly discovered by Schrödinger in 1930 [48]). Trembling motion in this case means that the position of free propagating wave packet performs oscillations with very small amplitude and high frequency.

In the case of optical conductivity the solutions of Heisenberg equations and proper substitution of results into current response correlators allowed to perform full calculation for a number of effective models. In the Fourth Chapter we firstly analyzed the optical conductivity of semi-Dirac model where the Dirac cones can move with varying parameters of the model and merge into one. The obtained exact expressions capture the contributions of different transitions into optical condctivity. In particular, the role of anisotropy and contribution of transitions between van Hove singularities into the high peaks in conductivity were shown. In addition, the dice and Lieb flat band models were studied. Notably, the flat bands always support transitions from the dispersive bands, but in the case of dice model no transitions between two dispersive bands are allowed [49]. This is in contrast to what is found for the Lieb lattice in Chapter Four.

Additional mathematical result in the Chapter is that the zitterbewe-

gung method can be applied to effective models with complicated matrix algebras. This enhances the potential applicability of a method to new systems with other pseudospin structures frequently uncovered in last years [15].

1.5.4   Chapter 5

The Fifth Chapter is devoted to the study of bilayer dice lattices. As it is known from experiments, the different stackings of the same single-atom-thick lattices give the systems with very different properties. The most prominent example is the twisted bilayer graphene [1], where the proper rotation angle between layers allowed to achieve superconductivity. The idea of the Fifth Chapter is to study more simple stackings of two identical dice lattices with different sublattices aligned on top of each other. Since the dice lattice itself has flat band in spectrum and thus contains the pseudospin-1 fermions as effective quasiparticles, it is interesting to see whether bilayer configuration would preserve such quasiparticles.

The results of the Chapter show that while the triply degenerate points are always preserved, the effective dispersion of quasiparticles might change. The classification of all commensurate simple stackings is performed and it is shown that one can achieve pseudospin-1, semi-Dirac type of dispersion (with different dispersion law - linear and quadratic depending on direction) or nodal line crossings where two bands cross each other along high-symmetry line. Also the triple points are shifted from the charge-neutrality points, which means that the pseudospin-1 quasiparticles would be accessible upon doping. The results of this Chapter show how reach physics one could obtain out of bilayer stacking of a very simple flat band model.

The studies of such multilayer systems might explain how the properties of underlying simple flat band models result in nontrivial physics observed in more complicated crystals. As an example, one could think about Kagome metals where the perfect flat-band lattice is placed as a layer of 3D crystal [23] and several such layers separated from each other are present in chemically-stable order in a sample.

1.5.5   Chapter 6

In the Sixth Chapter the discussion about the role of flat bands in magnetic properties of 2D crystals is extended to the case of high-order van

Hove singularities. As it was shown in the literature, the usual van Hove singularities lead to paramagnetic response of the system [50], the exactly flat bands in the dice lattice lead to very strong paramagnetic response [13]. The corresponding paramagnetic response is manifestedvi a Dirac delta-function shape of the orbital susceptibility as function of chemical potential. Notably, in dice lattice this paramagnetic response dominates the diamagnetic Delta-like response of Dirac cones, which was present in graphene [51].

The focus of the Chapter is concentrated on studying the role of not perfectly flat bands - high-order van Hove singulatiries, in orbital susceptibility. As an example, the square-octagon lattice is analyzed. Such lattice was expected to occur as a stable 2D graphene allotrope - T-graphene, [52], but now is studied in connection with transition-metal dichalcogenides [53]. The chapter contains detailed characterization of tight-binding model describing square-octagon lattice, effective models that have form of 1) relativistic pseudospin-1 type and 2) second-order that capture precisely dispersion of high-order saddle point. Based on these models it is shown that paramagnetic contribution from van Hove singularity is weaker than that of flat band. The numerical calculations of orbital susceptibility show that the para-to-diamagnetic phase transition is possible if the parameters of the system are tuned.

The results on orbital susceptibility presented in the chapter show that magnetic properties of van Hove singularities of different kinds are more complicated that for exactly flat bands, and the full analysis of their role in orbital susceptibility for the novel 2D materials should be performed in future.

Next follow the additional chapters that are not focused on flat bands, but are related to zero-energy modes.

1.5.6 Chapter 7

This is the first out of two chapters devoted to the study of the Majorana zero modes and Andreev bound states. The topic of this Chapter is focused on the ways of distinguishing Majorana zero modes from Majorana fermions via transport experiments.

Majorana fermions in superconductors are coherent superpositions of electrons and holes. At the same time, Majorana zero modes are collective modes related to the winding of superconducting phase field by 2π that form a vortex. Such vortex typically contains bound state at zero energy,

which is called Majorana zero mode (MZM). While Majorana fermions satisfy usual Fermi-Dirac statistics, the MZMs satisfy non-Abelian anyon statistics. The transport of MZMs is governed by edge vortices that are domain walls with phase jump π on the boundary of superconductor.

As a way to distinguish these two "Majoranas" from each other, the measurement of shot noise in two similar devices (see Fig.7.1) is proposed. The shot noise power is calculated as a charge variance per injected single electron charge. For the Majorana fermion the result is known [54] ans constitutes e^2 per injected fermion. For MZM it is found to be dependent on the separation between two vortices on the edge. Thus, the shot noise has a nonlocal nature that signatures about long-range correlations between vortices. As an experimentally measurable consequence, the voltage dependence of shot noise can be used: for Majorana fermions shot noise increases linearly with growing voltage V, while for MZM it grows as $V \log V$.

1.5.7   Chapter 8

The Eighth Chapter is devoted to the study of effect that happens very similarly for Andreev bound states and Majorana modes. This effect, firstly predicted by S-J. Choi et.al. [55] in 2020 for Majorana qubit, is manifested as appearance of sharp voltage steps in the current-voltage characteristic for DC current injected into resistively-shunted junction with qubit. Notably, while Josephson junctions with quantum dots were studied experimentally for many decades, such effect was found only now.

However, it is known that Andreev levels close to charge-neutrality point typically mimic the behavior of topological qubits with Majorana modes. The study in the Chapter is performed for current-biased, resistively shunted quantum-dot Josephson junction. One of the key properties of this system is the existence of resonant state on the quantum dot. Such state leads to the appearance of particle-hole symmetric pair of Andreev bound states with finite lifetime. The existence of gaps separating these bound states from continuum of states in superconductors and from each other allows one to achieve nontrivial dynamics of the junction.

The results presented in the Chapter are the following: the non-topological Josephson junction demonstrates similar voltage staircase (sharp steps in average voltage for slowly changing current). In addition, there is a hysteresis curve - when current is slowly increased and then decreased, averaged voltage follow different path and the stairs appear at

different absolute values of current. Also there are found several minor distinctions from Majorana qubit behavior, which shows that Andreev levels do not fully mimic the topological qubit physics, but difference are hard to measure. To make effect observable the size of gaps should be not too small - which is different to typically studied systems with closed gap between levels.

Chapter 2

RKKY interaction in a doped pseudospin-1 fermion system at finite temperature

2.1 Introduction

The Ruderman-Kittel-Kasuya-Yosida (RKKY) interaction [32–34] is an indirect exchange interaction between two localized magnetic moments mediated by a background of electrons. It is an important characteristic of electron system and a fundamental interaction responsible for magnetic ordering in spin glasses and alloys. Besides three dimensions, it has been extensively studied for the electron gas in one [56] and two [57] dimensions. After the experimental discovery of graphene, the RKKY interaction in systems with Dirac-like dispersion attracted a great interest [58–67] due to the richness of their structures. Moreover, the final results for the complete structure of the RKKY interaction in graphene were obtained only after a decade of debates [61, 68]. The RKKY interaction was studied also in strained graphene [69], bilayer graphene [70, 71], biased single-layer silicene [72], 8-Pmmn borophene [73], on the surface of three-dimensional Dirac semimetals [74].

Graphene has given a start to a proliferation of fermionic quasiparticles emerging in condensed matter systems which have no counterparts in particle physics where Poincaré symmetry constrains fermions to the three types: Dirac, Weyl, and Majorana (not discovered yet) particles with spin 1/2. In condensed matter systems, symmetries are less restric-

tive and besides fermions with pseudospin 1/2 other types of fermions with a higher pseudospin can appear in two- and three-dimensional solids. A recent paper [15] has given a classification of possible low-energy fermionic excitations protected by space group symmetries of lattices in solid state systems with spin-orbit coupling and time-reversal symmetry. The $\mathcal{T}_3$ lattice provides one of the well-known realizations of pseudospin-1 fermions in two dimensions [11, 12]. Pseudospin-1 fermions appear also in the Lieb [21] and kagome lattices [75]. Recently an experimental evidence of Dirac fermions as well as flat bands was reported in the antiferromagnetic kagome metal FeSn [23]. Also, the realizations of Lieb lattice as electronic lattice formed by the surface state electrons of Cu(111) [7] as well as the Lieb-like lattices in covalent-organic frameworks were reported [9, 10]. Fermions of different pseudospins may coexist in some lattices, for example, Dirac and pseudospin-1 fermions are found to coexist in the $\alpha - \mathcal{T}_3$ model [76], the edge-centered honeycomb lattice [77], and the 2D triangular kagome lattice [78], Weyl fermions coexist with pseudospin-1 and pseudospin-3/2 fermions in transition metal silicides [79] under the protection of crystalline symmetries.

In this work we analyze the RKKY interaction in the so-called $\alpha - \mathcal{T}_3$ model [13] which contains the mixing of Dirac and pseudospin-1 fermions as low-energy excitations. The $\alpha - \mathcal{T}_3$ model is a tight-binding model of two-dimensional fermions on the $\mathcal{T}_3$ (or dice) lattice whose atoms are situated at vertices of hexagonal lattice and the hexagons centers [11, 80]. The parameter α describes the relative strength of couplings between the honeycomb lattice sites and the central site. Thus, as α changes the $\alpha - \mathcal{T}_3$ model reveals a smooth transition from graphene ($\alpha = 0$) to dice or $\mathcal{T}_3$ lattice ($\alpha = 1$). Since the $\alpha - \mathcal{T}_3$ model has three sites per unit cell, the electron states in this model are described by three-component fermions. It is natural then that the spectrum of the model is comprised of three bands. Two of them form Dirac cones as in graphene, and the third band is completely flat, dispersionless, and has zero energy in the whole Brillouin zone [13]. All three bands meet at the K and K' points, which are situated at the corners of the Brillouin zone. In the linear order in momentum deviations from the K and K' points, the low-energy Hamiltonian of the dice model with $\alpha = 1$ describes massless pseudospin-1 fermions and is given by the scalar product of momentum and the spin-1 matrices.

Recently several physical quantities have been studied in the $\alpha - \mathcal{T}_3$

model such as orbital susceptibility [13], optical and magneto-optical conductivity [49, 81–83], magnetotransport [76, 84–86]. The role of transverse magnetic field on *zitterbewegung* was studied in Ref.[87] and the enhancement of thermoelectric properties of a nanoribbon made of $\alpha - \mathcal{T}_3$ model was discussed in a recent paper [88]. The stability of flat band with respect to different perturbations such as terminations of the lattice as well as the phenomenon of atomic collapse the Coulomb field of the charged impurity were studied in Refs.[14, 89, 90].

The presence of completely flat energy band is a remarkable feature of the considered model, for example, it results in strong paramagnetic response in a magnetic field [13]. In general, the Fermi systems hosting flat bands attract a lot of attention last time because quenching of the kinetic energy strongly enhances the role of electron-electron and other interactions and may lead to the realization of many very interesting correlated states. The most striking recent example is the observation of superconductivity in twisted bilayer graphene [6] when tuned to special "magic angles" at which isolated and relatively flat bands appear. The three-bands models with a flat band found their applicability in many physical systems (see, for example, reviews [91, 92]), surprisingly even for the description of equatorial waves [93]. The special role of flat zero Landau level on RKKY interaction in graphene was analyzed in Ref.[63].

The RKKY interaction of impurities placed on dice lattice demonstrates larger richness compared to graphene. As in case of graphene, the RKKY interaction can be written as a product of oscillating part $f_{ab}(\mathbf{R})$ resulting from intervalley scattering times an interaction integral $I(R)$ (a, b refer to sublattices A, B, C). We show that while some relative locations of impurities can be reduced to graphene case (multiplied by α dependent coefficients), there is also a new type of interaction. Like in graphene, the RKKY interaction in undoped $\alpha - \mathcal{T}_3$ model decays as $1/R^3$ while there are envelope oscillations for finite doping at large distances. We also show that in some cases the flat band gives an essential contribution in the RKKY interaction, especially for the undoped case and small temperature.

The paper is organized as follows: In Sec.2.2 we discuss a general expression for the RKKY interaction. In Sec.2.3 we describe the general properties of the $\alpha - \mathcal{T}_3$ model and derive the corresponding Green functions in the mixed real space - frequency representation. In Sec.2.4 we calculate the RKKY interaction for impurities placed on different sublat-

tices of dice lattice, concentrating on the most interesting case of impurity positions which is absent in graphene. In Appendix 2.6 we present the expression for the retarded Green's function of pseudospin-1 excitations near K points. In Appendices 2.7 and 2.8 we derive the exact expressions for interaction integrals in terms of Mellin-Barnes type integrals.

2.2   Basic formulas

Generally, the RKKY interaction defined by second-order correction to the free energy $\delta F = \frac{1}{2}T\,\mathrm{Tr}\,VG_0VG_0$, where trace goes over all degrees of freedom. Here the free Green function is defined by the standard tight-binding or low energy Hamiltonian, which contains contributions from both valleys. The interaction potential of impurity and electron spins is given by [63, 65]

$$V^{(\mu_1,\mu_2)} \equiv V^{(\mu_1)} + V^{(\mu_2)} = -\lambda\left[\mathbf{S}_1 \cdot \mathbf{s}\,\delta\left(\mathbf{r} - \mathbf{R}_1\right) P_{\mu_1} + \mathbf{S}_2 \cdot \mathbf{s}\,\delta\left(\mathbf{r} - \mathbf{R}_2\right) P_{\mu_2}\right],$$
(2.1)

where $\mathbf{S}_i$ are the spin operators of impurities and $\mathbf{s} = \hbar\boldsymbol{\sigma}/2$ is the spin of itinerant electrons. The spin-spin coupling constant can be estimated as $\lambda \simeq 1\mathrm{eV}$. The sublattice projectors are denoted by P_μ, and can be written as the following diagonal matrices $P_A = \mathrm{diag}(1,0,0), \quad P_C = \mathrm{diag}(0,1,0)$ and $P_B = \mathrm{diag}(0,0,1)$. The contribution, which accounts for the interaction between two different spins, is given by

$$\delta F_{12} = \frac{\lambda^2\hbar^2}{2}\boldsymbol{S}_1\boldsymbol{S}_2 \int\limits_0^{1/T} d\tau\,\mathrm{tr}\left[P_{\mu_1}G_0(\boldsymbol{R}_1,\boldsymbol{R}_2;\tau)P_{\mu_2}G_0(\boldsymbol{R}_2,\boldsymbol{R}_1;-\tau)\right]. \tag{2.2}$$

Using the following Fourier decomposition of imaginary-time Green function,

$$G_0(\tau) = T\sum_n G_0\left(i\omega_n\right)e^{-i\omega_n\tau}, \quad \omega_n = (2n+1)\pi T, \tag{2.3}$$

we can replace the integral over imaginary time τ by $T\sum\limits_{i\omega_n}$. For example, for δF_{12} we get

$$\delta F_{12} = \frac{\lambda^2\hbar^2}{2}\boldsymbol{S}_1\boldsymbol{S}_2 T\sum_n \mathrm{tr}\left[P_{\mu_1}G_0(\boldsymbol{R}_1,\boldsymbol{R}_2;i\omega_n+\mu)P_{\mu_2}G_0(\boldsymbol{R}_2,\boldsymbol{R}_1;i\omega_n+\mu)\right],$$
(2.4)

where we introduced the chemical potential μ. Performing the sum over the Matsubara frequencies by means of the formula

$$T \sum_n f(i\omega_n) = - \int\limits_{-\infty}^{\infty} \frac{d\omega}{\pi} n_F(\omega) \mathrm{Im} f^R(\omega + i\varepsilon), \qquad (2.5)$$

where $n_F(\omega) = 1/(\exp(\omega/T) + 1)$ is the Fermi distribution function and superscript R denotes retarded function. Hence we find an effective RKKY interaction between two magnetic impurities with the spins $\mathbf{S}_1$, and $\mathbf{S}_2$, sitting at the positions $\mathbf{R}_1$ and $\mathbf{R}_2$

$$\delta F_{12} = J_{\mu_1 \mu_2} \mathbf{S}_1 \mathbf{S}_2, \quad J_{\mu_1 \mu_2} = (\lambda^2 \hbar^2/4) \chi_{\mu_1 \mu_2}(\mathbf{R}_1, \mathbf{R}_2), \qquad (2.6)$$

where χ is the spin-independent susceptibility, however, it depends upon whether atoms belong to the same or different sublattices.

$$\chi_{\mu_1 \mu_2}(\mathbf{R}_1, \mathbf{R}_2) = \qquad\qquad\qquad\qquad\qquad\qquad\qquad\qquad (2.7)$$
$$- \frac{2}{\pi} \int\limits_{-\infty}^{\infty} d\omega \, n_F(\omega) \mathrm{Im} \, \mathrm{tr} \left[P_{\mu_1} G_0(\mathbf{R}_1, \mathbf{R}_2; \omega + \mu) P_{\mu_2} G_0(\mathbf{R}_2, \mathbf{R}_1; \omega + \mu) \right].$$

After calculating the trace, the role of projectors is reduced to taking specific components of Green functions $G_{\mu_1 \mu_2}$ and $G_{\mu_2 \mu_1}$.

2.3   Green function of the $\alpha - \mathcal{T}_3$ model

The lattice Green's function in the tight-binding approximation for $\alpha - \mathcal{T}_3$ model Hamiltonian (1.3) is given by

$$G_0(\omega, \mathbf{k}) = (\omega - H_0(\mathbf{k}))^{-1} = \frac{1}{\omega \left(\omega^2 - |f(\mathbf{k})|^2 \right)} \times$$
$$\begin{pmatrix} \omega^2 - \sin^2 \Theta \, |f(\mathbf{k})|^2 & \omega \cos \Theta f(\mathbf{k}) & \frac{1}{2} \sin(2\Theta) f(\mathbf{k})^2 \\ \omega \cos \Theta f^*(\mathbf{k}) & \omega^2 & \omega \sin \Theta f(\mathbf{k}) \\ \frac{1}{2} \sin(2\Theta) f^*(\mathbf{k})^2 & \omega \sin \Theta f^*(\mathbf{k}) & \omega^2 - \cos^2 \Theta |f(\mathbf{k})|^2 \end{pmatrix}. \qquad (2.8)$$

In the low-energy model near the $K(K')$ points ($\xi = \pm$), it can be decomposed as

$$G_0^\xi(\omega, \boldsymbol{k}) = \frac{1}{\omega\left(\omega^2 - (\hbar v_F \boldsymbol{k})^2\right)} \times \tag{2.9}$$

$$\begin{pmatrix} \omega^2 - \sin^2\Theta\hbar^2 v_F^2 \boldsymbol{k}^2 & \omega\cos\Theta\hbar v_F k_{-,\xi} & \frac{\sin(2\Theta)}{2}(\hbar v_F k_{-,\xi})^2 \\ \omega\cos\Theta\hbar v_F k_{+,\xi} & \omega^2 & \omega\sin\Theta\hbar v_F k_{-,\xi} \\ \frac{\sin(2\Theta)}{2}(\hbar v_F k_{+,\xi})^2 & \omega\sin\Theta\hbar v_F k_{+,\xi} & \omega^2 - \cos^2\Theta(\hbar v_F \boldsymbol{k})^2 \end{pmatrix},$$

with notation $k_{\pm,\xi} = \xi k_x \pm i k_y$. As was shown in Sec.2.2, the representation of Green's function in the mixed coordinate-frequency variables $(\boldsymbol{r}, \omega)$ is the most useful for the calculation of susceptibility, and related to Eq.(2.9) by Fourier transformation over wave number $\boldsymbol{k}$. The Fourier transform of full retarded low-energy Green's function should contain contributions from both valleys

$$G_0(\boldsymbol{R}_1, \boldsymbol{R}_2, \omega) = \frac{1}{\Omega_{BZ}} \int \frac{d^2q}{(2\pi)^2} e^{i\boldsymbol{q}\cdot(\boldsymbol{R}_1 - \boldsymbol{R}_2)}$$

$$\times \left[e^{i\boldsymbol{K}(\boldsymbol{R}_1 - \boldsymbol{R}_2)} G_0(\boldsymbol{q} + \boldsymbol{K}, \omega) + e^{i\boldsymbol{K}'(\boldsymbol{R}_1 - \boldsymbol{R}_2)} G_0\left(\boldsymbol{q} + \boldsymbol{K}', \omega\right) \right], \tag{2.10}$$

where K and K' are any two adjacent Dirac points in the Brillouin zone, and $\Omega_{BZ} = \frac{2}{3\sqrt{3}d^2}$ is the area of the BZ. Replacing wave number by derivative in the matrix part of (2.9), and performing integration as shown in Appendix 2.6, we obtain the Green function in valley ξ:

$$G_0^R(\mathbf{R}_1 - \mathbf{R}_2, \omega, \xi) = \frac{1}{\Omega_{BZ}} \frac{\omega}{4(\hbar v_F)^2} \times$$

$$\begin{pmatrix} -i\cos^2\Theta H_0^{(1)}(z) & \cos\Theta\xi e^{-i\xi\phi}H_1^{(1)}(z) & \frac{i\sin(2\Theta)}{2}e^{-2i\xi\phi}H_2^{(1)}(z) \\ \cos\Theta\xi e^{i\xi\phi}H_1^{(1)}(z) & -iH_0^{(1)}(z) & \sin\Theta\xi e^{-i\xi\phi}H_1^{(1)}(z) \\ \frac{i\sin(2\Theta)}{2}e^{2i\xi\phi}H_2^{(1)}(z) & \sin\Theta\xi e^{i\xi\phi}H_1^{(1)}(z) & -i\sin^2\Theta H_0^{(1)}(z) \end{pmatrix},$$
$$\tag{2.11}$$

where we used notation $z = |\mathbf{R}|(\omega + i\varepsilon)/\hbar v_F$, and $H_n^{(1)}(z)$ is the Hankel function of the first kind. The polar angle of the vector $\boldsymbol{R}_1 - \boldsymbol{R}_2$ is denoted by ϕ. Below we insert Eq.(2.11) into (2.10) and then calculate susceptibility and the RKKY interaction via Eq.(2.7) in all 6 relative positions of impurities AA, AB, BB, AC, BC, CC.

In addition, it is important to note that the second quantized tight-binding Hamiltonian of $\alpha - \mathcal{T}_3$ model

$$\hat{\mathcal{H}} = \int\limits_{BZ} \frac{d^2k}{(2\pi)^2} \hat{\Psi}_{\boldsymbol{k}}^{\dagger} H_0(\boldsymbol{k}) \hat{\Psi}_{\boldsymbol{k}} \tag{2.12}$$

possesses the particle-hole symmetry, which is realized by antiunitary operator $\hat{\mathcal{C}}$. It acts on the second quantized wave functions $\hat{\Psi}$ as

$$\hat{\mathcal{C}}\hat{\Psi}\hat{\mathcal{C}}^{-1} = S\hat{\Psi}^*, \quad S = \mathrm{diag}(1, -1, 1). \tag{2.13}$$

The invariance of the Hamiltonian $\hat{\mathcal{H}}$ under the particle-hole symmetry, $\hat{\mathcal{C}}\hat{\mathcal{H}}\hat{\mathcal{C}}^{-1} = \hat{\mathcal{H}}$, is guaranteed if the following condition is satisfied:

$$SH_0(\boldsymbol{k})S = -H_0(\boldsymbol{k}), \tag{2.14}$$

which is automatically fulfilled for the momentum space Hamiltonian in Eq.(1.3). Below we show that this symmetry gives restrictions on the sign of the RKKY interactions, similar to the graphene case considered in Ref.[59].

2.4 RKKY interaction of impurities on dice lattice

As was noted before, there are 6 different relative positions of impurities. The corresponding exchange interactions are

$$J_{AA}(\boldsymbol{R}) = \frac{4C}{\hbar^2 v_F^2} \cos^4 \Theta f_{AA}(\boldsymbol{R}) I_0(R, \mu, T), \tag{2.15}$$

$$J_{BB}(\boldsymbol{R}) = \frac{4C}{\hbar^2 v_F^2} \sin^4 \Theta f_{BB}(\boldsymbol{R}) I_0(R, \mu, T), \tag{2.16}$$

$$J_{CC}(\boldsymbol{R}) = \frac{4C}{\hbar^2 v_F^2} f_{CC}(\boldsymbol{R}) I_0(R, \mu, T), \tag{2.17}$$

$$J_{AC}(\boldsymbol{R}) = \frac{4C}{\hbar^2 v_F^2} \cos^2 \Theta f_{AC}(\boldsymbol{R}) I_1(R, \mu, T), \tag{2.18}$$

$$J_{BC}(\boldsymbol{R}) = \frac{4C}{\hbar^2 v_F^2} \sin^2 \Theta f_{BC}(\boldsymbol{R}) I_1(R, \mu, T), \tag{2.19}$$

$$J_{AB}(\boldsymbol{R}) = \frac{C}{\hbar^2 v_F^2} \sin^2(2\Theta) f_{AB}(\boldsymbol{R}) I_2(R, \mu, T). \tag{2.20}$$

In these expressions we introduced short-hand notations $\boldsymbol{R} = \boldsymbol{R}_1 - \boldsymbol{R}_2$ and $C = 3\lambda^2\hbar^2 d^2/64\pi t^2$. The temperature-independent functions $f_{\mu_1\mu_2}$ describe oscillations from contribution of different K points for impurities placed on μ_1 and μ_2 sublattices

$$f_{\mu\mu}(\boldsymbol{R}) = 1 + \cos\left(\boldsymbol{K} - \boldsymbol{K}'\right)\boldsymbol{R}, \tag{2.21}$$
$$f_{AB}(\boldsymbol{R}) = 1 + \cos[(\boldsymbol{K} - \boldsymbol{K}')\boldsymbol{R} - 4\phi],$$
$$f_{BA}(\boldsymbol{R}) = 1 + \cos[(\boldsymbol{K} - \boldsymbol{K}')\boldsymbol{R} + 4\phi], \tag{2.22}$$
$$f_{AC}(\boldsymbol{R}) = f_{CB}(\boldsymbol{R}) = 1 - \cos((\boldsymbol{K} - \boldsymbol{K}')\boldsymbol{R} - 2\phi), \tag{2.23}$$
$$f_{BC}(\boldsymbol{R}) = f_{CA}(\boldsymbol{R}) = 1 - \cos((\boldsymbol{K} - \boldsymbol{K}')\boldsymbol{R} + 2\phi). \tag{2.24}$$

The functions $f_{\mu_1\mu_2}$ are the only ones which depend on the direction of the vector $\mathbf{R}$ while other functions are direction-independent. In the graphene limit, $\Theta = 0$ or $\Theta = \pi/2$, only three interactions are left, which correspond to coupled lattices C and A (B). The AB interaction type vanishes in both graphene cases and reaches its maximum value in dice model $\Theta = \pi/4$.

The frequency integrals on the right-hand side of the expressions are

$$I_n(R, \mu, T) = \int_{-\infty}^{\infty} \frac{d\omega f(\omega)}{e^{\frac{\omega-\mu}{T}} + 1}, \tag{2.25}$$
$$f(\omega) = \text{Im}\left[(\omega + i\varepsilon)^2 \left(H_n^{(1)}\left(\frac{(\omega + i\varepsilon)R}{\hbar v_F}\right)\right)^2\right].$$

We find that the most interesting is the AB case, which cannot be reduced to any known graphene cases due to the lattice geometry, which corresponds to the appearance of the $H_2^{(1)}(z)$ function. For the functions $H_0^{(1)}(z + i\varepsilon)$ and $H_1^{(1)}(z + i\varepsilon)$ we can take the limit $\varepsilon \to 0$ in the integrand, however, this is not the case for $H_2^{(1)}(z + i\varepsilon)$ due to its more singular behavior when $z \to 0$ which is a reflection of a special role of the flat band with $\omega = 0$. Near $\omega = 0$ we find the singular term in the following integral

$$(\omega + i\varepsilon)^2 \left(H_2^{(1)}\left(\frac{(\omega + i\varepsilon)R}{\hbar v_F}\right)\right)^2 \simeq -\frac{16(\hbar v_F)^4}{\pi^2 R^4(\omega + i\varepsilon)^2} - \frac{8(\hbar v_F)^2}{\pi^2 R^2}, \quad (2.26)$$

hence

$$\text{Im}\left[(\omega + i\varepsilon)^2 \left(H_2^{(1)}\left(\frac{(\omega + i\varepsilon)R}{\hbar v_F}\right)\right)^2\right] \simeq \frac{32\varepsilon\omega(\hbar v_F)^4}{\pi^2 R^4(\omega^2 + \varepsilon^2)^2};$$
$$\frac{32\varepsilon\omega(\hbar v_F)^4}{\pi^2 R^4(\omega^2 + \varepsilon^2)^2} \to -\frac{16(\hbar v_F)^4}{\pi R^4}\delta'(\omega), \quad \varepsilon \to 0. \tag{2.27}$$

Adding and subtracting the term $16(\hbar v_F)^4/\pi^2 R^4(\omega + i\varepsilon)^2$ in the expression

$$I_2(R, \mu, T) = \int\limits_{-\infty}^{\infty} \frac{d\omega}{e^{\frac{\omega-\mu}{T}} + 1} \, \text{Im} \left[(\omega + i\varepsilon)^2 \left(H_2^{(1)} \left(\frac{(\omega + i\varepsilon)R}{\hbar v_F} \right) \right)^2 + \right.$$

$$\left. + \frac{16(\hbar v_F)^4}{\pi^2 R^4(\omega + i\varepsilon)^2} - \frac{16(\hbar v_F)^4}{\pi^2 R^4(\omega + i\varepsilon)^2} \right], \tag{2.28}$$

we can safely take the limit $\varepsilon = 0$ for the first two terms in the square brackets while the third term produces an additional contribution

$$I_2(R, \mu, T) = \int\limits_{-\infty}^{\infty} \frac{d\omega \omega^2}{e^{\frac{\omega-\mu}{T}} + 1} \, \text{Im} \left[\left(H_2^{(1)} \left(\frac{\omega R}{\hbar v_F} \right) \right)^2 \right] - \frac{4(\hbar v_F)^4}{\pi R^4} \frac{1}{T \cosh^2 \frac{\mu}{2T}}. \tag{2.29}$$

For finite μ the additional term does not contribute in the zero temperature limit, $T \to 0$, while at zero chemical potential, $\mu = 0$, it gives a divergent contribution $\sim -1/T$.

The evaluation of the integral (2.25) with $\varepsilon = 0$ represents a nontrivial task due to the combination of Bessel functions. It can be written as

$$I_n(R, \mu, T) = 2 \left(\frac{\hbar v_F}{R} \right)^3 \int\limits_0^{\infty} dx x^2 J_n(x) Y_n(x) \left(\frac{1}{z e^{x/a} + 1} + \frac{z}{e^{x/a} + z} - 1 \right), \tag{2.30}$$

where $a = \frac{TR}{\hbar v_F}$ and $z = e^{-\mu/T}$. The last term in brackets is divergent at the upper limit, that corresponds to physical divergence at $\omega = -\infty$ in Eq.(2.25). In such a case one can introduce frequency cut-off, or another well defined regularization [59, 61]. We choose the regularization by replacing x^2 by $x^{\alpha-1}$ and take the limit $\alpha = 3$ only in finite expressions. We checked that the frequency cut-off regularization gives the same result. Eq.(2.30) is written in terms of the corresponding more general integral $I(\alpha, \nu, z, a)$, Eq.(2.65), studied in Appendix 2.7, as follows

$$I_n(R, \mu, T) = \left(\frac{\hbar v_F}{R} \right)^3 I(\alpha = 3, n, z, a), \quad n = 0, 1,$$

$$I_2(R, \mu, T) = \left(\frac{\hbar v_F}{R} \right)^3 \left[I(\alpha = 3, n = 2, z, a) - \frac{4\hbar v_F}{\pi R T} \frac{1}{\cosh^2(\mu/2T)} \right]. \tag{2.31}$$

Generally, the answer can be expressed as inverse Mellin transform (see Eq.(2.74) or (2.79)) which is suitable for studying different physically relevant asymptotics such as low and high temperature expansions, or the behavior at large distances R.

2.4.1   Small temperature expansion

To find small temperature corrections at finite chemical potential, one can apply the Sommerfeld expansion for the frequency integral (2.25) rewriting it in the form

$$I_n(R, \mu, T) = \int\limits_{-\infty}^{\mu} d\omega\, f(\omega) + T \int\limits_{0}^{\infty} \frac{dx[f(\mu + Tx) - f(\mu - Tx)}{e^x + 1}$$

$$\simeq \int\limits_{-\infty}^{\mu} d\omega\, f(\omega) + \frac{\pi^2 T^2}{6} f'(\mu) + O\left(\frac{T}{\mu}\right)^4. \qquad (2.32)$$

Using the first equality, one can evaluate interaction numerically. As discussed in Appendix 2.7, we can find all terms of the expansion in powers of T/μ. Here we present only two lowest terms of this expansion, which are given by (2.85).

$$I_n(R, \mu, T) = \left(\frac{\hbar v_F}{R}\right)^3 \left[\frac{1}{\sqrt{\pi}} G_{24}^{30}\left((k_F R)^2 \Big|\begin{array}{c} 2, 1 \\ 0, \frac{3}{2}, \frac{3}{2} + n, \frac{3}{2} - n \end{array}\right) \right.$$

$$\left. + \frac{2\pi^{3/2} T^2}{3\mu^2} G_{24}^{30}\left((k_F R)^2 \Big|\begin{array}{c} 2, \frac{1}{2} \\ \frac{3}{2}, \frac{3}{2}, \frac{3}{2} + n, \frac{3}{2} - n \end{array}\right) \right], \qquad (2.33)$$

where we defined the Fermi momentum as $k_F = \mu/\hbar v_F$. Clearly, non-analytic in the temperature term in I_2 (2.31) does not contribute in the Sommerfeld expansion. For zero temperature, using the value of Meijer function at zero argument,

$$G_{24}^{30}\left(0 \Big|\begin{array}{c} 2, 1 \\ 0, \frac{3}{2}, \frac{3}{2} + n, \frac{3}{2} - n \end{array}\right) = \frac{(4n^2 - 1)\sqrt{\pi}}{8}, \qquad (2.34)$$

we get for exchange integrals of undoped $\alpha - \mathcal{T}_3$ system

$$J_{AA}^0(\mathbf{R}) = -\frac{\hbar v_F \cos^4 \Theta}{2R^3} C f_{AA}(\mathbf{R}), \quad J_{AC}^0(\mathbf{R}) = \frac{3\hbar v_F \cos^2 \Theta}{2R^3} C f_{AC}(\mathbf{R}),$$

$$J_{AB}^0(\mathbf{R}) = \frac{15\hbar v_F \sin^2(2\Theta)}{8R^3} C f_{AB}(\mathbf{R}). \qquad (2.35)$$

For $\Theta = 0$, $J_{AA}^0(\mathbf{R})$ and $J_{AC}^0(\mathbf{R})$ coincide with expressions derived in [61, 68]. [Note that our definition of the constant C coincides up to a sign with Ref.[68] while Ref.[61] uses a different definition.] The minus sign for the exchange interaction means ferromagnetic coupling for spins while the positive sign corresponds to antiferromagnetic one. We see that couplings J_{AB}^0, J_{AC}^0 describing the interaction of impurities on different sublattices are of antiferromagnetic nature in undoped $\alpha - \mathcal{T}_3$ system, like in the case of graphene [58, 59, 61]. For angles Θ close to $\pi/4$ (dice model) the coupling J_{AB}^0 is significantly larger than graphene-like couplings: $|J_{AB}^0| > |J_{AC}^0| > |J_{AA}^0|$. All couplings feature $1/R^3$ behavior familiar in graphene.

At finite doping, the short distance (or small k_F) behavior is given by

$$J_{AA}(\mathbf{R}) = J_{AA}^0(\mathbf{R}) \left[1 - \frac{32(k_F R)^3}{3\pi} \left(\ln\left(\frac{k_F R}{2}\right) + \gamma - \frac{1}{3} \right) \right] \quad (2.36)$$

$$J_{AC}(\mathbf{R}) = J_{AC}^0(\mathbf{R}) \left[1 - \frac{16(k_F R)^3}{9\pi} \right], \quad (2.37)$$

$$J_{AB}(\mathbf{R}) = J_{AB}^0(\mathbf{R}) \left[1 - \frac{8(k_F R)^3}{45\pi} \right]. \quad (2.38)$$

Expanding Eq.(2.33) at large values $k_F R$, we find the following results for the exchange interactions when both impurities are on the same sublattice AA or couple to different sublattices (AC and AB, for example):

$$J_{AA}(\boldsymbol{R}, \mu, T) = \frac{8}{\pi} J_{AA}^0(\boldsymbol{R}) \left[k_F R \sin(2k_F R) + \frac{1}{4} \cos(2k_F R) \right.$$
$$\left. - \frac{2\pi^2 T^2 R^2}{3(\hbar v_F)^2} \left(k_F R \sin(2k_F R) - \frac{3}{4} \cos(2k_F R) \right) \right], \quad (2.39)$$

$$J_{AC}(\boldsymbol{R}, \mu, T) = \frac{8}{3\pi} J_{AC}^0(\boldsymbol{R}) \left[k_F R \sin(2k_F R) + \frac{5}{4} \cos(2k_F R) \right.$$
$$\left. - \frac{2\pi^2 R^2 T^2}{3(\hbar v_F)^2} \left(k_F R \sin(2k_F R) + \frac{1}{4} \cos(2k_F R) \right) \right], \quad (2.40)$$

$$J_{AB}(\boldsymbol{R}, \mu, T) = -\frac{8}{15\pi} J_{AB}^0(\boldsymbol{R}) \left[k_F R \sin(2k_F R) + \frac{17}{4} \cos(2k_F R) \right.$$
$$\left. - \frac{2\pi^2 T^2 R^2}{3(\hbar v_F)^2} \left(k_F R \sin(2k_F R) + \frac{13}{4} \cos(2k_F R) \right) \right]. \quad (2.41)$$

One should note that the exchange interactions oscillate with a distance R. The terms with $\sin(2k_F R)$ in square brackets are equal in all cases while
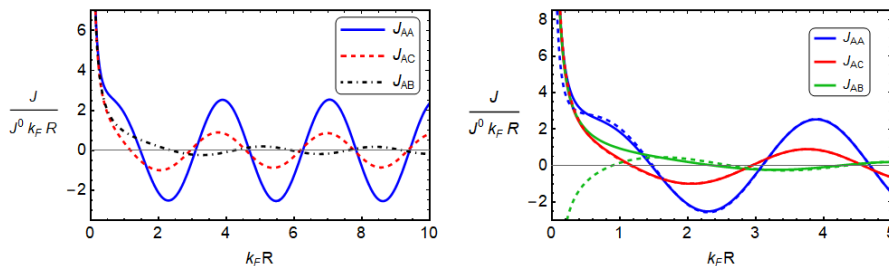
Figure 2.1. RKKY interactions as functions of $k_F R$ at zero temperature and finite chemical potential calculated through Meijer G-functions. (Left panel) RKKY interactions normalized to their values at $\mu = 0$ and divided by $k_F R$. (Right panel) RKKY interactions (solid lines) versus their asymptotic expansions, Eqs.(2.39)-(2.41), at $T = 0$ (dashed lines) with the same normalizations.

more decreasing terms with $\cos 2k_F R$ are different and have the largest amplitude in case of magnetic impurities situated on sublattices A and B. Zero temperature behavior is given by first two oscillating factors in square brackets. A comparison of Eqs.(2.39)-(2.41) with the exact formulas (2.33) shows that these asymptotic expressions work quite well for $k_F R > 0.5$ in AA case and $k_F R > 1.5$ in AB case (the right panel in Fig.2.1). We note that while the normalized couplings J_{AA}/J_{AA}^0, J_{AC}/J_{AC}^0 oscillate in phase, the coupling J_{AB}/J_{AB}^0 oscillates out of phase (see left panel in Fig.2.1). Physically this is related to the fact that A atom does not interact directly with B atom but only indirectly via the hub atom C.

We also compare the Sommerfeld expansion (2.33) with numerically calculated interaction (via the first expression in (2.32)) at temperature $T = 50\,\mathrm{K}$ and chemical potential $\mu = 0.1\,\mathrm{eV}$ (see Fig.2.2). The approximations work very well in a large interval of distances. As one can see from the asymptotic expressions (2.39)-(2.41), the temperature correction grows with distance. Thus, when $\frac{2\pi^2 T^2 R^2}{3(\hbar v_F)^2} \sim 0.5$, the next terms in expansion (2.82) become important.

2.4.2 Large distance behavior at finite temperature

In this section we present an exchange interaction in physically relevant case of large distances and finite temperature, thus obtaining more general asymptotic than in Eqs.(2.39)-(2.41). For this purpose we use the general expansion in powers of T/μ (See Eq.(2.87) in Appendix 2.7). However,
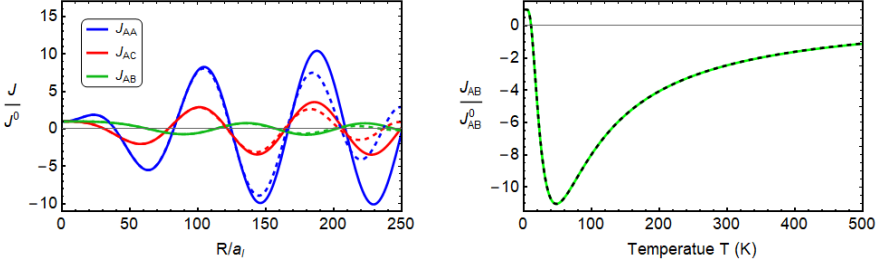
Figure 2.2. (Left panel) Numerically calculated interactions (solid lines) are compared with the second-order Sommerfeld expansion (2.33) (dashed lines). The chemical potential equals $\mu = 0.1\,\text{eV}$ and temperature $T = 50\,\text{K}$. Distances are measured in terms of the lattice constant $a_l = \sqrt{3}d = 0.246\,\text{nm}$. The expansion parameter in Eq.(2.82) equals $\frac{2\pi T}{\mu} \approx 0.3$. (Right panel) AB interaction at $R = 20a_l$ and $\mu = 0.01\,\text{eV}$ (solid line) and Sommerfeld expansion Eq.(2.33) with additional term from Eq.(2.29) (dashed line). The nonmonotonic dependence on temperature comes from an additional term in integral (2.29), while the nonsingular part remains constant due to very small value of $(k_F R)^2$. Also we note that the sign of interaction changes with temperature.

instead of taking several terms of this expansion we sum up the leading asymptotic terms in series. The obtained Eq.(2.91) allows us to recover approximations similar to those in Ref.[68] using one general expression. Here we present the result for the new AB-type interaction integral

$$J_{AB}(\boldsymbol{R}, \mu, T) = -\frac{8}{15} J_{AB}^0(\boldsymbol{R}) \frac{R}{\hbar v_F} F_1 \left[k_F R \sin\left(2k_F R\right) + \frac{15}{4} \cos\left(2k_F R\right) \right.$$
$$\left. + \frac{\pi R}{\hbar v_F} F_2 \cos\left(2k_F R\right) \right], \tag{2.42}$$

where we used the following definitions in analogy with Ref.[68]:

$$F_1 = \frac{T}{\sinh\left(\frac{2\pi T R}{\hbar v_F}\right)}, \quad F_2 = \frac{T}{\tanh\left(\frac{2\pi T R}{\hbar v_F}\right)}. \tag{2.43}$$

Again in this case the term with $\cos(2k_F R)$ in square brackets has much larger magnitude comparing to the other two interactions J_{AA}, J_{AC}, which are similar to graphene case in [68]. This is an interesting property of AB-type interaction.

As was mentioned in Ref.[68], the term which is proportional to the product $F_1 F_2$ should have a nonmonotonic dependence on temperature.

Here we should note that depending on relative distance between impurities, other terms in square brackets in Eq.(2.42) can destroy this effect.

2.4.3   Zero chemical potential

The results in the case of zero chemical potential are not given in the literature in its fullest form even for graphene. Only partial results can be found in the recent paper [64]. Here we discuss the asymptotics for low and high temperature which follow from expansion of the expression (2.79).

Firstly, we start from the low temperature limit. In fact, it is easier to determine a low temperature expansion of the integral (2.25) itself. Making replacement $x \to ax$ in Eq.(2.69), we find

$$I_n(\mu = 0) = \left(\frac{\hbar v_F}{R}\right)^3 \left[-2C_{2,n} + 4a^3 \int_0^\infty \frac{x^2 dx}{e^x + 1} J_n(ax) Y_n(ax)\right], \quad (2.44)$$

where a is defined in Eq.(2.30). Expanding the product of Bessel functions near zero, and then performing integration over x, we find the following expressions for interactions:

$$J_{AA}(\boldsymbol{R}, 0, T) = J_{AA}^0(\boldsymbol{R}) \times$$
$$\left[1 + \frac{16}{\pi}a^3 \left(-6\zeta(3)\ln(a) - 6\zeta'(3) + \zeta(3)(\ln(16) - 9)\right)\right], \quad (2.45)$$

$$J_{AC}(\boldsymbol{R}, 0, T) = J_{AC}^0(\boldsymbol{R}) \left[1 - \frac{16a^3\zeta(3)}{\pi}\right], \quad (2.46)$$

$$J_{AB}(\boldsymbol{R}, 0, T) = J_{AB}^0(\boldsymbol{R}) \left[1 - \frac{32}{15\pi a} - \frac{8a^3\zeta(3)}{5\pi}\right], \quad (2.47)$$

where $\zeta(x)$ denotes the Riemann zeta-function. Note that the leading temperature correction is of order T^3 (or $T^3 \log T$) instead of T^2 in the case of finite chemical potential (see left panel in Fig.2.3). In addition one should note the presence of singular $1/T$ term in the AB interaction. As was shown in Eqs.(2.26)-(2.29), this term comes from singular behavior of H_2 function, and is related to the effects of flat band. The effect of this term is demonstrated on right panel in Fig.2.3. Such singular behavior of the AB interaction at low temperature can be used as a benchmark of

flat band physics in experiment, for example, in the recently discovered systems [7, 23].

The case of high temperatures (or large distances) is much more complicated. The details of calculation are presented in Appendix 2.8, and here we present main results for the AA, AC and AB cases:

$$J_{AA}(\boldsymbol{R}, 0, T) = J_{AA}^0(\boldsymbol{R}) \frac{16a^2}{\sinh(2\pi a)} \left(\frac{\pi}{\tanh(2\pi a)} - \frac{1}{4a} \right), \qquad (2.48)$$

$$J_{AC}(\boldsymbol{R}, 0, T) = J_{AC}^0(\boldsymbol{R}) \frac{16a^2}{3\sinh(2\pi a)} \left(\frac{\pi}{\tanh(2\pi a)} + \frac{3}{4a} \right), \qquad (2.49)$$

$$J_{AB}(\boldsymbol{R}, 0, T) = -J_{AB}^0(\boldsymbol{R}) \frac{16a^2}{15\sinh(2\pi a)} \left(\frac{\pi}{\tanh(2\pi a)} + \frac{15}{4a} \right). \qquad (2.50)$$

The main difference between the last expression for the AB interaction and the AA, AC cases is the changed sign of interaction in Eq.(2.50) comparing to Eq.(2.47). This change comes from the additional term in Eq.(2.29), which is related to existence of flat band, and exactly cancels $1/R^4$ term in integral, see Appendix 2.8. As is seen, all exchange interactions exponentially decrease at large $RT \gg 1$ in the absence of doping. Mathematically this comes from the structure of Mellin-Barnes integral (2.93), for details we refer the reader to Appendix 2.8.
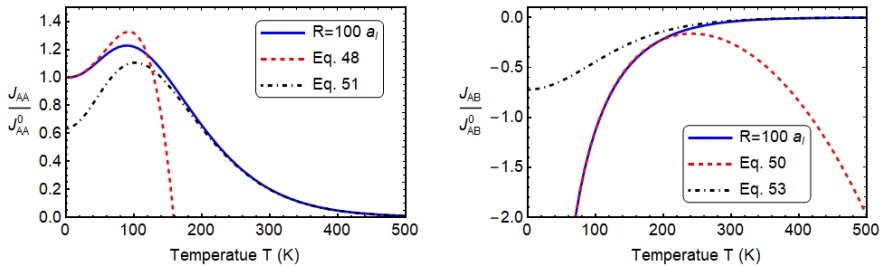
Figure 2.3. Temperature dependence of normalized interactions AA and AB is compared with asymptotic expressions at small values of parameter a (2.45),(2.47) and expansions (2.48), (2.50) at large values of a. (Left panel) Non-monotonic behavior of J_{AA} integral, which was discussed in detail in Ref.[68]. (Right panel) Behavior of relative AB interaction, which has opposite sign comparing to J_{AB}^0 at zero doping, and becomes very strong as T goes to 0. Such behavior represents a special feature of the $\alpha - T_3$ model and is directly related to the existence of flat band.

.

2.4.4　Sign of interaction at zero chemical potential and temperature

For completeness it is worth noting the sign difference between $J_{AB}^0(\boldsymbol{R})$ and the limit $a \to 0$ in Eq.(2.47) (which is divergent). For bipartite lattices, the signs of interactions $J^0(\boldsymbol{R})$ in undoped case and for zero temperature are fixed by general considerations based on particle-hole symmetry, which result in theorem proved in [59] (and generalized in [71]). Here we find that the same arguments with particle-hole symmetry (2.13) contain subtleties, which do not allow to fix the sign of J_{AB}^0.

Using the fact that the ground state is particle-hole symmetric, we find the following symmetry restriction for Green's function:

$$G_0(\boldsymbol{R}_1 - \boldsymbol{R}_2, \tau_1 - \tau_2) = \left\langle \hat{\mathcal{C}} \Psi_1(\boldsymbol{R}_1, \tau_1) \Psi_2^\dagger(\boldsymbol{R}_2, \tau_2) \hat{\mathcal{C}}^{-1} \right\rangle$$
$$= -S G_0^T(\boldsymbol{R}_2 - \boldsymbol{R}_1, \tau_2 - \tau_1) S, \qquad (2.51)$$

where the operator $\hat{\mathcal{C}}$ and the matrix S are defined in Eq.(2.13). Substituting this into susceptibility at zero temperature, we obtain

$$\chi_{\mu_1\mu_2}(\mathbf{R}_1 - \mathbf{R}_2) = -\int\limits_0^\infty d\tau \, \mathrm{tr}\left[P_{\mu_1} G_0(\mathbf{R}_1 - \mathbf{R}_2; \tau) P_{\mu_2} S G_0^T(\mathbf{R}_1 - \mathbf{R}_2; \tau) S \right].$$
$$(2.52)$$

Calculating the trace, we find susceptibility in terms of single elements of $G_0(\boldsymbol{r}, \tau)$

$$\chi_{\mu\mu}(\boldsymbol{r}) = -\int d\tau (G_0)_{\mu\mu}^2(\boldsymbol{r}, \tau), \ \ \chi_{AB}(\boldsymbol{r}) = -\int d\tau (G_0)_{AB}^2(\boldsymbol{r}, \tau),$$
$$\chi_{AC}(\boldsymbol{r}) = \int d\tau (G_0)_{AC}^2(\boldsymbol{r}, \tau), \ \ \chi_{BC}(\boldsymbol{r}) = \int d\tau (G_0)_{BC}^2(\boldsymbol{r}, \tau). \qquad (2.53)$$

By using the Fourier transformation of Eq.(2.8),

$$G_0(\mathbf{r}, \tau) = \int_{-\infty}^\infty \frac{d\omega}{2\pi} \int_{BZ} \frac{d^2 k}{(2\pi)^2} G_0(\mathbf{k}, i\omega) \exp(-i\omega\tau + i\mathbf{k}\mathbf{r}), \qquad (2.54)$$

one can easily check that the elements of Green's function in imaginary time representation $G_{0\mu_1\mu_2}(\boldsymbol{r}, \tau)$ are real. Then, (2.53) gives the following signs for interactions at zero temperature and doping:

$$\frac{J_{\mu\mu}^0}{|J_{\mu\mu}^0|} = -1, \quad \frac{J_{AC}^0}{|J_{AC}^0|} = \frac{J_{BC}^0}{|J_{BC}^0|} = 1, \quad \frac{J_{AB}^0}{|J_{AB}^0|} = -1. \qquad (2.55)$$

Clearly, the sign of J_{AB}^0 does not agree with our result (2.35). However, one should note that this theorem fixes the sign of interaction only if the integrals in (2.53) exist. This is not the case for the elements G_{0AB} and G_{0BA}, because the frequency integral in (2.54) diverges at the origin. The divergence comes from the pole at $\omega = 0$, which is a manifestation of highly-degenerate flat band. Therefore we cannot fix the sign of such interaction *a priori*, and should find it from the physically relevant limiting cases, $\mu \to 0$ or $T \to 0$, and the answer depends on the order of these limits.

2.5   Conclusions

In recent years, there was an increasing interest to materials which host fermionic excitations with no analogues in high-energy physics [15]. In particular, the so-called pseudospin-1 fermions provide a platform for studying exotic physical properties such as transport anomalies, topological Lifshitz transitions, as well as dispersionless flat bands which may lead to the realization of many very interesting strongly correlated states. Quasiparticle excitations with pseudospin one can be realized in many ways, as we discussed in Introduction.

In this paper we provided results for the RKKY interaction of magnetic impurities, placed on sites of $\mathcal{T}_3$ lattice, mediated by a background of pseudospin-1 fermions. Our calculations are performed mainly in the low-energy linear-band approximation where we managed to obtain general analytical expressions for the RKKY interactions which are expressed in terms of Mellin-Barnes type integrals for finite chemical potential and temperature. This allowed us to obtain analytically all asymptotics from one expression. The asymptotic behavior at large distances was analyzed in detail. In particular, we found, that oscillatory behavior at large distances was controlled by the same two parameters, the distance between K-points and Fermi wave vector, as in graphene.

Our results show that there are three types of interaction, two of them (for impurities on hub and rim sites) can be reduced to graphene case while the third one (between impurities on different rim sites) is new. This new type of interaction, which comes as a special feature of $\mathcal{T}_3$ lattice geometry, becomes very strong at small temperatures and doping. Physically this is an effect of the flat band, which results in a singular behavior of Green's function at $\omega = 0$. For bipartite lattices, it is known that the signs of

RKKY interactions at zero temperature and in the absence of doping are fixed by general considerations based on particle-hole symmetry, which result in the theorem proved in [59] (and generalized in [71]). We discussed the subtleties of this theorem, as applied to the $\mathcal{T}_3$ lattice, related to the existence of a dispersionless flat band. The breakdown of the theorem for the interaction J_{AB}^0 is refered to the divergence of the Green's function at zero energy due to flat band. The divergence is regularized in the presence of finite temperature and/or doping, but taking the limits $\mu = 0$ and $T = 0$ depends on the order of these limits what is reflected in the last term in the integral $I_2(R, \mu, T)$ of Eq.(2.31). This dramatic change of behavior could be utilized to reveal the presence of a flat band in experiment and can be tested, for example, in recently discovered flat-band systems, such as kagome metal FeSn [23], Lieb-like lattices in covalent-organic frameworks [9, 10] or the electronic Lieb lattice formed by the surface state electrons of Cu(111) [7]. The RKKY interaction may lead to the realization of magnetic order in these materials.

The described strong temperature dependence in $\alpha - \mathcal{T}_3$ lattice systems may manifest also in Friedel oscillations. The last ones could be detected using STM-based quasiparticle interference measurements [94]. As is known, the flat band emerging in tiny-angle twisted bilayer graphene results in a strong sensitivity to perturbations leading to strongly correlated states including superconductivity [1]. While the RKKY interaction was already studied in bilayer graphene [68, 71], the corresponding calculation for twisted bilayer graphene is still ahead.

2.6 Appendix: Green's function in coordinate-frequency representation

The contribution to the retarded Green's function in r space (2.10) from one K point is given by Fourier transform

$$G_0^R\left(\mathbf{R}_1 - \mathbf{R}_2, \omega, \xi\right) = \frac{1}{\Omega_{BZ}} \int \frac{d^2k}{(2\pi)^2} e^{i\mathbf{k}(\mathbf{R}_1 - \mathbf{R}_2)} G_0^\xi(\mathbf{k}, \omega + i\varepsilon). \qquad (2.56)$$

Using the expression for Green function in the low energy model (2.9) and replacing wave numbers by derivatives, we write

$$G_0^R\left(\boldsymbol{r}, \omega, \xi\right) = \frac{1}{\omega} \times$$

$$\begin{pmatrix} \omega^2 + \sin^2\Theta \hbar^2 v_F^2 \partial_{\boldsymbol{r}}^2 & -i\omega \cos\Theta \hbar v_F \partial_{-,\xi} & -\frac{1}{2}\sin(2\Theta)(\hbar v_F \partial_{-,\xi})^2 \\ -i\omega \cos\Theta \hbar v_F \partial_{+,\xi} & \omega^2 & -i\omega \sin\Theta \hbar v_F \partial_{-,\xi} \\ -\frac{1}{2}\sin(2\Theta)(\hbar v_F \partial_{+,\xi})^2 & -i\omega \sin\Theta \hbar v_F \partial_{+,\xi} & \omega^2 + \cos^2\Theta(\hbar v_F \partial_{\boldsymbol{r}})^2 \end{pmatrix} \times$$

$$\times \frac{1}{\Omega_{BZ}} \int \frac{d^2 k}{(2\pi)^2} \frac{e^{i\mathbf{k}\mathbf{r}}}{(\omega + i\varepsilon)^2 - (\hbar v_F \boldsymbol{k})^2}. \tag{2.57}$$

Here $\partial_{\pm,\xi} = \xi\partial_x \pm i\partial_y$. Now we integrate over the angle and then use the formula 2.12.4.28 from book [95],

$$\int_0^\infty \frac{x^{\nu+1} J_\nu(cx)}{x^2 + z^2} dx = z^\nu K_\nu(cz), \quad c > 0, \ \mathrm{Re}\, z > 0, \tag{2.58}$$

and get

$$F(\mathbf{r}) = \int \frac{d^2 k}{(2\pi)^2} \frac{e^{i\mathbf{k}\mathbf{r}}}{(\omega + i\varepsilon)^2 - (\hbar v_F \mathbf{k})^2} = \int_0^\infty \frac{dk\, k}{2\pi} \frac{J_0(k|\mathbf{r}|)}{(\omega + i\varepsilon)^2 - (\hbar v_F k)^2}$$

$$= -\frac{1}{2\pi(\hbar v_F)^2} K_0\left(\frac{-i|\mathbf{r}|(\omega + i\varepsilon)}{\hbar v_F}\right), \tag{2.59}$$

where $J_0 \, and \, K_0$ are the Bessel's functions. Using the relation between Macdonald's functions and the Hankel function of first kind,

$$H_\nu^{(1)}(z) = -\frac{2i}{\pi} e^{-\frac{i\pi\nu}{2}} K_\nu\left(ze^{-\frac{i\pi}{2}}\right), \quad z = \frac{|\mathbf{r}|(\omega + i\varepsilon)}{\hbar v_F}, \tag{2.60}$$

we find

$$F(\boldsymbol{r}) = -\frac{i}{4(\hbar v_F)^2} H_0^{(1)}\left(\frac{|\mathbf{r}|(\omega + i\varepsilon)}{\hbar v_F}\right). \tag{2.61}$$

Next, we evaluate all matrix elements of Green's function. Let's calculate all needed derivatives

$$(\hbar v_F)^2 \partial_{\boldsymbol{r}}^2 F(\boldsymbol{r}) = \frac{i\omega^2}{4(\hbar v_F)^2} H_0^{(1)}(z), \tag{2.62}$$

$$\hbar v_F(\xi\partial_x \pm i\partial_y) F(\boldsymbol{r}) = \xi \frac{i\omega e^{\pm i\xi\phi}}{4(\hbar v_F)^2} H_1^{(1)}(z), \tag{2.63}$$

$$(\hbar v_F)^2(\xi\partial_x \pm i\partial_y)^2 F(\boldsymbol{r}) = -\frac{i\omega^2 e^{\pm 2i\xi\phi}}{4(\hbar v_F)^2} H_2^{(1)}(z). \tag{2.64}$$

Substituting these expressions back to Green's function, we find result which is given by Eq.(2.11) in the main text. Note that all elements of the Green function are proportional to ω.

2.7 Appendix: Evaluation of the interaction integral

In this Appendix we consider the integral

$$
I(\alpha, \nu, z, a) = 2 \int\limits_0^\infty dx\, x^{\alpha-1} J_\nu(x) Y_\nu(x) \left(\frac{1}{ze^{x/a}+1} + \frac{z}{e^{x/a}+z} - 1 \right),
$$
$$
-1 < \operatorname{Re}\alpha < 1. \tag{2.65}
$$

In the region $0 < \alpha < 1$ we can calculate the terms in round brackets separately, for example, the term with -1 can be evaluated using Eq.2.24.3.1 from the book [96],

$$
C_{\alpha,\nu} = \int\limits_0^\infty dz\, z^{\alpha-1} J_\nu(z) Y_\nu(z) = -\frac{1}{2\sqrt{\pi}} \frac{\Gamma\left(\frac{\alpha}{2}\right) \Gamma\left(\frac{\alpha}{2}+\nu\right)}{\Gamma\left(\frac{1+\alpha}{2}\right) \Gamma\left(1+\nu-\frac{\alpha}{2}\right)}, \tag{2.66}
$$

which gives the following values for $\alpha = 3$ and $\nu = 0, 1, 2$:

$$
C_{3,0} = \frac{1}{16}, \quad C_{3,1} = -\frac{3}{16}, \quad C_{3,2} = -\frac{15}{16}. \tag{2.67}
$$

Thus, we can rewrite the integral as follows

$$
I(\alpha, \nu, z, a) = -2C_{\alpha,\nu} + J(\alpha, \nu, z, a), \tag{2.68}
$$

where, for $\nu \geq 0$ and $\operatorname{Re}\alpha > 0$,

$$
J(\alpha, \nu, z, a) = 2 \int\limits_0^\infty dx\, x^{\alpha-1} J_\nu(x) Y_\nu(x) \left(\frac{1}{ze^{x/a}+1} + \frac{z}{e^{x/a}+z} \right). \tag{2.69}
$$

We calculate the last integral using the Mellin transform

$$
J(\alpha, \nu, z, s) = \int_0^\infty da\, a^{s-1} J(\alpha, \nu, z, a)
$$
$$
= 2 \int_0^\infty dx\, x^{\alpha-1} J_\nu(x) Y_\nu(x) \int_0^\infty da\, a^{s-1} \left(\frac{1}{ze^{x/a}+1} + \frac{z}{e^{x/a}+z} \right). \tag{2.70}
$$

After the change $a \to ax$ and then $a \to 1/a$ Eq.(2.70) takes the form

$$J(\alpha, \nu, z, s) = \int_0^\infty dx x^{\alpha+s-1} J_\nu(x) Y_\nu(x) Q(s, z), \quad 0 < \alpha + s < 1, \quad (2.71)$$

where

$$Q(s, z) = 2 \int_0^\infty da a^{-s-1} \left(\frac{1}{ze^a + 1} + \frac{z}{e^a + z} \right), \quad \operatorname{Re} s < 0. \quad (2.72)$$

The function $Q(s, z)$ possesses the symmetry $Q(s, 1/z) = Q(s, z)$. The integral over x in Eq.(2.71) is evaluated using Eq.(2.66). There exists the range of parameters α, s where the Mellin transform $J(\alpha, \nu, s, z)$ is defined. We obtain for $0 < \alpha + \operatorname{Re} s < 0, \quad \nu \geq 0$:

$$J(\alpha, \nu, s, z) = -\frac{\Gamma\left(\nu + \frac{\alpha+s}{2}\right) \Gamma\left(\frac{\alpha+s}{2}\right)}{2\sqrt{\pi}\Gamma\left(\frac{\alpha+1+s}{2}\right) \Gamma\left(\nu + 1 - \frac{\alpha+s}{2}\right)} Q(s, z), \quad (2.73)$$

hence

$$I(\alpha, \nu, z, a) = -2C_{\alpha,\nu} - \frac{1}{2\pi i} \int\limits_{\gamma-i\infty}^{\gamma+i\infty} ds \, a^{-s} \frac{\Gamma\left(\nu + \frac{\alpha+s}{2}\right) \Gamma\left(\frac{\alpha+s}{2}\right) Q(s, z)}{2\sqrt{\pi}\Gamma\left(\frac{\alpha+1+s}{2}\right) \Gamma\left(\nu + 1 - \frac{\alpha+s}{2}\right)}, \quad (2.74)$$

where the contour separates poles of the function $Q(s, z)$ (at $s = 0$ and $s = 2n + 1$, n=0, 1,..., see below) from poles of gamma functions in the numerator. The integrals in Eq.(2.72) can be evaluated explicitly through the polylogarithm function [97] and we get

$$Q(s, z) = -2\Gamma(-s) \left[\operatorname{Li}_{-s}(-1/z) + \operatorname{Li}_{-s}(-z) \right]. \quad (2.75)$$

The function $\operatorname{Li}_s(z)$ has the following properties. It is an analytical function of complex variables s, z. For fixed z, it does not have poles or branch cuts in a finite region of complex s-plane, the point $s = \infty$ is the only (essential) singularity. For fixed s, $\operatorname{Li}_s(z)$ does not have poles and essential singularities but has a cut in the z-plane along the interval $[1, \infty]$, where it is continuous from below side of the cut. It has the symmetry property with respect to complex conjugation $\operatorname{Li}_{s^*}(z^*) = \operatorname{Li}_s^*(z)$ for z not belonging to the interval $(-\infty, 0)$.

Analytic continuation of $\operatorname{Li}_s(z)$ into the region $|z| > 1$ can be performed by means of the formula (see Eq.(1.11.16) in [98])

$$\operatorname{Li}_s(z) + e^{i\pi s}\operatorname{Li}_s\left(\frac{1}{z}\right) = \frac{(2\pi)^s}{\Gamma(s)} e^{i\pi s/2} \zeta\left(1 - s, \frac{1}{2} + \frac{\ln(-z)}{2\pi i}\right), \quad \operatorname{Re} s < 0, \quad (2.76)$$

where $\zeta(s,q)$ is the Hurwitz ζ-function. When s is a negative even integer, $s = -2m$, $m = 1, 2, \ldots$, we get $\mathrm{Li}_{-m}(-z) + \mathrm{Li}_{-m}\left(-1/z\right) = 0$. It follows then from Eq.(2.75) that $Q(s,z)$ has poles only for $s = 0$ and odd positive $s = 2n+1$, $n = 0, 1, \ldots$, while for even positive $s = 2n$ the poles of $\Gamma(-s)$ are canceled by zeros of the sum of polylogarithm functions. Applying this formula to Eq.(2.75) we get

$$Q(s,z) = -\frac{1}{(2\pi)^s \cos(\pi s/2)} \left[\zeta\left(1+s, \frac{1}{2} + \frac{\ln z}{2\pi i}\right) + \zeta\left(1+s, \frac{1}{2} - \frac{\ln z}{2\pi i}\right) \right].$$
(2.77)

Near $s = 0$ the function $Q(s,z)$ behaves as

$$Q(s,z) \simeq -\frac{2}{s},$$
(2.78)

then moving the contour in Eq.(2.74) to slightly right of the point $s = 0$ ($\gamma > 0$) and calculating the residue at $s = 0$, we get

$$I(\alpha,\nu,z,a) = -\frac{1}{2\pi i} \int\limits_{\gamma-i\infty}^{\gamma+i\infty} ds\, a^{-s} \frac{\Gamma\left(\nu + \frac{\alpha+s}{2}\right)\Gamma\left(\frac{\alpha+s}{2}\right)}{2\sqrt{\pi}\,\Gamma\left(\frac{\alpha+1+s}{2}\right)\Gamma\left(\nu+1-\frac{\alpha+s}{2}\right)} Q(s,z)$$
(2.79)

[the residue at $s = 0$ cancels the first term in Eq.(2.74)].

Expanding the functions $\zeta(s, 1/2 \pm iv)$ (where $v = \frac{\ln z}{2\pi}$) in series around $v = 0$, we find the following representation of the function $Q(s,z)$ near the point $z = 1$:

$$Q(s,z) = -\frac{2}{(2\pi)^s \cos(\pi s/2)}$$
$$\times \sum_{k=0}^{\infty} \frac{(-1)^k \Gamma(1+s+2k)\zeta(2k+1+s,1/2)}{\Gamma(1+s)(2k)!} \left(\frac{\ln z}{2\pi}\right)^{2k}.$$
(2.80)

This expansion can be used to find a high temperature expansion of Eq.(2.79), hence the integral (2.25), when $|\mu|/(2\pi T) \ll 1$.

To obtain the expansion at large $|v| = |\mu|/(2\pi T) \gg 1$ we start from the asymptotic expansion [99]:

$$\zeta(s,q) = \frac{1}{\Gamma(s)} \sum_{k=0}^{\infty} \frac{\left(2^{1-2k} - 1\right) B_{2k}\Gamma(s+2k-1)}{(2k)!(q-1/2)^{s+2k-1}},$$
(2.81)

where B_{2k} are Bernoulli numbers. For the function $Q(s, z)$ we get the asymptotic series at large $|v|$:

$$Q(s, z) = -\frac{2}{(2\pi|v|)^s\Gamma(s+1)} \sum_{k=0}^{\infty} \frac{(-1)^k \left(2^{1-2k} - 1\right) B_{2k}\Gamma(s+2k)}{(2k)!v^{2k}}. \quad (2.82)$$

The first terms of the expansion of $Q(s, z)$ at small z (large $|v|$) are:

$$Q(s, z) = -\frac{2}{(2\pi|v|)^s\Gamma(s+1)} \left[\Gamma(s) + \frac{\Gamma(s+2)}{24v^2} + \frac{7\Gamma(s+4)}{5760v^4} + O\left(\frac{1}{v^6}\right)\right]. \quad (2.83)$$

Hence, for small z (or $\mu/T \gg 1$) we obtain, keeping two lowest terms,

$$I(\alpha, \nu, u) = \frac{1}{2\pi i} \int_{\gamma-i\infty}^{\gamma+i\infty} ds\, u^{-s} \frac{\Gamma\left(\nu + \frac{\alpha+s}{2}\right)\Gamma\left(\frac{\alpha+s}{2}\right)}{2\sqrt{\pi}\Gamma\left(\frac{\alpha+1+s}{2}\right)\Gamma\left(\nu + 1 - \frac{\alpha+s}{2}\right)}$$

$$\times \left[\frac{\Gamma\left(\frac{s}{2}\right)}{\Gamma\left(1 + \frac{s}{2}\right)} + \frac{1}{6v^2}\frac{\Gamma\left(1 + \frac{s+1}{2}\right)}{\Gamma\left(\frac{s+1}{2}\right)}\right], \quad u = \frac{\mu R}{\hbar v_F} = k_F R. \quad (2.84)$$

Changing $s \to 2s$ and calculating integrals we get equivalent expressions

$$I(\alpha, \nu, u) = \frac{1}{\sqrt{\pi}}G_{24}^{30}\left(u^2\bigg|\begin{matrix}\frac{\alpha+1}{2}, 1\\ 0, \frac{\alpha}{2}, \frac{\alpha}{2} + \nu, \frac{\alpha}{2} - \nu\end{matrix}\right)$$

$$+ \frac{1}{6\sqrt{\pi}v^2}G_{24}^{30}\left(u^2\bigg|\begin{matrix}\frac{\alpha+1}{2}, \frac{1}{2}\\ \frac{3}{2}, \frac{\alpha}{2}, \frac{\alpha}{2} + \nu, \frac{\alpha}{2} - \nu\end{matrix}\right)$$

$$= -\frac{1}{\sqrt{\pi}}G_{24}^{21}\left(u^2\bigg|\begin{matrix}1, \frac{\alpha+1}{2}\\ \frac{\alpha}{2}, \frac{\alpha}{2} + \nu, \frac{\alpha}{2} - \nu, 0\end{matrix}\right)$$

$$- \frac{1}{6\sqrt{\pi}v^2}G_{24}^{21}\left(u^2\bigg|\begin{matrix}\frac{1}{2}, \frac{\alpha+1}{2}\\ \frac{\alpha}{2}, \frac{\alpha}{2} + \nu, \frac{\alpha}{2} - \nu, \frac{3}{2}\end{matrix}\right), \quad (2.85)$$

where we used Eq.8.2.1.17 from [96],

$$G_{pq}^{mn}\left(z\bigg|\begin{matrix}(a_{p-1}), b \pm l\\ b, (b_{q-1})\end{matrix}\right) = (-1)^l G_{p,q}^{m-1,n+1}\left(z\bigg|\begin{matrix}b \pm l, (a_{p-1})\\ (b_{q-1}), b\end{matrix}\right). \quad (2.86)$$

The first term in Eq.(2.85) corresponds to the case of zero temperature, and for $\alpha = 3$, $\nu = 0, 1$ it agrees with the result of Ref.[61]. In general, the expansion of the expression (2.82) over $1/|v|$ corresponds to the expansion

over T/μ (Sommerfeld's expansion). At large $k_F R$, Eq.(2.85) gives for interested cases $\alpha = 3, \nu = 0, 1, 2$ the results in Eqs. (2.39)-(2.41).

From our final formula (2.79) we can obtain an expansion for μ near zero by means of Eq.(2.80), and an expansion for $T \ll \mu$ using Eq.(2.82). To find a large $k_F R$ expansion at fixed $RT/\hbar v_F$ we consider the expression (2.79) using $Q(s, z)$ represented by the asymptotic series (2.82),

$$
I(\alpha, \nu, z, a) = \frac{1}{\sqrt{\pi}} \sum_{k=0}^{\infty} \frac{(-1)^k \left(1 - 2^{2k-1}\right) B_{2k}}{(2k)! v^{2k}}
$$

$$
\times \frac{1}{2\pi i} \int_{\gamma-i\infty}^{\gamma+i\infty} ds \, (2\pi a v)^{-s} \frac{\Gamma\left(\nu + \frac{\alpha+s}{2}\right) \Gamma\left(\frac{\alpha+s}{2}\right) \Gamma\left(k + \frac{s}{2}\right) \Gamma\left(k + \frac{1+s}{2}\right)}{\Gamma\left(\frac{1+s}{2}\right) \Gamma\left(1 + \frac{s}{2}\right) \Gamma\left(\frac{1+\alpha+s}{2}\right) \Gamma\left(1 + \nu - \frac{\alpha+s}{2}\right)}
$$

$$
= \frac{2}{\sqrt{\pi}} \sum_{k=0}^{\infty} \frac{(-1)^k \left(1 - 2^{2k-1}\right) B_{2k}}{(2k)! v^{2k}}
$$

$$
\times G_{35}^{40} \left((2\pi a v)^2 \middle| \begin{array}{c} \frac{1}{2}, 1, \frac{1+\alpha}{2} \\ k, k + \frac{1}{2}, \frac{\alpha}{2}, \frac{\alpha}{2} + \nu, \frac{\alpha}{2} - \nu \end{array} \right), \tag{2.87}
$$

where we used the duplication formula for $\Gamma(2k + s)$ and $\Gamma(1 + s)$. Since $2\pi a v = k_F R$, we consider the asymptotic of Meijer function at large $k_F R \gg 1$. For $\alpha = 3$ and nonnegative integer ν we get

$$
G_{35}^{40} \left((2\pi a v)^2 \middle| \begin{array}{c} \frac{1}{2}, 1, 2 \\ k, k + \frac{1}{2}, \frac{3}{2}, \frac{3}{2} + \nu, \frac{3}{2} - \nu \end{array} \right) \simeq
$$

$$
\frac{(-1)^{(k+\nu)} (2\pi a v)^{2k}}{\sqrt{\pi}} \left[-2\pi a v \sin(4\pi a v) + (k - \nu^2 - 1/4) \cos(4\pi a v) \right]. \tag{2.88}
$$

Using the representation for Bernoulli numbers

$$
\left(1 - 2^{1-2k}\right) B_{2k} = (-1)^{k+1} \pi \int_0^\infty \frac{dt \, t^{2k}}{\cosh^2(\pi t)}, \tag{2.89}
$$

we get after performing the summation over k,

$$
I(3, \nu, z, a) = \frac{(-1)^{\nu+1}}{\pi} \int_0^\infty \frac{dt}{\cosh^2 t} \left[2at \sin(4at) \cos(2k_F R) \right.
$$

$$
\left. + \cos(4at) \left(\frac{\mu R}{\hbar v_F} \sin(2k_F R) + \frac{4\nu^2 + 1}{4} \cos(2k_F R) \right) \right]. \tag{2.90}
$$

Calculating the integrals over t, we finally obtain

$$I(3, \nu, z, a) = (-1)^{\nu+1} \frac{2R^2}{(\hbar v_F)^2} F_1 \left[\mu \sin(2k_F R) + \frac{\hbar v_F (4\nu^2 - 1)}{4R} \cos(2k_F R) \right.$$

$$\left. + \pi F_2 \cos(2k_F R) \right], \quad k_F R \gg 1, \tag{2.91}$$

where F_1 and F_2 are defined in Eq.(2.43). The last expression for $\nu = 0, 1$ leads to the same expressions as were found in graphene for exchange interactions [68], while the expression for $\nu = 2$ is completely new and corresponds to interaction between impurities on rim sites in considered pseudospin-1 fermion system.

2.8   Appendix: Zero chemical potential and finite temperature

Asymptotics of the integrals I_n with $n = 0, 1$ were at least partially analyzed in graphene literature, except the integral I_2. However, in the case of zero chemical potential, $\mu = 0$, such an analysis was not performed to the best of our knowledge. The evaluation of corresponding integrals in the large distance limit poses a rather complicated task. This is because the leading correction is given by exponentially small term, and thus any power series decomposition can not give the desired result. However, our formula (2.79) allows us to analyze the case $\mu = 0$ straightforwardly. First, we write the function $Q(s, z = 1)$ from Eq.(2.80) in the form

$$Q(s, 1) = -\frac{2\zeta(1 + s, 1/2)}{(2\pi)^s \cos(\pi s/2)} = -\frac{4}{\pi^{s+1}} \Gamma\left(\frac{1+s}{2}\right) \Gamma\left(\frac{1-s}{2}\right) \sum_{k=0}^{\infty} \frac{1}{(2k+1)^{s+1}}, \tag{2.92}$$

where $\mathrm{Re}\, s > 0$. Then for the integral (2.79) we obtain

$$I(\alpha, \nu, 1, a) = \frac{2a}{\sqrt{\pi}} \sum_{k=0}^{\infty} \frac{1}{2\pi i} \int_{\gamma-i\infty}^{\gamma+i\infty} ds \, [\pi a(2k+1)]^{-s-1}$$

$$\times \frac{\Gamma\left(\nu + \frac{\alpha+s}{2}\right) \Gamma\left(\frac{\alpha+s}{2}\right) \Gamma\left(\frac{1+s}{2}\right) \Gamma\left(\frac{1-s}{2}\right)}{\Gamma\left(\frac{\alpha+1+s}{2}\right) \Gamma\left(\nu + 1 - \frac{\alpha+s}{2}\right)}, \quad 0 < \gamma < 1. \tag{2.93}$$

Finally, making the change $s \to 2s - 1$ we get the expression in terms of Meijer functions,

$$I(\alpha, \nu, 1, a) = \frac{4a}{\sqrt{\pi}} \sum_{k=0}^{\infty} G_{2,4}^{3,1} \left(\pi^2 a^2 (2k+1)^2 \middle| \begin{array}{c} 0, \frac{\alpha}{2} \\ 0, \frac{\alpha-1}{2}, \nu + \frac{\alpha-1}{2}, \frac{\alpha-1}{2} - \nu \end{array} \right).$$
(2.94)

The function $G_{24}^{31}(z)$ is an analytic in z function in the sector $|\mathrm{arg}z| < \pi$. To find asymptotic behavior of $J(\alpha, \nu, 1, a)$ at large a, we use two terms of asymptotic expansion of Meijer function at large argument and then evaluate the sum. Below we present results for three cases $\nu = 0, 1, 2$:

$$I(3, 0, 1, a) = -\frac{2a^2}{\sinh(2\pi a)} \left(\frac{\pi}{\tanh(2\pi a)} - \frac{1}{4a} \right), \quad a > 1.$$
(2.95)

$$I(3, 1, 1, a) = \frac{2a^2}{\sinh(2\pi a)} \left(\frac{\pi}{\tanh(2\pi a)} + \frac{3}{4a} \right), \, a > 1.$$
(2.96)

$$I(3, 2, 1, a) = \frac{4}{\pi a} - \frac{2a^2}{\sinh(2\pi a)} \left(\frac{\pi}{\tanh(2\pi a)} + \frac{15}{4a} \right), \, a > 1.$$
(2.97)

The last expression contains the power decreasing term $\sim 1/a$ in contrast to the first two expressions. This is because the corresponding Mellin-Barnes integrand has one pole (at $s = 1$) to the right of the integration contour while the integrands for $\alpha = 3$ and $\nu = 1, 2$ do not contain poles at all in that region. Hence they have only exponentially decreasing terms, for example, the first correction is exponentially small, $\sim a^2 \exp(-2\pi a)$, at large $a \gg 1$. On the other hand, since the expression for $\nu = 2$ decreases as $\sim 1/a$ the corresponding integral in Eq.(2.30) has $1/R^4$ decrease with a distance. However, as we find from Eq.(2.29) in main text, this power-decreasing term is exactly canceled by the flat-band correction.

Chapter 3

Gap generation and flat band catalysis in dice model with local interaction

3.1 Introduction

The experimental discovery of graphene [22] draw attention of condensed matter physicists to the systems with relativisticlike quasiparticle spectrum. It was shown [15] that in crystals with special space groups more complicated electron spectra could be realized with no analogues in high-energy physics where the Poincare symmetry provides strong restrictions. One remarkable example is a possibility to possess strictly flat bands [100, 101], whose high degeneracy was shown to be stabilized by permutation symmetries [102] (for a recent review of artificial flat band systems, see Ref.[92] and Ref.[103] where many systems with pseudospin-1 fermions have been discussed). The dice model is the paradigmatic example of such a system with a flat band which hosts pseudospin-1 fermions [11].

The dice model is a tight-binding model of two-dimensional fermions living on the $\mathcal{T}_3$ (or dice) lattice where atoms are situated both at the vertices of hexagonal lattice and the hexagons centers [11, 80]. Since the dice model has three sites per unit cell, the electron states in this model are described by three-component fermions. It is natural then that the energy spectrum of the model is comprised of three bands. The two of them form a Dirac cone and the third band is completely flat and has zero energy [13]. All three bands meet at the K and K' points, which are situated at

the corners of the Brillouin zone. The $\mathcal{T}_3$ lattice has been experimentally realized in Josephson arrays [16, 17], metallic wire networks [18] and its optical realization by laser beams was proposed in Ref.[19].

Perfectly flat bands are expected to be unstable with respect to generic perturbations such as the presence of boundaries, magnetic field, Coulomb impurities, and disorder. In a recent paper [89], we showed that, remarkably, the energy dispersion of the completely flat energy band of the dice model is not affected by the presence of boundaries except the trivial reduction of the number of degenerated electron states due to the finite spatial size of the system. It was shown also that the flat band of the dice model remains unaltered in the presence of circularly polarized radiation [104, 105] and magnetic field [12]. The electron states of gapped pseudospin-1 fermions in the dice model for impurities with short- and long-range potential were studied by us in Ref.[[14]] leading to qualitatively different results. Indeed, it was found that while the flat band survives in the presence of a potential well, it is absent in the case of the Coulomb potential.

It is well known that a soft kinetic spectrum favors the gap generation. For example, the low energy electron spectrum $\varepsilon(\mathbf{p}) \sim |\mathbf{p}|^n$ in ABC-stacked multilayer graphene becomes more flat with n. The interaction parameter r_s, defined as the ratio of inter-electron Coulomb interaction energy to the Fermi energy, scales like $r_s \sim n_{el}^{(1-n)/2}$ [106], where n_{el} is the electron charge density. Obviously, the electron-electron interactions become more important at low electron density as the number of layers n increases in ABC-stacked multilayer graphene. This suggests that the gap generation in chiral multilayer graphene should be enhanced [35–37] as the number of layers n becomes larger. This conclusion agrees with the experimental findings. Meanwhile no gap is observed in monolayer graphene at the neutrality point in the absence of external electromagnetic fields, gap 2 meV is reported in bilayer graphene [38–41]. The recent experiments [42, 43] demonstrate the presence of gaps of almost room temperature magnitude ~ 25 meV in high mobility ABC-stacked trilayer graphene. A large interaction-induced transport gap up to 80 meV was quite recently observed experimentally in suspended rhombohedral-stacked tetralayer graphene [44].

Obviously, the flat band represents the most extreme case of a soft kinetic spectrum where the kinetic energy is completely quenched. The above mentioned experimental results suggest that the generated gap

should have the largest magnitude in the flat band system. This motivates us to study the gap generation in the dice model. A recent theoretical study of the band structure of magic angle twisted bilayer graphene [107] also shows the crucial role of the flat band and the possibility of large gap generation. This provides an additional motivation for the present study. We would like to add also that since the pseudospin-1 fermions with flat band were already realized in kagome metals such as FeSn [23] and in electronic Lieb lattice [7], our results for the flat band catalysis of gap generation can be tested experimentally.

To get an insight into the gap generation in the dice lattice we considered in this paper a model with local interaction. We studied both intravalley and intervalley types of gap and analyzed their free energies.

The paper is organized as follows. The dice model and its general properties are considered in Sec.3.2. In Sec.3.3, we study the intravalley gap generation. The intervalley gap generation is investigated in Sec.3.4. In Sec.3.4.3, we calculate the free energy for intra- and intervalley gap states and discuss the phase diagram of the model. Technical details of calculations are presented in Appendices 3.6, 3.7, 3.8.

3.2   Model

The lattice of the $\mathcal{T}_3$ (dice) lattice model is schematically shown in Fig.1.1. The tight-binding equations are given by system (1.1) (with equal hoppings t between atoms C and A, B).

There are two values of momentum where $f_{\boldsymbol{k}} = 0$ in tight-binding Hamiltonian (1.3) and all three bands meet. They are situated at the corners of the hexagonal Brillouin zone

$$K = \frac{2\pi}{a}\left(\frac{1}{3}, \frac{1}{\sqrt{3}}\right), \quad K' = \frac{2\pi}{a}\left(-\frac{1}{3}, \frac{1}{\sqrt{3}}\right). \tag{3.1}$$

For momenta near the K and K' points, the function $f_{\boldsymbol{k}}$ is linear in $\boldsymbol{q} = \boldsymbol{k} - \xi\boldsymbol{K}$, i.e., $f_{\boldsymbol{k}} = v_F(\xi q_x - iq_y)$, $v_F = \sqrt{3}ta/2$ is the Fermi velocity, and $\xi = \pm$ is the valley index. In addition, we set $\hbar = 1$ for convenience. The low-energy Hamiltonian for electron states of the dice model in both valleys has the form

$$H_0(\boldsymbol{k}, \xi) = \begin{pmatrix} 0 & \xi k_x - ik_y & 0 \\ \xi k_x + ik_y & 0 & \xi k_x - ik_y \\ 0 & \xi k_x + ik_y & 0 \end{pmatrix}. \tag{3.2}$$

Here we absorbed dimensional constant $v_F/\sqrt{2}$ into the definition of momenta $\boldsymbol{k} = (v_F/\sqrt{2})\,\boldsymbol{q}$ (this $\boldsymbol{k}$ should not be confused with the initial $\boldsymbol{k}$ in the Brillouin zone in Eq.(4.25)). The Hamiltonian acts on three-component wave functions $\psi^T = (\psi_A, \psi_C, \psi_B)$. The electron states at the K' point are described like in graphene by the interchange of the A and B spinor components. The two valley Hamiltonian, $H_0(\boldsymbol{k}, +1) \oplus H_0(\boldsymbol{k}, -1)$, is time-reversal invariant because of the relation $H_0^*(\boldsymbol{k}, \xi) = H_0(-\boldsymbol{k}, -\xi)$, which can be directly checked for Eq.(3.2). The time-reversal operator $\mathcal{T}$ for the dice model is defined in the same way as in graphene: it interchanges valleys, changes the sign of momentum, and contains complex conjugation operator [108]. The spectrum of the Hamiltonian consists of three energy bands $\pm\sqrt{2}|\mathbf{k}|$, 0. Clearly, two bands form a Dirac cone and one band is completely flat.

Although electrons interact through the Coulomb interaction $V(\boldsymbol{x} - \boldsymbol{y}) = e^2/|\mathbf{x} - \mathbf{y}|$, to get an insight into the gap generation for quasiparticles in the dice model we will study the gap generation for a local Coulomb interaction $V_{local}(\boldsymbol{x} - \boldsymbol{y}) = U\delta^2(\boldsymbol{x} - \boldsymbol{y})$. This significantly simplifies the analysis because the gap equations are algebraic in the Hartree–Fock approximation rather than the integral ones as for the genuine Coulomb interaction. The interaction V_{local} is attractive between electrons and holes. There are two main possibilities of order parameters of the exciton type, namely, the intravalley and intervalley pairing which will be investigated in the two subsequent sections.

We will study the gap generation by using the Baym–Kadanoff formalism [109–111]. The corresponding effective action for the quasiparticle propagator G in the Hartree–Fock (mean field) approximation in the model with the local four-fermion interaction has the form (for a similar consideration in the case of graphene, see, e.g., [112])

$$
\begin{aligned}
\Gamma(G) = -\mathrm{i}\,\mathrm{Tr}\left[\mathrm{Ln}\,G^{-1}S + \left(S^{-1}G - 1\right)\right] \\
+ \frac{U}{2}\int d^3x \left\{\,\mathrm{tr}[G(x,x)G(x,x)] - [\mathrm{tr}\,G(x,x)]^2\,\right\},
\end{aligned}
\tag{3.3}
$$

where Tr and Ln are taken in the functional sense, S is the free propagator related to Hamiltonian (3.2), and trace is taken over the valley and spinor components. Let us begin our analysis with the case of the intravalley gap generation.

3.3   Intravalley gap

First of all, let us consider possible intravalley gap terms in the dice model, whose dynamical generation will be analyzed below. Obviously, the most general momentum-independent intravalley gap term is given by

$$H_{\text{gap}} = \begin{pmatrix} m_1 & c & a \\ c^* & m_2 & b \\ a^* & b^* & m_3 \end{pmatrix}. \tag{3.4}$$

It is easy to check that parameters a, b, and c lead to an energy dispersion relation which is anisotropic in momentum space. Since it is natural to expect that the solution with the lowest energy should be isotropic in a rotation-invariant system, we will set $a = b = c = 0$ in what follows. Then m_1, m_2, and m_3 are possible mass terms and. The electron states at the two different valleys are independent, therefore, m_i could be valley dependent (note that valley-polarized states are well-known in graphene [113–115]). Next we find the following characteristic equation which determines the energy spectrum of the Hamiltonian $H_0(\mathbf{k}, \xi) + H_{\text{gap}}$:

$$(m_1 - \varepsilon) \left((m_2 - \varepsilon)(m_3 - \varepsilon) - k^2 \right) + (\varepsilon - m_3)k^2 = 0, \quad k = |\mathbf{k}|. \tag{3.5}$$

Clearly, there are three solutions of the above equation. Two of them tend to $\varepsilon(\mathbf{k}) \to \pm\sqrt{2}\,k$ at $k \to \infty$ and describe the upper and lower energy branches of the non-perturbated Hamiltonian (3.2). Obviously, if $m_1 = -m_3$, then the middle branch tends to the flat energy band $\varepsilon = 0$ of the free Hamiltonian (3.2) at large $|\mathbf{k}|$. Therefore, we will assume in what follows that $m_1 = -m_3 = m$. In this case, Eq.(3.5) takes the form

$$(\varepsilon - m_2)(m^2 - \varepsilon^2) + 2\varepsilon k^2 = 0. \tag{3.6}$$

The examples of spectrum defined by this equation are shown in Fig.3.1. It is easy to check that $\varepsilon = 0$ is the exact solution of Eq.(3.6) for all $\mathbf{k}$ if $m_2 = 0$. The flat band solution $\varepsilon = 0$ is realized also if $m = 0$. In what follows, we will study only solutions with $m \neq 0$ and $m_2 \neq 0$ when the flat band is absent. Equation (3.6) implies that the particle-hole symmetry could be preserved even in the case $m_2 \neq 0$ if we consider the mass term $-m_2$ at the valley $\xi = -$. Since the choice of the sign of m is irrelevant for the energy dispersion, without loss of generality we can assume
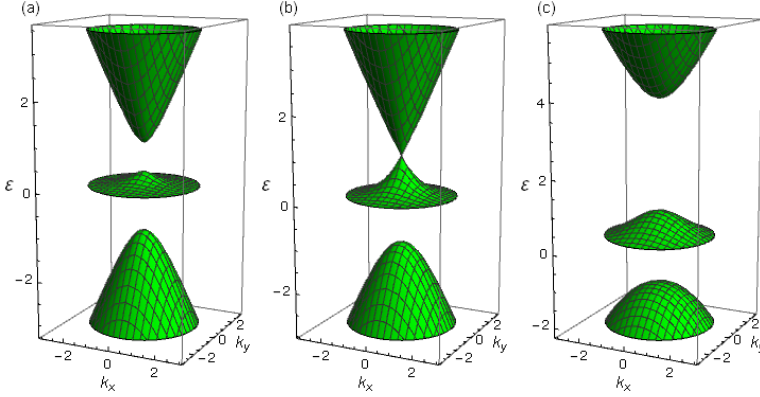
Figure 3.1. Energy spectrum defined by Eq.(3.6) for three values of m_2 (a): $m_2 = 0.35m$, (b): $m_2 = m$, (c): $m_2 = 4m$. At the middle panel the crossing point of two bands is shown. Here energy ε and momenta **k** are measured in units of m.

that m takes the same value in both valleys. Thus, we have the following intravalley gapped Hamiltonian at valley ξ:

$$
H_\xi = \begin{pmatrix} 0 & \xi k_x - i k_y & 0 \\ \xi k_x + i k_y & 0 & \xi k_x - i k_y \\ 0 & \xi k_x + i k_y & 0 \end{pmatrix} + \begin{pmatrix} m & 0 & 0 \\ 0 & \xi m_2 & 0 \\ 0 & 0 & -m \end{pmatrix}.
\tag{3.7}
$$

It is worth noting that this Hamiltonian for $m_2 = 0$ possesses the intravalley particle-hole symmetry $\mathcal{C} = AK$

$$
\mathcal{C} H_\xi(\mathbf{k}) + H_\xi(\mathbf{k}) \mathcal{C} = 0, \qquad A = \begin{pmatrix} 0 & 0 & 1 \\ 0 & -1 & 0 \\ 1 & 0 & 0 \end{pmatrix},
\tag{3.8}
$$

where K is the complex conjugation. The relation above can be checked straightforwardly. The existence of this particle-hole symmetry explains why the energy spectrum is particle-hole symmetric in a given valley for $m_2 = 0$. The second term in Hamiltonian (3.7) defines an ansatz for the full inverse propagator in the theory with the Hamiltonian $H_0 + V_{local}$, where gap parameters m and m_2 are determined by solving the Schwinger–Dyson equation.

3.3.1 Gap equations

Varying the Baym–Kadanoff action (3.3) with respect to G, we obtain the following Schwinger–Dyson equation in the Hartree-Fock (mean field) approximation:

$$G_\xi^{-1}(\Omega, \mathbf{p}) = S_\xi^{-1}(\Omega, \mathbf{p}) - i\frac{2U}{v_F^2} \int \frac{d\omega d^2 k}{(2\pi)^3} G_\xi(\omega, \mathbf{k}), \qquad (3.9)$$

where we retained only the exchange contribution because the Hartree contribution vanishes at the neutrality point of the considered particle-hole symmetric state. Note that H_ξ does not mix states from the two valleys, therefore, the Schwinger–Dyson equation (3.9) for the intravalley gaps is diagonal in the valley indices. The additional factor $2/v_F^2$ appears due to the definition of k below Eq.(3.2).

As was discussed above, we study the gap generation in a neutral particle-hole symmetric system with m_2 and $-m_2$ mass terms in the valleys $+$ and $-$, respectively. Therefore, there is no need to introduce the chemical potential. However, the valley dependent chemical potential $\xi\mu_v$ with opposite signs in the two valleys could be dynamically generated. Hence it should be added to the Hamiltonian H_ξ. Such chemical potential defines filling at particular valley ξ. The corresponding gap equations for m, m_2, and μ_v are derived in Appendix 3.6. It is useful to perform the Wick rotation $\omega \to i\omega$ in the gap equations (3.55)-(3.57) and integrate over ω and polar angle ϕ. Then we obtain the following system of equations for $\mu_v, m,$ and m_2:

$$\mu_v = \frac{U}{v_F^2} \int_0^\Lambda \frac{kdk}{2\pi} \left[\frac{k^2 + r_0(m_2 - r_0)}{(r_1 - r_0)(r_0 - r_2)} \mathrm{sign}[\mu_v - r_0] + c.p. \right], \qquad (3.10)$$

$$m = m\frac{U}{v_F^2} \int_0^\Lambda \frac{kdk}{2\pi} \left[\frac{(m_2 - r_0)}{(r_0 - r_1)(r_0 - r_2)} \mathrm{sign}[\mu_v - r_0] + c.p. \right], \qquad (3.11)$$

$$m_2 = -\frac{U}{v_F^2} \int_0^\Lambda \frac{kdk}{2\pi} \left[\frac{k^2 - m^2 + m_2 r_0}{(r_0 - r_1)(r_0 - r_2)} \mathrm{sign}[\mu_v - r_0] + c.p. \right], \qquad (3.12)$$

where c.p. means summation over two terms with cyclic permutations of roots r_0, r_1, and r_2. Here r_0, r_1, and r_2 are functions of k defined in Appendix in Eq.(3.52) and describe the momentum dispersion of energy

bands. The symmetry under permutations of r_0, r_1, and r_2 is obvious in these equations. Here we also introduced an ultraviolet cutoff Λ for energy, which is of order $\hbar v_F \pi/(a\sqrt{2})$, where a is the lattice constant $a = 2.46\,\text{Å}$, and we take $v_F = 10^6\,m/s$ as for graphene [115]. This cutoff determines the range of applicability of the low-energy model.

3.3.2 Properties of gap equations and critical coupling constant

Before solving the gap equations numerically, we should note several their algebraic properties. At first, if a certain set m, m_2, μ_v is a solution, then sets with changed signs of masses and valley chemical potential, i.e., $-m$, m_2, μ_v and m, $-m_2$, $-\mu_v$ are also solutions. This follows from the symmetry properties of roots r_n defined in Eq.(3.52).

Another important property is that there are no solutions of the gap equations (3.10)-(3.12) for weak coupling U. This can be shown in the following way: nontrivial solutions are possible for $U \to 0$ only if there are poles in the integrands at $k = 0$. This can happen only if two bands meet, i.e., $r_i(\boldsymbol{k} = 0) = r_j(\boldsymbol{k} = 0)$. Near the $k = 0$ point the denominator is linear in k, and the integral over d^2k cancels this singularity. In other words, there are no infrared singularities and therefore nontrivial solutions require a critical value U_c for their appearance.

Further, let us find the critical coupling constant above which a nontrivial solution exists. Near the critical value, both gaps m, m_2 and the valley chemical potential μ_v should tend to zero. Since there are no infrared singularities, the critical coupling constant can be found from the ultraviolet limit of the gap equations at large k. In such a limit, the gap equation (3.11) reduces to

$$m = m\frac{U}{v_F^2}\int^{\Lambda}\frac{kdk}{2\pi}\frac{1}{\sqrt{2}k},\tag{3.13}$$

which results in the following coupling constant for $m \neq 0$:

$$U_c = \frac{2\pi\sqrt{2}v_F^2}{\Lambda} \approx 8.89\frac{v_F^2}{\Lambda}.\tag{3.14}$$

Finally, let us proceed to numerical solution of the gap equations. It is convenient to measure U in terms of v_F^2/Λ. The gap equations (3.10)-(3.12) form a set of coupled nonlinear equations. We solve them numerically by
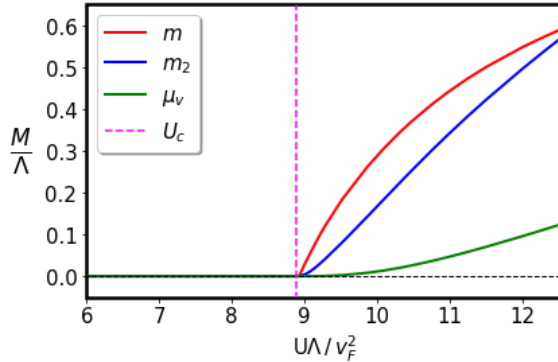
Figure 3.2. Solutions $M = m$, m_2, μ_v for the system of gap equations (3.10)-(3.12) as a function of coupling constant U. The critical value U_c of coupling constant, estimated in Eq.(3.14), is marked by dashed vertical line.

using standard iterative methods (see, for example, Ref.[116]). Guessing initial points in a wide range for both masses and valley chemical potential, we were able to find solutions just above the critical constant (3.14). The corresponding results are shown in Fig.3.2. Near $U = U_c$ gaps m, m_2 are small and valley chemical potential μ_v is still several orders of magnitude smaller. All these dynamical parameters grow quickly with U. We determined also the corresponding critical exponents by using numerically obtained solutions near U_c. We found that the dynamical parameters scale as $m \sim (U - U_c)$, $m_2 \sim (U - U_c)^{1.5}$, and $\mu_v \sim (U - U_c)^{3.3}$.

3.4   Intervalley gap

Since the denominator in the gap equations (3.10)-(3.12) contains the difference of energy dispersions of two bands, this difference is approximately like that in graphene or two times less. This is the mathematical reason for the existence of a nonzero critical coupling constant for the gap generation like in graphene. However, there is the middle completely flat band in the dice model. This suggests that it might be favorable to consider an intervalley gap which couples the electron and holes from different valleys. Additional reason to study such a gap is that similar valley-polarized states are well-known in graphene [113–115]. As we will see below, the most crucial property of the intervalley gap is that the difference of the energy dispersion of the flat bands in the two valleys does not increase with

k at large k. The most general two-valley Hamiltonian which describes the intervalley pairing is given by

$$H_{2v} = \begin{pmatrix} H_0^+ & P \\ P^\dagger & H_0^- \end{pmatrix}, \tag{3.15}$$

where we used the short-hand notation $H_0^\pm = H_0(\boldsymbol{k}, \pm)$ for the free Hamiltonians in the K and K' valleys defined by Eq.(3.2), and matrix P describes the invervalley gap and, in general, is arbitrary. Since

$$T H_0^- T^{-1} = H_0^+, \quad T = \begin{pmatrix} 0 & 0 & 1 \\ 0 & 1 & 0 \\ 1 & 0 & 0 \end{pmatrix}, \tag{3.16}$$

it is convenient to exchange the A and B components of wave functions in the K' valley multiplying them by T. Then the intervalley Hamiltonian (3.15) takes the form

$$H_{iv} = \begin{pmatrix} H_0^+ & F \\ F^\dagger & -H_0^+ \end{pmatrix}, \tag{3.17}$$

where its block diagonal elements differ only by sign and $F = PT^{-1}$. Hamiltonian (3.17) acts on six-component wave functions

$$\psi^T = \left(\psi_A^K, \psi_C^K, \psi_B^K, \psi_B^{K'}, \psi_C^{K'}, \psi_A^{K'} \right).$$

In order to determine the gap equation for the intervalley gap, we need to calculate Green's function

$$G(\omega, \mathbf{k}) = \frac{1}{\omega - H_{iv}} = \begin{pmatrix} \omega - H_0^+ & F \\ F^\dagger & \omega + H_0^+ \end{pmatrix}^{-1}, \tag{3.18}$$

where F should be determined self-consistently from the Schwinger-Dyson equation which we derive below.

3.4.1   Ansatz and gap equation

Let us to consider the following ansatz for the intervalley gap with diagonal matrix F whose elements, however, are different:

$$F = \mathrm{diag}\,(\Delta, \Delta_2, \Delta) \tag{3.19}$$

and, without loss of generality, we assume that Δ and Δ_2 are real. This specific ansatz, whose first and third diagonal elements are the same, is consistent with the intervalley particle-hole symmetry (compare it with the particle-hole symmetry (3.8) for the intravalley electron and hole pairing) because the anticommutator of the operator $\mathcal{C}_{iv} = AKV$ with H_{iv} is zero

$$\{\mathcal{C}_{iv}, H_{iv}\} = 0, \quad V = \begin{pmatrix} I & 0 \\ 0 & -I \end{pmatrix}. \tag{3.20}$$

Here A is defined in Eq.(3.8), K is the complex conjugation, and V acts on the intervalley indices. The particular form of matrix V is motivated by the order of sublattice wave functions in 6-component spinor and is in agreement with Eq.(3.17). Note that since the intervalley particle-hole symmetry is preserved, it is no need to introduce the valley dependent chemical potential $\xi\mu_v$ like we did in the previous section for the case of intravalley pairing, where m_2 breaks the intravalley particle-hole symmetry. Green's function (3.18) for the intervalley gap function (3.19) is derived in Appendix 3.7.

Using this Green's function, we readily find that the Schwinger–Dyson equation leads to the following gap equation:

$$F = i\frac{2U}{v_F^2} \int \frac{d\omega d^2 k}{(2\pi)^3} \frac{B}{\det[\omega - H_{iv}]}, \tag{3.21}$$

where B is the off-diagonal block of Green's function defined in Eq.(3.61). The determinant in the denominator equals

$$\det[\omega - H_{iv}] = (\omega^2 - \Delta^2)(\omega^2 - a^2)(\omega^2 - b^2), \tag{3.22}$$

where

$$a^2, b^2 = \frac{1}{2}\left(4k^2 + \Delta^2 + \Delta_2^2 \pm |\Delta - \Delta_2|\sqrt{8k^2 + (\Delta + \Delta_2)^2}\right). \tag{3.23}$$

The corresponding spectrum is shown in Fig.3.3 for several values of Δ and Δ_2. We will find below that $\Delta_2 \ll \Delta$ for solutions of the gap equations, therefore, panel (c) describes the most relevant case. Equation (3.21) after the Wick rotation $\omega \to i\omega$ gives the equations for gap parameters which
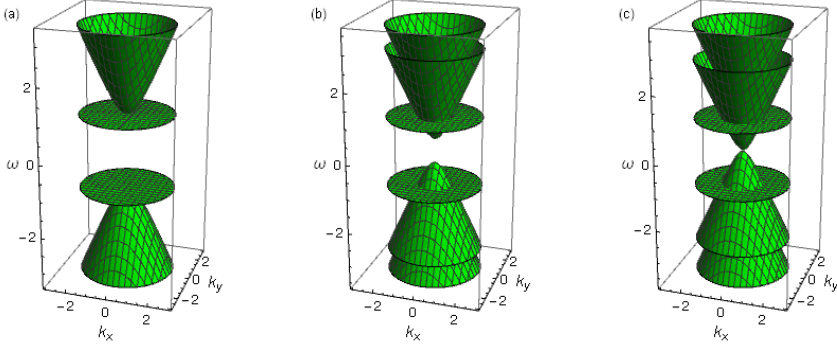
Figure 3.3. Energy dispersion for $\Delta_2 = \Delta$ (panel (a)), $\Delta_2 = 0.35\Delta$ (panel (b)), and $\Delta_2 = 0.02\Delta$ (panel (c)). Here ω and $\mathbf{k}$ are measured in units of Δ.

can be written as follows:

$$\Delta = \frac{2U}{v_F^2} \int \frac{d\omega d^2 k}{(2\pi)^3} \left[\frac{A}{\omega^2 + a^2} + \frac{B}{\omega^2 + b^2} + \frac{C}{\omega^2 + \Delta^2} \right], \tag{3.24}$$

$$\Delta_2 = \frac{2U}{v_F^2} \int \frac{d\omega d^2 k}{(2\pi)^3} \left[\frac{\Delta_2(a^2 - \Delta^2) - 2\Delta k^2}{(a^2 - b^2)(a^2 + \omega^2)} + \frac{\Delta_2(\Delta^2 - b^2) + 2\Delta k^2}{(a^2 - b^2)(b^2 + \omega^2)} \right], \tag{3.25}$$

where a^2 and b^2 are defined in Eq.(3.23) and coefficients A, B, C are

$$A = \frac{a^4\Delta - a^2(\Delta^3 + \Delta\Delta_2^2 + 2\Delta k^2 + \Delta_2 k^2) + \Delta(\Delta\Delta_2 + k^2)(\Delta\Delta_2 + 2k^2)}{(a^2 - b^2)(a^2 - \Delta^2)},$$

$$B = A(a \leftrightarrow b), \quad C = \frac{2\Delta k^2(k^2 - \Delta^2 + \Delta\Delta_2)}{(a^2 - \Delta^2)(b^2 - \Delta^2)}. \tag{3.26}$$

The structure of the gap equations (3.24), (3.25) implies that we can assume without loss of generality that $\Delta \geq 0$ and leave the sign of Δ_2

undefined. Then integrating over frequency and angle, we obtain $(a, b > 0)$

$$\Delta = \frac{2U}{v_F^2} \int_0^\Lambda \frac{kdk}{2\pi} \frac{1}{a+b} \left[\frac{k^2(a^2 + a\Delta_2 - k^2)}{a(a-b)(a+\Delta)} + (a \leftrightarrow b) + \frac{\Delta}{2} \right.$$
$$\left. + \frac{\Delta_2(\Delta\Delta_2 + 3k^2)}{2ab} \right], \tag{3.27}$$

$$\Delta_2 = \frac{2U}{v_F^2} \int_0^\Lambda \frac{kdk}{2\pi} \frac{1}{a+b} \left[\frac{\Delta(\Delta\Delta_2 + 2k^2)}{2ab} + \frac{\Delta_2}{2} \right]. \tag{3.28}$$

The above equations form a coupled system of equations for Δ and Δ_2. Note the symmetry under the exchange $a \leftrightarrow b$. We will solve this system numerically in Subsec.3.4.3. As we argued above, the flat band should play the principal role for intervalley gap generation. Therefore, before finding numerical solutions to the gap equations (3.27) and (3.28), it is instructive to study in the next subsection the intervalley gap generation by retaining only the flat bands in the two valleys.

3.4.2   Flat band approximation

To study the intervalley gap generation in the flat band approximation (FBA), we should find explicitly the corresponding flat band electron states. First of all, by using Eq.(3.2), we obtain that the normalized states of zero energy of the free Hamiltonian H_0^+ are given by

$$\psi_0^T(\mathbf{k}) = \frac{1}{\sqrt{2}\, 2\pi} \left(1,\, 0,\, -\frac{k_+}{k_-} \right), \tag{3.29}$$

where $k_\pm = k_x \pm i k_y$. In order to proceed and consider the intervalley gap generation, we should determine the eigenstates of Hamiltonian (3.17) in the subspace composed of flat band states in two valleys, i.e.,

$$H_{iv}\Psi = E\Psi, \tag{3.30}$$

where Ψ consists of the flat band states (3.29) in two valleys with two unknown constants $C_1 \equiv N$ and $C_2 \equiv NC$

$$\Psi^T = N \left(1,\, 0,\, -\frac{k_+}{k_-},\, C,\, 0,\, -C\frac{k_+}{k_-} \right). \tag{3.31}$$

The eigenstate equation (3.30) for $F = \mathrm{diag}\,(\Delta, \Delta_2, \Delta)$ gives two nontrivial relations

$$E - \Delta C = 0, \quad \Delta - EC = 0. \tag{3.32}$$

Note that the gap Δ_2 is not present in the above equations. Clearly, the system of equations (3.32) means that there are two solutions

$$C = 1, \quad E = -\Delta, \qquad\qquad C = -1, \quad E = \Delta. \qquad (3.33)$$

Obviously, the two former degenerate flat band solutions in two valleys are now split in energy by 2Δ.

Green's function connected with the flat band states has the form

$$G_{FB}(\omega, \mathbf{k}) = \frac{\Psi_{-\Delta}\Psi_{-\Delta}^{\dagger}}{\omega + \Delta} + \frac{\Psi_{\Delta}\Psi_{\Delta}^{\dagger}}{\omega - \Delta}, \qquad (3.34)$$

where

$$\Psi_{-\Delta}^{T} = \frac{1}{4\pi}\left(1,\, 0,\, -\frac{k_{+}}{k_{-}},\, -1,\, 0,\, \frac{k_{+}}{k_{-}}\right), \quad \Psi_{\Delta}^{T} = \frac{1}{4\pi}\left(1,\, 0,\, -\frac{k_{+}}{k_{-}},\, 1,\, 0,\, -\frac{k_{+}}{k_{-}}\right). \qquad (3.35)$$

In order to study the gap generation, we should consider the off-diagonal elements of the matrix G_{FB}. Let us consider the upper off-diagonal block (the consideration of the lower off-diagonal block gives the same results). Since the element 25 of the matrix G_{FB} is zero, we conclude that $\Delta_2 = 0$ in the flat band approximation. The elements 14 and 36 of the matrix G_{FB} coincide. Therefore, the ansatz with $F = \mathrm{diag}\,(\Delta, \Delta_2, \Delta)$, whose 11 and 33 elements are the same, is indeed consistent. Thus, we have the following gap equation in the flat band approximation defined by the element 14 or 36 of the matrix G_{FB}:

$$\Delta = -i\frac{2U}{v_F^2}\int\frac{d\omega d^2 k}{(2\pi)^3}\frac{1}{4\pi}\left(-\frac{1}{\omega - \Delta} + \frac{1}{\omega + \Delta}\right)$$
$$= \frac{iU}{\pi v_F^2}\int\frac{d\omega d^2 k}{(2\pi)^3}\frac{\Delta}{\omega^2 - \Delta^2 + i\delta}. \qquad (3.36)$$

Integrating over ω and introducing a cut-off Λ over momentum, we easily find the following gap in the flat band approximation:

$$\Delta = \frac{U\Lambda^2}{8\pi^2 v_F^2}. \qquad (3.37)$$

Clearly, the critical coupling constant is zero like in the case of the magnetic catalysis of the gap generation [117] in a model with local four-fermion interaction in $2 + 1$ dimensions. Note that there is no trivial solution again as in the magnetic catalysis case. The calculated gap (3.37)
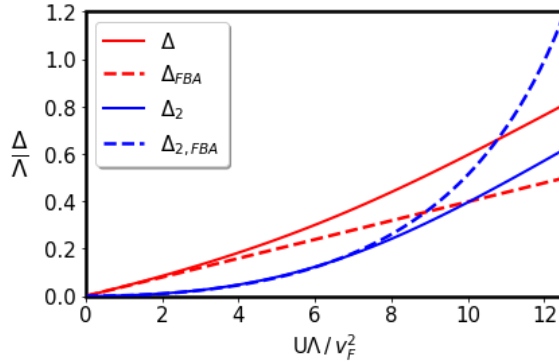
Figure 3.4. Numerical solutions of the gap equations (3.27) and (3.28).

is quadratically divergent and is much larger than the gap in the lowest Landau level (LLL) approximation. The reason is that Green's function in the LLL approximation in fermion systems with relativistic-like energy dispersion and dynamically generated mass m is quite similar to the flat band Green's function (3.34)

$$S_{LLL}(q) = e^{-\frac{\mathbf{q}^2}{|eB|}} \frac{\omega\gamma_0 - m}{\omega^2 - m^2} \left(1 - i\gamma_1\gamma_2\right) \tag{3.38}$$

except that it contains an exponentially decreasing factor in momenta $\mathbf{q}$ (here γ_0, γ_1, and γ_2 are the Dirac γ-matrices). Therefore, the corresponding solution to the gap equation is proportional to the magnetic field strength $|eB|$ rather than the cut-off squared Λ^2 (see Eq.(64) in [117]). This is the reason why the intravalley gap is so large.

In addition, we should note that the flat band approximation in the model under consideration can be obtained as a large momentum limit of gap equations. Assuming that $\Delta, \Delta_2 \ll \Lambda$, we can approximate coefficients a, b in (3.23) as follows:

$$a^2, b^2 \approx 2k^2. \tag{3.39}$$

Substituting this back in Eqs.(3.27) and (3.28), we find the following solutions for gap parameters:

$$\Delta = \frac{U}{v_F^2} \frac{\Lambda^2}{8\pi}, \quad \Delta_2 = \frac{\sqrt{2}U\Lambda\Delta}{8\pi v_F^2 - \sqrt{2}U\Lambda} = \frac{\sqrt{2}}{1 - \sqrt{2}\Delta/\Lambda} \frac{\Delta^2}{\Lambda}. \tag{3.40}$$

These expressions extend the results obtained in the two-band FBA discussed above and incorporate corrections from other energy bands for Δ_2. Before proceeding to the numerical analysis, it is instructive to estimate the values of generated gaps. Using cut-off $\Lambda = v_F \pi/(a\sqrt{2})$, we find $\Delta = \pi U/(16a^2)$. For local Coulomb interaction, we can use the corresponding estimate in graphene $V_C = e^2\sqrt{3}/(a\pi) \approx 3.3\,\text{eV}$ [118]. This gives the coupling constant $U = V_C/\Omega_{BZ}$ (here $\Omega_{BZ} = 2/(\sqrt{3}a^2)$ is the area of the Brillouin zone), we find $\Delta = 0.56\,\text{eV}$. Interestingly, the obtained result qualitatively agrees with the study of gap generation in twisted graphene bilayers near a magic angle [107], where the flat band is present. Indeed, due to the very large length of the moire lattice unit $a_{TBG} \approx 12\,nm$, the corresponding gaps are suppressed by factor a^2/a_{TBG}^2 leading to gaps of order few meV in twisted bilayer graphene. Finally, we note that it is crucial that there are two flat bands in different valleys and our analysis shows that the presence of a single flat band is not sufficient for the gap generation for an arbitrary small coupling constant.

3.4.3   Numerical analysis of solutions and their free energy

In the numerical analysis, it is convenient to measure U in units of v_F^2/Λ. Like in Sec.3.3.2 we use the iteration method to solve the gap equations. The corresponding numerical solutions are presented in Fig.3.4 and are compared with the flat band approximation result.

One should note that gap Δ_2 is one order of magnitude smaller that gap Δ for small values of U such that $U\Lambda/v_F^2 < 2$. For example, at $U\Lambda/v_F^2 = 1.4$ we find $\Delta \approx 0.06\Lambda$, $\Delta_2 \approx 0.005\Lambda$. However, Δ_2 grows much faster with coupling constant U, approximately as U^2, which quantitatively agrees with Eq.(3.40) at small coupling constant. $U\Lambda/v_F^2 > 4$, the FBA solution starts to deviate from the exact solution. Of course, we should note that the low-energy model is not applicable when gaps become of order Λ.

Among all solutions of the Schwinger Dyson equation the stable one is selected as the solution with the lowest free-energy density. The free energy density of a certain solution is determined by the value of the Baym–Kadanoff effective action (3.3) for the corresponding extremum of the Schwinger-Dyson equation $\delta\Gamma(G)/\delta G = 0$ which takes the form [112]

$$\Gamma = -\mathrm{i}\,\mathrm{Tr}\left[\mathrm{Ln}\,G^{-1}S + \frac{1}{2}\left(S^{-1}G - 1\right)\right]. \qquad (3.41)$$
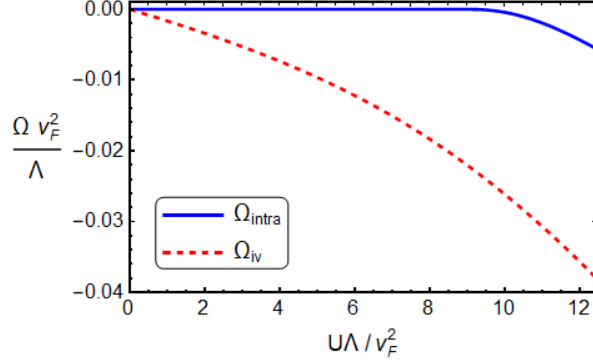
Figure 3.5. Numerical results for the free energy density Ω as a function of coupling constant U. The free energy density Ω_{intra} for the intravalley gap solution is given by Eq.(3.65) and Ω_{iv} for the intervalley gap solution is defined in Eq.(3.67).

The free energy density is given by $\Omega = -\Gamma/TV$ where TV is a space-time volume. Integrating by parts the logarithm term and omitting the irrelevant surface term (which does not depend on gaps), we find

$$\Omega = i \int\limits_{-\infty}^{\infty} \frac{d\omega}{2\pi} \frac{2}{v_F^2} \int \frac{d^2k}{(2\pi)^2} \, \mathrm{tr} \left\{ -\omega \left[\frac{\partial G^{-1}(\omega)}{\partial \omega} G(\omega) + S^{-1}(\omega) \frac{\partial S(\omega)}{\partial \omega} \right] \right.$$
$$\left. + \frac{1}{2} \left[S^{-1}(\omega) G(\omega) - 1 \right] \right\}. \tag{3.42}$$

The technical details of calculation of the energy density of the intravalley and intervalley gap solutions are presented in Appendix 3.8. Here we present the results of numerical evaluation by using Eqs.(3.65) and (3.67) and plot the free energies for both types of gaps in Fig.3.5. Clearly, the intervalley gap solution is always preferable including the region above the critical coupling constant (3.14).

3.5   Summary

We studied the gap generation in the dice model at the neutrality point. We found that there are two main intravalley and intervalley types of the electron-hole pairing which pairs the electron and hole states in the same

and different valleys, respectively. The neutrality of the system provides an important reduction of the number of order parameters. Indeed, it turned out that the particle-hole symmetry restricts the number of possible order parameters to three in the case of the intravalley gap and the intervalley particle-hole symmetry gives two independent order parameters for the intervalley pairing. Thus, there are three and two gap equations in the case of the intra- and intervalley gap generation, respectively.

To get an insight into the gap generation in the dice model and reveal the role of the flat band, we employed a local four-fermion interaction in our study. The main technical advantage of local interaction is that the gap equations are algebraic and admit an efficient numerical and partially analytic analysis. Our main finding is that the intervalley gap is generated for an arbitrary small coupling constant unlike the intravalley gap which requires a critical coupling constant. These qualitatively different results are due to the crucial role which plays the flat band in the intra- and intervalley gap generation.

Indeed, the intravalley gap pairs the electron and hole states in the same valley, therefore, it cannot pair states from the flat band only because such states cannot be the electron and hole ones simultaneously. In contrast, the intervalley gap relates the electron and hole states in flat bands from different valleys. The dispersionless band has a singular density of states that strongly enhances the intervalley gap generation leading to an extremely large gap proportional to the coupling constant times the area of the Brillouin zone. This result agrees with the heuristic argument that the completely flat band is the most favorable for the gap generation [119–122]. The intervalley gap generation in the dice model is also qualitatively similar to that in the case of magnetic catalysis in (2+1) dimensions in fermion systems with relativistic-like energy spectrum [117]. Indeed, magnetic field produces completely flat Landau levels and a fermion gap is generated for an arbitrary small coupling constant and is proportional to the degeneracy of the lowest Landau level defined by the inverse of the magnetic length squared l^{-2}. Since the magnetic length is typically much larger than the lattice constant (e.g., in graphene, l is 26 nm at $B = 1\,T$ and the lattice constant $a = 0.246\,nm$), the intravalley gap is strongly enhanced in the dice model by factor $l^2/a^2 \approx 10^4$ compared to the gap generated due to the magnetic catalysis. Thus, we conclude that the flat band catalysis is very efficient indeed. The underlying physical reason is very simple. Due to the dispersionless flat band, the integration over

momentum leads to a gap proportional to the area of the Brillouin zone, thus, very strongly enhancing the gap. This means that even if the middle band is not completely flat, still the intervalley gap generation should be very efficient and robust. Finally, we note that our results emphasize and shed additional light on the important role of flat band in the gap generation for magic angle twisted bilayer graphene.

3.6   Appendix: Intravalley Green's function and gap equations

Green's function of quasiparticles in the dice model with intravalley gaps at given valley ξ in momentum space equals

$$G_\xi(\omega, \mathbf{k}) = \frac{1}{\omega - H_\xi + \xi\mu_v} = \frac{1}{\det[\omega - H_\xi + \xi\mu_v]} \begin{pmatrix} G_{11} & D & E \\ B & G_{22} & H \\ C & F & G_{33} \end{pmatrix},$$

(3.43)

$$\det[\omega - H_\xi + \xi\mu_v] = (\omega + \xi\mu_v - \xi m_2)((\omega + \xi\mu_v)^2 - m^2) - 2\tilde{k}^2(\omega + \xi\mu_v),$$

where the diagonal matrix elements are

$$G_{11} = (\omega + \xi\mu_v + m)(\omega + \xi\mu_v - \xi m_2) - k^2, \tag{3.44}$$

$$G_{22} = (\omega + \xi\mu_v)^2 - m^2, \tag{3.45}$$

$$G_{33} = (\omega + \xi\mu_v - m)(\omega + \xi\mu_v - \xi m_2) - k^2, \tag{3.46}$$

and the off-diagonal elements are

$$D = (\omega + \xi\mu_v + m)k_-^\xi, \quad E = (k_-^\xi)^2, \quad B = (\omega + \xi\mu_v + m)k_+^\xi,$$
$$H = (\omega + \xi\mu_v - m)k_-^\xi, \quad C = (k_+^\xi)^2, \quad F = (\omega + \xi\mu_v - m)k_+^\xi, \tag{3.47}$$

and $k_-^\xi = (\xi k_x - ik_y)/\sqrt{2}$ and $k_+^\xi = (\xi k_x + ik_y)/\sqrt{2}$.

Clearly, all off-diagonal terms in $G_\xi(\omega, \mathbf{k})$ depend linearly or quadratically on k_+^ξ and k_-^ξ, therefore, all such terms vanish after integration over momentum in Eq.(3.9). Hence the Schwinger–Dyson equation gives three

equations for μ_v, m, and m_2 for the diagonal terms. They are

$$\xi\mu_v = -i\frac{2U}{v_F^2}\int\frac{d\omega d^2k}{(2\pi)^3}\frac{(\omega+\xi\mu_v)(\omega+\xi\mu_v-\xi m_2)-k^2}{\det[\omega+i0\mathrm{sgn}(\omega)-H_\xi+\xi\mu_v]}, \qquad (3.48)$$

$$m = i\frac{2U}{v_F^2}\int\frac{d\omega d^2k}{(2\pi)^3}\frac{m(\omega+\xi\mu_v-\xi m_2)}{\det[\omega+i0\mathrm{sgn}(\omega)-H_\xi+\xi\mu_v]}, \qquad (3.49)$$

$$\xi m_2 = i\frac{2U}{v_F^2}\int\frac{d\omega d^2k}{(2\pi)^3}\frac{(\omega+\xi\mu_v)\xi m_2+k^2-m^2}{\det[\omega+i0\mathrm{sgn}(\omega)-H_\xi+\xi\mu_v]}. \qquad (3.50)$$

Note that Eq.(3.49) for gap m is explicitly homogeneous unlike Eqs.(3.48) and (3.50) for μ_v and m_2. As we stated above, we seek solutions with $m\neq 0$, otherwise, the flat band with $\varepsilon=0$ is realized and it is not clear how to define a half-filled state.

Since ξ equals $\pm$ in two valleys, in fact, the system of equations (3.48)-(3.50) consists of six equations for three unknowns μ_v, m, and m_2. It is convenient to change the variable $\omega\to\xi\omega$ on the right-hand side of these equations to see that this system of equations is consistent. In order to calculate the integral over ω in the above gap equations and make it explicitly convergent we represent the integrands as $I(\omega) = [I(\omega) + I(-\omega)]/2$ utilizing the symmetric integration in ω. The denominators in the integrands is convenient to write in terms of roots of the cubic equation

$$\det[\omega-H_\xi+\xi\mu_v] = (\omega+\xi\mu_v-m_2)((\omega+\xi\mu_v)^2-m^2)-2k^2(\omega+\xi\mu_v)=0 \tag{3.51}$$

which are given by

$$r_n = \omega_n + \mu_v = \frac{m_2}{3} + 2m\sqrt{-\frac{p}{3}}\cos\left(\frac{1}{3}\arccos\left(\frac{3q}{2p}\sqrt{-\frac{3}{p}}\right)-\frac{2\pi n}{3}\right), \tag{3.52}$$

with $n = 0,1,2$ and where

$$p = -\left(1+\frac{2k^2}{m^2}+\frac{m_2^2}{3m^2}\right),$$

$$q = \frac{m_2}{m}\left(1-\frac{1+\frac{2k^2}{m^2}}{3}-\frac{2m_2^2}{27m^2}\right) = \frac{m_2}{m}\left(\frac{2}{3}\left(1-\frac{k^2}{m^2}\right)-\frac{2m_2^2}{27m^2}\right). \tag{3.53}$$

Thus, the determinant can be conveniently rewritten as

$$\det[\omega-H_\xi+\xi\mu_v] = (\omega+\xi\mu_v-r_0)(\omega+\xi\mu_v-r_1)(\omega+\xi\mu_v-r_2). \tag{3.54}$$

Then we obtain

$$\mu_v = -\frac{iU}{v_F^2} \int \frac{d\omega d^2 k}{(2\pi)^3} \left(\frac{(\omega + \mu_v)(\omega + \mu_v - m_2) - k^2}{\det[\omega + i\delta - H_\xi + \xi\mu_v]} - \left[\begin{array}{c} \mu_v \to -\mu_v, \\ m_2 \to -m_2 \end{array} \right] \right),$$

$$(3.55)$$

$$m = \frac{iU}{v_F^2} \int \frac{d\omega d^2 k}{(2\pi)^3} \left(\frac{m(\omega + \mu_v - m_2)}{\det[\omega + i\delta - H_\xi + \xi\mu_v]} + \left[\begin{array}{c} \mu_v \to -\mu_v, \\ m_2 \to -m_2 \end{array} \right] \right), \quad (3.56)$$

$$m_2 = \frac{iU}{v_F^2} \int \frac{d\omega d^2 k}{(2\pi)^3} \left(\frac{(\omega + \mu_v)m_2 + k^2 - m^2}{\det[\omega + i\delta - H_\xi + \xi\mu_v]} - \left[\begin{array}{c} \mu_v \to -\mu_v, \\ m_2 \to -m_2 \end{array} \right] \right),$$

$$(3.57)$$

where $\delta = 0\,\mathrm{sgn}(\omega)$. This form of equations is convenient for further integration over frequency leading to Eqs.(3.10) - (3.12) in the main text.

3.7 Appendix: Intervalley Green's function

For Green's function of the intervalley gap ansatz (3.18), we find the following explicit expression:

$$G_{ij} = \frac{1}{\det[\omega - H_{iv}]} \left(\begin{array}{cc} A & B \\ C & D \end{array} \right), \quad (3.58)$$

and the determinant in denominator equals to

$$\det[\omega - H_{iv}] = (\omega^2 - \Delta^2) \left[\omega^4 - \omega^2(4k^4 + \Delta^2 + \Delta_2^2) + (2k^2 + \Delta\Delta_2)^2 \right]. \quad (3.59)$$

The elements of the matrix A are

$$A_{11} = \omega \left(\left(\Delta^2 - \omega^2 \right) \left(\Delta_2^2 - \omega^2 \right) + 2k^4 + \tilde{k}^2 \left(\Delta^2 + 2\Delta_2\Delta - 3\omega^2 \right) \right),$$
$$A_{12} = k_- \left(\Delta^2 - \omega^2 \right) \left(\Delta\Delta_2 + 2k^2 - \omega^2 \right),$$
$$A_{13} = k_-^2 \omega \left(\Delta^2 - 2\Delta\Delta_2 - 2k^2 + \omega^2 \right),$$

$$A_{21} = k_+ \left(\Delta^2 - \omega^2 \right) \left(\Delta\Delta_2 + 2k^2 - \omega^2 \right),$$
$$A_{22} = \omega \left(\Delta^2 - \omega^2 \right) \left(\Delta^2 + 2k^2 - \omega^2 \right),$$
$$A_{23} = k_- \left(\Delta^2 - \omega^2 \right) \left(\Delta\Delta_2 + 2k^2 - \omega^2 \right),$$

$$A_{31} = k_+^2 \omega \left(\Delta^2 - 2\Delta\Delta_2 - 2k^2 + \omega^2 \right),$$
$$A_{32} = k_+ \left(\Delta^2 - \omega^2 \right) \left(\Delta\Delta_2 + 2k^2 - \omega^2 \right),$$
$$A_{33} = \omega \left(\left(\Delta^2 - \omega^2 \right) \left(\Delta_2^2 - \omega^2 \right) + 2k^4 + k^2 \left(\Delta^2 + 2\Delta_2\Delta - 3\omega^2 \right) \right).$$
$$(3.60)$$

It turned out that $B = C$ and the elements of B are

$$B_{11} = \Delta \left(\Delta^2 - \omega^2 \right) \left(\Delta_2^2 - \omega^2 \right) + 2\Delta k^4 + k^2 \left(3\Delta^2\Delta_2 - (2\Delta + \Delta_2)\omega^2 \right),$$
$$B_{12} = (\Delta - \Delta_2) \, k_- \omega \left(\Delta^2 - \omega^2 \right),$$
$$B_{13} = -k_-^2 \left(\Delta^2\Delta_2 - 2\Delta\omega^2 + \Delta_2\omega^2 + 2\Delta k^2 \right),$$

$$B_{21} = (\Delta - \Delta_2) \, (-k_+)\omega \left(\Delta^2 - \omega^2 \right),$$
$$B_{22} = \left(\Delta^2 - \omega^2 \right) \left(\Delta_2 \left(\Delta^2 - \omega^2 \right) + 2\Delta k^2 \right),$$
$$B_{23} = (\Delta - \Delta_2) \, (-k_-)\omega \left(\Delta^2 - \omega^2 \right),$$

$$B_{31} = -k_+^2 \left(\Delta^2\Delta_2 - 2\Delta\omega^2 + \Delta_2\omega^2 + 2\Delta k^2 \right),$$
$$B_{32} = (\Delta - \Delta_2) \, k_+\omega \left(\Delta^2 - \omega^2 \right),$$
$$B_{33} = \Delta \left(\Delta^2 - \omega^2 \right) \left(\Delta_2^2 - \omega^2 \right) + 2\Delta k^4 + k^2 \left(3\Delta^2\Delta_2 - (2\Delta + \Delta_2)\omega^2 \right).$$
$$(3.61)$$

Finally, the elements of D are

$$D_{11} = \omega \left(\left(\Delta^2 - \omega^2 \right) \left(\Delta_2^2 - \omega^2 \right) + 2k^4 + k^2 \left(\Delta^2 + 2\Delta_2\Delta - 3\omega^2 \right) \right),$$
$$D_{22} = \omega \left(\Delta^2 - \omega^2 \right) \left(\Delta^2 + 2k^2 - \omega^2 \right),$$
$$D_{21} = -k_+(\Delta^2 - \omega^2)(2k^2 - \omega^2 + \Delta\Delta_2),$$

$$D_{31} = k_+^2 \omega(-2k^2 + \Delta^2 + \omega^2 - 2\Delta\Delta_2),$$
$$D_{12} = -k_-(\Delta^2 - \omega^2)(2k^2 - \omega^2 + \Delta\Delta_2),$$
$$D_{32} = -k_+(\Delta^2 - \omega^2)(2k^2 - \omega^2 + \Delta\Delta_2),$$

$$D_{13} = k_-^2 \omega(-2k^2 + \Delta^2 + \omega^2 - 2\Delta\Delta_2),$$
$$D_{23} = -k_-(\Delta^2 - \omega^2)(2k^2 - \omega^2 + \Delta\Delta_2),$$
$$D_{33} = \omega \left(\left(\Delta^2 - \omega^2 \right) \left(\Delta_2^2 - \omega^2 \right) + 2k^4 + k^2 \left(\Delta^2 + 2\Delta_2\Delta - 3\omega^2 \right) \right).$$
$$(3.62)$$

In the main text we use the diagonal elements of B to write the gap equations in the explicit form. Note, that off-diagonal components vanish after integration over polar angle ϕ in momentum space.

3.8 Appendix: Evaluation of free energy

In this Appendix we present the detailed calculation of the free energy density for intravalley and intervalley gap states in the dice model. The final results are given by Eqs.(3.65) and (3.67).

Using expression (3.42) for the Baym–Kadanoff free energy, we denote the integrand as

$$\tilde{\Omega}(\boldsymbol{k}, \omega) = \text{tr} \left\{ \frac{S^{-1}(\omega)G(\omega) - 1}{2} - \omega \left[\frac{\partial G^{-1}(\omega)}{\partial \omega} G(\omega) + S^{-1}(\omega) \frac{\partial S(\omega)}{\partial \omega} \right] \right\}.$$
$$(3.63)$$

First we evaluate the trace and perform summation over valleys, decomposing the result into fractions. Next it is convenient to perform the Wick rotation $\omega \to i\omega$. For the intravalley gap state, we obtain

$$\tilde{\Omega}_{intra}(\boldsymbol{k}, i\omega) = -\frac{8k^2}{\omega^2 + 2k^2} - \left((\mu_v - r_0) \times \right.$$
$$\left. \frac{m^2(3m_2 - 2r_0 - \mu_v) - 2k^2(4r_0 + \mu_v) + r_0(3r_0\mu_v - m_2(r_0 + 2\mu_v))}{(r_1 - r_0)(r_0 - r_2)((\mu_v - r_0)^2 + \omega^2)} + c.p. \right),$$
$$(3.64)$$

where $(c.p.)$ denotes cyclic permutation of r_i. The integration over frequency ω is easily performed and we come at the free energy density for

the intravalley gap state given by

$$\Omega_{intra} = \frac{1}{v_F^2} \int_0^\Lambda \frac{k\,dk}{\pi} \left[2\sqrt{2}k + \right.$$

$$\left(\frac{-2k^2\left(4r_0 + \mu_v\right) + m^2\left(3m_2 - 2r_0 - \mu_v\right) + r_0\left(3r_0\mu_v - m_2\left(r_0 + 2\mu_v\right)\right)}{2\left(r_1 - r_0\right)\left(r_0 - r_2\right)} \right.$$

$$\left. \left. \times \operatorname{sign}\left[\mu_v - r_0\right] + c.p. \right) \right], \tag{3.65}$$

This expression is invariant under the change of sign $m \to -m$ or $(m_2, \mu_v) \to (-m_2, -\mu_v)$. Using the numerically found solutions from Sec.3.3 (see Fig.3.2), we evaluate the integral over k. The corresponding results for the free energy are shown in Fig.3.5.

In the case of the intervalley gap state, we obtain for the integrand in the Baym–Kadanoff free energy (3.42) after the Wick rotation $\omega \to i\omega$

$$\tilde{\Omega}_{iv}(\boldsymbol{k}, \omega) = \frac{\Delta^2}{\Delta^2 + \omega^2} - \frac{8k^2}{2k^2 + \omega^2}$$
$$+ \frac{\Delta^2\left(2\Delta_2^2 + \omega^2\right) + \Delta_2^2\omega^2 + 12\Delta\Delta_2 k^2 + 8k^2\left(2k^2 + \omega^2\right)}{(\omega^2 + a^2)(\omega^2 + b^2)}. \tag{3.66}$$

Expanding the middle fraction and performing integration over ω, we find the free energy density for the intervalley gap state

$$\Omega_{iv} = -\frac{2}{v_F^2} \int_0^\Lambda \frac{k\,dk}{2\pi} \left[\frac{|\Delta|}{2} - 2\sqrt{2}k + \right.$$

$$\left. \left(\frac{a^2\Delta_2^2 + \Delta^2\left(a^2 - 2\Delta_2^2\right) + 8k^2\left(a^2 - 2k^2\right) - 12\Delta\Delta_2 k^2}{2a\left(a^2 - b^2\right)} + (a \leftrightarrow b) \right) \right]. \tag{3.67}$$

The free energy density Ω for the intervalley gap from Sec.3.4.3 is shown in Fig.3.5 by red dashed line.

Chapter 4

Optical conductivity of semi-Dirac and pseudospin-1 models: Zitterbewegung approach

4.1 Introduction

The optical studies of electronic systems is one of the main sources of information about charge dynamics in different condensed matter systems: high-Tc superconducting cuprates [123, 124], graphene [125–130], topological insulators [131] together with Dirac and Weyl materials [132–134]. Recently it was shown [15] that in crystals with special space symmetry groups more complicated quasiparticle spectra could be realized with no analogues in high-energy physics where the Poincare symmetry provides strong restrictions. Some of such systems possess strictly flat (dispersionless) bands [92, 100, 101] with high degeneracy potentially leading to a large enhancement of some physical quantities.

In the present paper we develop the method to calculate frequency-dependent optical and Hall conductivities in low-energy models containing also new types of quasiparticles. The presented method is based on the solution of the Heisenberg equations for the time-dependent quasiparticle velocity operators, which also describe the phenomena of zitterbewegung (trembling motion) [47, 135]. The formulation of this method is very similar to the proper time approach of Schwinger [136] and the obtained

expressions extend previously derived formulas for longitudinal conductivity in Refs.[137, 138]. We rewrite the Kubo formula through quasiparticle velocity correlators, and use the solutions of the Heisenberg equations. We demonstrate the applicability of the described method to the semi-Dirac model and gapped pseudospin-1 models of the dice and Lieb lattices. As a result, we obtain closed-form analytic expressions, which in turn are used to investigate the dependence of conductivities on frequency, gap size and temperature.

The phenomenon of Dirac points merging in two-dimensional materials has received much attention in the literature [139–141]. Such system was realized experimentally in optical lattices [142] and in microwave cavities [143]. The analytical and numerical calculations of optical conductivity for semi-Dirac systems were discussed in several recent papers [144–148]. Quite recently the magneto-conductivity of the semi-Dirac model was studied [149].

The dice model is a tight-binding model of two-dimensional fermions living on the $\mathcal{T}_3$ (or dice) lattice where atoms are situated both at the vertices of hexagonal lattice and the hexagons centers [11, 80]. Since the dice model has three sites per unit cell, the electron states in this model are described by three-component fermions and the energy spectrum of the model is comprised of three bands. The two of them form Dirac cones and the third band is completely flat and has zero energy [12, 13]. The $\mathcal{T}_3$ lattice has been experimentally realized in Josephson arrays [16, 17], metallic wire networks [18] and its optical realization by laser beams was proposed in Refs.[12, 19]. The optical and Hall conductivities for the $\alpha - \mathcal{T}_3$ model were studied in Refs. [49, 150–152]. We show that our method allows one to obtain fully analytic expressions for the case of S_z model even without magnetic field, thus extending the previous results.

Another example of pseudospin-1 system considered in this paper is the gapped low-energy model of the Lieb lattice [21]. Due to the presence of flat band in spectrum [21, 153, 154], the Lieb lattice served as a platform for theoretical studies of many strongly-correlated phenomena - ferromagnetism [20, 155] and superconductivity [156, 157]. The Lieb lattice was realized in many experimental setups: arrays of optical waveguides [8, 158] via the surface state electrons of Cu(111) confined by an array of carbon monoxide molecules [7], in vacancy lattice in chlorine monolayer on Cu(100) surface [159] and in covalent organic frameworks [9, 10].

The chapter is organized as follows: in Sec.4.2 we present the most
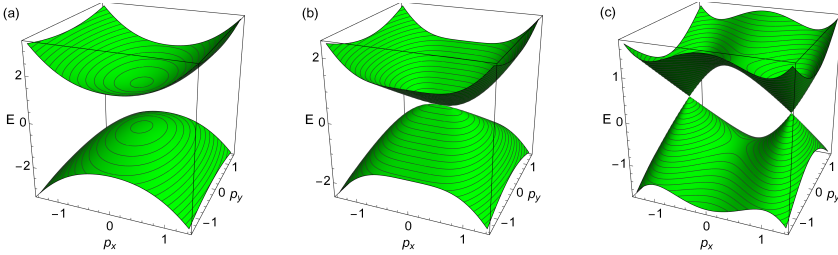
Figure 4.1. Spectrum given by Hamiltonian H_{semi} in Eq.(4.9). The values of gap parameter are (a) $\Delta = 1$, (b) $\Delta = 0$ and (c) $\Delta = -1$. We choose units $v = 1$, $a = 1$. The panel (a) represents a fully gapped regime, while the panel (c) corresponds to the regime with two Dirac cones separated by $2\sqrt{\Delta/a}$ along the x-direction.

general formulas for the optical and Hall conductivity in terms of quasiparticle velocity correlators. In Sec.4.3 we apply the method for a simple, but physically reach semi-Dirac model with merging Diral cones. Next, we apply the described approach to calculate the optical conductivity of the gapped dice model. For this purpose in Sec.4.4.1 we solve the Heisenberg equations for the dice model with gap and discuss properties of the quasiparticle dynamics. Combining the results with general formulas for conductivity in Sec.4.4.2, we find the optical and Hall conductivity and analyze their dependence on external frequency. Finally, in Sec.4.5 we perform similar calculation for the Lieb lattice model, whose underlying matrix algebra is much more complicated. In the Appendices we present the details of Kubo formula transformations and conductivity integrals evaluation.

4.2 Expression for conductivity through particle velocity correlators

The method described below is an extension of the approach used in Ref.[135] to an arbitrary pseudospin model with different dispersions. We start the derivation from the Kubo formula for frequency-dependent elec-

trical conductivity tensor written in the following form [138]:

$$\sigma_{\mu\nu}(\omega) = \frac{i}{(\omega + i\varepsilon)V}$$
$$\times \left[\langle \tau_{\mu\nu} \rangle - \frac{i}{\hbar} \int_0^\infty dt e^{i(\omega + i\varepsilon)t} \operatorname{Tr} \left(\hat{\rho} \left[J_\mu(t), J_\nu(0) \right] \right) \right], \qquad (4.1)$$

where V is the volume (area) of the system, $\hat{\rho} = \exp\left(-\beta H\right)/Z$ is the density matrix with the Hamiltonian H in the grand canonical ensemble, $Z = \operatorname{Tr} \exp\left(-\beta H\right)$ is the partition function, $\beta = 1/k_B T$, and J_μ are the current operators. The diamagnetic or stress tensor $\langle \tau_{\mu\nu} \rangle$ in the Kubo formula (4.1) is a thermal average of the operator defined as $\tau_{\mu\nu} = \partial^2 H/\partial(A^\mu/c)\partial(A^\nu/c)$. In the case of a linear dispersion law the term with $\langle \tau_{\mu\nu} \rangle$ in Eq.(4.1) is absent. In what follows we set $\hbar = 1$ and restore it in the final expressions.

The important symmetry properties of the conductivity are

$$\operatorname{Re}\sigma_{\mu\nu}(\omega) = \operatorname{Re}\sigma_{\mu\nu}(-\omega), \qquad (4.2)$$

$$\operatorname{Im}\sigma_{\mu\nu}(\omega) = -\operatorname{Im}\sigma_{\mu\nu}(-\omega). \qquad (4.3)$$

Using the representation of conductivity tensor through the correlation functions of currents (see Ref.[137] and Appendix 4.7) and expressing them in terms of time-dependent particle velocity correlators, we arrive at the following general expressions:

$$\operatorname{Re}\sigma_{\{\mu,\nu\}}(\omega) = \frac{e^2}{2\omega} \int_{-\infty}^\infty dE \rho(E) \left[f(E) - f(E+\omega) \right]$$
$$\times \int_{-\infty}^\infty dt e^{i\omega t} \left\langle v_{\{\mu}(t) v_{\nu\}}(0) \right\rangle_E, \qquad (4.4)$$

where the velocity operator $v_\mu(t) = e^{iHt} v_\mu(0) e^{-iHt}$. Here we defined the microcanonical average of an operator $\hat{A}$ at given energy E as

$$\langle \hat{A} \rangle_E = \frac{\operatorname{Tr}[\delta(E - \hat{H})\hat{A}]}{\operatorname{Tr}[\delta(E - \hat{H})]} \qquad (4.5)$$

where $\operatorname{Tr}[\delta(E - \hat{H})] = \rho(E)V$ and $\rho(E)$ is the density of states (DOS). It is easy to check that the last expression is real using

$$\left\langle v_{\{\mu}(-t) v_{\nu\}}(0) \right\rangle_E^* = \left\langle v_{\{\mu}(t) v_{\nu\}}(0) \right\rangle_E. \qquad (4.6)$$

The expression (4.4) for $T = 0$ is in accordance with Ref.[160] for diagonal conductivity. The numerator in Eq.(4.5) can be represented using the Fourier transformation:

$$\text{Tr}[\delta(E - \hat{H})\hat{A}] = \frac{V}{2\pi} \int_{-\infty}^{\infty} ds e^{iEs} \text{Tr}\left[e^{-i\hat{H}s}\hat{A}\right]$$

$$= \frac{V}{2\pi} \int_{-\infty}^{\infty} ds e^{iEs} \int \frac{d^2 p}{(2\pi)^2} \text{tr}\left[e^{-iH(\boldsymbol{p})s}\hat{A}(\boldsymbol{p})\right]. \tag{4.7}$$

Similarly, for the imaginary antisymmetric part of conductivity we have

$$\text{Im}\,\sigma_{[\mu,\nu]}(\omega) = \frac{e^2}{2\omega} \text{Im} \int_{-\infty}^{\infty} dE \rho(E) \left[f(E) - f(E + \hbar\omega)\right]$$

$$\times \int_{-\infty}^{\infty} dt e^{i\omega t} \left\langle v_{[\mu}(t)v_{\nu]}(0)\right\rangle_E. \tag{4.8}$$

We note that the integral over t is purely imaginary due to the property $\left\langle v_{[\mu}(-t)v_{\nu]}(0)\right\rangle_E^* = -\left\langle v_{[\mu}(t)v_{\nu]}(0)\right\rangle_E$.

To calculate $\text{Im}\,\sigma_{\{\mu,\nu\}}(\omega)$ and $\text{Re}\,\sigma_{[\mu,\nu]}(\omega)$ we use the Kramers-Krönig relation (4.60). The equations (4.4) and (4.8) together with Eqs.(4.5) and (4.7) allow one to obtain the final result after two Fourier transformations.

4.3 Optical conductivity of the semi-Dirac model

In this section we analyze the conductivity of the semi-Dirac model, which was extensively used to describe the low-energy physics of phosphorene [144, 147, 148, 161, 162]. The main feature of such model is that it mixes linear and quadratic terms in the Hamiltonian

$$H_{semi} = \left(\Delta + a p_x^2\right)\sigma_x + v p_y \sigma_y. \tag{4.9}$$

The dispersion defined by this Hamiltonian consists of two bands:

$$\varepsilon_\pm = \pm\sqrt{(a p_x^2 + \Delta)^2 + v^2 p_y^2}. \tag{4.10}$$

The spectrum described by Eq.(4.10) is presented in Fig.4.1. By tuning the gap parameters, one can achieve a completely different types of spectrum - fully gapped, one band-touching point or two band-touching points separated by $2\sqrt{\Delta/a}$ distance along p_x momentum.

Writing the Heisenberg equations for this Hamiltonian, we find

$$\boldsymbol{v}(t) = \frac{d\boldsymbol{x}}{dt} = -i[\boldsymbol{x}(t),\, H_{semi}(t)] = (2ap_x(t)\sigma_x(t),\, v\sigma_y(t)), \qquad (4.11)$$

$$\frac{dp_i}{dt} = -i[p_i,\, H_{semi}] = 0. \qquad (4.12)$$

From the first equation we find that velocity depends on momentum $p_x(t)$, which does not evolve as a result of the second equation: $p_x(t) = p_x(0)$. Also, velocity depends on the Pauli matrices, which evolve with time according to another Heisenberg equation:

$$\frac{d\boldsymbol{\sigma}(t)}{dt} = -i[\boldsymbol{\sigma}(t), H_{semi}] = 2[\tilde{\boldsymbol{p}}(0) \times \boldsymbol{\sigma}(t)]. \qquad (4.13)$$

Here we used notation $\tilde{\boldsymbol{p}}(0) = [\Delta + ap_x^2, vp_y, 0]$ and the fact that the commutator of the Pauli matrices is $[\sigma_i(t), \sigma_j(t)] = 2i\varepsilon_{ijk}\sigma_k(t)$. Cross means the vector product of $\tilde{\boldsymbol{p}}$ and $\boldsymbol{\sigma}$. The initial condition for the Pauli matrices is $\boldsymbol{\sigma}(0) = (\sigma_x, \sigma_y, \sigma_z)$, thus the operator $\boldsymbol{\sigma}(0)$ is in the Schrödinger picture, i.e., it is time independent.

Equation (4.13) describes the time evolution of the pseudospin degree of freedom in terms of Pauli matrices acting on states in Hilbert space. Such an unusual temporal evolution of matrix operators first appeared in the original paper by Schrödinger [48] on the zitterbewegung of the electron described by the Dirac Hamiltonian. It is clear from Eq.(4.13) that the pseudospin vector $\boldsymbol{\sigma}(t)$ precesses around the vector $\boldsymbol{p}$. Below we demonstrate that similar Heisenberg equations describe the dynamics of pseudospin degree of freedom for another matrix types depending on effective Hamiltonian of quasiparticles.

The Heisenberg equation above gives a system of differential equations for matrices $\dot{\sigma}_i(t) = P_{ij}\sigma_j(t)$, $P_{ij} = 2\varepsilon_{ikj}\tilde{p}_k$, whose solution is

$$\sigma_i(t) = \left(e^{Pt}\right)_{ij}(\tilde{\boldsymbol{p}})\sigma_j(0), \qquad \left(e^{Pt}\right)_{ij}(\tilde{\boldsymbol{p}}) =$$

$$\begin{pmatrix} \frac{\tilde{p}_y^2 \cos(2\tilde{p}t) + \tilde{p}_x^2}{\tilde{p}^2} & \frac{\tilde{p}_x\tilde{p}_y(1 - \cos(2\tilde{p}t))}{\tilde{p}^2} & \frac{\tilde{p}_y \sin(2\tilde{p}t)}{\tilde{p}} \\ \frac{\tilde{p}_x\tilde{p}_y(1 - \cos(2\tilde{p}t))}{\tilde{p}^2} & \frac{\tilde{p}_x^2 \cos(2\tilde{p}t) + \tilde{p}_y^2}{\tilde{p}^2} & -\frac{\tilde{p}_x \sin(2\tilde{p}t)}{\tilde{p}} \\ -\frac{\tilde{p}_y \sin(2\tilde{p}t)}{\tilde{p}} & \frac{\tilde{p}_x \sin(2\tilde{p}t)}{\tilde{p}} & \cos(2\tilde{p}t) \end{pmatrix}. \qquad (4.14)$$

Here we denoted $\tilde{p} = \sqrt{\tilde{p}_x^2 + \tilde{p}_y^2}$. The time-dependent velocity is obtained from these solutions by combining them with Eq.(4.11). The velocity $v_i(t)$

contains zitterbewegung terms which stem from the oscillatory terms (the cosine and sine terms) in Eq.(4.14).

The zitterbewegung phenomenon was first regarded as a relativistic effect related to the Dirac equation and describing "trembling" or oscillatory motion of the center of a free wave packet [48, 163]. The appearance of zitterbewegung phenomena in graphene and other two-dimensional condensed matter systems [47, 135, 164] indicates that the effect is not purely relativistic, originating from inter-band transitions between states with positive and negative energy. The direct experimental observation of the zitterbewegung became recently possible in a Bose–Einstein condensate of ultracold atoms [165].

We now proceed by calculating the traces of velocity products with matrix exponential of the Hamiltonian as they appear in Eq.(4.7). Due to the anisotropy in the electron dispersion, the conductivity is also anisotropic, therefore, we present the results of its calculation in separate sections.

4.3.1 Optical conductivity in xx-direction

We start with the evaluation of real part of optical conductivity in the x-direction. For this purpose we start with the calculation of trace which has the form as in Eq.(4.7):

$$\text{Tr}\left[e^{-iH_{semi}s}v_x(t)v_x(0)\right] = \int \frac{d^2p}{(2\pi)^2} \frac{8a^2p_x^2}{\varepsilon_+^2} \times$$

$$\left(v^2p_y^2 \cos\left((s-2t)\varepsilon_+\right) + \left(ap_x^2 + \Delta\right)^2 \cos\left(s\varepsilon_+\right)\right). \qquad (4.15)$$

Next we substitute this result into the expression for the real part of the xx longitudinal conductivity (4.4), and calculate the Fourier transforms over t and s. The result has the form of double integral:

$$\text{Re}\,\sigma_{xx}(\omega) = \frac{e^2}{\omega} \int_{-\infty}^{\infty} \frac{dE}{2\pi}[f(E) - f(E+\omega)] \int d^2p \frac{2a^2p_x^2}{\varepsilon_+^2}$$

$$\times \left[\delta\left(E + \varepsilon_+\right)\left(v^2p_y^2\delta\left(\omega + 2\varepsilon_-\right) + \delta(\omega)\left(ap_x^2 + \Delta\right)^2\right)\right.$$

$$\left. + \delta\left(E + \varepsilon_-\right)\left(v^2p_y^2\delta\left(\omega + 2\varepsilon_+\right) + \delta(\omega)\left(ap_x^2 + \Delta\right)^2\right)\right]. \qquad (4.16)$$

The procedure of integration over momentum depends on the sign of Δ parameter, and is described in details in Appendix 4.8. The main trick
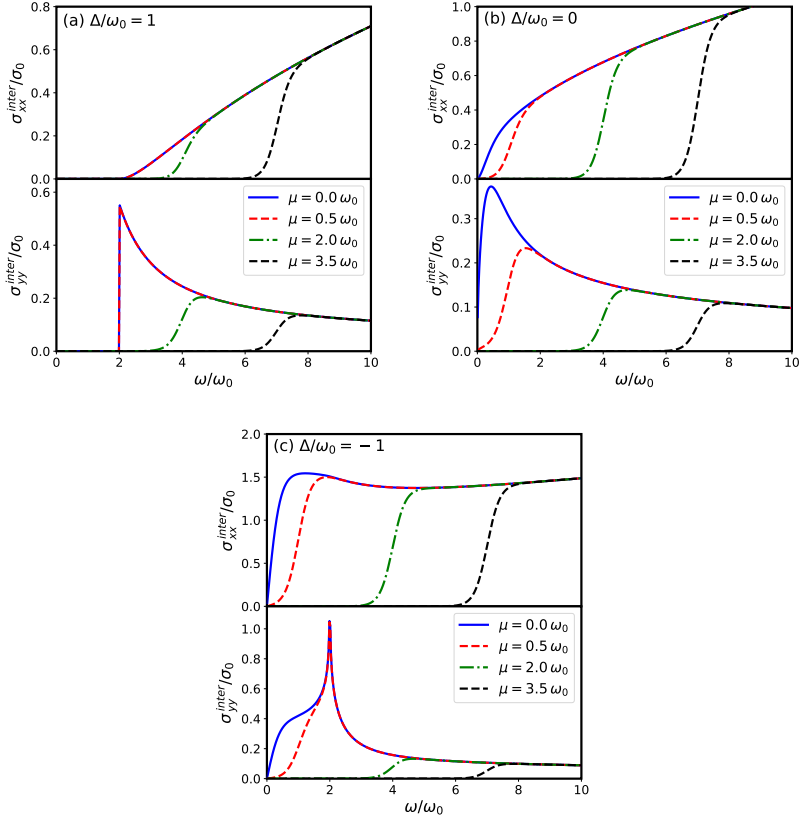
Figure 4.2. Real part of longitudinal interband ac conductivity in x- and y-directions (top and bottom plots) as a function of frequency for the fixed values of gap Δ for the semi-Dirac model. The frequency is measured in units of $\omega_0 = v^2/a$. The normalization parameters are $\sigma_0 = \frac{e^2\sqrt{a}}{2\pi\hbar v}$ for the x-direction and $\sigma_0 = \frac{e^2 v}{2\pi\hbar\sqrt{a}}$ for the y-direction. The values of gap parameter are (a) $\Delta/\omega_0 = 1$, (b) $\Delta/\omega_0 = 0$ and (c) $\Delta/\omega_0 = -1$.

in calculation is to introduce modified polar coordinates, which take into account the anisotropy of dispersion (4.10) in each case $\Delta < 0$, $\Delta = 0$ and $\Delta > 0$ with the proper regions of integration. As a result, we were able to express all integrals in terms of complete elliptic integrals. The results for the real part of interband ac and intraband dc conductivities are:

$$\operatorname{Re}\sigma_{xx}^{inter}(\omega) = \operatorname{sgn}\omega\frac{e^2}{2\pi\hbar}\frac{\sqrt{2|\omega|a}}{4v}\left[f\left(-\frac{\omega}{2}\right) - f\left(\frac{\omega}{2}\right)\right] \times$$

$$\times \begin{cases} \begin{aligned} & 2\Theta(|\Delta| - |\omega/2|)I_3^{xx}(2\Delta/|\omega|) \\ & +2\Theta(|\omega/2| - |\Delta|)I_1^{xx}(2\Delta/|\omega|) \end{aligned}, & \Delta < 0, \\[2ex] \frac{16\pi^{3/2}}{5\sqrt{2}\Gamma^2\left(\frac{1}{4}\right)}, & \Delta = 0, \\[2ex] 2\Theta(|\omega/2| - \Delta)I_1^{xx}(2\Delta/|\omega|), & \Delta > 0. \end{cases} \qquad (4.17)$$

The integrals I_1^{xx}, I_3^{xx}, and similar integrals occurring below, are defined in Appendix 4.8, they are given in terms of complete elliptic integrals of the first and second kind.

We plot the conductivity $\operatorname{Re}\sigma_{xx}^{inter}(\omega)$ as a function of ω at different values of Δ in upper plots of Fig.4.2. In all plots we set $Ta = 0.1$, and absorb v and a parameters into normalization constant σ_0. As is seen, the behavior of the conductivities at small frequencies, $\omega < 2|\Delta|$, is radically different for $\Delta > 0$ and $\Delta < 0$: the case $\Delta > 0$ corresponds to insulating phase while $\Delta \leq 0$ corresponds to metallic phase.

The analytic expression (4.17) allows one to get asymptotes at small and large ω, for example, in the most interesting case $\Delta < 0$ they are

$$\operatorname{Re}\sigma_{xx}^{inter}(\omega) \simeq \frac{e^2}{2\pi\hbar}\begin{cases} \frac{\sqrt{|\Delta|a}}{v}\frac{\pi\omega}{8T\cosh^2\frac{\mu}{2T}}, & \omega \to 0, \\[2ex] \frac{\sqrt{\omega a}}{v}\frac{4\pi^{3/2}}{5\Gamma^2\left(\frac{1}{4}\right)}, & \omega \to \infty. \end{cases} \qquad (4.18)$$

In the intraband part of conductivity with $\delta(\omega)$ the result contains
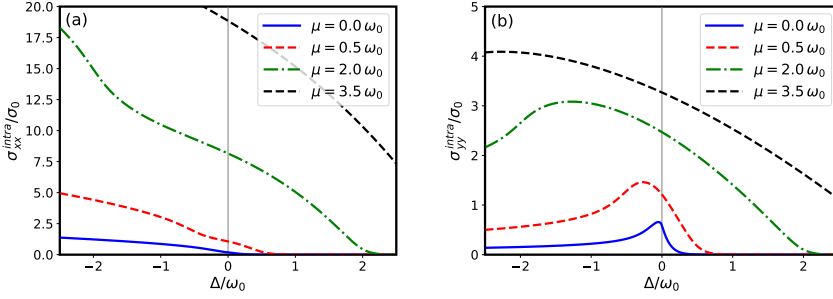
Figure 4.3. Real part of xx (a) and yy (b) intraband dc conductivities as functions of the gap Δ for different values of chemical potential. The temperature is equal to $T = 0.1\,\omega_0$ in both cases with $\omega_0 = v^2/a$. The pronounced peak at $\mu = 0$ in panel (b) manifests the possibility of dc transport through the charge-neutrality point.

integral over energy,

$$\mathrm{Re}\,\sigma_{xx}^{intra}(\omega) = \delta(\omega)\frac{e^2\sqrt{a}}{4\pi\hbar v T}\int_{-\infty}^{\infty}\frac{dE|E|^{3/2}}{\cosh^2\left(\frac{E-\mu}{2T}\right)}\times$$

$$\times\begin{cases}2\Theta(|\Delta|-|E|)I_4^{xx}(\Delta/|E|) \\ +2\Theta(|E|-|\Delta|)I_2^{xx}(\Delta/|E|)\end{cases}, \quad \Delta < 0, \\[2mm] \dfrac{3\pi^{3/2}}{10\sqrt{2}\Gamma^2\left(\frac{5}{4}\right)}, \qquad\qquad \Delta = 0, \\[4mm] 2\Theta(|E|-\Delta)I_2^{xx}(\Delta/|E|), \qquad \Delta > 0.\end{cases}\qquad(4.19)$$

The integral over energy can be evaluated analytically only in the special case of zero temperature $T \to 0$. We plot $\mathrm{Re}\,\sigma_{xx}^{intra}$ as a function of the gap parameter Δ in Fig.4.3. One can observe the monotonous decrease with growing Δ for all values of chemical potential.

4.3.2 Optical conductivity in the y-direction

For the longitudinal conductivity along the y-direction the technical details of calculation are very similar to the xx-case. They are presented in

Appendix 4.8. The results for interband ac optical conductivity are:

$$\mathrm{Re}\,\sigma_{yy}^{inter}(\omega) = \mathrm{sgn}\,\omega\,\frac{e^2}{2\pi\hbar}\frac{v}{4\sqrt{2|\omega|a}}\left[f\left(-\frac{\omega}{2}\right)-f\left(\frac{\omega}{2}\right)\right]\times$$

$$\times\begin{cases} 2\Theta(|\Delta|-|\omega/2|)I_4^{yy}(2\Delta/|\omega|)+ \\ +2\Theta(|\omega/2|-|\Delta|)I_2^{yy}(2\Delta/|\omega|) \end{cases},\quad \Delta<0, \\[2mm] \dfrac{\Gamma^2\left(\frac{1}{4}\right)}{3\sqrt{2\pi}},\qquad\qquad\qquad\quad \Delta=0, \\[2mm] 2\Theta(|\omega/2|-\Delta)I_2^{yy}(2\Delta/|\omega|),\qquad \Delta>0.\end{cases}\quad(4.20)$$

They are presented in Fig.4.2 in lower panels for all three different cases of Δ. As is seen in the lower panel in Fig.4.2(c), the optical conductivity in the y-direction diverges at the point $\omega=-2\Delta$ for $\Delta<0$. This divergence was also observed in numerical calculations in Refs.[146, 147]. Using our exact expressions, we can derive asymptotic expansions in the integrals $I_2^{yy}(2\Delta/|\omega|)$ and $I_4^{yy}(2\Delta/|\omega|)$ at $\omega=2|\Delta|$ for negative Δ. Expanding the integrals near this point up to leading order, we find:

$$I_2^{yy}(2\Delta/|\omega|)_{\omega\to 2|\Delta|+}\approx\frac{1}{\sqrt{2}}\log\frac{2|\Delta|}{\omega-2|\Delta|}+\mathrm{const},\qquad(4.21)$$

$$I_4^{yy}(2\Delta/|\omega|)_{\omega\to 2|\Delta|-}\approx\frac{1}{\sqrt{2}}\log\frac{2|\Delta|}{|2\Delta|-\omega}+\mathrm{const}.\qquad(4.22)$$

The logarithmic singularity has the same amplitudes from both sides. In Ref.[147] this singularity was related to the joint density of states for initial and final states involved in an optical transition, hence the van Hove singularity appears at $\omega=2|\Delta|$, while the density of states itself has a van Hove logarithmic singularity at $\omega=|\Delta|$. The density of states for the considered system was derived in Ref.[140], it is expressed also in terms of complete elliptic integrals of the first and second kind.

We also present the asymptotes for the case $\Delta<0$ at small and large ω:

$$\mathrm{Re}\,\sigma_{yy}^{inter}(\omega)\simeq\frac{e^2}{2\pi\hbar}\begin{cases}\dfrac{v}{\sqrt{|\Delta|a}}\dfrac{\pi\omega}{32T\cosh^2\frac{\mu}{2T}},&\omega\to 0, \\[3mm] \dfrac{v}{\sqrt{\omega a}}\dfrac{\Gamma^2\left(\frac{1}{4}\right)}{24\sqrt{\pi}},&\omega\to\infty.\end{cases}\qquad(4.23)$$

For intraband dc optical conductivity we find

$$\text{Re}\,\sigma_{yy}^{intra}(\omega) = \delta(\omega)\frac{e^2}{16\pi\hbar T}\int_{-\infty}^{\infty}\frac{dE}{\cosh^2\left(\frac{E-\mu}{2T}\right)}\frac{v\sqrt{|E|}}{\sqrt{a}}\times$$

$$\times\begin{cases}\begin{aligned}&2\Theta(|\Delta|-|E|)I_3^{yy}(\Delta/|E|)+\\&+2\Theta(|E|-|\Delta|)I_1^{yy}(\Delta/|E|)\end{aligned}, & \Delta < 0,\\[2ex]\frac{\sqrt{2}\Gamma^2\left(\frac{1}{4}\right)}{3\sqrt{\pi}}, & \Delta = 0,\\[2ex]2\Theta(|E|-\Delta)I_1^{yy}(\Delta/|E|), & \Delta > 0.\end{cases} \tag{4.24}$$

Interband and intraband conductivities were studied recently in Ref.[147] at zero temperature, the authors have obtained also asymptotic expressions at small and large frequencies. We checked that their asymptotics follow straightforwardly from our analytical results for $T = 0$ while at finite temperature we get different dependence for $\text{Re}\,\sigma_{yy}^{inter}(\omega)$ when ω goes to zero.

Finally, in Fig.4.3 we plot intraband parts as functions of the gap Δ for different values of chemical potential. The interesting feature presented in Fig.4.3(b) is the appearance of a small peak near $\Delta = 0$ on the negative side at small chemical potentials. This peak can be related to the crossing of saddle point level with chemical potential. At zero chemical potential this peak appears only at small Δ values and attain maximum for $\Delta \approx 0$, which shows that temperature-broadened van Hove singularities intersect with the Fermi level and allow transport even at zero frequency. Such signature can be used as a manifestation of the regime that is close to topological transition with Δ in dc transport measurements.

4.4 Optical conductivity of gapped dice model

4.4.1 Solution of the Heisenberg equations for the quasi-particle in dice model

The $\mathcal{T}_3$ (dice) lattice is schematically shown in Fig.1.1. The corresponding tight-binding Hamiltonian is expressed through the function $f_{\mathbf{k}} = -\sqrt{2}t(1 + e^{-i\mathbf{k}\mathbf{a}_2} + e^{-i\mathbf{k}\mathbf{a}_3})$ with equal hoppings t between atoms C (green hubs) and A, B (red, blue rim sites) [12, 80] and the corresponding energy
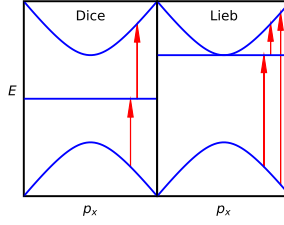
Figure 4.4. Possible interband transitions which contribute to optical conductivity and define frequency thresholds for gapped dice and Lieb lattice models.

spectrum is [13]

$$\varepsilon_0 = 0,$$

$$\varepsilon_\pm = \pm\sqrt{2}t\left[3 + 2(\cos(\boldsymbol{a}_1\boldsymbol{k}) + \cos(\boldsymbol{a}_2\boldsymbol{k}) + \cos(\boldsymbol{a}_3\boldsymbol{k}))\right]^{1/2}, \qquad (4.25)$$

where $\boldsymbol{a}_1 = (1, 0)a$ and $\boldsymbol{a}_2 = (1/2, \sqrt{3}/2)a$ are the basis vectors of the triangle sublattices and $\boldsymbol{a}_3 = \boldsymbol{a}_2 - \boldsymbol{a}_1$ with the lattice constant denoted by a.

There are two values of momentum where $f_{\boldsymbol{k}} = 0$ and all three bands meet. They are situated at the corners of the hexagonal Brillouin zone

$$K = \frac{2\pi}{a}\left(\frac{1}{3}, \frac{1}{\sqrt{3}}\right), \quad K' = \frac{2\pi}{a}\left(-\frac{1}{3}, \frac{1}{\sqrt{3}}\right). \qquad (4.26)$$

For momenta near the K and K' points, the function $f_{\boldsymbol{k}}$ is linear in $\boldsymbol{p} = \boldsymbol{k} - \xi\boldsymbol{K}$, i.e., $f_{\boldsymbol{k}} = v_F(\xi p_x - ip_y)$, $v_F = \sqrt{3}ta/2$ is the Fermi velocity, and $\xi = \pm$ is the valley index. In addition, we set $\hbar = 1$ for convenience. The low-energy Hamiltonian near K(K') $\xi = \pm 1$ three-band-touching point reads:

$$H_{dice} = v_F(p_x S_x + \xi p_y S_y + p_z S_z), \qquad (4.27)$$

with a constant gap $v_F p_z$ and pseudospin-1 matrices S_i are

$$S_x = \frac{1}{\sqrt{2}}\begin{pmatrix} 0 & 1 & 0 \\ 1 & 0 & 1 \\ 0 & 1 & 0 \end{pmatrix}, \; S_y = \frac{1}{\sqrt{2}}\begin{pmatrix} 0 & -i & 0 \\ i & 0 & -i \\ 0 & i & 0 \end{pmatrix},$$

$$S^z = \begin{pmatrix} 1 & 0 & 0 \\ 0 & 0 & 0 \\ 0 & 0 & -1 \end{pmatrix}. \qquad (4.28)$$

These matrices form a closed algebra with respect to commutator operation: $[S_i, S_j] = i\varepsilon_{ijk}S_k$.

The S_z-type term in the Hamiltonian H_{dice} describes the spectral gap, which can be opened by adding on-site potential on A and B sites [14], in the Haldane model [151] or dynamically generated in special cases of electron-electron interactions [166] and in the Floquet setup under circularly polarized radiation [167, 168].

Let us perform analysis for K ($\xi = 1$) valley, and then account for K' valley with proper sign changes. The Heisenberg equations for the coordinate and momentum operators in this case take the form:

$$\boldsymbol{v}(t) = \frac{d\boldsymbol{x}}{dt} = -i[x(t), H_{dice}] = v_F \boldsymbol{S}(t), \qquad (4.29)$$

$$\frac{d\boldsymbol{p}}{dt} = -i[p(t), H_{dice}] = 0. \qquad (4.30)$$

Again, using the solution of the second equation, that states $p(t) = p(0)$, we arrive at the following Heisenberg equation for matrices S_i:

$$\frac{dS_i(t)}{dt} = -i[S_i(t), H_{dice}] = iP_{ij}S_j(t), \qquad (4.31)$$

with

$$P_{ij} = iv_F\varepsilon_{ijk}p_k = iv_F \begin{pmatrix} 0 & p_z & -p_y \\ -p_z & 0 & p_x \\ p_y & -p_x & 0 \end{pmatrix}. \qquad (4.32)$$

The solution of this equation has the form

$$S_i(t) = \left(e^{iPt}\right)_{ij} S_j(0), \qquad (4.33)$$

where the matrix exponential is

$$\left(e^{iPt}\right)_{ij} =$$

$$\begin{bmatrix} \frac{(p_y^2+p_z^2)\cos(ptv_F)+p_x^2}{p^2} & \frac{p_xp_yC-pp_z\sin(ptv_F)}{p^2} & \frac{p_xp_zC+pp_y\sin(ptv_F)}{p^2} \\ \frac{p_xp_yC+pp_z\sin(ptv_F)}{p^2} & \frac{(p_x^2+p_z^2)\cos(ptv_F)+p_y^2}{p^2} & \frac{p_yp_zC-pp_x\sin(ptv_F)}{p^2} \\ \frac{p_xp_zC-pp_y\sin(ptv_F)}{p^2} & \frac{pp_x\sin(ptv_F)+p_yp_zC}{p^2} & \frac{(p_x^2+p_y^2)\cos(ptv_F)+p_z^2}{p^2} \end{bmatrix}.$$

$$(4.34)$$

Here we used the notation $p = \sqrt{p_x^2 + p_y^2 + p_z^2}$ and $C = 1 - \cos(ptv_F)$. The eigenvalues of the matrix P are $\pm v_F p$, 0. The matrix exponential greatly simplifies for the gapless case with $p_z = 0$ (compare with Eq.(4.14)):

$$
\left(e^{iPt} \right)_{ij} (p_z = 0) =
$$

$$
= \begin{pmatrix}
\frac{p_y^2 \cos(ptv_F) + p_x^2}{p^2} & \frac{p_x p_y (1 - \cos(ptv_F))}{p^2} & \frac{p_y \sin(ptv_F)}{p} \\
\frac{p_x p_y (1 - \cos(ptv_F))}{p^2} & \frac{p_x^2 \cos(ptv_F) + p_y^2}{p^2} & -\frac{p_x \sin(ptv_F)}{p} \\
-\frac{p_y \sin(ptv_F)}{p} & \frac{p_x \sin(ptv_F)}{p} & \cos(ptv_F)
\end{pmatrix}.
\tag{4.35}
$$

Thus, from the solutions (4.33) and (4.34) we find the time-dependent velocity operators:

$$
v_x(t) = v_F \left(\frac{\left(p_y^2 + p_z^2 \right) \cos(ptv_F) + p_x^2}{p^2} S_x + \right.
$$

$$
+ \frac{p_x p_y (1 - \cos(ptv_F)) - pp_z \sin(ptv_F)}{p^2} S_y +
$$

$$
\left. + \frac{p_x p_z (1 - \cos(ptv_F)) + pp_y \sin(ptv_F)}{p^2} S_z \right),
\tag{4.36}
$$

$$
v_y(t) = v_F \left(\frac{p_x p_y (1 - \cos(ptv_F)) + pp_z \sin(ptv_F)}{p^2} S_x + \right.
$$

$$
+ \frac{\left(p_x^2 + p_z^2 \right) \cos(ptv_F) + p_y^2}{p^2} S_y +
$$

$$
\left. + \frac{p_y p_z (1 - \cos(ptv_F)) - pp_x \sin(ptv_F)}{p^2} S_z \right).
\tag{4.37}
$$

Below we insert these results into Eqs.(4.4) and (4.8) to evaluate the longitudinal and Hall conductivities. Again, we see that the velocities $v_i(t)$ contain zitterbewegung terms which stem from the oscillating terms.

4.4.2   Longitudinal and Hall conductivities in massive dice model

Substituting the obtained velocities into Eqs.(4.5),(4.7) and performing Fourier transform over pairs of (s, E) and (t, ω) variables, we find

$$\mathcal{F}_{t,s} \operatorname{Tr} \left[e^{-iHs} v_x(t) v_x(0) \right] =$$

$$\pi v_F^2 \delta(E) \left(\frac{p^2 + p_z^2}{2p^2} \right) (\delta(\omega - p v_F) + \delta(\omega + p v_F)) +$$

$$+ \pi v_F^2 \delta(E + p v_F) \left(\frac{p^2 + p_z^2}{2p^2} \delta(\omega - p v_F) + \frac{p^2 - p_z^2}{p^2} \delta(\omega) \right) +$$

$$+ \pi v_F^2 \delta(E - p v_F) \left(\frac{p^2 + p_z^2}{2p^2} \delta(\omega + p v_F) + \frac{p^2 - p_z^2}{p^2} \delta(\omega) \right), \qquad (4.38)$$

$$\mathcal{F}_{t,s} \operatorname{Tr} \left[e^{-iHs} v_{[x,}(t) v_{y]}(0) \right] = \frac{v_F^2 p_z}{ip} \times$$

$$\left[\delta(\omega - p v_F) \delta(E + p v_F) - \delta(\omega + p v_F) \delta(E - p v_F) \right.$$

$$\left. - \delta(E) \delta(\omega + p v_F) - \delta(\omega - p v_F) \right]. \qquad (4.39)$$

where the double Fourier transform is defined as

$$\mathcal{F}_{t,s} f(t, s) = \int_{-\infty}^{\infty} \frac{dt \, ds}{(2\pi)^2} e^{i\omega t + iEs} f(t, s) \qquad (4.40)$$

Using the first expression in the general formula for longitudinal conductivity, we find:

$$\operatorname{Re} \sigma_{xx}(\omega) = \frac{e^2}{4\hbar} \left[\delta(\omega) \int_{-\infty}^{\infty} \frac{dE}{4T \cosh^2 \left(\frac{E - \mu}{2T} \right)} \times \right.$$

$$\times \frac{E^2 - \Delta^2 v_F^2}{|E|} \Theta(|E| - \Delta v_F) +$$

$$\left. + \frac{\omega^2 + \Delta^2 v_F^2}{2\omega^2} \Theta(|\omega| - \Delta v_F) [f(-|\omega|) - f(|\omega|)] \right], \qquad (4.41)$$

where we relabeled $p_z = \Delta > 0$ and took into account the presence of two valleys that contribute equally. Note that the term proportional to $\Theta(|\omega| - \Delta v_F)$ defines the energy threshold after which the transitions

from and to flat band become possible. However, no special threshold
is present for transitions between the two dispersive bands, which means
that only transitions through flat band are possible. This was already
pointed out for the gapless dice model in Refs.[49, 152]. In addition we
note that in the gapless limit the obtained expression agrees with that
obtained for arbitrary pseudospin models with the same matrix algebra
$[S_i, S_j] = i\varepsilon_{ijk}S_k$ in Ref.[169].

Similarly, for the imaginary part of the Hall conductivity in one valley
we find

$$\text{Im}\,\sigma_{[x,y]}(\omega) = \frac{e^2 p_z v_F}{4\hbar\omega}\Theta\left(|\omega| - v_F|p_z|\right)\left[f(|\omega|) - f(-|\omega|)\right]. \qquad (4.42)$$

Note that the Hall conductivity is proportional to the gap parameter p_z
and the sum over two valleys with different signs of p_z will lead to the
zero total Hall conductivity. This is because the system is T-invariant,
and the operation of T-invariance interchanges K and K' valleys [14].
These conductivities are shown in Fig.4.5 for different values of chemical
potential and temperature.

Using the Kramers-Kronig relations, one can evaluate the real part of
the Hall conductivity, see Eq.(4.106). At zero temperature we find the
following expression:

$$\text{Re}\,\sigma_{xy}(\omega) = -\frac{e^2 v_F p_z}{4\pi\hbar\omega}\log\left|\frac{\max(|\mu|, v_F|p_z|) + \omega}{\max(|\mu|, v_F|p_z|) - \omega}\right|. \qquad (4.43)$$

At the energy $\omega = \max(|\mu|, v_F|p_z|)$, there is a logarithmic divergence
in the Hall conductivity. For large energies, $\omega \to \infty$, this expression
approaches zero as $\sim 1/\omega^2$. This expression is very similar to those ob-
tained in graphene-like systems (see, for example, [170, 171]). The dc limit
$\omega \to 0$ leads to the quantized Hall conductivity $\text{Re}\,\sigma_{xy} = -e^2\text{sign}(p_z)/h$
for $|\mu| \leq v_F|p_z|$ in the absence of a magnetic field [172].

4.5 Optical conductivity of the Lieb model

In this section we evaluate the optical conductivity of the gapped Lieb
model [21] using the method presented above. The main complication
arises in solving Heisenberg equations for matrices: due to commutation
relations the whole set of the Gell-Mann matrices enters the calculation.
Below we show how one can still perform calculation and arrive at rela-
tively simple expression for the conductivity. We start with description
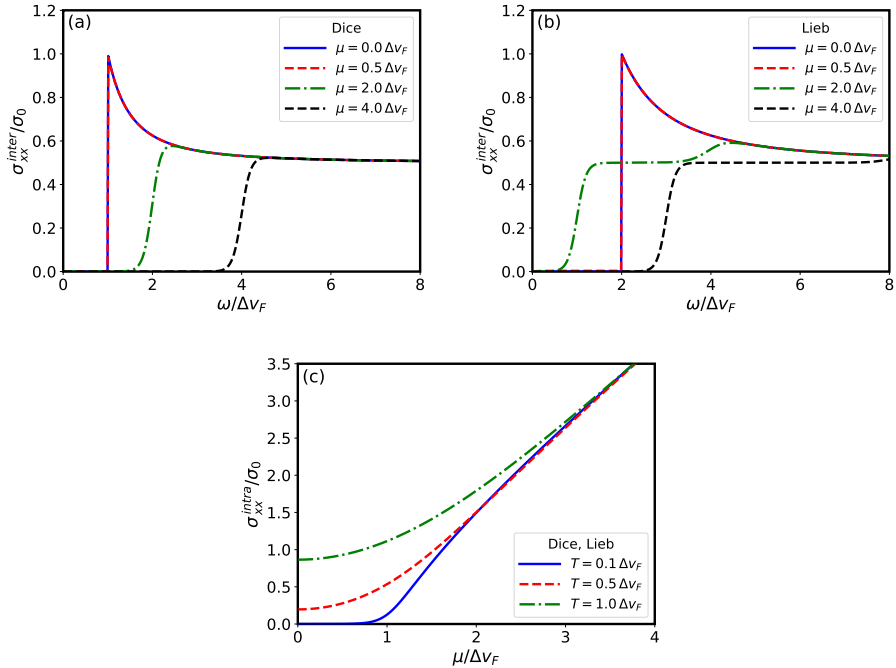
Figure 4.5. Panels (a) and (b): the real part of optical conductivity for gapped dice and Lieb lattices given by Eqs.(4.41) and (4.52) at temperature $T = 0.1\Delta v_F$. Panel (c): the real part of intraband dc conductivity which is the same for both lattices (for dice lattice in a single valley).

of the main properties of the Lieb lattice and corresponding low-energy model.

4.5.1 Lieb lattice and low-energy model

The Lieb lattice is schematically shown in Fig.1.2. It consists of three square sublattices, with atoms placed in the corners and in the middle of each side of big squares forming a line-centered-square lattice. The tight-binding Hamiltonian, described in Ref.[21], reduces to the following low-energy model near the center of BZ $k_{x,y} = \frac{\pi}{a} + q_{x,y}$:

$$H_{Lieb} = \begin{pmatrix} \Delta v_F & v_F q_x & 0 \\ v_F q_x & -\Delta v_F & v_F q_y \\ 0 & v_F q_y & \Delta v_F \end{pmatrix}, \tag{4.44}$$

where the site energies are set as $\varepsilon_B = \varepsilon_C = -\varepsilon_A = \Delta v_F$. In terms of the Gell-Mann λ-matrices the Hamiltonian takes the form

$$H_{Lieb} = v_F \left[\lambda_1 q_x + \lambda_6 q_y + \Delta \left(\frac{\lambda_0}{3} + \lambda_3 - \frac{\lambda_8}{\sqrt{3}} \right) \right]. \tag{4.45}$$

Here λ_0 is the 3×3 unit matrix. The energy dispersions defined by this Hamiltonian are given by three bands, one is flat band and the other two are dispersive bands (see Fig.4.4c):

$$\varepsilon_0 = \Delta v_F, \ \ \varepsilon_\pm = \pm v_F \sqrt{\Delta^2 + q_x^2 + q_y^2}. \tag{4.46}$$

Let us check the T-invariance of this Hamiltonian. The operator T should contain complex conjugation, the change of the sign of both momenta and contain the proper matrix transformation in sublattice space:

$$\hat{T} H(\boldsymbol{q}) \hat{T}^{-1} = H(-\boldsymbol{q}), \quad \hat{T} = F\hat{K}. \tag{4.47}$$

In the absence of the gap the matrix F has the form

$$F = \begin{pmatrix} 1 & 0 & 0 \\ 0 & -1 & 0 \\ 0 & 0 & 1 \end{pmatrix}. \tag{4.48}$$

Thus we conclude that the gap presented in Ref.[21] does not break T-invariance. Consequently, the Hall conductivity is zero in this model in the absence of a magnetic field.

4.5.2   Solution of the Heisenberg equations

The Heisenberg equations for the coordinate and momentum operators are very similar to that obtained in previous sections: velocities evolve with time as the corresponding matrices in the Hamiltonian near q_x and q_y, and the momenta do not evolve at all. The nontrivial part comes from the equation that describes the evolution of matrices. The system of equations for the Gell-Mann matrices has the form:

$$\frac{d\lambda_i(t)}{dt} = -i[\lambda_i(t), H_{Lieb}] = v_F A_{ij}\lambda_j(t), \tag{4.49}$$

where we used the commutation relations $[\lambda_i, \lambda_k] = 2if_{ikj}\lambda_j$ with f_{ikj} being the structure constants of the $su(3)$ algebra, hence the matrix A_{ij} has the form:

$$A = \begin{pmatrix} 0 & -2\Delta & 0 & 0 & q_y & 0 & 0 & 0 \\ 2\Delta & 0 & -2q_x & -q_y & 0 & 0 & 0 & 0 \\ 0 & 2q_x & 0 & 0 & 0 & 0 & -q_y & 0 \\ 0 & q_y & 0 & 0 & 0 & 0 & -q_x & 0 \\ -q_y & 0 & 0 & 0 & 0 & q_x & 0 & 0 \\ 0 & 0 & 0 & 0 & -q_x & 0 & 2\Delta & 0 \\ 0 & 0 & q_y & q_x & 0 & -2\Delta & 0 & -\sqrt{3}q_y \\ 0 & 0 & 0 & 0 & 0 & 0 & \sqrt{3}q_y & 0 \end{pmatrix}. \tag{4.50}$$

For the eigenvalues of the matrix $v_F A_{ij}$ we find:

$$a_{1,2} = 0, \quad a_{3,4} = \pm 2ipv_F$$
$$a_{5,6} = \pm iv_F(\Delta + p), \quad a_{7,8} = \pm iv_F(p - \Delta), \tag{4.51}$$

where we defined $p = \sqrt{q_x^2 + q_y^2 + \Delta^2}$. The initial conditions for velocities are $v_x(0) = v_F\lambda_1$, $v_y(0) = v_F\lambda_6$. After calculation of the matrix exponent $\exp[At]$, we find velocities at time t by taking the corresponding rows in resulting matrix - the first for v_x and the sixth for v_y. The solutions for v_x and v_y are defined as vectors in the Gell-Mann basis - see Eqs.(4.108) and (4.109) in Appendix 4.11. The identity matrix is not present because it does not evolve with time and the coefficient before this matrix is zero. Next we evaluate the conductivity using the obtained solutions $v_{x,y}(t)$ and previously established method.

4.5.3   Optical conductivity

Performing trace evaluation and using the double-Fourier transform, we arrive at the following final answer for the optical conductivity of the Lieb lattice in the x-direction (see Appendix 4.11):

$$
\operatorname{Re}\sigma_{xx}(\omega) = \frac{e^2}{4\hbar}\left[\delta(\omega)\int_{-\infty}^{\infty} \frac{dE}{4T\cosh^2\left(\frac{E-\mu}{2T}\right)} \times \right.
$$

$$
\times\, \frac{E^2 - \Delta^2 v_F^2}{|E|}\Theta\left(|E| - \Delta v_F\right) +
$$

$$
+\Theta(|\omega| - 2\Delta v_F)\left[\frac{2\Delta^2 v_F^2}{\omega^2}\left(f\left(-\frac{|\omega|}{2}\right) - f\left(\frac{|\omega|}{2}\right)\right) + \right.
$$

$$
\left.+\frac{f(\Delta v_F - |\omega|) - f(\Delta v_F)}{2}\right] + \left.\frac{f(\Delta v_F) - f(\Delta v_F + |\omega|)}{2}\right]. \tag{4.52}
$$

For the conductivity in the y-direction we find the same answer.

The physical meaning of the terms in Eq.(4.52) is the following: the first term corresponds to intraband dc conductivity, the second term describes interband transitions through the gap - that is why the threshold is $2\Delta v_f$, and the last term corresponds to transitions between flat and upper dispersive band. This conductivity is presented in Fig.4.5 in comparision with gapped dice model. Qualitatively, the behavior of conductivities in both models is similar.

The interesting difference compared to the dice model conductivity (4.41) is the presence of both dispersive-to-dispersive band transitions and dispersive-to-flat band transitions in the interband ac part of optical conductivity (schematically shown in Fig.4.4c).

4.6   Conclusions

In the present paper we further developed the approach of Refs.[47, 135] for calculating longitudinal and Hall conductivities of systems with arbitrary pseudospin and dispersion law of quasiparticles. The conductivities are written through quasiparticle velocity correlators at time t for states of energy E which also describe the phenomenon of zitterbewegung. For non-interacting systems the Heisenberg equations for velocities can be solved that allows one to significantly reduce the complexity of the conductivity calculation and obtain in some cases closed-form analytic expressions. The

method under consideration is well adapted also to the presence of impurities in the system. The velocity correlators in this case can be computed numerically utilizing time dependent Schrödinger equation with averaging over impurities [138, 173].

We applied this method to evaluate the optical conductivity of the semi-Dirac model, which is an example of low-energy theory with anisotropic spectrum. We obtained exact expressions which allowed us to identify the signatures of topological phase transition with gap closing and merging Dirac points. The previously unobserved result is the peak in the intraband dc conductivity along the y-direction at zero chemical potential when the two Dirac cones nearly merge with each other. Physically, one would expect that this is related to the intersection of broadened van Hove singularities with the Fermi level. Such an intersection leads to the appearance of a number of propagating states carrying a nonzero current. At low temperatures, nonzero transport through the charge-neutrality point may indicate the appearance of a topological phase transition.

In addition, we analyzed two gapped pseudospin-1 models that correspond to dice and Lieb lattices. The optical conductivities for the considered gap parameters were not studied previously. The key physical difference that we observed is the fact that in the gapped Lieb model all transitions between three bands (dispersive-to-flat, flat-to-dispersive and between two dispersive) contribute to the optical conductivity at large frequencies, while in dice lattice only transitions to and from flat band play a role.

4.7   Appendix: Derivation of general conductivity expressions from Kubo formula

4.7.1 Expression of the conductivity tensor through retarded correlation function

It is well known that the conductivity (4.1) can be written through the Fourier transform of the retarded correlation function $\Pi^r_{\mu\nu}(t)$:

$$\Pi^r_{\mu\nu}(t) = -i\theta(t) \langle [J_\mu(t) J_\nu(0)]\rangle$$

$$\sigma_{\mu\nu}(\omega) = \frac{iK_{\mu\nu}(\omega + i\varepsilon)}{\omega + i\varepsilon},$$

$$K_{\mu\nu}(\omega + i\varepsilon) = \frac{\langle\tau\rangle}{V}\delta_{\mu\nu} + \frac{\Pi^r_{\mu\nu}(\omega + i\varepsilon)}{V}. \tag{4.53}$$

The function $\Pi^r_{\mu\nu}(\omega)$ can be obtained by analytical continuation from its imaginary time expression $\left(\Pi^r_{\mu\nu}(\omega) = \Pi_{\mu\nu}(i\omega_m \to \omega + i\varepsilon)\right)$. For noninteracting fermions, using the Matsubara diagram technique for evaluating τ-ordered product of operators we get

$$\Pi_{\mu\nu}(i\omega_m) = \frac{1}{\beta}\sum_{n=-\infty}^{\infty} \mathrm{Tr}\left[j_\mu \frac{1}{i\Omega_n - H_0} j_\nu \frac{1}{i\Omega_n - i\omega_m - H_0}\right]. \tag{4.54}$$

In the energy representation it takes the form

$$\Pi_{\mu\nu}(i\omega_m) = \frac{1}{\beta}\sum_{\alpha,\beta} j_\mu^{\alpha\beta} j_\nu^{\beta\alpha} \sum_{n=-\infty}^{\infty} \frac{1}{(i\Omega_n - E_\beta)(i\Omega_n - i\omega_m - E_\alpha)}. \tag{4.55}$$

The summation over the Matsubara frequencies can be easily performed, thus we get

$$\Pi_{\mu\nu}(i\omega_m) = \sum_{\alpha,\beta} j_\mu^{\alpha\beta} j_\nu^{\beta\alpha} \frac{f(E_\alpha) - f(E_\beta)}{E_\alpha - E_\beta + i\omega_m}, \tag{4.56}$$

where $f(E)$ is the Fermi-Dirac distribution function, $f(E) = 1/(\exp(\beta(E-\mu))+1)$. We now write

$$J_\mu^{\alpha\beta} J_\nu^{\beta\alpha} = J_{\{\mu}^{\alpha\beta} J_{\nu\}}^{\beta\alpha} + J_{[\mu}^{\alpha\beta} J_{\nu]}^{\beta\alpha}, \tag{4.57}$$

where $J_{\{\mu}J_{\nu\}} \equiv (J_\mu J_\nu + J_\nu J_\mu)/2$ and $J_{[\mu}J_{\nu]} \equiv (J_\mu J_\nu - J_\nu J_\mu)/2$ denote symmetric and antisymmetric parts of the tensor $J_\mu J_\nu$, respectively. Using hermiticity of the current it is easy to show that the symmetric part $J_{\{\mu}J_{\nu\}}$ is a real quantity while the antisymmetric part $J_{[\mu}J_{\nu]}$ is the purely

imaginary one. Therefore, after performing analytical continuation over frequency, we find the real symmetric part of $\sigma_{\mu\nu}$,

$$\operatorname{Re}\sigma_{\{\mu,\nu\}}(\omega) = \frac{\pi e^2}{V\omega}\sum_{\alpha,\beta}v^{\alpha\beta}_{\{\mu}v^{\beta\alpha}_{\nu\}}\left[f\left(E_\alpha\right)-f\left(E_\beta\right)\right]\delta\left(E_\alpha-E_\beta+\omega\right), \quad (4.58)$$

where we used the relation $j_\mu = -ev_\mu$ between the current density and the velocity $(e > 0)$. Accordingly, for the imaginary antisymmetric part of $\sigma_{\mu\nu}$ we have

$$\operatorname{Im}\sigma_{[\mu,\nu]}(\omega) = \frac{\pi e^2}{V\omega}\sum_{\alpha,\beta}\operatorname{Im}\left(v^{\alpha\beta}_{[\mu}v^{\beta\alpha}_{\nu]}\right)\left[f\left(E_\alpha\right)-f\left(E_\beta\right)\right]\delta\left(E_\alpha-E_\beta+\omega\right).$$
$$(4.59)$$

To restore remaining imaginary and real parts we can use the Kramers-Krönig relationships,

$$\operatorname{Im}\sigma_{\{\mu,\nu\}}(\Omega) = -\frac{1}{\pi}\operatorname{P.v.}\int_{-\infty}^{\infty}\frac{d\omega\operatorname{Re}\sigma_{\{\mu,\nu\}}(\omega)}{\omega-\Omega},$$
$$\operatorname{Re}\sigma_{[\mu,\nu]}(\Omega) = \frac{1}{\pi}\operatorname{P.v.}\int_{-\infty}^{\infty}\frac{d\omega\operatorname{Im}\sigma_{[\mu,\nu]}(\omega)}{\omega-\Omega}. \quad (4.60)$$

Writing

$$\delta\left(E_\alpha-E_\beta+\omega\right) = \int_{-\infty}^{\infty}dE\delta\left(E-E_\alpha\right)\delta\left(E-E_\beta+\omega\right) \quad (4.61)$$

we have for the symmetric part

$$\operatorname{Re}\sigma_{\{\mu,\nu\}}(\omega)$$
$$= \frac{\pi e^2}{V\omega}\sum_{\alpha,\beta}\int_{-\infty}^{\infty}dEv^{\alpha\beta}_{\{\mu}v^{\beta\alpha}_{\nu\}}\delta\left(E-E_\alpha\right)\delta\left(E-E_\beta+\omega\right)\left[f\left(E_\alpha\right)-f\left(E_\beta\right)\right]$$
$$= \frac{\pi e^2}{V\omega}\int_{-\infty}^{\infty}dE[f(E-\omega)-f(E)]\operatorname{Tr}\left[v_{\{\mu}\delta(E-H)v_{\nu\}}\delta(E-H-\omega)\right].$$
$$(4.62)$$

In the last line we replaced the eigenvalues $E_{\alpha,\beta}$ by the Hamiltonian and sum over eigenstates by the trace over quantum numbers describing the

system eigenstates. Similarly, for the imaginary antisymmetric part we find:

$$\operatorname{Im} \sigma_{[\mu,\nu]}(\omega) = \frac{\pi e^2}{V\omega} \int_{-\infty}^{\infty} dE[f(E-\omega) - f(E)]$$
$$\times \operatorname{Im} \operatorname{Tr} \left[v_{[\mu}\delta(E-H)v_{\nu]}\delta(E-H-\omega)\right]. \qquad (4.63)$$

Using the relation between traces and velocity correlators averaged at fixed energy (see Sec. 4.7.2), we find the results presented in the main text, Eqs.(4.4) and (4.8).

4.7.2 Relation between trace and time-dependent velocity operators

Let us consider the term $\operatorname{Tr}\left[v_\mu\delta(E-H)v_\nu\delta(E-H-\omega)\right]$ in the expressions (4.62) and (4.63) for interband ac conductivity. Also, $J_\mu(t)$ is the actual current measured experimentally, the corresponding total current-density is obtained by differentiating the Hamiltonian with respect to the vector potential,

$$J_\mu(\mathbf{r},t) = -\frac{\delta H}{\delta\left(A_\mu(\mathbf{r},t)/c\right)}. \qquad (4.64)$$

Using the representation for the first delta function,

$$\delta(E-H) = \frac{1}{2\pi} \int_{-\infty}^{\infty} dt e^{i(E-H)t}, \qquad (4.65)$$

and the cyclic property of a trace, then changing the variable of integration $E \to E + \omega$, we can write

$$\operatorname{Tr}\left[v_\mu\delta(E-H)v_\nu\delta(E-H-\omega)\right] = \frac{1}{2\pi}\int_{-\infty}^{\infty} dt e^{i\omega t} \operatorname{Tr}\left[\delta(E-H)v_\mu(t)v_\nu(0)\right]., \qquad (4.66)$$

Defining the microcanonical average of an operator $\hat{A}$ at given energy E,

$$\langle\hat{A}\rangle_E = \frac{\operatorname{Tr}[\delta(E-\hat{H})\hat{A}]}{\operatorname{Tr}[\delta(E-\hat{H})]}, \qquad (4.67)$$

where $\operatorname{Tr}[\delta(E-\hat{H})] = \rho(E)V$ is the total density of states (DOS), we get the following expression for the symmetric ac conductivity through the

correlator of velocities:

$$\operatorname{Re}\sigma_{\{\mu,\nu\}}(\omega) = \frac{e^2}{2\omega}\int\limits_{-\infty}^{\infty} dE\rho(E)\left[f(E) - f(E+\omega)\right]\int\limits_{-\infty}^{\infty} dt e^{i\omega t}\left\langle v_{\{\mu}(t)v_{\nu\}}(0)\right\rangle_E.$$

(4.68)

It is easy to check the reality of the last expression using the relationship $\left\langle v_{\{\mu}(-t)v_{\nu\}}(0)\right\rangle_E^* = \left\langle v_{\{\mu}(t)v_{\nu\}}(0)\right\rangle_E$.

The expression (4.4) for $T = 0$ is in accordance with Ref.[160] for diagonal conductivity. Similarly, for the imaginary antisymmetric part of conductivity we obtain

$$\operatorname{Im}\sigma_{[\mu,\nu]}(\omega) = \frac{e^2}{2\omega}\operatorname{Im}\int\limits_{-\infty}^{\infty} dE\rho(E)\left[f(E) - f(E+\omega)\right]$$

$$\times \int\limits_{-\infty}^{\infty} dt e^{i\omega t}\left\langle v_{[\mu}(t)v_{\nu]}(0)\right\rangle_E.$$

(4.69)

To calculate $\operatorname{Im}\sigma_{\{\mu,\nu\}}(\omega)$ and $\operatorname{Re}\sigma_{[\mu,\nu]}(\omega)$ we use the Kramers-Krönig relation (4.60).

4.8   Appendix: Momentum integration in expressions for conductivity of the semi-Dirac model.

In this Appendix we discuss technical details regarding evaluation of longitudinal conductivity in the semi-Dirac model. Following Ref.[137], one can express the diamagnetic term $\langle\tau_{\mu\mu}\rangle$ appearing in Eq.(4.1) as

$$\frac{\langle\tau_{\alpha\alpha}\rangle}{V} = e^2\int\limits_{BZ}\frac{d^2p}{(2\pi)^2}\frac{f(\varepsilon_+(\mathbf{p})) - f(-\varepsilon_+(\mathbf{p}))}{2\varepsilon(\mathbf{p})}\left(\Phi(\mathbf{p})\frac{\partial^2}{\partial p_\alpha^2}\Phi^*(\mathbf{p}) + \text{ c.c. }\right),$$

(4.70)

where $\Phi(\boldsymbol{p})$ is defined by model Hamiltonian (4.9) as

$$H_{semi} = \begin{pmatrix} 0 & \Phi(\boldsymbol{p}) \\ \Phi^*(\boldsymbol{p}) & 0 \end{pmatrix}, \quad \Phi(\boldsymbol{p}) = \left(\Delta + ap_x^2\right) - ivp_y.$$

(4.71)

Thus, only the $\langle\tau_{xx}\rangle$ contribution is nonzero. After substituting the exact form of the dispersion and taking derivative of $\Phi(\boldsymbol{p})$, we find that the term

$\langle \tau_{xx} \rangle$ is real:

$$\frac{\langle \tau_{xx} \rangle}{V} = e^2 \int \frac{d^2 \mathbf{p}}{(2\pi)^2} \frac{2a \left(\Delta + a p_x^2 \right)}{\varepsilon_+(\mathbf{p})} \left[f \left(\varepsilon_+(\mathbf{p}) \right) - f \left(-\varepsilon_+(\mathbf{p}) \right) \right]. \qquad (4.72)$$

The contribution of this term into optical conductivity does not depend on the frequency and we neglect it in our studies.

To evaluate the real parts of longitudinal optical conductivity along the x- and y-directions, we first calculate traces with time-dependent velocity operators, which are obtained from Eqs.(4.11) and (4.14),

$$\text{Tr} \left[e^{-iH_{semis}} v_x(t) v_x(0) \right] =$$

$$= \int \frac{d^2 p}{(2\pi)^2} \frac{8a^2 p_x^2 \left(v^2 p_y^2 \cos \left((s-2t)\varepsilon_+ \right) + \left(a p_x^2 + \Delta \right)^2 \cos \left(s\varepsilon_+ \right) \right)}{\varepsilon_+^2}, \qquad (4.73)$$

$$\text{Tr} \left[e^{-iH_{semis}} v_y(t) v_y(0) \right] =$$

$$= \int \frac{d^2 p}{(2\pi)^2} \frac{2v^2 \left[\left(a p_x^2 + \Delta \right)^2 \cos \left((s-2t)\varepsilon_+ \right) + v^2 p_y^2 \cos \left(s\varepsilon_+ \right) \right]}{\varepsilon_+^2}. \qquad (4.74)$$

Here the notation $\varepsilon_+ \equiv \varepsilon_+(\mathbf{p})$ was used. As described in the main text, we then make Fourier transforms over t and s to obtain the delta-functions under integrals which technically simplify integrals. The resulting expressions for longitudinal optical conductivity are:

$$\text{Re}\, \sigma_{xx}(\omega) = \frac{2e^2}{\omega} \int_{-\infty}^{\infty} \frac{dE}{2\pi} [f(E) - f(E+\omega)] \int d^2 p \frac{a^2 p_x^2}{\varepsilon_+^2} \times$$

$$\times \left[\delta \left(E + \varepsilon_+ \right) \left(v^2 p_y^2 \delta \left(\omega - 2\varepsilon_+ \right) + \delta(\omega) \left(a p_x^2 + \Delta \right)^2 \right) \right.$$

$$\left. + \delta \left(E - \varepsilon_+ \right) \left(v^2 p_y^2 \delta \left(\omega + 2\varepsilon_+ \right) + \delta(\omega) \left(a p_x^2 + \Delta \right)^2 \right) \right], \qquad (4.75)$$

$$\text{Re}\, \sigma_{yy}(\omega) = \frac{e^2}{2\omega} \int_{-\infty}^{\infty} \frac{dE}{2\pi} [f(E) - f(E+\omega)] \int d^2 p \frac{v^2}{\varepsilon_+^2} \times$$

$$\times \left[\delta \left(E + \varepsilon_+ \right) \left(\left(a p_x^2 + \Delta \right)^2 \delta \left(\omega - 2\varepsilon_+ \right) + v^2 \delta(\omega) p_y^2 \right) \right.$$

$$\left. + \delta \left(E - \varepsilon_+ \right) \left(\left(a p_x^2 + \Delta \right)^2 \delta \left(\omega + 2\varepsilon_+ \right) + v^2 \delta(\omega) p_y^2 \right) \right]. \qquad (4.76)$$

To perform the integration over momentum, we use the symmetry $p_x \to -p_x$, $p_y \to -p_y$ of the integrals and the following change of coordinates that simplifies square root in ε_+:

$$a p_x^2 + \Delta = L \cos \phi, \quad v p_y = L \sin \phi, \quad \varepsilon_+ = L. \qquad (4.77)$$

For the functions even in p_x and p_y we can write

$$\int d^2 p f(p_x, p_y) = 4 \int\limits_0^\infty dp_x dp_y f(p_x, p_y)$$

$$= \int\limits_0^\infty dL \int\limits_0^\pi d\phi \frac{2L\,\theta(L\cos\phi - \Delta)}{v\sqrt{a(L\cos\phi - \Delta)}} f\left(\sqrt{\frac{L\cos\phi - \Delta}{a}}, \frac{L\sin\phi}{v}\right). \qquad (4.78)$$

The presence of the theta function takes into account that the regions of integration of the L and ϕ variables will be different depending on the sign of the Δ parameter. In what follows, we extensively use the following integral (Eq. 3.197.8 from book [174]):

$$\int_0^u x^{\nu-1}(x+a)^\lambda (u-x)^{\mu-1} dx = a^\lambda u^{\mu+\nu-1}\, \mathrm{B}(\mu,\nu)\, {}_2F_1\left(-\lambda, \nu; \mu+\nu; -\frac{u}{a}\right), \qquad (4.79)$$

with $\arg \frac{u}{a} < \pi$. Performing the momentum integration in Eqs.(4.75), (4.76) by means of Eq .(4.78), we obtain:

$$\mathrm{xx}: \quad \int d^2 p[\dots] = \frac{2\sqrt{a}}{v} \int\limits_0^\infty dL \int\limits_0^\pi d\phi L\sqrt{(L\cos\phi - \Delta)}\theta(L\cos\phi - \Delta)\times$$

$$\left[\delta(E+L)\left(\sin^2\phi\delta(\omega - 2L) + \delta(\omega)\cos^2\phi\right)\right.$$

$$\left.+\delta(E-L)\left(\sin^2\phi\delta(\omega + 2L) + \delta(\omega)\cos^2\phi\right)\right], \qquad (4.80)$$

$$\mathrm{yy}: \quad \int d^2 p[\dots] = \frac{2v}{\sqrt{a}} \int\limits_0^\infty dL \int\limits_0^\pi \frac{L\,d\phi}{\sqrt{L\cos\phi - \Delta}}\theta(L\cos\phi - \Delta)\times$$

$$\left[\cos^2\phi(\delta(E+L)\,\delta(\omega - 2L) + \delta(E-L)\delta(\omega + 2L))\right.$$

$$\left.+\sin^2\phi\delta(\omega)(\delta(E+L) + \delta(E-L))\right]. \qquad (4.81)$$

The integration over angle depends on the sign of Δ. For $1 > \delta = \Delta/L \geq$

0, we find the following four integrals:

$$I_1^{xx}(\delta) = \int_0^{\phi_L} \sqrt{\cos\phi - \delta} \sin^2\phi \, d\phi$$

$$= \frac{2\sqrt{2}}{15} \left[2(3 + \delta^2)E(k) - (3 + \delta)(1 + \delta)K(k) \right], \qquad (4.82)$$

$$I_2^{xx}(\delta) = \int_0^{\phi_L} \sqrt{\cos\phi - \delta} \cos^2\phi \, d\phi$$

$$= \frac{\sqrt{2}}{15} \left[(1 + \delta)(2\delta - 9)K(k) + \left(18 - 4\delta^2\right)E(k) \right], \qquad (4.83)$$

$$I_1^{yy}(\delta) = \int_0^{\phi_L} \frac{\sin^2\phi \, d\phi}{\sqrt{\cos\phi - \delta}} = \frac{2\sqrt{2}}{3} \left[(1 + \delta)K(k) - 2\delta E(k) \right], \qquad (4.84)$$

$$I_2^{yy}(\delta) = \int_0^{\phi_L} \frac{\cos^2\phi \, d\phi}{\sqrt{\cos\phi - \delta}} = \frac{\sqrt{2}}{3} \left[(1 - 2\delta)K(k) + 4\delta E(k) \right], \qquad (4.85)$$

where $K(k)$ and $E(k)$ are complete elliptic integrals, $k = \sqrt{\frac{1-\delta}{2}}$, and
$\phi_L = \arccos(\delta)$. To calculate the above integrals we made the variable
change $x = \cos\phi$, then used Eq.(4.79), the relation

$$_2F_1(a, b; c; z) = (1 - z)^{-a} {_2F_1}\left(a, c - b; c; \frac{z}{z-1}\right). \qquad (4.86)$$

and Eqs. 7.3.2.18, 7.3.2.20 and 7.3.2.75 from the book [96].

Case $\Delta < 0$: in this case the angular integration is separated into two
regions,

$$\phi \in \begin{cases} \left[0, \arccos \frac{-|\Delta|}{L}\right], & L > |\Delta|, \\ [0, \pi], & L \leq |\Delta|. \end{cases} \qquad (4.87)$$

This example can be seen as integrating with the centers in the Dirac
point. Performing integration over angle in Eqs.(4.80), (4.81) we find the
following: the integrals for $L > |\Delta|$ are the same as in $\Delta > 0$ case with
the changes $\Delta \to -|\Delta|$. The integrals for $L < |\Delta|$ ($|\delta| > 1$) are different

and have the following form:

$$I_3^{xx}(\delta < -1) = \int_0^\pi \sqrt{\cos\phi + |\delta|}\, \sin^2\phi\, d\phi$$
$$= \frac{4}{15}\sqrt{|\delta|+1}\left[(3+\delta^2)E(k') - |\delta|(|\delta|-1)K(k')\right], \quad (4.88)$$

$$I_4^{xx}(\delta < -1) = \int_0^\pi \sqrt{\cos\phi + |\delta|}\, \cos^2\phi\, d\phi$$
$$= \frac{2}{15}\sqrt{|\delta|+1}\left[(9-2\delta^2)E(k') + 2|\delta|(|\delta|-1)K(k')\right], \quad (4.89)$$

$$I_3^{yy}(\delta < -1) = \int_0^\pi \frac{\sin^2\phi\, d\phi}{\sqrt{\cos\phi + |\delta|}} = \frac{4}{3}\sqrt{|\delta|+1}\left[|\delta|E(k') - (|\delta|-1)K(k')\right],$$
$$(4.90)$$

$$I_4^{yy}(\delta < -1) = \int_0^\pi \frac{\cos^2\phi\, d\phi}{\sqrt{\cos\varphi + |\delta|}}$$
$$= \frac{2}{3\sqrt{|\delta|+1}}\left[-2|\delta|(|\delta|+1)E(k') + (1+2\delta^2)K(k')\right], \quad (4.91)$$

where $k' = \sqrt{\frac{2}{|\delta|+1}}$.

Evaluating the integrals over L in all these cases gives the following results for longitudinal conductivities in the $x-$ and $y-$directions:

$$\operatorname{Re}\sigma_{xx}(\omega) = \frac{e^2}{4\pi\hbar\omega}\int_{-\infty}^{\infty} dE[f(E) - f(E+\omega)]\frac{4|E|^{3/2}a^{1/2}}{v}\times$$

$$\times \begin{cases} 2\Theta(|\Delta| - |E|)\left(I_3^{xx}(\Delta/|E|)\delta\left(\omega + 2E\right) + I_4^{xx}(\Delta/|E|)\delta(\omega)\right) + \\ +2\Theta(|E| - |\Delta|)\left(I_1^{xx}(\Delta/|E|)\delta\left(\omega + 2E\right) + I_2^{xx}(\Delta/|E|)\delta(\omega)\right) \end{cases}, \quad \Delta < 0, \\ \frac{8\pi^{3/2}}{5\sqrt{2}\Gamma^2\left(\frac{1}{4}\right)}[2\delta(\omega + 2E) + 3\delta(\omega)], \qquad\qquad\qquad\qquad \Delta = 0, \\ 2\Theta(|E| - \Delta)\left[I_1^{xx}(\Delta/|E|)\delta(\omega + 2E) + I_2^{xx}(\Delta/|E|)\delta(\omega)\right], \qquad \Delta > 0, \end{cases}$$
$$(4.92)$$

and

$$\mathrm{Re}\,\sigma_{yy}(\omega) = \frac{e^2}{4\pi\hbar\omega} \int_{-\infty}^{\infty} dE [f(E) - f(E+\omega)] \frac{v\sqrt{|E|}}{\sqrt{a}} \times$$

$$\times \begin{cases} \begin{aligned} &2\Theta(|\Delta| - |E|)\,(I_4^{yy}(\Delta/|E|)\delta(\omega + 2E) + I_3^{yy}(\Delta/|E|)\delta(\omega)) + \\ &+2\Theta(|E| - |\Delta|)\,(I_2^{yy}(\Delta/|E|)\delta(\omega + 2E) + I_1^{yy}(\Delta/|E|)\delta(\omega)) \end{aligned} &, \quad \Delta < 0, \\[2ex] \frac{\Gamma^2(\frac{1}{4})}{3\sqrt{2\pi}}[\delta(\omega + 2E) + 2\delta(\omega)], & \Delta = 0, \\[2ex] 2\Theta(|E| - \Delta)\Big[I_2^{yy}(\Delta/|E|)\delta\,(\omega + 2E) + I_1^{yy}(\Delta/|E|)\delta(\omega)\Big], & \Delta > 0. \end{cases}$$

$$(4.93)$$

Separating interband ac and intraband dc parts, we find the results given by Eqs.(4.17) and (4.19) together with (4.20) and (4.24) in the main text.

4.9   Appendix: Longitudinal conductivity of the gapped dice model.

First we evaluate traces of commutators with matrix exponential of the Hamiltonian:

$$\mathrm{Tr}\,[e^{-iHs}v_x(t)v_x(0)] = \frac{v_F^2 \cos(psv_F)\left(2\left(p_y^2 + p_z^2\right)p^2\cos(ptv_F) + 4p_x^2 p^2\right)}{2p^4} +$$

$$+ \frac{v_F^2\left(2\left(p_y^2 + p_z^2\right)\left(p^2\sin(psv_F)\sin(ptv_F) + p^2\cos(ptv_F)\right)\right)}{2p^4}, \qquad (4.94)$$

$$\mathrm{Tr}\,[e^{-iHs}v_y(t)v_y(0)] = \frac{v_F^2\left(\cos(psv_F)\left(2\left(p_x^2 + p_z^2\right)p^2\cos(ptv_F) + 4p_y^2 p^2\right)\right)}{2p^4} +$$

$$+ \frac{v_F^2\left(+2\left(p_x^2 + p_z^2\right)\left(p^2\sin(psv_F)\sin(ptv_F) + p^2\cos(ptv_F)\right)\right)}{2p^4}. \qquad (4.95)$$

Next, we Fourier transform this expressions twice with respect to $t \to \omega$ and $s \to E$, and integrate over the polar angle

$$
\begin{aligned}
\mathcal{F}_{t,s}\,\mathrm{Tr}\left[e^{-iHs}v_x(t)v_x(0)\right] &= \\
= \delta(E) &\left(\frac{\pi v_F^2\,(p^2 + p_z^2)\,\delta\left(\omega - pv_F\right)}{2p^2} + \frac{\pi v_F^2\,(p^2 + p_z^2)\,\delta\left(\omega + pv_F\right)}{2p^2}\right) + \\
+ \delta\left(E + pv_F\right) &\left(\frac{\pi v_F^2\,(p^2 + p_z^2)\,\delta\left(\omega - pv_F\right)}{2p^2} + \frac{\pi(p^2 - p_z^2)v_F^2\delta(\omega)}{p^2}\right) + \\
+ \delta\left(E - pv_F\right) &\left(\frac{\pi v_F^2\,(p^2 + p_z^2)\,\delta\left(\omega + pv_F\right)}{2p^2} + \frac{\pi(p^2 - p_z^2)v_F^2\delta(\omega)}{p^2}\right).
\end{aligned}
$$

$$(4.96)$$

Due to isotropy of the model we get the same result for the Fourier transform $\mathcal{F}_{t,s}\,\mathrm{Tr}\left[e^{-iHs}v_y(t)v_y(0)\right]$.

The longitudinal conductivity is given by the expression

$$
\mathrm{Re}\,\sigma_{xx}(\omega) = \frac{\pi e^2}{\omega}\int\limits_{-\infty}^{\infty} dE[f(E) - f(E + \omega)]\int\limits_{0}^{\infty}\frac{k\,dk}{(2\pi)^2}\mathcal{F}_{t,s}\,\mathrm{Tr}\left[e^{-iHs}v_x(t)v_x(0)\right].
$$

$$(4.97)$$

where $k = \sqrt{p_x^2 + p_y^2}$. Finally, performing integrations we find

$$
\begin{aligned}
\mathrm{Re}\,\sigma_{xx}(\omega) = \frac{e^2}{4}&\left[x\delta(\omega)\int\limits_{-\infty}^{\infty} dE\frac{f(E) - f(E + \omega)}{\omega}\Theta\left(|E| - \Delta\right)\frac{|E|^2 - \Delta^2}{|E|}\right. \\
&\left. + \frac{f(-\omega) - f(\omega)}{\omega}\frac{\omega^2 + \Delta^2}{2|\omega|}\Theta(|\omega| - \Delta)\right],
\end{aligned}
$$

$$(4.98)$$

where in the last equality we took into account that $v_F p_z = \Delta > 0$. This expression appears in the main text, Eq.(4.41), in slightly different form and is plotted for different values of parameters.

4.10   Appendix: Evalution of Hall conductivity σ_{xy} in gapped dice model

Let us evaluate the quasiparticle velocity operator averages for the Hall conductivity. First, we evaluate the matrix traces:

$$
\mathrm{tr}\left[e^{-iv_F \mathbf{S} \mathbf{p} s}\left(v_x(t)v_y(0) + v_y(t)v_x(t)\right)\right] =
$$
$$
= -\frac{2v_F^2 p_x p_y \left(\cos\left(pv_F(s-t)\right) - 2\cos\left(psv_F\right) + \cos\left(ptv_F\right)\right)}{p^2}, \tag{4.99}
$$
$$
\mathrm{tr}\left[e^{-iv_F \mathbf{S} \mathbf{p} s}\left(v_x(t)v_y(0) - v_y(t)v_x(0)\right)\right] = \frac{2v_F^2 p_z(\sin(pv_F(s-t)) - \sin(ptv_F))}{p}. \tag{4.100}
$$

The first trace vanishes after the angle integration. Thus the symmetric part is absent for the Hall conductivity, as expected. For the antisymmetric part we find (again $k = \sqrt{p_x^2 + p_y^2}$):

$$
\mathrm{Tr}\left[\delta(E - H)\left(v_x(t)v_y(0) - v_y(t)v_x(0)\right)\right] =
$$
$$
= \frac{V}{2\pi}\int_{-\infty}^{\infty} ds\, e^{iEs}\int_0^{\infty} \frac{kdk}{(2\pi)}\frac{2v_F^2 p_z\left(\sin\left(pv_F(s-t)\right) - \sin\left(ptv_F\right)\right)}{p} =
$$
$$
= V\int_0^{\infty} \frac{kdk}{(2\pi)}\frac{2v_F^2 p_z}{p}\times
$$
$$
\left[\frac{e^{-ipv_F t}\delta(E + pv_F) - e^{ipv_F t}\delta(E - pv_F)}{2i} - \delta(E)\sin(ptv_F)\right]. \tag{4.101}
$$

Next we perform integration over time and find

$$
\int_{-\infty}^{\infty} dt\, e^{i\omega t}\, \mathrm{Tr}\left[\delta(E - H)\left(v_x(t)v_y(0) - v_y(t)v_x(0)\right)\right] = \tag{4.102}
$$
$$
= V\int_0^{\infty} kdk\frac{2v_F^2 p_z}{p}\left(\frac{\delta(\omega - pv_F)\delta(E + pv_F) - \delta(\omega + pv_F)\delta(E - pv_F)}{2i}\right.
$$
$$
\left. -\delta(E)\frac{\delta(\omega + pv_F) - \delta(\omega - pv_F)}{2i}\right).
$$

Thus, for the imaginary part of the Hall conductivity we find

$$
\operatorname{Im} \sigma_{[x,y]}(\omega) = \frac{1}{2} \frac{e^2}{4\hbar\omega} \int\limits_0^\infty k\,dk \frac{2v_F^2 p_z}{p} \int\limits_{-\infty}^\infty dE[f(E) - f(E + \hbar\omega)]
$$

$$
\times \left(-\delta(\omega - pv_F)\delta(E + pv_F) + \delta(\omega + pv_F)\delta(E - pv_F) + \right.
$$
$$
+ \delta(E)[\delta(\omega + pv_F) - \delta(\omega - pv_F)]) =
$$

$$
= \frac{e^2 v_F^2 p_z}{4\hbar\omega} \int\limits_0^\infty \frac{k\,dk}{p} \left(\delta(\omega + pv_F)[f(pv_F) - f(pv_F + \omega) + f(0) - f(\omega)] - \right.
$$

$$
- \delta(\omega - pv_F)[f(-pv_F) - f(-pv_F + \omega) + f(0) - f(\omega)] \Big). \qquad (4.103)
$$

Also in the first line we canceled $\rho(E)$ and V with the normalization $\operatorname{Tr} \delta(E - H)$. The factor $1/2$ in the first line of the last equation accounts for the definition of the antisymmetric part of the tensor. Now we can integrate over momenta and obtain

$$
\operatorname{Im} \sigma_{[x,y]}(\omega > 0) = \frac{e^2}{4\omega} v_F p_z \Theta\left(\omega - v_F|p_z|\right)\left(f(\omega) - f(-\omega)\right), \qquad (4.104)
$$

$$
\operatorname{Im} \sigma_{[x,y]}(\omega < 0) = \frac{e^2}{4\omega} v_F p_z \Theta\left(-\omega - v_F|p_z|\right)\left(f(-\omega) - f(\omega)\right). \qquad (4.105)
$$

Combining these formulas together we arrive at Eq.(4.42).

Now using the Kramers-Kronig relation we can evaluate the real part:

$$
\operatorname{Re} \sigma_{[x,y]}(\Omega) = \frac{1}{\pi} \text{ P.v.} \int\limits_{-\infty}^\infty \frac{d\omega \operatorname{Im} \sigma_{[\mu,\nu]}(\omega)}{\omega - \Omega}
$$

$$
= \frac{e^2 v_F p_z}{4\pi} \text{ P.v.} \int\limits_{-\infty}^\infty d\omega \frac{\Theta\left(|\omega| - v_F|p_z|\right)\left(f(|\omega|) - f(-|\omega|)\right)}{\omega(\omega - \Omega)}. \qquad (4.106)
$$

It is easy to check that $\operatorname{Re} \sigma_{[x,y]}(\Omega)$ is even function in Ω by changing the integration variable. The integral simplifies for the zero temperature when

$$
f\left(|\omega|\right) - f\left(-|\omega|\right) \to \theta\left(\mu - |\omega|\right) - \theta\left(|\omega| + \mu\right) = -\theta(|\omega| - |\mu|). \qquad (4.107)
$$

Thus, Eq.(4.106) gives Eq.(4.43).

4.11   Appendix: Conductivities of the Lieb model.

The system of equations for the Gell-Mann matrices is given by Eq.(4.49) with the initial values $\lambda_i(t=0) = \lambda_i$. The solutions for the $v_x(t)$ and $v_y(t)$ are defined as vectors in the Gell-Mann basis (the identity matrix is not present because it does not evolve with time and the coefficient before this matrix is zero): $v_x(t) = v_F \left(e^{At}\right)_{1j} \lambda_j$, $v_y(t) = v_F \left(e^{At}\right)_{6j} \lambda_j$ where $\left(e^{At}\right)_{1j}$ and $\left(e^{At}\right)_{6j}$ are

$$(1j) = \tag{4.108}$$

$$
\begin{pmatrix}
\dfrac{\Delta^2 q_x^2 \cos(2ptv_F)+pq_y^2(p\cos(ptv_F)\cos(\Delta tv_F)-\Delta\sin(ptv_F)\sin(\Delta tv_F))+(p^2-\Delta^2)q_x^2}{p^2(p^2-\Delta^2)} \\[6pt]
-\dfrac{\cos(ptv_F)\left(2\Delta q_x^2 \sin(ptv_F)+pq_y^2 \sin(\Delta tv_F)\right)+\Delta q_y^2 \sin(ptv_F)\cos(\Delta tv_F)}{p(p^2-\Delta^2)} \\[6pt]
\dfrac{q_x \sin(ptv_F)\left(\Delta\left(2q_x^2+q_y^2\right)\sin(ptv_F)+pq_y^2 \sin(\Delta tv_F)\right)}{p^2(p^2-\Delta^2)} \\[6pt]
\dfrac{q_y \sin(ptv_F)\left(2\Delta q_x^2 \sin(ptv_F)+p\left(q_y^2-q_x^2\right)\sin(\Delta tv_F)\right)}{p^2(p^2-\Delta^2)} \\[6pt]
\dfrac{q_y \sin(ptv_F)\cos(\Delta tv_F)}{p} \\[6pt]
\dfrac{q_x q_y(-\Delta^2-p^2\cos(ptv_F)\cos(\Delta tv_F)+\Delta^2\cos(2ptv_F)+\Delta p\sin(ptv_F)\sin(\Delta tv_F)+p^2)}{p^2(p^2-\Delta^2)} \\[6pt]
-\dfrac{q_x q_y(-\Delta\sin(2ptv_F)+\Delta\sin(ptv_F)\cos(\Delta tv_F)+p\cos(ptv_F)\sin(\Delta tv_F))}{p(p^2-\Delta^2)} \\[6pt]
\dfrac{\sqrt{3}q_x q_y^2 \sin(ptv_F)(p\sin(\Delta tv_F)-\Delta\sin(ptv_F))}{p^2(p^2-\Delta^2)}
\end{pmatrix}^T ,
$$

$$(6j) = \tag{4.109}$$

$$
\begin{pmatrix}
\dfrac{q_x q_y\left(-\Delta^2-p^2\cos(ptv_F)\cos(\Delta tv_F)+\Delta^2\cos(2ptv_F)+\Delta p\sin(ptv_F)\sin(\Delta tv_F)+p^2\right)}{p^2(p^2-\Delta^2)} \\[6pt]
\dfrac{q_x q_y(-\Delta\sin(2ptv_F)+\Delta\sin(ptv_F)\cos(\Delta tv_F)+p\cos(ptv_F)\sin(\Delta tv_F))}{p(p^2-\Delta^2)} \\[6pt]
\dfrac{q_y \sin(ptv_F)\left(\Delta\left(2q_x^2+q_y^2\right)\sin(ptv_F)-pq_x^2 \sin(\Delta tv_F)\right)}{p^2(p^2-\Delta^2)} \\[6pt]
\dfrac{q_x \sin(ptv_F)\left(p\left(q_x^2-q_y^2\right)\sin(\Delta tv_F)+2\Delta q_y^2 \sin(ptv_F)\right)}{p^2(p^2-\Delta^2)} \\[6pt]
-\dfrac{q_x \sin(ptv_F)\cos(\Delta tv_F)}{p} \\[6pt]
\dfrac{pq_x^2(p\cos(ptv_F)\cos(\Delta tv_F)-\Delta\sin(ptv_F)\sin(\Delta tv_F))+\Delta^2 q_y^2 \cos(2ptv_F)+(p^2-\Delta^2)q_y^2}{p^2(p^2-\Delta^2)} \\[6pt]
\dfrac{\Delta q_x^2 \sin(ptv_F)\cos(\Delta tv_F)+pq_x^2 \cos(ptv_F)\sin(\Delta tv_F)+\Delta q_y^2 \sin(2ptv_F)}{p(p^2-\Delta^2)} \\[6pt]
-\dfrac{\sqrt{3}q_y \sin(ptv_F)\left(pq_x^2 \sin(\Delta tv_F)+\Delta q_y^2 \sin(ptv_F)\right)}{p^2(p^2-\Delta^2)}
\end{pmatrix}^T .
$$

Integrating over t and s in Eqs.(4.4), (4.7) we find:

$$
\operatorname{Re}\sigma_{xx}(\omega) = 2\pi \frac{\pi e^2 v_F^2}{2\omega} \int\limits_{-\infty}^{\infty} dE[f(E) - f(E+\omega)] \int\limits_{0}^{\infty} \frac{k\,dk}{(2\pi)^2} \bigg[\delta\left(E - pv_F\right)
$$

$$
\times \left(\frac{\Delta^2 \delta\left(\omega + 2pv_F\right) + \delta(\omega)(p^2 - \Delta^2)}{p^2} - \left(\frac{\Delta}{2p} - \frac{1}{2}\right) \delta(\omega + (p-\Delta)v_F) \right)
$$

$$
+ \delta\left(E + pv_F\right) \times
$$

$$
\left(\frac{\Delta^2 \delta\left(\omega - 2pv_F\right) + \delta(\omega)(p^2 - \Delta^2)}{p^2} + \frac{(\Delta + p)\delta\left((p+\Delta)v_F - \omega\right)}{2p} \right)
$$

$$
+ \delta\left(E - \Delta v_F\right) \times
$$

$$
\left(\left(\frac{1}{2} - \frac{\Delta}{2p}\right) \delta(\omega - (p-\Delta)v_F) + \left(\frac{\Delta}{2p} + \frac{1}{2}\right) \delta(\omega + (p+\Delta)v_F) \right) \bigg],
$$

$$(4.110)$$

where $k = \sqrt{q_x^2 + q_y^2}$. At the same time we find $\operatorname{Im}\sigma_{[x,y]} = 0$ after taking the trace of the product of velocities. Next, we calculate the integrals which involve the delta-functions, first we integrate over E and then over momenta, we get the expression

$$
\operatorname{Re}\sigma_{xx}(\omega) = \frac{e^2}{4} \Bigg[\delta(\omega) \int\limits_{\Delta v_F}^{\infty} pv_F d(pv_F) \left(\frac{1}{4T\cosh^2((pv_F - \mu)/2T)} + \right.
$$

$$
\left. + \frac{1}{4T\cosh^2((pv_F + \mu)/2T)} \right) \frac{p^2 - \Delta^2}{p^2} +
$$

$$
+ \Theta(|\omega| - 2\Delta v_F) \left[\frac{2\Delta^2 v_F^2}{\omega^2} \left(f\left(-\frac{|\omega|}{2}\right) - f\left(\frac{|\omega|}{2}\right) \right) + \right.
$$

$$
\left. + \frac{1}{2}(f(\Delta v_F - |\omega|) - f(\Delta v_F)) \right] + \frac{f(\Delta v_F) - f(\Delta v_F + |\omega|)}{2} \Bigg], \quad (4.111)
$$

which is in fact Eq.(4.52) in the main text after restoring $\hbar$. The remaining integral can be evaluated in terms of the polylogarithm functions.

Chapter 5

Stackings and effective models of bilayer dice lattices

5.1 Introduction

The search for novel materials with unusual dispersion relations is one of the major topics in modern condensed matter physics. There are several successful examples of this search that lead to vigorous research directions. Among them, graphene is, perhaps, the most well-known example of a solid with an unusual dispersion relation. Indeed, at low energies, graphene's electron quasiparticles are described by a two-dimensional (2D) Dirac equation [22, 108, 175]. The 2D Dirac spectrum can be also realized at the surface of three-dimensional (3D) topological insulators [176–178]. Finally, the 3D linear energy spectrum appears in Weyl and Dirac semimetals [179–183].

Intermediate between 2D and 3D materials are layered systems. The energy spectrum of these systems can be engineered by stacking the layers in a certain order. The electronic properties of the corresponding few-layer systems can be drastically different from their single-layer counterparts. For example, bilayer graphene in the Bernal $(A - B)$ stacking reveals a quadratic quasiparticle spectrum in the vicinity of band touching points [108, 184, 185]. This leads to a different integer quantum Hall effect [184, 186] and optical response [187] compared to single-layer graphene.

Recently, there is a surge of interest in materials containing even more exotic energy spectra with flat bands. Among these systems, perhaps, the most well-known is twisted bilayer graphene (TBG) [1, 6, 188–192]; see also Ref. [193] for a review. In essence, TBG is composed of two layers of graphene rotated with respect to each other by some angle. It was shown [189, 190] that for the specific, so-called "magic", twist angles, 2D isolated flat bands appear in the energy spectrum of TBG. The presence of flat bands is directly related to the nontrivial properties of TBG including interaction effects such as superconductivity near integer band-filling factors [1, 6, 191, 192, 194].

While TBG receives significant attention nowadays, historically, the appearance of flat bands was predicted a few decades ago in Kagomé [195], dice or $\mathcal{T}_3$ [11, 80], and Lieb [20] lattices. A Kagomé lattice consists of equivalent lattice points and equivalent bonds forming equilateral triangles and regular hexagons; each hexagon is surrounded by triangles and vice versa. A Lieb lattice is described by three sites in a square unit cell where two of the sites are neighbored by two other sites and the third site has four neighbors. In essence, a dice lattice has a hexagonal structure with an additional atom placed in the center of each hexagon. The central atom acts as a hub connected to six rims while each of the rims is connected to three hubs; see also Fig. 5.1(a) for a dice lattice. If one of the rims is removed, a conventional honeycomb (graphene) lattice is restored. In the rest of this work, we focus on dice lattice as a representative system. As for experimental setups, dice lattices were proposed in artificial systems such as optical lattices [12, 19]; see Ref. [92] for a review. As an example of the experimental realizations of dice lattices, we mention Josephson arrays [17] as well as optical realizations [19].

The lattice structure of the dice model with three atoms per unit cell leads to three bands in the energy spectrum which is similar to that in graphene albeit with Dirac points intersected by a flat band [13]. The corresponding low-energy spectrum can be described in terms of spin-1 fermions, which have no analogs in high-energy physics. The flat band leads to strikingly different physical properties with a paramagnetic response [13, 196] instead of the diamagnetic one as in graphene [197] being a representative example. To the best of our knowledge, multi-layer dice lattices were not investigated before and, as in multi-layer graphene, are expected to be different from their single-layer counterparts.

In this work, we combine two vigorous research directions related to

exotic lattices and heterostructures by studying the properties of *bilayer dice lattices* [1]. We classify nonequivalent commensurate stackings of dice lattices and formulate the corresponding tight-binding and effective low-energy models. Depending on the type of the stacking, the low-energy spectrum comprises Dirac points intersected by flat bands, three-fold-corrugated bands, tilted bands, or even a semi-Dirac spectrum. For the semi-Dirac spectrum, the energy bands are anisotropic with a linear dispersion relation along one direction and the quadratic dispersion along the other [139]. For all four nonequivalent stackings, the sets of band-crossing points originating from different layers are separated in energy with the separation determined by the interlayer coupling constant. The obtained bilayer models are illustrated by calculating the density of states (DOS) and the spectral function. Being strongly modified by the inter-layer coupling, the DOS and the spectral function provide an efficient way to distinguish the stackings and set up the stage for the investigation of the optical response in our forthcoming work [199].

The paper is organized as follows. We discuss the key properties of a single-layer dice lattice in Sec. 5.2. The commensurate stackings are classified as well as the tight-binding and effective models of a bilayer dice lattice are formulated in Sec. 5.3. The spectral functions and the DOS for each of the four stackings are presented in Sec. 5.4. The results are summarized in Sec. 5.5. Technical details concerning the derivation of the effective models, low-energy spectral functions, and the properties of the bilayer lattices at larger coupling constants are presented in Appendices 5.6, 5.7, and 5.8, respectively.

5.2   Single-layer dice lattice

As a warm-up and to set up the stage for the discussion of the bilayer dice lattice, we present the model and the key properties of a *single-layer dice lattice*. In the essence, a dice lattice is a hexagonal lattice composed of two sublattices (denoted as A and B) with additional sites (C sublattice) placed in the center of hexagons. The resulting inter-sublattice connections are shown in Fig. 5.1(a). As one can see, the atoms of the C sublattice act as hubs that connect to six neighbors, while the atoms of the A and B sublattices (rims) connect only to three neighbors.

---

[1]Bilayer dice lattices should not be confused with the double-layer lattice studied in Ref. [198].

(a)   (b)
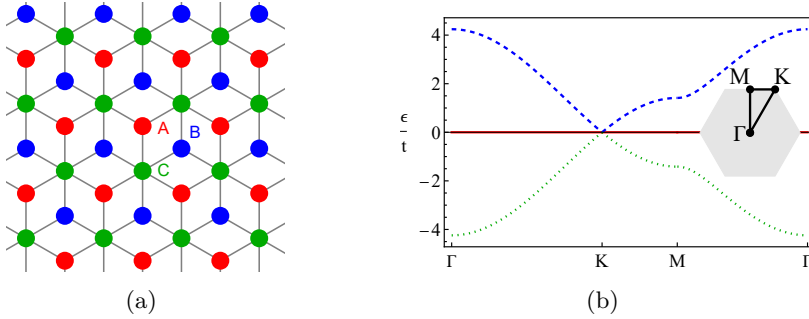
Figure 5.1. Panel (a): The schematic representation of single-layer dice lattice. The A, B, and C sites are denoted by red, blue, and green dots. Panel (b): The energy spectrum given in Eq. (5.3) along the $\Gamma - K - M - \Gamma$ line in the Brillouin zone (inset). Here, t is the hopping constant.

In the basis of states corresponding to the A, C, and B sublattices, the tight-binding Hamiltonian reads [13]

$$H(\mathbf{q}) = \begin{pmatrix} 0 & -t\sum_j e^{-i\mathbf{q}\cdot\boldsymbol{\delta}_j} & 0 \\ -t\sum_j e^{i\mathbf{q}\cdot\boldsymbol{\delta}_j} & 0 & -t\sum_j e^{-i\mathbf{q}\cdot\boldsymbol{\delta}_j} \\ 0 & -t\sum_j e^{i\mathbf{q}\cdot\boldsymbol{\delta}_j} & 0 \end{pmatrix}, \qquad (5.1)$$

where t is the hopping constant, $\mathbf{q}$ is the wave vector in the Brillouin zone, and

$$\boldsymbol{\delta}_1 = a\left\{0, 1\right\}, \quad \boldsymbol{\delta}_2 = a\left\{\frac{\sqrt{3}}{2}, -\frac{1}{2}\right\}, \quad \boldsymbol{\delta}_3 = a\left\{-\frac{\sqrt{3}}{2}, -\frac{1}{2}\right\} \qquad (5.2)$$

denote the relative positions of the sites A with respect to the sites C; a is the distance between the neighboring A and C sites. The same vectors but with the minus sign denote the relative positions of sites B with respect to sites C. In this model, the A and B sublattices are equivalent.

The energy spectrum of Hamiltonian (5.1) reads

$$\varepsilon_0 = 0, \qquad \varepsilon_\pm = \pm t\sqrt{6}\sqrt{1 + \frac{2}{3}\cos\left(\sqrt{3}aq_x\right) + \frac{4}{3}\cos\left(\frac{\sqrt{3}}{2}aq_x\right)\cos\left(\frac{3}{2}aq_y\right)}.$$

$$(5.3)$$

In essence, the dispersive bands $\varepsilon_\pm$ are the same as in graphene where the quasiparticle spectrum contains two nonequivalent Dirac nodes K and K'. We show the corresponding energy spectrum in Fig. 5.1(b).

In the vicinity of the Dirac points, Hamiltonian (5.1) can be linearized and reads as

$$H_\xi(\mathbf{k}) = \hbar v_F \left(\xi S_x k_x + S_y k_y \right), \tag{5.4}$$

where $\mathbf{k} = \mathbf{q} - \mathbf{K}_\xi$ is the wave vector measured relative to the Dirac points located at $\mathbf{K}_\xi = \xi 4\pi/(3\sqrt{3}a)\{1,0\}$, corresponding to K ($\xi = +$) and K' ($\xi = -$) points, and $v_F = 3ta/(\sqrt{2}\hbar)$ is the Fermi velocity. Further, we introduced the following spin-1 matrices:

$$S_x = \frac{1}{\sqrt{2}} \begin{pmatrix} 0 & 1 & 0 \\ 1 & 0 & 1 \\ 0 & 1 & 0 \end{pmatrix}, \qquad S_y = \frac{1}{\sqrt{2}} \begin{pmatrix} 0 & -i & 0 \\ i & 0 & -i \\ 0 & i & 0 \end{pmatrix}. \tag{5.5}$$

The corresponding energy spectrum contains a Dirac point intersected by a flat band

$$\varepsilon_0 = 0, \qquad \varepsilon_\pm = \pm \hbar v_F k. \tag{5.6}$$

As we discussed in the Introduction, heterostructures made of different stackings of single-layer graphene is a major topic in graphene physics. In the next section, we will introduce and study the simplest multi-layer dice lattices composed of two commensurately stacked single-layer dice lattices.

5.3   Bilayer dice lattice

5.3.1   Stackings of bilayer dice lattices

For the *bilayer dice lattice*, there are a few ways to commensurately stack two dice lattices. The most obvious way is to have the sublattices of the same type in two layers aligned with each other. Therefore, we call this type of stacking the *aligned $AA - BB - CC$ stacking*. Other stackings can be obtained starting from the aligned stacking by rotating or shifting one of the layers. A commensurate stacking is obtained by rotating one of the layers around a C site by $\pi/3$. In this case, the sublattices A and B in one of the layers are aligned with the sublattices B and A of the other layer. Because the hub atoms C remain aligned, we dub this type of the stacking the *hub-aligned $AB - BA - CC$ stacking*. We notice that the A and B sublattices have different connectivity compared to the C sublattice. Therefore, a nonequivalent stacking is realized for rotating around an A site by $\pi/3$; rotation around a B site (with the resulting

$AC - BB - CA$ stacking) is equivalent since the sublattices A and B are assumed to be interchangeable within each of the layers. This results in the *mixed $AA - BC - CB$ stacking* where the sublattices B and C in one layer are aligned with the sublattices C and B in the other, i.e., hubs and rims intermix. Finally, we can shift one of the layers with respect to the other by a lattice constant. For the corresponding commensurate stacking, the sublattices A, B, and C in one layer are aligned with the sublattices C, A, and B in the other. We call this type of the stacking the *cyclic $AB - BC - CA$ stacking*. Other stackings are either equivalent or non-commensurate.

Certainly, it would be interesting to determine which of these commensurate stacking has the lowest energy. Such an analysis would depend on the realization of the dice lattice and is beyond the scope of this paper. We find it instructive, however, to remind the corresponding results for bilayer graphene. Bilayer graphene can exist in the Bernal-stacked $A - B$ form and, less commonly, in the $A - A$ form, where the layers are exactly aligned. Using the quantum Monte Carlo methods, it was found that the Bernal stacking is more energetically favorable [200].

Thus, there are four nonequivalent commensurate stackings in a bilayer dice lattice: (i) aligned $AA - BB - CC$, (ii) hub-aligned $AB - BA - CC$, (iii) mixed $AA - BC - CB$, and (iv) cyclic $AB - BC - CA$. We model interlayer hoppings in these stackings by the following inter-layer coupling Hamiltonians:

$$H_c^{(a)} = g \begin{pmatrix} 1 & 0 & 0 \\ 0 & 1 & 0 \\ 0 & 0 & 1 \end{pmatrix}, \qquad H_c^{(h)} = g \begin{pmatrix} 0 & 0 & 1 \\ 0 & 1 & 0 \\ 1 & 0 & 0 \end{pmatrix},$$

$$H_c^{(m)} = g \begin{pmatrix} 1 & 0 & 0 \\ 0 & 0 & 1 \\ 0 & 1 & 0 \end{pmatrix}, \qquad H_c^{(c)} = g \begin{pmatrix} 0 & 0 & 1 \\ 1 & 0 & 0 \\ 0 & 1 & 0 \end{pmatrix}, \qquad (5.7)$$

where g is the coupling constant. In writing Eq. (5.7), we assumed only the nearest-neighbor tunneling. For simplicity, the coupling constants for all sites are taken to be equivalent.

The tight-binding Hamiltonian for a bilayer dice lattice reads as

$$H_{\text{tot}}(\mathbf{q}) = \begin{pmatrix} H(\mathbf{q}) & H_c \\ H_c^{\text{T}} & H(\mathbf{q}) \end{pmatrix}, \qquad (5.8)$$

where $H(\mathbf{q})$ is given by the single-layer tight-binding Hamiltonian (5.1) and H_c is defined by one of the coupling Hamiltonians in Eq. (5.7).

Before discussing the effective models, it is instructive to analyze the discrete symmetries of the tight-binding Hamiltonian (5.8) and compare them with their counterparts in a single-layer dice lattice.

5.3.2 Discrete symmetries

Discrete symmetries including charge-conjugation, time-reversal, and inversion symmetries play an important role in many systems allowing for the classification of electron states and order parameters. The single-layer dice lattice respects all of these symmetries as well as possesses the C_3 rotational symmetry. The coupling Hamiltonian of the bilayer lattice might, however, break one or more of the discrete symmetries. We summarize the symmetries in Table 5.1 and provide a more detailed discussion below.

Dice lattice	Charge-conjugation symmetry	Time-reversal symmetry	Inversion symmetry
Single-layer	$M_0 \hat{K}$	$\mathbb{1}_3 \hat{K}$	W_0
Aligned $AA - BB - CC$	$M_1 \hat{K}, \ M_2 \hat{K}$	$\mathbb{1}_3 \hat{K}$	$W_1, \ W_2$
Hub-aligned $AB - BA - CC$	$M_1 \hat{K}, \ M_2 \hat{K}$	$\mathbb{1}_3 \hat{K}$	$W_1, \quad W_2$
Mixed $AA - BC - CB$	-	$\mathbb{1}_3 \hat{K}$	-
Cyclic $AB - BC - CA$	-	$\mathbb{1}_3 \hat{K}$	W_2

Table 5.1. Symmetry properties of the tight-binding Hamiltonian for a bilayer dice lattice (5.8) in different commensurate stackings. The tight-binding Hamiltonian of a single-layer dice lattice is given in Eq. (5.1) and the coupling Hamiltonians are defined in Eq. (5.7). The symmetry matrices $M_{1,2}$ and $W_{1,2}$ are defined in Eqs. (5.10) and (5.13).

We begin our symmetry analysis with the charge-conjugation or particle-hole symmetry ($\mathcal{C}$-symmetry). The operator of the charge-conjugation symmetry is defined as

$$\hat{C} H(\mathbf{q}) \hat{C}^{-1} = -H(\mathbf{q}). \tag{5.9}$$

The corresponding operator necessarily contains the complex conjugation operator $\hat{K}$ and a matrix, i.e., $\hat{C} = M\hat{K}$. For the aligned $AA - BB - CC$

and hub-aligned $AB-BA-CC$ stackings, there are the following matrices M:

$$M_1 = \tau_z \otimes M_0 \quad \text{and} \quad M_2 = i\tau_y \otimes M_0 \quad \text{with} \quad M_0 = \begin{pmatrix} 0 & 0 & 1 \\ 0 & -1 & 0 \\ 1 & 0 & 0 \end{pmatrix}. \quad (5.10)$$

Here, $\boldsymbol{\tau}$ is the vector of the Pauli matrices defined in the layer space and M_0 is the charge-conjugation symmetry matrix for a single-layer dice lattice [166]. No charge-conjugation symmetry exists for the mixed $AA - BC - CB$ and cyclic $AB - BC - CA$ stackings.

Let us proceed to the time-reversal symmetry ($\mathcal{T}$-symmetry), which is defined as

$$\hat{T}H(\mathbf{q})\hat{T}^{-1} = H(-\mathbf{q}), \quad (5.11)$$

where $\hat{T}^2 = 1$ because we do not explicitly include the spin degree of freedom for the dice lattice. It is straightforward to check that the single-layer dice lattice is time-reversal symmetric with $\hat{T} = \hat{K}$. Since the interlayer coupling in Eq. (5.7) is real, all stackings considered in this work are time-reversal-symmetric.

Finally, let us analyze the inversion symmetry ($\mathcal{P}$-symmetry). This symmetry changes sign of momentum and interchanges sublattices leaving the Hamiltonian invariant. The operator of the inversion symmetry is $\hat{P} = W\Pi_{\mathbf{q}\rightarrow-\mathbf{q}}$ where the matrix W satisfies the following equation:

$$WH(\mathbf{q}) = H(-\mathbf{q})W. \quad (5.12)$$

In a single-layer dice lattice, the sublattices A and B interchange under the inversion symmetry. The corresponding matrix W_0 is given by the antidiagonal 3×3 matrix [89]. For aligned $AA - BB - CC$ and hub-aligned $AB - BA - CC$ stackings, we find the following matrices:

$$W_1 = \mathbb{1}_2 \otimes W_0 \quad \text{and} \quad W_2 = \tau_x \otimes W_0 \quad \text{with} \quad W_0 = \begin{pmatrix} 0 & 0 & 1 \\ 0 & 1 & 0 \\ 1 & 0 & 0 \end{pmatrix}. \quad (5.13)$$

As with the other discrete symmetries, the aligned $AB-BA-CC$ stacking preserves the inversion symmetry of the dice lattice. As for the hub-aligned $AB - BA - CC$ stacking, the interchange of the layers is equivalent to the rotation by $\pi/3$ with respect to sites C. Since the bilayer lattice in the hub-aligned stacking retains the C_3 rotation symmetry, it is also invariant with respect to the interchange of the layers. On the other hand,

the mixed $AA - BC - CB$ stacking breaks the inversion symmetry. This follows from the fact that the mixed stacking explicitly distinguishes one of the sublattices (A-sublattice). It is interesting that the cyclic stacking is inversion-symmetric albeit the corresponding symmetry operator necessarily involves the interchange of layers, i.e., only the W_2 matrix in Eq. (5.13) is valid. The interchange of layers compensates for the change made by the in-plane inversion and restores the cyclic order of atoms.

5.3.3 Energy spectrum and effective models

In this Section, we present effective low-energy Hamiltonians for bilayer dice models and compare their energy spectra with those of the tight-binding counterparts. In the derivation of the effective models, we follow the standard approach used, e.g., for bilayer graphene. The details of the derivation of the effective models can be found in Appendix 5.6. The effective models are derived assuming strong interlayer coupling compared to momenta in the vicinity of the Dirac points, i.e., $g \gg \hbar v_F k$. In addition, in writing linearised effective models, we focus on the K point; the Hamiltonian for the K' point can be obtained by replacing $k_x \to -k_x$.

As we show in Figs. 5.2–5.5, while the dispersion relation is strongly modified by the inter-layer coupling, the band-crossing points remain gapless. The inter-layer coupling shifts the points in energy: instead of a doubly degenerate band-crossing point at $g = 0$, there are two band-crossing points located at $\pm g$. Effective models are able to capture the most significant features of the dispersion relation in the vicinity of the band-crossing points. To simplify the notations, we consider effective models only for the band-crossing point at g; the effective models and the energy spectrum for the band-crossing point at $-g$ can be obtained by the replacement $g \to -g$.

Aligned $AA - BB - CC$ stacking

We start with the simplest, aligned $AA - BB - CC$, stacking. The effective Hamiltonian in the vicinity of the K point is

$$H_{\text{eff}}^{(\text{a})} = g \mathbb{1}_3 + \hbar v_F \left(\mathbf{S} \cdot \mathbf{k} \right). \tag{5.14}$$

As one can see, in the leading nontrivial order in $\hbar v_F k / g$, the effective model for the $AA - BB - CC$ stacking comprises two copies of the single-layer linearized Hamiltonians (the other copy is obtained by replacing
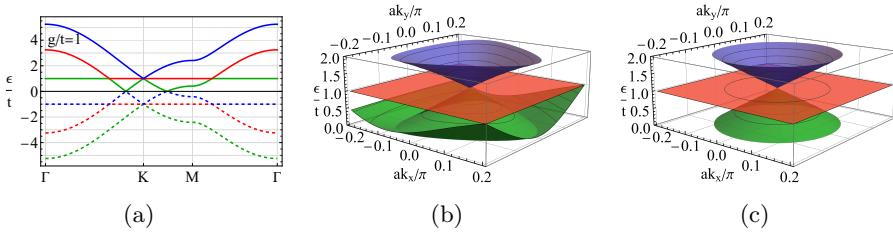
Figure 5.2. The energy spectrum of the tight-binding Hamiltonian (5.8) for the aligned $AA - BB - CC$ stacking along the $\Gamma - K - M - \Gamma$ line in the Brillouin zone (panel (a)). The tight-binding and effective (see Eq. (5.15)), energy spectra at the K point and $\varepsilon > 0$ are compared in panels (b) and (c), respectively. In all panels, we set $g = t$.

$g \to -g$), see Eq. (5.4), separated by $2g$ in energy. The energy spectrum is given by Eq. (5.6) where the positive and negative branches are shifted by g, respectively, i.e.,

$$\varepsilon_0 = g, \qquad \varepsilon_1 = g + \hbar v_F k, \quad \text{and} \quad \varepsilon_2 = g - \hbar v_F k. \tag{5.15}$$

We present the energy dispersion for the tight-binding Hamiltonian (5.8) in Fig. 5.2(a). The energy spectrum in the vicinity of the K point is compared with that of the effective model in Figs. 5.2(b) and 5.2(c), respectively. Notice that the flat band remains intact. Furthermore, both tight-binding and effective Hamiltonians are particle-hole symmetric.

Evidently, the evolution of the energy spectrum with the inter-layer coupling constant is drastically different from that in bilayer graphene. While the band-touching points in the latter remain at zero energy, the band-crossing points in a bilayer dice lattice become separated in energy. The energy spectrum at $\varepsilon = 0$ contains nodal rings around K points. The cross-section of such a nodal ring is shown in Fig. 5.2; see also Fig. 5.8 for the spectral function.

Hub-aligned $AB - BA - CC$ stacking

In contrast to the aligned stacking considered in Sec. 5.3.3, the hub-aligned $AB - BA - CC$ stacking requires one to include the second-order in $\hbar v_F k/g$ terms to reproduce an anisotropy of the energy dispersion. The corre-

sponding effective Hamiltonian reads

$$H_{\text{eff}}^{\text{(h)}} = g\mathbb{1}_3 + \frac{\hbar v_F}{\sqrt{2}} k_x \begin{pmatrix} 0 & 1 & 0 \\ 1 & 0 & 1 \\ 0 & 1 & 0 \end{pmatrix} + \left(\frac{\hbar v_F}{\sqrt{2}}\right)^2 \frac{k_y^2}{2g} \begin{pmatrix} 1 & 0 & -1 \\ 0 & 2 & 0 \\ -1 & 0 & 1 \end{pmatrix}$$

$$+ \frac{\hbar v_F}{\sqrt{2}} \frac{a}{4} \left(k_y^2 - k_x^2\right) \begin{pmatrix} 0 & 1 & 0 \\ 1 & 0 & 1 \\ 0 & 1 & 0 \end{pmatrix}. \tag{5.16}$$

The second-order terms are responsible for the asymmetry of the energy spectrum. We have the following energy spectrum in the vicinity of the K point:

$$\varepsilon_0 = g + \frac{(\hbar v_F k_y)^2}{2g}, \tag{5.17}$$

$$\varepsilon_1 = g + \frac{(\hbar v_F k_y)^2}{4g} + \frac{\hbar v_F}{4g} \sqrt{(\hbar v_F)^2 k_y^4 + g^2 \left[4k_x - a(k_x^2 - k_y^2)\right]^2}, \tag{5.18}$$

$$\varepsilon_2 = g + \frac{(\hbar v_F k_y)^2}{4g} - \frac{\hbar v_F}{4g} \sqrt{(\hbar v_F)^2 k_y^4 + g^2 \left[4k_x - a(k_x^2 - k_y^2)\right]^2}. \tag{5.19}$$

If $\hbar v_F/g \gg a$, the terms containing ak_x^2 and ak_y^2, i.e., the last term in Eq. (5.16) can be neglected. Then, the energy spectrum in Eqs. (5.18)–(5.19) corresponds to a particle-hole asymmetric version of the semi-Dirac spectrum [139] in which the dispersion relation is linear in one direction and quadratic in the other. The particle-hole symmetry breakdown around each of the band-crossing points is quantified by momentum-dependent $\sim (\hbar v_F k_y)^2/g$ term.

We present the energy dispersion for the tight-binding Hamiltonian (5.8) in Fig. 5.3(a). The energy spectrum in the vicinity of the K point is compared with that of the effective model in Figs. 5.3(b) and 5.3(c), respectively. The spectrum is clearly anisotropic with a linear dispersion relation along k_x and the quadratic one along k_y. Furthermore, the particle-hole symmetry is broken for the effective model (i.e., the bands in the vicinity of the band-crossing points are particle-hole asymmetric) but is preserved in the tight-binding one; see Fig. 5.3(a). It is interesting to notice also that the energy spectrum for the hub-aligned $AB - BA - CC$ stacking retains some features of the spectrum of the aligned $AA - BB - CC$ stacking, namely, the band remains flat along certain directions (k_y); cf. Figs. 5.2(a) and 5.3(a). In addition, the bands
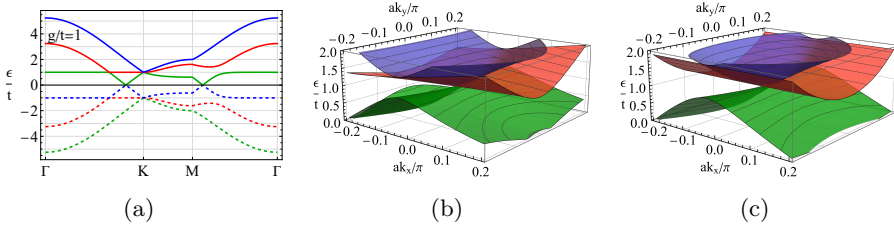
Figure 5.3. The energy spectrum of the tight-binding Hamiltonian (5.8) for the hub-aligned $AB-BA-CC$ stacking along the $\Gamma-\mathrm{K}-\mathrm{M}-\Gamma$ line in the Brillouin zone (panel (a)). The tight-binding and effective, see Eqs. (5.17)–(5.19), energy spectra at the K point and $\varepsilon > 0$ are compared in panels (b) and (c), respectively. In all panels, we set $g = t$.

at $\varepsilon = 0$ intersect along lines in momentum space rather than form nodes; see also Fig. 5.8 for the spectral function.

Mixed $AA - BC - CB$ stacking

In the case of the mixed $AA - BC - CB$ stacking with the coupling Hamiltonian defined by $H_{\mathrm{c}}^{(\mathrm{m})}$ in Eq. (5.7), we derive the following effective Hamiltonian:

$$
\begin{aligned}
H_{\mathrm{eff}}^{(\mathrm{m})} &= \frac{\hbar v_F}{2\sqrt{2}}
\begin{pmatrix}
0 & 2k_x & k_- \\
2k_x & 0 & k_- \\
k_+ & k_+ & 0
\end{pmatrix}
+ \frac{\hbar^2 v_F^2}{16g}
\begin{pmatrix}
k_x^2 + 5k_y^2 & 0 & 0 \\
0 & k_x^2 + 5k_y^2 & 0 \\
0 & 0 & 2k^2
\end{pmatrix} \\
&+ g\mathbb{1}_3 - \left(\frac{\hbar v_F}{4}\right)^2 \frac{1}{g}
\begin{pmatrix}
0 & k^2 & 2ik_y k_- \\
k^2 & 0 & 2ik_y k_- \\
-2ik_y k_+ & -2ik_y k_+ & 0
\end{pmatrix} \\
&- \frac{\hbar v_F a}{8\sqrt{2}}
\begin{pmatrix}
0 & 2(k_x^2 - k_y^2) & k_+^2 \\
2(k_x^2 - k_y^2) & 0 & k_+^2 \\
k_-^2 & k_-^2 & 0
\end{pmatrix}.
\end{aligned}
\tag{5.20}
$$

The energy spectrum up to the second order in momentum is quite cumbersome. Therefore, we leave the second-order terms only in the ε_0 branch where they are crucial to describe the anisotropy and provide leading order corrections at $k_x = 0$. For other branches, the second-order terms can be neglected compared to the leading-order linear terms.

Therefore, we have

$$\varepsilon_0 = g - \frac{\hbar v_F}{\sqrt{2}} k_x + \frac{(\hbar v_F)^2}{8g} \left(k_x^2 + 3k_y^2 \right) + \frac{\hbar v_F}{4\sqrt{2}} a \left(k_x^2 - k_y^2 \right), \quad (5.21)$$

$$\varepsilon_1 = g + \frac{\hbar v_F}{2\sqrt{2}} k_x + \frac{\hbar v_F}{2\sqrt{2}} \sqrt{3k_x^2 + 2k_y^2}, \quad (5.22)$$

$$\varepsilon_2 = g + \frac{\hbar v_F}{2\sqrt{2}} k_x - \frac{\hbar v_F}{2\sqrt{2}} \sqrt{3k_x^2 + 2k_y^2}. \quad (5.23)$$

We present the energy dispersion for the tight-binding Hamiltonian (5.8) with the coupling Hamiltonian $H_c^{(m)}$ defined in Eq. (5.7) in Fig. 5.4(a). The tight-binding energy spectrum in the vicinity of the K point is compared with that of the effective model (5.20) in Figs. 5.4(b) and 5.4(c), respectively. As one can see, dispersive Dirac-like bands become anisotropic. Furthermore, as in the case of the hub-aligned $AB - BA - CC$ stacking, the additional band is no longer flat but acquires a noticeable anisotropic dispersion along all directions. Another noticeable feature of the spectrum is the absence of particle-hole symmetry in the tight-binding and effective models. This is qualitatively different from the hub-aligned $AB-BA-CC$ stacking where the particle-hole symmetry is broken only in the effective model; cf. Figs. 5.3(a) and 5.4(a).

Compared to the aligned and hub-aligned stackings, the energy spectrum at $\varepsilon = 0$ is drastically different. As is evident from Fig. 5.4(a), the bands no longer cross. However, the band structure retains its semimetallic nature with electron and hole bands located in different parts of the Brillouin zone.

Cyclic $AB - BC - CA$ stacking

The effective linearized Hamiltonian for the cyclic $AB-BC-CA$ stacking reads

$$H_{\text{eff}}^{(c)} = g\mathbb{1}_3 + \frac{\hbar v_F}{2\sqrt{2}} \begin{pmatrix} 0 & k_- & k_+ \\ k_+ & 0 & 2k_- \\ k_- & 2k_+ & 0 \end{pmatrix}. \quad (5.24)$$

The energy spectrum is determined by the following third-order equation:

$$(\varepsilon - g)^3 - A_1 (\varepsilon - g) + A_2 = 0, \quad (5.25)$$

where

$$A_1 = \frac{27}{8} (atk)^2 \quad \text{and} \quad A_2 = \frac{27}{16} (at)^3 k_x \left(k_x^2 - 3k_y^2 \right). \quad (5.26)$$

Figure 5.4. The energy spectrum of the tight-binding Hamiltonian (5.8) for the mixed $AA - BC - CB$ stacking along the $\Gamma - \mathrm{K} - \mathrm{M} - \Gamma$ line in the Brillouin zone (panel (a)). The tight-binding and effective, see Eqs. (5.21)–(5.23), energy spectra at the K point and $\varepsilon > 0$ are compared in panels (b) and (c), respectively. In all panels, we set $g = t$.

The solutions to Eq. (5.25) are

$$\varepsilon_0 = g + 2\sqrt{\frac{A_1}{3}} \cos\left[\frac{1}{3}\arccos\left(\frac{3A_2}{2A_1}\sqrt{\frac{3}{A_1}}\right) - \frac{2\pi}{3}\right]$$
$$= g + \hbar v_F k \cos\left\{\frac{1}{3}\arccos\left[\frac{\cos(3\varphi)}{\sqrt{2}}\right] - \frac{2\pi}{3}\right\}, \qquad (5.27)$$

$$\varepsilon_1 = g + 2\sqrt{\frac{A_1}{3}} \cos\left[\frac{1}{3}\arccos\left(\frac{3A_2}{2A_1}\sqrt{\frac{3}{A_1}}\right)\right]$$
$$= g + \hbar v_F k \cos\left\{\frac{1}{3}\arccos\left[\frac{\cos(3\varphi)}{\sqrt{2}}\right]\right\}, \qquad (5.28)$$

$$\varepsilon_2 = g + 2\sqrt{\frac{A_1}{3}} \cos\left[\frac{1}{3}\arccos\left(\frac{3A_2}{2A_1}\sqrt{\frac{3}{A_1}}\right) - \frac{4\pi}{3}\right]$$
$$= g + \hbar v_F k \cos\left\{\frac{1}{3}\arccos\left[\frac{\cos(3\varphi)}{\sqrt{2}}\right] - \frac{4\pi}{3}\right\}. \qquad (5.29)$$

In the second expressions in Eqs. (5.27)–(5.29), we used the polar coordinate system with $\{k_x, k_y\} = k\{\cos\varphi, \sin\varphi\}$.

We present the energy dispersion for the tight-binding Hamiltonian (5.8) with the coupling Hamiltonian $H_{\mathrm{c}}^{(\mathrm{c})}$, see Eq. (5.7), in Fig. 5.5(a). The tight-binding energy spectrum in the vicinity of the K point is compared with that of the effective model in Figs. 5.5(b) and 5.5(c), respectively. As one can see, both dispersive and flat bands become corrugated
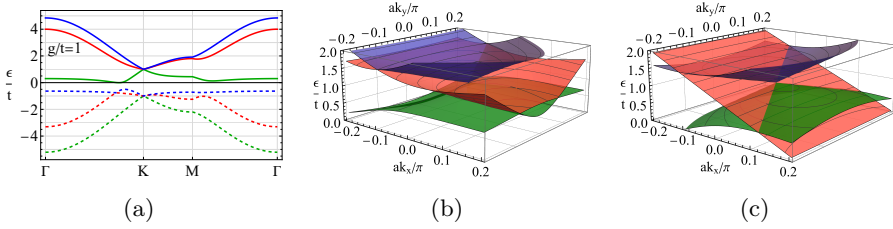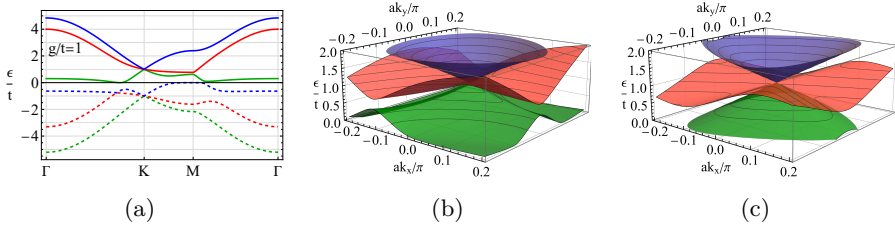
Figure 5.5. The energy spectrum of the tight-binding Hamiltonian (5.8) for the cyclic $AB - BC - CA$ stacking along the $\Gamma - K - M - \Gamma$ line in the Brillouin zone (panel (a)). The tight-binding and effective, see Eqs. (5.27)–(5.29), energy spectra at the K point and $\varepsilon > 0$ are compared in panels (b) and (c), respectively. In all panels, we set $g = t$.

due to the inter-layer coupling. The corrugation has C_3 symmetry, see also Eqs. (5.27)–(5.29). Despite being linear in momentum, the effective model captures the main features of the energy spectrum reasonably well. The particle-hole symmetry is broken both for tight-binding and effective models.

The low-energy spectrum $|\varepsilon|/t \ll 1$ is similar to that for the mixed stacking and also shows a semimetallic behavior, see Fig. 5.5(a). The electron and hole pockets form a rather intricate Kagome pattern at $\varepsilon = 0$, see Fig. 5.8(d).

5.4 Density of states and spectral function

In this Section, we discuss the spectral function and the DOS for the bilayer dice lattices. To start with, we introduce the Green function in the momentum space

$$G(\omega \pm i0; \mathbf{k}) = \frac{i}{\hbar\omega - \mu - H(\mathbf{k}) \pm i0}, \qquad (5.30)$$

where $H(\mathbf{k})$ is the Hamiltonian (effective or tight-binding), μ is the Fermi energy, and signs $\pm$ define the retarded $(+)$ and advanced $(-)$ Green functions. By using the Green function (5.30), we define the spectral function

$$A(\omega; \mathbf{k}) = \frac{1}{2\pi} \left[G(\omega + i0; \mathbf{k}) - G(\omega - i0; \mathbf{k}) \right] \Big|_{\mu=0}. \qquad (5.31)$$

While the complete information about the spectral properties is provided by the spectral function $A(\omega; \mathbf{k})$, another useful quantity measured in, e.g., scanning tunneling spectroscopy experiments, is the DOS $\nu(\omega)$ defined as

$$\nu(\omega) = \int \frac{d^2k}{(2\pi)^2} \text{tr}\{A(\omega; \mathbf{k})\}, \tag{5.32}$$

where the integration proceeds over the Brillouin zone if the tight-binding Hamiltonian is used.

The explicit form of the Green and spectral functions is rather cumbersome even for the effective Hamiltonians. Only the case of the aligned $AA - BB - CC$ stacking is relatively simple because it corresponds to two copies of a single-layer dice model. The Green function for the effective model of the aligned stacking reads

$$G^{(\text{a})}(\omega; \mathbf{k}) = \frac{i}{\mathcal{D}^{(\text{a})}(\omega)} \times$$

$$\begin{pmatrix} (\hbar\omega - g)^2 - \frac{(\hbar v_F k)^2}{2} & \frac{\hbar v_F k_-}{\sqrt{2}}(\hbar\omega - g) & \frac{(\hbar v_F k_-)^2}{2} \\ \frac{\hbar v_F k_+}{\sqrt{2}}(\hbar\omega - g) & (\hbar\omega - g)^2 & \frac{\hbar v_F k_-}{\sqrt{2}}(\hbar\omega - g) \\ \frac{(\hbar v_F k_+)^2}{2} & \frac{\hbar v_F k_+}{\sqrt{2}}(\hbar\omega - g) & (\hbar\omega - g)^2 - \frac{(\hbar v_F k)^2}{2} \end{pmatrix}. \tag{5.33}$$

Here, we used the effective Hamiltonian $H_{\text{eff}}^{(\text{a})}$ given in Eq. (5.14) and defined

$$\mathcal{D}^{(\text{a})} \equiv \det\left(\hbar\omega - H_{\text{eff}}^{(\text{a})}\right) = (\hbar\omega - g)\left[(\hbar\omega - g)^2 - (\hbar v_F k)^2\right]. \tag{5.34}$$

The spectral function is

$$A^{(\text{a})}(\omega; \mathbf{k}) = -i\mathcal{D}^{(\text{a})}(\omega)F^{(\text{a})}(\omega)G^{(\text{a})}(\omega; \mathbf{k}), \tag{5.35}$$

where

$$F^{(\text{a})}(\omega) = \frac{1}{(\hbar v_F k)^2}\left\{\frac{\delta(\hbar\omega - g - \hbar v_F k) + \delta(\hbar\omega - g + \hbar v_F k)}{2} - \delta(\hbar\omega - g)\right\}. \tag{5.36}$$

Then the DOS reads as

$$\nu^{(\text{a})}(\omega) = \frac{1}{2\pi(\hbar v_F)^2}\left\{\frac{\Lambda^2}{2}\delta(\hbar\omega - g) + |\hbar\omega - g|\right\}, \tag{5.37}$$

where Λ is the energy cutoff. The first term in Eq. (5.37) is related to the flat band and the second term has the same form as the DOS in monolayer

graphene. The DOS (5.37) is essentially the same as for a single-layer dice model [12].

The spectral functions for the four stackings are presented in Fig. 5.6. We focus on the energies in the vicinity of the band-touching points and set $g/t = 1$. As one can see, there is a rather intricate pattern where the particle-hole symmetry is evidently broken for all stackings except the aligned one; see Figs. 5.6(a) and 5.6(e). Furthermore, the spectral functions explicitly show an asymmetry of the energy spectrum in the vicinity of the band touching points. The shape of the spectrum is noticeably different for the energies below and above the band crossing point for the hub-aligned $AB - BA - CC$ stacking which is related to its peculiar particle-hole asymmetric semi-Dirac spectrum; see Fig. 5.3 as well as Figs. 5.6(b) and 5.6(f). The Dirac point intersected with the tilted band can be inferred from Figs. 5.6(c) and 5.6(g) for the mixed $AA - BC - CB$ stacking. Finally, the asymmetry is related primarily to the additional C_3-corrugated band for the cyclic $AB - BC - CA$ stacking; see Figs. 5.6(d) and 5.6(h).

By integrating the spectral function over the Brillouin zone, we obtain the DOS in Fig. 5.7. As expected, the DOS has the simplest structure for the aligned $AA - BB - CC$ stacking and reveals the peaks corresponding to the flat bands at $\hbar\omega = \pm g$ as well as two sets of smaller peaks corresponding to the van Hove singularities; see Fig. 5.7(a). A similar structure of the DOS with well-pronounced peaks at $\hbar\omega = \pm g$ is observed for the hub-aligned $AB - BA - CC$ stacking with, however, different locations of the van Hove singularities; see Fig. 5.7(b). The DOS for the mixed $AA - BC - CB$ and cyclic $AB - BC - CA$ stackings has a rather complicated structure with several peaks and absent particle-hole symmetry. In both cases, there are peaks near $\hbar\omega = 0$ and $\hbar\omega = -g$, while the DOS at $\hbar\omega = g$ is suppressed. Unlike the aligned and hub-aligned stackings where the peaks at $\hbar\omega = \pm g$ are related to flat or partially flat (having a softer dispersion relation along one of the directions) bands, all peaks for the mixed and cyclic stackings correspond to the extrema in the energy spectrum. Another difference between these stackings is related to the particle-hole symmetry. The DOS for the aligned and hub-aligned stackings are particle-hole symmetric and demonstrate approximate particle-hole symmetry around the band-crossing points (see Appendix 5.8 for the results at larger g where the approximate symmetry becomes evident). On the other hand, there is no particle-hole symmetry of any form for the
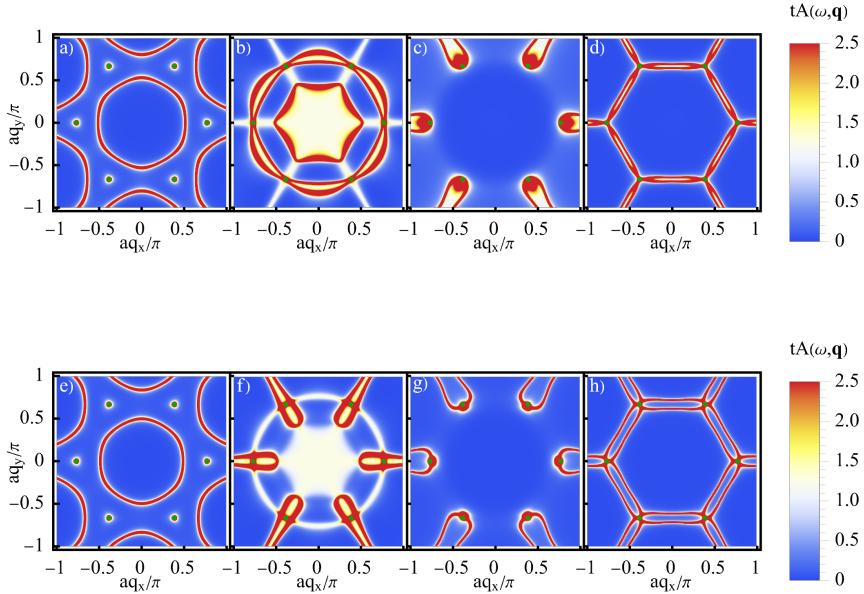
Figure 5.6. The spectral functions in the vicinity of the band-crossing points. The upper and lower panels correspond to $\hbar\omega/t = 0.9$ and $\hbar\omega/t = 1.1$, respectively. The columns represent the results for the aligned $AA - BB - CC$ (panels (a) and (e)), hub-aligned $AB - BA - CC$ (panels (b) and (f)), mixed $AA - BC - CB$ (panels (c) and (g)), and cyclic $AB - BC - CA$ (panels (d) and (h)) stackings. In all panels, we set $g = t$. We use tight-binding models with the spectral function defined in Eq. (5.31) and introduce a phenomenological broadening $\Gamma = 0.05\,t$ by replacing $i0 \to i\Gamma$ in the Green function.

mixed $AA - BC - CB$ and cyclic $AB - BC - CA$ stackings; this result persists also for larger g, see Appendix 5.8.

5.5   Summary

In this work, we introduced and classified the nonequivalent commensurate stackings for a bilayer dice ($\mathcal{T}_3$) lattice. These four stackings are the aligned $AA - BB - CC$, hub-aligned $AA - BC - CB$, mixed $AB - BA - CC$, and cyclic $AB - BC - CA$ stacking. Other stackings are either equivalent or non-commensurate. We found that the bilayer dice model demonstrates a unique energy spectrum for each of the stackings.
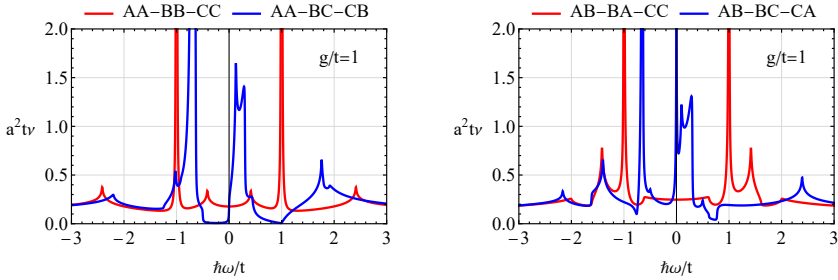
Figure 5.7. The density of states for bilayer dice lattices. Panel (a): aligned $AA - BB - CC$ (solid red line) and mixed $AA - BC - CB$ (dashed blue line). Panel (b): hub-aligned $AB - BA - CC$ (solid red line) and cyclic $AB - BC - CA$ (dashed blue line). For all stackings, we employed the tight-binding model with the spectral function defined in Eq. (5.31) and introduced the phenomenological broadening $\Gamma/t = 0.005$ by replacing $i0 \to i\Gamma$ in the Green function.

In all stackings considered in this work, three energy bands intersect at the K and K' points; the band-crossing points are separated in energy with the separation determined by the inter-layer coupling constant g. The spectrum of the aligned $AA - BB - CC$ stacking resembles that of two copies of the single-layer dice model and contains Dirac points intersected by a completely flat in the whole Brillouin zone band; see Fig. 5.2. The hub-aligned $AB - BA - CC$ stacking allows one to realize the semi-Dirac spectrum in the vicinity of the band-crossing points, for which the dispersion relation is quadratic in one direction and linear in the other; see Fig. 5.3. An unusual spectrum composed of a Dirac point intersected by a tilted anisotropic band occurs for the mixed $AA - BC - CB$ stacking; see Fig. 5.4. Somewhat similar to the case of the hub-aligned $AB - BA - CC$ stacking, all bands have a semi-Dirac spectrum. Finally, the cyclic $AB - BC - CA$ stacking realizes an anisotropic energy spectrum with a C_3-corrugated additional band intersecting the Dirac point; see Fig. 5.5. The low-energy spectrum, i.e., at $|\varepsilon| \ll g$, also depends on the stackings and shows either nodal-line crossings (aligned and hub-aligned stackings) or semimetallic behavior (mixed and cyclic stackings) where conduction and valence bands acquire the same energy but are separated in the Brillouin zone. Therefore, similar to multi-layer graphene structures, a multi-layer dice lattice also holds the potential to be a flexible platform for realizing different types of quasiparticle spectra.

To clarify the shape of the energy spectrum and set up the stage for analytical calculations, we derived effective low-energy models in the vicinity of the band-crossing points. The corresponding models are given in Eqs. (5.14), (5.16), (5.20), and (5.24). The energy spectrum of these models captures the main features of the tight-binding spectrum such as the anisotropy of the dispersion relation. Furthermore, the effective models allow us to introduce effective particle-hole symmetry with respect to the band-crossing points. In particular, both tight-binding and effective models are particle-hole symmetric for the aligned $AA - BB - CC$ stacking. While the tight-binding model is particle-hole symmetric, there is no particle-hole symmetry for the effective model of the hub-aligned $AB - BA - CC$ stacking. The other two stackings, i.e., the mixed $AA - BC - CB$ and cyclic $AB - BC - CA$ ones, both tight-binding and effective models are particle-hole asymmetric. The derived effective models might be useful in various applications including the studies of transport, collective modes, edge states, etc.

We used the obtained tight-binding models to calculate the spectral function and the DOS in Sec. 5.4; see Figs. 5.6 and 5.7. The spectral function provides an access to the cross-sections of the energy dispersion, which could become rather intricate for certain stackings. The nontrivial band structure of the bilayer dice model also has a direct manifestation in the DOS. In particular, the flat band of the aligned $AA - BB - CC$ stacking leads to peaks corresponding to the band-crossing points. The peaks are also observed for the hub-aligned $AB - BA - CC$ stacking due to a soft dispersion relation of the additional band. On the other hand, the DOS of the mixed $AA - BC - CB$ and cyclic $AB - BC - CA$ stackings is dominated by the van Hove singularities related to the features of the spectrum away from the band-crossing points. In solid-state realizations of the dice lattice, the spectral function and the DOS can be probed via angle-resolved photoemission and scanning tunneling spectroscopy experiments.

In the derivation of bilayer dice models, we have made a few simplifying assumptions related to the structure of the lattice and the coupling Hamiltonian. First, we considered only commensurate stackings where sublattices of both layers are aligned. In writing the coupling Hamiltonians (5.7), only the nearest-neighbor hopping and equal coupling constants for all sites were assumed. The breakdown of the symmetry between the A and B sublattices might lead to a few additional stackings. It would be

also interesting to investigate which of the proposed stackings is the most energetically favorable. These studies are beyond this work and will be reported elsewhere. Finally, we notice that the rich energy spectrum and nontrivial DOS promise unusual optical responses of bilayer dice lattices. The studies of the optical response will be presented in our forthcoming work [199].

5.6 Appendix: Derivation of the effective model

In this Section, we discuss the derivation of the effective low-energy Hamiltonians presented in Sec. 5.3.3; see also Ref. [185] for the corresponding discussion for bilayer graphene. We focus on the dynamics in the vicinity of band crossing points, i.e., at $|\varepsilon| \approx g$. Then, the off-diagonal terms in the Hamiltonian (5.8) with the coupling Hamiltonians defined in Eq. (5.7) are assumed to be large compared to the diagonal ones, i.e., $g/(\hbar v_F q) \gg 1$. In this case, it is convenient to transform the full Hamiltonian (5.8) into a new basis where the part of the Hamiltonian responsible for the interlayer coupling, i.e., the Hamiltonian (5.8) with $H(\mathbf{q}) = 0$, is diagonal. This allows us to separate the low- and high-energy (with respect to the band-crossing point at $\varepsilon = g$) parts of the full Hamiltonian as

$$H = \begin{pmatrix} h_{\mathrm{L}} & u \\ u^{\dagger} & h_{\mathrm{H}} \end{pmatrix}, \qquad (5.38)$$

where h_{L} and h_{H} correspond to low- and high-energy states, respectively. The coupling between them is denoted by u. Now, the off-diagonal terms are small compared to the diagonal ones. In the latter, it is convenient to separate

$$h_{\mathrm{L}} = h_{\mathrm{L}}^{(0)} + \delta h_{\mathrm{L}} \quad \text{and} \quad h_{\mathrm{H}} = h_{\mathrm{H}}^{(0)} + \delta h_{\mathrm{H}}. \qquad (5.39)$$

Here, $h_{\mathrm{L}}^{(0)}$ and $h_{\mathrm{H}}^{(0)}$ are large compared to δh_{L} and δh_{H}, respectively. In addition, we separate $\varepsilon = \varepsilon^{(0)} + \delta\varepsilon$. For the effective model for the Dirac point at $\varepsilon = g$, we have $h_{\mathrm{L}}^{(0)} = g\mathbb{1}_3$, $h_{\mathrm{H}}^{(0)} = -g\mathbb{1}_3$, and $\varepsilon^{(0)} = g$. The corrections δh_{L}, δh_{H}, and $\delta\varepsilon$ are determined by deviations from the band-crossing point, e.g., $\delta\varepsilon \sim \hbar v_F k$.

By using the eigenvalue equation $H\Psi = \varepsilon\Psi$ with H given in Eq. (5.38) and $\Psi = \{\psi_{\mathrm{L}}, \psi_{\mathrm{H}}\}$, we can re-express the high-energy states via the low-energy ones:

$$\psi_{\mathrm{H}} = (\varepsilon\mathbb{1}_3 - h_{\mathrm{H}})^{-1} u^{\dagger}\psi_{\mathrm{L}}. \qquad (5.40)$$

This allows us to write an equation for ψ_{L} only,

$$\left[h_{\mathrm{L}} + u\left(\varepsilon\mathbb{1}_3 - h_{\mathrm{H}}\right)^{-1}u^{\dagger}\right]\psi_{\mathrm{L}} = \varepsilon\psi_{\mathrm{L}}. \tag{5.41}$$

By using Eq. (5.39) and expanding up to the leading nontrivial order in deviations from the band-crossing point, we obtain

$$\left(\varepsilon\mathbb{1}_3 - h_{\mathrm{H}}\right)^{-1} = \left(\varepsilon^{(0)}\mathbb{1}_3 - h_{\mathrm{H}}^{(0)} + \delta\varepsilon\mathbb{1}_3 - \delta h_{\mathrm{H}}\right)^{-1}$$
$$\approx \left[1 - \left(\varepsilon^{(0)}\mathbb{1}_3 - h_{\mathrm{H}}^{(0)}\right)^{-1}\left(\delta\varepsilon\mathbb{1}_3 - \delta h_{\mathrm{H}}\right)\right]\left(\varepsilon^{(0)}\mathbb{1}_3 - h_{\mathrm{H}}^{(0)}\right)^{-1}. \tag{5.42}$$

This allows us to rewrite Eq. (5.41) as

$$\left\{h_{\mathrm{L}}^{(0)} - \varepsilon^{(0)}\mathbb{1}_3 + \delta h_{\mathrm{L}} + u\left[1 + \left(\varepsilon^{(0)}\mathbb{1}_3 - h_{\mathrm{H}}^{(0)}\right)^{-1}\delta h_{\mathrm{H}}\right] \times \tag{5.43}$$
$$\times \left(\varepsilon^{(0)}\mathbb{1}_3 - h_{\mathrm{H}}^{(0)}\right)^{-1}u^{\dagger}\right\}\psi_{\mathrm{L}} = \delta\varepsilon\left[\mathbb{1}_3 + u\left(\varepsilon^{(0)}\mathbb{1}_3 - h_{\mathrm{H}}^{(0)}\right)^{-2}u^{\dagger}\right]\psi_{\mathrm{L}}.$$

By introducing the wave function $\chi = S^{1/2}\psi_{\mathrm{L}}$, which has a proper norm, i.e., $\chi^{\dagger}\chi = \psi_{\mathrm{L}}^{\dagger}\psi_{\mathrm{L}} + \psi_{\mathrm{H}}^{\dagger}\psi_{\mathrm{H}}$, we rewrite Eq. (5.43) in the conventional form $H_{\mathrm{eff}}\chi = \delta\varepsilon\,\chi$. Therefore, the effective Hamiltonian reads

$$H_{\mathrm{eff}} = S^{-1/2}\left\{h_{\mathrm{L}}^{(0)} - \varepsilon^{(0)}\mathbb{1}_3 + \delta h_{\mathrm{L}}\right.$$
$$\left. + u\left[\mathbb{1}_3 + \left(\varepsilon^{(0)}\mathbb{1}_3 - h_{\mathrm{H}}^{(0)}\right)^{-1}\delta h_{\mathrm{H}}\right]\left(\varepsilon^{(0)}\mathbb{1}_3 - h_{\mathrm{H}}^{(0)}\right)^{-1}u^{\dagger}\right\}S^{-1/2}, \tag{5.44}$$

where

$$S = \mathbb{1}_3 + u\left(\varepsilon^{(0)}\mathbb{1}_3 - h_{\mathrm{H}}^{(0)}\right)^{-2}u^{\dagger}. \tag{5.45}$$

We use Eqs. (5.44) and (5.45) to derive the effective models in Sec. 5.3.3. While the calculations are straightforward, the intermediate expressions are bulky. Therefore, we do not present them here.

5.7   Appendix: Spectral functions at low energies $\hbar\omega = 0$

For the sake of completeness, let us also show the spectral function at $\hbar\omega = 0$ in Fig. 5.8. As one can see, the low-energy ($\varepsilon = 0$) spectrum demonstrates nodal rings either surrounding the K-points (aligned stacking) or the Γ-point (hub-aligned stacking); see Figs. 5.8(a) and 5.8(b). The mixed stacking is characterized by separated patches. The most intricate, Kagome, pattern occurs for the cyclic stacking shown in Fig. 5.8(d).
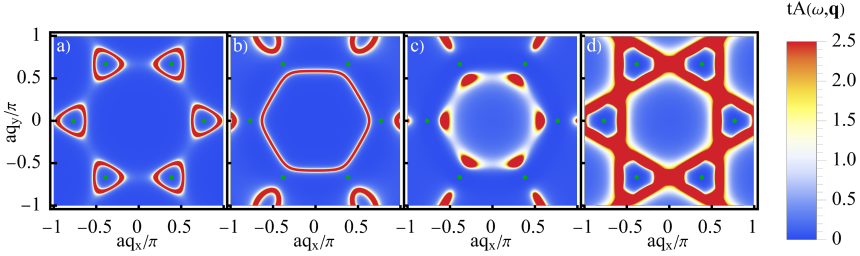
Figure 5.8. The spectral functions at $\hbar\omega = 0$. We used the aligned $AA - BB - CC$ (panel (a)), hub-aligned $AB - BA - CC$ (panel (b)), mixed $AA - BC - CB$ (panel (c)), and cyclic $AB - BC - CA$ (panel (d)) stackings. In all panels, we set $g = t$. Green points represent the positions of the band-crossing points. We use tight-binding models with the spectral function defined in Eq. (5.31) and introduce the phenomenological broadening $\Gamma = 0.05\,t$ by replacing $i0 \rightarrow i\Gamma$ in the Green function.

5.8   Appendix: Results for $g/t > 1$

Let us discuss the case of strong inter-layer coupling $g/t \gtrsim 1$. It corresponds to a somewhat exotic system where the inter-layer coupling constant g is larger than the in-layer hopping parameter t. Nevertheless, it might be relevant for artificial systems.

We show the energy spectrum and the DOS for the four nonequivalent stackings in Fig. 5.9. Compared to the case of smaller coupling constant, cf. with Figs. 5.2–5.5 and Fig. 5.7, the spectra and the DOS for the low- and high-energy parts of the tight-binding model do not overlap. The shape of the energy spectrum away from the band-crossing points becomes less relevant at larger g/t for the aligned $AA - BB - CC$ stacking. Further, the particle-hole symmetry with respect to the band crossing points becomes evident for the aligned $AA - BB - CC$ and hub-aligned $AB - BA - CC$ stackings; see Figs. 5.9(a), 5.9(e), 5.9(b), and 5.9(f). In agreement with the effective model, the anisotropy of the additional band is suppressed at larger g; cf. red lines in Figs. 5.9(b) and 5.9(f). The particle-hole asymmetry and complicated structure of the DOS remain for the mixed $AA - BC - CB$ and cyclic $AB - BC - CA$ stackings; see Figs. 5.9(c), 5.9(g), 5.9(d), and 5.9(h).
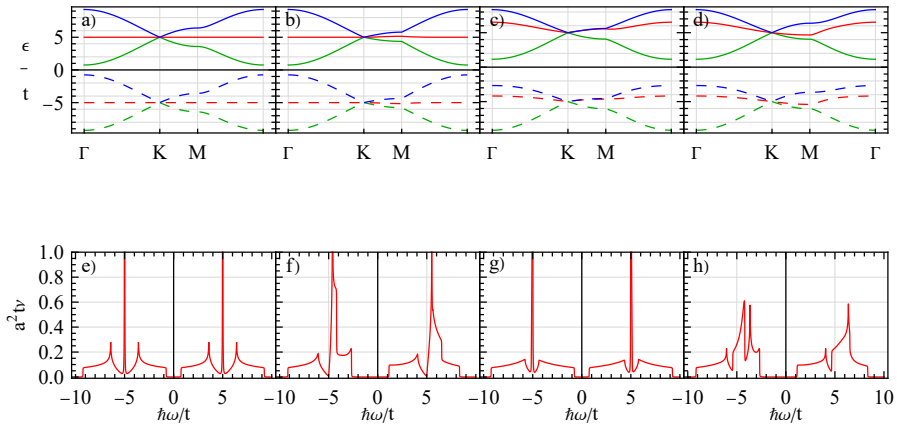
Figure 5.9. The energy spectrum (top row) and the corresponding DOS (bottom row) for the tight-binding Hamiltonian (5.8) along the $\Gamma - K - M - \Gamma$ line in the Brillouin zone at $g/t = 5$. The columns represent the results for the aligned $AA - BB - CC$ (panels (a) and (e)), hub-aligned $AB - BA - CC$ (panels (b) and (f)), mixed $AA - BC - CB$ (panels (c) and (g)), and cyclic $AB - BC - CA$ (panels (d) and (h)) stackings.

Chapter 6

Orbital susceptibility of T-graphene: Interplay of high-order van Hove singularities and Dirac cones

6.1 Introduction

Possible existence of two new graphene allotropes, planar tetragraphene (or octagraphene) and buckled T-graphene composed of carbon octagons with tetrarings, was demonstrated some time ago using the Density Functional Theory (DFT) [52]. Several previous attempts to find such allotropes were made in Refs.[201, 202]. It was noted that planar T-graphene allotrope should be the most stable one after graphene while the buckled T-graphene is not stable, and its fully relaxed state is very similar to planar T-graphene [179]. Recently, the tetragraphene allotrope has been predicted to possess superconductivity with critical temperature up to around 20.8 K [203].

Some geometrical and electronic properties, as well as low-energy physics of octagraphene were studied in Ref.[204], the phase diagrams were analyzed and the existence of Mott metal-insulator phase transitions in the Hubbard model on square-octagon lattice was pointed out in [205–209]. In addition, structural and electronic properties of T-graphene and its modifications were studied by DFT calculations in Refs.[210–213] and the kinetic stability with time was analyzed in Ref.[214]. Later, it was shown

[53] that the 2D monolayers of Zn_2O_2 and Zn_4O_4 also have nearly ideal square-octagon lattice. In recent paper [53] the stability of multilayer materials such as ZnO composed of square-octagon lattice was studied with the help of DFT technique. Also it was shown that MoS_2 transition metal dichalcogenide with square-octagon lattice can possess Dirac fermions with Fermi velocity comparable to that of graphene [207]. The coexistence of Dirac fermions and nearly flat bands seems to be a very interesting property of square-octagon lattice and motivates us to study physical quantities such as orbital susceptibility in terms on newly introduced concept of high-order van Hove singularities [25].

As is known, when the doping level approaches VHS, system can exhibit strong responses such as orbital paramagnetism in two-dimensional case [50] or chiral superconductivity in the case of graphene [26]. An *ordinary* VHS in two-dimensional electron system corresponds to logarithmic divergence of the density of states (DOS). The distinctive feature of high-order VHS is a more singular, power-law divergence of DOS with an asymmetric peak [25, 215]. At the same time, the recent studies of two-dimensional lattices uncovered a wide family of exotic band structures [15] with flat bands and multi-band touching points, at which the quasiparticles are effectively described by high-pseudospin Hamiltonians. Flat bands can be considered as a limiting case of VHS with delta-function divergence of DOS.

The prominent examples of materials with high-order VHS of different kind are bilayer graphene with tuned dispersion with the help of an interlayer voltage bias [216], $Sr_3Ru_2O_7$ [217] and $\beta - YbAlB_4$ [218]. Recently it was also shown that when a high-order VHS is placed close to the Fermi level, density wave, Pomeranchuk orders, and superconductivity can all be enhanced [27]. The role of high-order VHS on different types of instabilities in twisted bilayer graphene was analyzed in Ref.[219]. The presence of van Hove singularities in twisted bilayer graphene [220] can lead to valley magnetism [221], density waves and unconventional superconductivity [222] such as topological and nematic superconductivity [223], the so-called "high-T_c" phase diagram [28], Kohn-Luttinger superconductivity [224].

The orbital susceptibility [225] measures the response of a time-reversal invariant electronic system to an external magnetic field. To evaluate susceptibility of T-graphene analytically and numerically we use the formulas for susceptibility derived in Refs.[226] and [227]. We analyze the
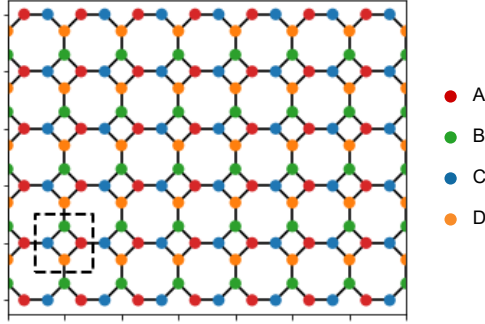
Figure 6.1. T-graphene lattice structure, which is described in main text. Each sublattice is denoted by its own color. Black dashed rectangle encircles one elementary cell. The hopping parameters between two small squares are t_1 and inside each small square - t_2.

role of VHS of both kinds in orbital susceptibility for electrons on square-octagon lattice. Particularly, we show that the flat lines in tight-binding band structure, which were firstly mentioned in Ref.[206], also represent high-order VHS with inverse square root divergence of DOS.

The paper is organized as follows. In Sec.6.2 we describe the tight-binding Hamiltonian of square-octagon lattice. Then, in Sec.6.3 we derive effective low-energy Hamiltonians that describe bands around highly-symmetric points in Brillouin zone (BZ). Also we identify the type of VHS which are present in T-graphene. In Sec.6.4 we perform numerical evaluation of susceptibility, and then analyze the qualitative physical effects of Dirac cones (Sec.6.4.2) and VHS using effective low-energy expansion (Secs. 6.4.3 and 6.4.4). The role of high-order VHS is discussed also in the Conclusions (Sec.6.5) where we summarize the obtained results. In Appendix 6.6 we analyze flat lines in the dispersion of middle bands, and in Appendix 6.7 we present expressions for the Green's functions of tight-binding and Löwdin Hamiltonians.

6.2   Tight-binding model

The square-octagon lattice consists of four atoms per unit cell which form a small square, and is shown on Fig.6.1. According to Ref.[202], the numerical values for all nearest neighbor interatomic distances are approximately equal to 1.429Å and lattice constant $a = 3.47$Å for T-graphene. Ref.[204]

gives the intra-square, 1.48Å, and inter-squares, 1.35Å, distances, and similar values were reported in Ref.[53]. The basis vectors of Bravais lattice and reciprocal lattice are

$$\boldsymbol{a}_1 = (a,\ 0), \quad \boldsymbol{a}_2 = (0,\ a);$$
$$\boldsymbol{b}_1 = \left(0,\ \frac{2\pi}{a}\right), \quad \boldsymbol{b}_2 = \left(\frac{2\pi}{a},\ 0\right). \tag{6.1}$$

In the tight-binding model, we take hopping parameters between atoms in two neighboring small squares to be t_1, and inside small square t_2. The corresponding tight-binding Hamiltonian has the form [204, 206]

$$H_{Tg}(\boldsymbol{k}) = - \begin{pmatrix} 0 & t_2 & t_1 e^{ik_x a} & t_2 \\ t_2 & 0 & t_2 & t_1 e^{ik_y a} \\ t_1 e^{-ik_x a} & t_2 & 0 & t_2 \\ t_2 & t_1 e^{-ik_y a} & t_2 & 0 \end{pmatrix}. \tag{6.2}$$

and acts on the four-component wave functions $\psi = (\psi_A, \psi_B, \psi_C, \psi_D)$ (see Fig.6.1 for sublattice labels). The above mentioned difference in interatomic distances can effectively described by tuning the hopping parameters t_1 and t_2. The values of these hopping parameters can be taken from DFT calculations: $t_1 = 2.9\,\text{eV}$ and $t_2 = 2.5\,\text{eV}$ were used in Ref.[204], while $t_1 = 2.98\,\text{eV}$ and $t_2 = 2.68\,\text{eV}$ were found from DFT calculations inside one layer of octagraphene [228].

The spectrum can be found from the equation $\det[\varepsilon\mathbb{I} - H_{Tg}(\boldsymbol{k})] = 0$, which after simplification reduces to [204, 206]

$$\varepsilon^4 - 2\left(t_1^2 + 2t_2^2\right)\varepsilon^2 + 4t_1 t_2^2 \varepsilon\left(\cos\left(ak_x\right) + \cos\left(ak_y\right)\right) -$$
$$- 4t_1^2 t_2^2 \cos\left(ak_x\right)\cos\left(ak_y\right) + t_1^4 = 0, \tag{6.3}$$

and has the form of depressed quartic equation. The spectrum is symmetric with respect to rotations on the angle $\frac{\pi}{4}$ in k-space, because the lattice has a C_4 point symmetry group. Also the spectrum is symmetric with respect to transformations $\varepsilon \to -\varepsilon$ together with $k_x \to k_x \pm \frac{\pi}{a}$, $k_y \to k_y \pm \frac{\pi}{a}$ (called chiral symmetry in [206]). The Brillouin zone of square-octagon lattice is a square with $-\frac{\pi}{a} < k_x,\ k_y < \frac{\pi}{a}$. The corresponding highly-symmetric points are defined as

$$\Gamma = (0,0), \quad M = \left(\pm\frac{\pi}{a}, \pm\frac{\pi}{a}\right),$$
$$X = \left(\pm\frac{\pi}{a}, 0\right),\ \left(0, \pm\frac{\pi}{a}\right), \tag{6.4}$$
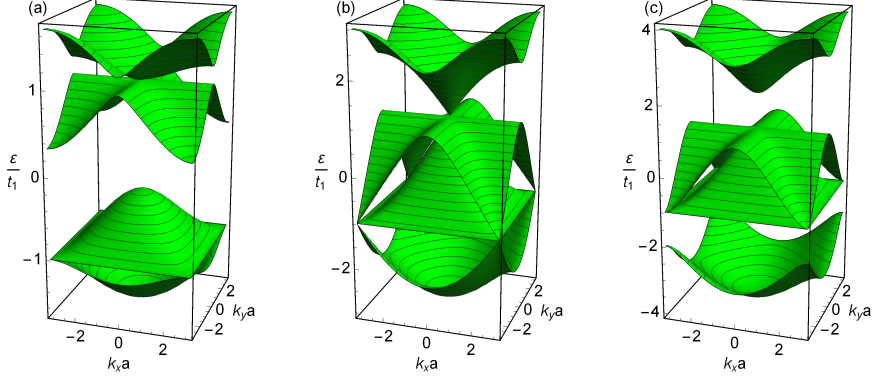
Figure 6.2. Spectrum which is given by Eq.(6.3) for three values of parameter
$\alpha = t_2/t_1$: panel (a) $\alpha = \frac{1}{3}$, panel (b) $\alpha = 1$ and panel (c) $\alpha = \frac{3}{2}$. The energy ε is
measured in units of hopping parameter t_1. On the panel (b) one can observe the
three-band-touching points where the two Dirac cones meet nearly flat middle
band. Black lines denote the lines of constant energies.

and are located in the center, corners and the middle of each square site,
respectively. It is convenient to measure the energy in terms of t_1 hopping
parameter, and introduce the dimensionless ratio of hopping parameters
$\alpha = t_2/t_1$. The 3D plots of the spectrum defined by Eq.(6.3) for several
values of α are shown in Fig.6.2, while the 2D plots along highly-symmetric
lines are represented in Fig.6.3. For $\alpha = 1$, near the three-band-touching
points Γ and M, one observes almost flat middle bands [206]. These two
middle bands support completely flat energy lines, which are extended over
full BZ. Below we proceed with description of highly-symmetric points in
terms of van Hove singularities in the DOS.

6.3 Spectrum structure around highly-symmetric points: van Hove singularities

Firstly, let us present general definitions that will be used throughout the
text. By definition, the one-electron DOS per spin is given by

$$D(\varepsilon) = \sum_{i=1}^{4} \int_{BZ} \frac{d^2k}{(2\pi)^2} \delta\left[\varepsilon - \varepsilon_i(\mathbf{k})\right], \tag{6.5}$$

with i running over the band dispersions $\varepsilon_i(\boldsymbol{k})$ found from Eq.(6.3). Due
to chiral symmetry the DOS is an even function of energy. The ordinary

VHS with the logarithmic diverging DOS occurs at saddle point $\boldsymbol{k}_s$ of a particular band in which

$$\nabla_{\mathbf{k}}\varepsilon(\mathbf{k}) = \mathbf{0} \text{ and } \det \mathcal{D} < 0, \tag{6.6}$$

where $\mathcal{D}_{ij} \equiv \frac{1}{2}\partial_i\partial_j\varepsilon(\mathbf{k})$ is the 2×2 Hessian matrix of a dispersion $\varepsilon(\mathbf{k})$ at $\boldsymbol{k}_s$. Here and below we use short-hand notation $\partial_i = \partial_{k_i}$. After proper rotation of a basis, the dispersion around saddle point can be conveniently represented as $\varepsilon - \varepsilon_s \approx -\zeta p_x^2 + \beta p_y^2$ with wave vector deviation $\mathbf{p} = \mathbf{k} - \mathbf{k}_s$. The two coefficients ζ and β are the eigenvalues of $\mathcal{D}$ and satisfy the condition $-\zeta\beta = \det \mathcal{D} < 0$.

The high-order VHS corresponds to saddle point with the following properties [25]:

$$\nabla_{\mathbf{k}}\varepsilon = \mathbf{0} \text{ and } \det \mathcal{D} = 0. \tag{6.7}$$

This class of VHS can be divided into two types: $\zeta = \beta = 0$ (multicritical VHS), or $\zeta \neq 0$, $\beta = 0$. The DOS is expected to have a power-law divergence at such points. The position of all VHS can be found by differentiating Eq.(6.3) and setting $\nabla_{\mathbf{k}}\varepsilon = 0$, from which we get the system of equations:

$$\begin{aligned} \sin(ak_x)\left(\varepsilon - t_1\cos(ak_y)\right) = 0, \\ \sin(ak_y)\left(\varepsilon - t_1\cos(ak_x)\right) = 0. \end{aligned} \tag{6.8}$$

Below we perform expansion of the energy spectrum of T-graphene around highly-symmetric points and flat lines and identify the corresponding VHS type with the DOS divergence.

6.3.1 Γ and M points

Before proceeding with calculation, we underline that previously mentioned symmetry of spectrum makes these two points equivalent up to change of energy sign. Thus, the analysis around the Γ point can be directly translated to the M point and vice versa by chiral symmetry.

To find the approximate expressions for band energies around highly-symmetric points, we perform the series expansion of spectral equation (6.3). We write $\varepsilon = \varepsilon_i^{(0)} + \delta$, with $\varepsilon_i^{(0)}$ is the energy of i-th band exactly at the given point in k-space. Then, we expand equation into series in δ and $\boldsymbol{k}a$ (measured from the given point), and find the solution for δ in

leading order. Performing this for Γ point, we find the following results in the case $\alpha > 1$:

$$\frac{\varepsilon_1}{t_1} \approx -1 - 2\alpha + \frac{\alpha|\boldsymbol{k}|^2 a^2}{4(\alpha+1)}, \tag{6.9}$$

$$\frac{\varepsilon_{2,3}}{t_1} \approx 1 - \frac{a^2\alpha}{4(\alpha^2-1)}\left[\alpha|\boldsymbol{k}|^2 \pm \sqrt{\left(\alpha^2|\boldsymbol{k}|^4 - 4(\alpha^2-1)k_x^2 k_y^2\right)}\right], \tag{6.10}$$

$$\frac{\varepsilon_4}{t_1} \approx -1 + 2\alpha + \frac{\alpha|\boldsymbol{k}|^2 a^2}{4(\alpha-1)}. \tag{6.11}$$

The numbering of bands goes from the lower one to the upper one (for $\alpha < 1$ the indices 2 and 4 should be interchanged). From expression (6.9) one can conclude that spectrum of tight-binding Hamiltonian (6.2) is bounded by $-1 - 2\alpha < \varepsilon < 1 + 2\alpha$ at zero temperature. In particular, it follows from Eq.(6.10) that the top of band ε_3 has completely flat lines along k_x and k_y axes.

In the case $\alpha = 1$ we find the following expansions for three upper bands (which have triply degenerate point (see also Ref.[206])):

$$\frac{\varepsilon_1}{t_1} \approx -3 + \frac{1}{8}a^2|\boldsymbol{k}|^2, \quad \frac{\varepsilon_3}{t_1} \approx 1 - \frac{k_x^2 k_y^2 a^2}{2|\boldsymbol{k}|^2}, \quad \frac{\varepsilon_{2,4}}{t_1} \approx 1 \pm \frac{a}{\sqrt{2}}|\boldsymbol{k}| - \frac{a^2\left(k_x^2 - k_y^2\right)^2}{16|\boldsymbol{k}|^2}. \tag{6.12}$$

The two bands $\varepsilon_{2,4}$ form Dirac cones with Fermi velocity $v_F = at_1/\sqrt{2}\hbar$ with additional square-order corrections in $|\boldsymbol{k}|a$. The middle band ε_3 is completely flat in first-order approximation, but has nontrivial anisotropic corrections of second-order in $|\boldsymbol{k}|a$.

The Γ and M points define the energy boundaries of each band (see Fig.6.2). For $\alpha \leq 1$ the bands are in the ranges $[-1 - 2\alpha, -1]$, $[-1, -1 + 2\alpha]$, $[1 - 2\alpha, 1]$, $[1, 1 + 2\alpha]$ measured in units of t_1. It follows from the expansions (6.9)-(6.11) taken at $\boldsymbol{k} = 0$. We find that the gap near $\varepsilon = 0$ opens for $\alpha < 1/2$. For the $\alpha \geq 1$ the bands' energy ranges are $\varepsilon/t_1 \in [-1 - 2\alpha, 1 - 2\alpha]$, $[-1, 1]$ for both middle bands, and $[-1 + 2\alpha, 1 + 2\alpha]$. In this case the gaps are opened for $\alpha > 1$ above $\varepsilon = t_1$ and below $\varepsilon = -t_1$, respectively. These features of spectrum are manifested in vanishing DOS in corresponding gap energy ranges, see Fig.6.3.

Next, we identify the type of VHS at $\varepsilon_3 = t_1$ in $\alpha = 1$ case. For this purpose, we evaluate the DOS contribution for each band separately, taking the leading term in wavevector expansion. The integration over

wavevector in Eq.(6.5) is extended to cut-off parameter Λ of effective expansions (6.12). Then, the Dirac cones give the standard graphene-like result:

$$D_2(\varepsilon) + D_4(\varepsilon) = \frac{|\varepsilon - t_1|}{\pi a^2 t_1^2}. \tag{6.13}$$

The evaluation of DoS for middle nearly flat band is more complicated, but can be performed in polar coordinates:

$$D_3(\varepsilon \lesssim t_1) = \int_0^\Lambda \int_0^{2\pi} \frac{kdkd\phi}{(2\pi)^2} \delta\left[\varepsilon - t_1 + t_1 \frac{k^2 a^2 \sin^2(2\phi)}{8}\right]. \tag{6.14}$$

We emphasize the fact that the middle band contributes only for $\varepsilon < t_1$ and the corresponding DOS is asymmetric. The integration over k is easily performed, and the integration over angle can be confined to first quadrant with adding a total factor 4. Then, one should integrate in the limits where the solutions under delta-function are possible $\phi_{min} < \phi < \phi_{max}$:

$$\phi_{min} = \frac{1}{2}\arcsin\left(\sqrt{\frac{8(1 - \varepsilon/t_1)}{\Lambda^2 a^2}}\right), \ \phi_{max} = \frac{\pi}{2} - \frac{1}{2}\arcsin\left(\sqrt{\frac{8(1 - \varepsilon/t_1)}{\Lambda^2 a^2}}\right). \tag{6.15}$$

Thus, the integral for DOS becomes

$$D_3(\varepsilon \lesssim t_1) = \frac{1}{t_1 a^2} \int_{\phi_{min}}^{\phi_{max}} d\phi \frac{4}{\sin^2(2\phi)} \approx \frac{2}{t_1 a} \frac{\Lambda}{\sqrt{2(1 - \varepsilon/t_1)}}. \tag{6.16}$$

with the $1/\sqrt{1 - \varepsilon/t_1}$ divergence, as was noted previously. This power-law divergence together with asymmetry of the DOS clearly indicates, that this point corresponds to high-order VHS (see middle peaks of the DOS in all panels of Fig.6.3). Below we show that this holds true for all points on flat lines in the dispersion $\varepsilon_3(\mathbf{k})$. Also one should note that this singularity has larger exponent $\kappa = 1/2$ (which is defined as $D_3(\varepsilon \leq t_1) \sim |t_1 - \varepsilon|^{-\kappa}$) than in twisted bilayer graphene ($\kappa = 1/4$, [25]), and the same as in $Sr_3Ru_2O_7$ [217] and $\beta - YbAlB_4$ [218] materials.

Above we have found the long wavelength expansions of spectrum for small values of wavevector $\mathbf{k}$. However, these expansions are violated if the model parameter α approaches 1. In this case we can use another series expansion of the spectrum: we assume that $|1 - \alpha| \sim |\mathbf{k}a|$ are of the
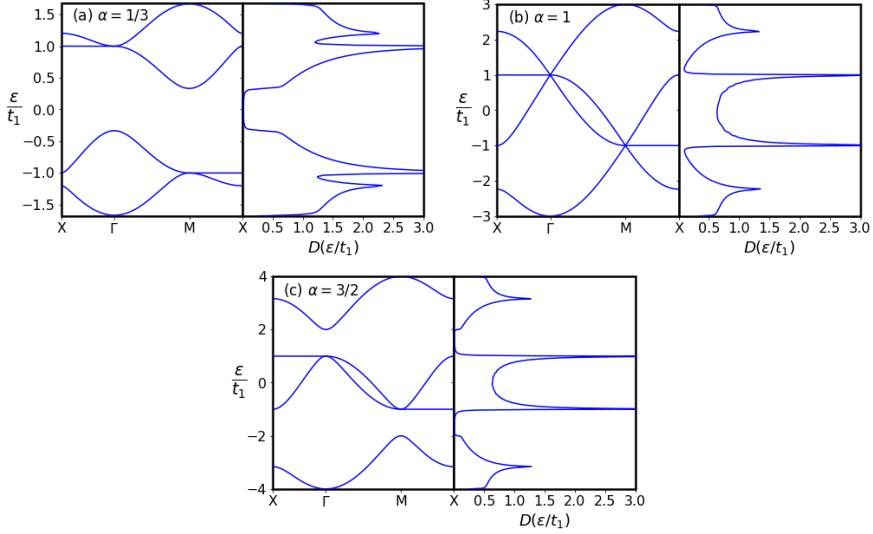
Figure 6.3. The spectrum of T-graphene along the closed path $X - \Gamma - M - X$ and DOS for $\alpha = 1/3, 1$ and $\alpha = 3/2$. DOS is plotted on the right of each spectrum, and is measured in units of $\frac{1}{a^2 t_1}$. DOS is regularized with finite broadening of levels, $\Gamma = 0.01 t_1$ to make plots smooth.

same order. Then, we replace both terms $|1 - \alpha|$ and $|ka|$ in Eq.(6.3) with $\zeta|1 - \alpha|$ and $\zeta|ka|$, respectively, and expand the obtained equation into powers of ζ. This guaranties that expansions keep contributions from both small values $|1 - \alpha|$ and $|ka|$ in the same leading order. Next, we solve the approximate spectral equation around each band, as for Eqs.(6.9)-(6.11), and set finally $\zeta = 1$, we find

$$\frac{\varepsilon_1}{t_1} = -1 - 2\alpha + \frac{(k_x^2 + k_y^2)a^2}{8}, \quad \frac{\varepsilon_3}{t_1} = 1 - \frac{k_x^2 k_y^2 a^2}{2(k_x^2 + k_y^2)},$$

$$\frac{\varepsilon_{2,4}}{t_1} = 1 - \left((1 - \alpha) \pm \sqrt{\frac{(k_x^2 + k_y^2)a^2}{2} + (1 - \alpha)^2} \right). \tag{6.17}$$

The last two expressions show that the $|1 - \alpha|$ competes with $|k|a$ and their larger value defines the spectrum form in the leading order.

6.3.2 X-points and flat lines

At X point the eigenvalues of Hamiltonian (6.2) are

$$\varepsilon_{1,4}^X = \mp t_1\sqrt{1 + 4\alpha^2}, \quad \varepsilon_{2,3}^X = \mp t_1. \tag{6.18}$$

The energies $\varepsilon_{1,4}$ belong to lower and upper and bands, respectively, and the energies $\varepsilon_{2,3}$ belong to flat lines for the points in k-space, which are situated in the middle between band-touching points. In Appendix 6.6 we show how the flat lines are related to the C_4 point symmetry group of the lattice and structure of tight-binding Hamiltonian. Performing the series expansion of spectral equation in the same way as discussed above Eq.(6.9) but for wavevectors around $X = (0, \frac{\pi}{a})$, we find:

$$\varepsilon_1 \approx \varepsilon_1^X + \frac{t_1 a^2}{4}\left[k_x^2\left(1 + \frac{t_1}{\varepsilon_1^X}\right) - \left(k_y - \frac{\pi}{a}\right)^2\left(1 - \frac{t_1}{\varepsilon_1^X}\right)\right], \tag{6.19}$$

$$\varepsilon_4 \approx \varepsilon_4^X + \frac{t_1 a^2}{4}\left[k_x^2\left(1 + \frac{t_1}{\varepsilon_4^X}\right) - \left(k_y - \frac{\pi}{a}\right)^2\left(1 - \frac{t_1}{\varepsilon_4^X}\right)\right]. \tag{6.20}$$

These two dispersion relations represent ordinary VHS, defined via the conditions (6.6). The Hessian matrix is diagonal and its' elements are the derivatives of above dispersion relations with respect to wavevectors, $\mathcal{D} = \text{diag}(\partial_{xx}\varepsilon, \partial_{yy}\varepsilon)$. The DOS exhibits a logarithmic divergence around $\varepsilon = \varepsilon_1^X$ and $\varepsilon = \varepsilon_4^X$: $D_{1,4}(\varepsilon) \sim \log\left(\frac{\Lambda a^2 t_1}{|\varepsilon - \varepsilon_{1,4}^X|}\right)$. These upper and lower peaks in DOS are clearly visible on Fig.6.3.

Next, we find the series expansion of $\varepsilon_{2,3}$ bands' dispersion around X point. Due to chiral symmetry mentioned after Eq.(6.3), it suffices to make expansion only for upper band, while for lower band it can be found by appropriate change of wavevectors. Expanding the spectral equation (6.3) for third band around energy $\varepsilon_3 = t_1$ into series in $k_x a$, we find:

$$\varepsilon_3 \approx t_1 - t_1\left[\frac{k_x^2 a^2}{2} - \frac{k_x^4 a^4}{4\alpha^2(1 - \cos(k_y a))}\right]. \tag{6.21}$$

This approximation works well only for $\frac{k_x^4 a^4}{4\alpha^2(1-\cos(k_y a))} < \frac{k_x^2 a^2}{2}$, since this band has $\varepsilon_3 \leq t_1$ energy for all points in BZ. The Hessian matrix for the dispersion (6.21) has only one nonzero component on diagonal $\mathcal{D} = \text{diag}\left(-\frac{t_1 a^2}{2}, 0\right)$. Thus, we observe that the middle bands at X-point and

in other points of flat line where $1 - \cos(k_y a) \neq 1$ exhibit a high-order saddle point ($\det \mathcal{D} = 0$). One can check that the DOS for dispersion (6.21) has a inverse square root divergence $1/\sqrt{t_1 - \varepsilon}$ with energy, with benchmark asymmetry:

$$D_3(\varepsilon \lesssim t_1) = \int \frac{d^2k}{(2\pi)^2} \delta \left[\varepsilon - t_1 \left(1 - \frac{k_x^2 a^2}{2} \right) \right] = \frac{\Lambda}{\sqrt{2}\pi^2 a t_1 \sqrt{1 - \varepsilon/t_1}}. \tag{6.22}$$

In Fig.6.3 we present dispersion relations for T-graphene along the path $X - \Gamma - M - X$ which represents the main features in spectrum (left part of each panel) and DOS (regularized by finite level broadening, right part of each panel) for the values $\alpha = 1/3$, 1 and $\alpha = 3/2$. Note that the path length in $M - \Gamma$ direction is $\sqrt{2}$ times larger than that in $X - M$ or $\Gamma - X$ directions. Our plots show that at energies $\mp t_1 \sqrt{1 + 4\alpha^2}$ DOS exhibits logarithmic divergences, which are the standard VHS at X points. At the same time, the much stronger peaks in DOS correspond to flat lines in spectrum at energies $\mp t_1$ which are 'high-order' VHS. Our results for spectra agree with the results of Refs.[204–206], however, the dispersion ε_3 in Eq.(6.12) was not recognized as the one exhibiting high-order VHS.

Fig.6.3 demonstrates also evolution of DOS as the function of the hopping parameter α. At $\varepsilon = 0$ we find that for $\alpha < 1/2$ there are no states (insulating phase), while for larger α the states are present. For energies $|\varepsilon| < t_1$ the DOS is always finite for $\alpha > 1/2$ meaning metallic behavior. On the other hand, for energies $|\varepsilon| > t_1$ and $\alpha > 1$ we observe the presence of gaps in the DOS.

In Sec.6.4 we will study the behavior of orbital susceptibility around van Hove singularities.

6.3.3 Effective models of band touching point: linear and quadratic approximations

In the tight-binding model of square-octagon lattice the band touching exists at two highly-symmetric points - Γ and M. Since they are related by chiral symmetry (see discussion after Eq.(6.3)), we need to build an effective Hamiltonian only at one of these points. As was proposed in Ref.[206], one can perform a rotation to C_{4v} basis utilizing the following

unitary matrix

$$U_{C_{4v}} = \frac{1}{2} \begin{pmatrix} 1 & \sqrt{2} & 0 & 1 \\ 1 & 0 & \sqrt{2} & -1 \\ 1 & -\sqrt{2} & 0 & 1 \\ 1 & 0 & -\sqrt{2} & -1 \end{pmatrix}, \tag{6.23}$$

which acts on four-component wave functions in sublattice space, defined below Eq.(6.2). After such unitary transformation we obtain the following first-order effective $SU(3)$ Hamiltonian near the Γ point:

$$H_{SU(3)}^{(1)} = t_1 \begin{pmatrix} 1 & 0 & -\frac{iak_x}{\sqrt{2}} \\ 0 & 1 & \frac{iak_y}{\sqrt{2}} \\ \frac{iak_x}{\sqrt{2}} & -\frac{iak_y}{\sqrt{2}} & 2\alpha - 1 \end{pmatrix}. \tag{6.24}$$

This Hamiltonian is useful for understanding how the Dirac cones emerge in spectrum for $\alpha = 1$. The spectrum defined by this Hamiltonian is

$$\frac{\varepsilon_0}{t_1} = 1, \quad \frac{\varepsilon_\pm}{t_1} = \alpha \pm \sqrt{\frac{a^2|\mathbf{k}|^2}{2} + (\alpha - 1)^2}, \tag{6.25}$$

where ε_0 corresponds to the ε_3 band of tight-binding model, and $\varepsilon_{-,+}$ to the bands $\varepsilon_{2,4}$ respectively. The corresponding eigenvectors are

$$\Psi_0 = \frac{1}{|\mathbf{k}|} \left(k_y, k_x, 0 \right),$$

$$\Psi_- = \frac{(ik_x a, -ik_y a, \sqrt{2}(1 - \varepsilon_-))}{\sqrt{2 \left(|\mathbf{k}|^2 a^2 + 2(1 - \alpha)(1 - \varepsilon_-) \right)}},$$

$$\Psi_+ = \frac{(-ik_x a, ik_y a, \sqrt{2}(\varepsilon_+ - 1))}{\sqrt{2 \left(|\mathbf{k}|^2 a^2 + 2(\alpha - 1)(\varepsilon_+ - 1) \right)}}. \tag{6.26}$$

One should note that the linear Hamiltonian of such type does not capture the spectral structure of middle band. Instead, the middle band is treated as completely flat, and the corresponding effective theory is an example of pseudospin-1 fermion models (see Ref.[229] for topological classification of such theories). Since the aim of present paper is to analyze the role of high-order VHS, we need to build the effective Hamiltonian that correctly captures the dispersion of middle band at leading order in $|\mathbf{k}|a$. The needed dispersion is presented, for example, in Eq.(6.12) in the $\alpha = 1$ case.

To find corresponding effective Hamiltonian, we use Löwdin method [230], which is also called Löwdin partitioning (the example calculation for Lieb-kagome Hamiltonian was performed in Ref.[231]). The idea is to perform the rotation of the full tight-binding Hamiltonian (6.2) via the unitary transformation (6.23), and then represent it in a block-like form:

$$H = \left(\begin{array}{c|c} H_{\alpha\alpha} & H_{\alpha\beta} \\ \hline H_{\beta\alpha} & H_{\beta\beta} \end{array} \right), \tag{6.27}$$

where the α subspace describes $SU(3)$ band-touching and β subspace corresponds to lower band, decoupled from other three bands by relatively large gap. Then, the effective second-order Hamiltonian around band-touching is written as

$$\mathcal{H}_\alpha = H_{\alpha\alpha} + H_{\alpha\beta} \left(\varepsilon_0 - H_{\beta\beta}\right)^{-1} H_{\beta\alpha}, \tag{6.28}$$

where $\varepsilon_0 = \varepsilon_{2,3}(\boldsymbol{k} = 0) = t_1$. For Γ point this Hamiltonian has the following form

$$H_{SU(3)}^{(2)} = \hat{\varepsilon}^{(0)} + t_1 \left(\begin{array}{ccc} -\frac{a^2(2\alpha+1)k_x^2}{4(\alpha+1)} & \frac{a^2 k_x k_y}{4(\alpha+1)} & -\frac{iak_x}{\sqrt{2}} \\ \frac{a^2 k_x k_y}{4(\alpha+1)} & -\frac{a^2(2\alpha+1)k_y^2}{4(\alpha+1)} & \frac{iak_y}{\sqrt{2}} \\ \frac{iak_x}{\sqrt{2}} & -\frac{iak_y}{\sqrt{2}} & \frac{\boldsymbol{k}^2 a^2}{4} \end{array} \right), \tag{6.29}$$

where $\hat{\varepsilon}^{(0)} = t_1 \text{diag}(1, 1, 2\alpha-1)$. Such simple Hamiltonian is particularly useful when the proper dispersion of all three bands is needed at leading order.

6.4   Orbital susceptibility

In this section we study the manifestation of T-graphene spectrum features considered above, in particular, VHS of both kinds, in the orbital susceptibility. The susceptibility measures the response of a electronic system to an external magnetic field and is defined standardly as the second derivative of the grand canonical potential at zero field. The main formula, which is most suitable in our case for numerical calculation, was given in Ref.[232], the more general formula was derived in Ref.[227]. The susceptibility can be represented as

$$\chi_{\text{orb}}\left(\mu, T\right) = -\frac{\mu_0 e^2}{12\hbar^2} \frac{\text{Im}}{\pi S} \int_{-\infty}^{\infty} n_{\text{F}}(\varepsilon) \, \text{Tr} \, \hat{X} \mathrm{d}\varepsilon. \tag{6.30}$$

Here $n_F(\varepsilon) = 1/(e^{(\varepsilon-\mu)/T} + 1)$ is the Fermi distribution, $\mu_0 = 4\pi \times 10^{-7}$ in SI units and S is the area of the sample. The operator $\hat{X}$ is written in terms of zero-field Green function $G(\boldsymbol{k})$ and Bloch Hamiltonian $H(\boldsymbol{k})$, and $\partial_{x,y}$ are partial derivatives over momenta:

$$\hat{X} = G(\boldsymbol{k})\partial_x^2 H(\boldsymbol{k})G(\boldsymbol{k})\partial_y^2 H(\boldsymbol{k}) - G(\boldsymbol{k})\partial_{xy}^2 H(\boldsymbol{k})G(\boldsymbol{k})\partial_{xy}^2 H(\boldsymbol{k}) +$$
$$+ 2\left([G(\boldsymbol{k})\partial_x H(\boldsymbol{k}), G(\boldsymbol{k})\partial_y H(\boldsymbol{k})]\right)^2. \tag{6.31}$$

The trace operation contains the integral over the BZ and the trace over band indices:

$$\text{Tr}(\bullet) = \sum_k \text{tr}(\bullet) = S \int_{\text{BZ}} \frac{\mathrm{d}^2 k}{4\pi^2} \, \text{tr}(\bullet). \tag{6.32}$$

The orbital susceptibility can be rewritten in several other forms, one of them without commutator [227],

$$\chi_{\text{orb}}(\mu, T) = -\frac{\mu_0 e^2}{12\hbar^2} \frac{\text{Im}}{\pi S} \int_{-\infty}^{+\infty} n_F(\varepsilon) \, \text{Tr}\left\{ GH^{xx}GH^{yy} \right.$$
$$\left. - GH^{xy}GH^{xy} - 4\left(GH^x GH^x GH^y GH^y - GH^x GH^y GH^x GH^y\right)\right\} \mathrm{d}\varepsilon. \tag{6.33}$$

Here $G = G(\boldsymbol{k})$ is the Green function and H^i, H^{ij} denote the first and second derivatives of Hamiltonian with respect to components of momenta $k_{i,j}$ and the trace contains momenta integration, as defined in Eq. (6.32). The last formula can be also rewritten [227] in terms of previously found one by Gomez-Santos [226],

$$\chi_{\text{orb}}(\mu, T) = -\frac{\mu_0 e^2}{2\hbar^2} \frac{\text{Im}}{\pi S} \int_{-\infty}^{+\infty} n_F(\varepsilon) \, \text{Tr}\left\{ GH^x GH^y GH^x \right.$$
$$\left. \times GH^y + \frac{1}{2}\left(GH^x GH^y + GH^y GH^x\right) GH^{xy} \right\} \mathrm{d}\varepsilon. \tag{6.34}$$

Here the first term represents the Fukuyama result [233]. Three formulas for susceptibility are equivalent of course, and the use of a specific formula depends on possible simplifications, for example, for Hamiltonians linear in momenta the expressions (6.31) or (6.33) are preferred since the terms with second derivatives H^{ij} vanish.

To check the numerical results below we use the sum rule which states that the integral of the orbital susceptibility over the whole band vanishes:

$$\int \chi_{\text{orb}}(\mu, T) d\mu = 0. \tag{6.35}$$

The derivation of the sum rule for general tight-binding model was given in Ref.[13]. Below we apply the formulas for orbital susceptibility to particular models, namely - tight-binding model of tetragraphene and effective low-energy $SU(3)$ models.

6.4.1 Application of general formulas to tetragraphene

Let us now apply the formula (6.30) to tetragraphene Hamiltonian (6.2). Since the second derivatives $\partial^2_{xy}H$ and $\partial^2_{yx}H$ vanish, the operator $\hat{X}$ reduces to

$$\hat{X} = G(\boldsymbol{k})\partial^2_x H(\boldsymbol{k})G(\boldsymbol{k})\partial^2_y H(\boldsymbol{k}) + 2\left([G(\boldsymbol{k})\partial_x H(\boldsymbol{k}), G(\boldsymbol{k})\partial_y H(\boldsymbol{k})]\right)^2. \tag{6.36}$$

The Green's function is given in Appendix 6.7. Then, calculating the trace of $\hat{X}$ for each term separately, we find the expressions presented in Appendix by Eqs.(6.59) and (6.60). We denote the first term with second derivatives in (6.36) as "*term 1*" and the term with commutator as "term 2". Here and thereafter we use dimensionless energy parameter $\varepsilon \to \varepsilon/t_1$ to simplify the form of expressions. One should notice that the numerators in both terms (6.59) and (6.60) are real, thus the imaginary part comes fully from integration over energy due to the presence of singular denominators. We write the determinants as $\prod_{i=1}^{4}(\varepsilon - \varepsilon_i(\boldsymbol{k}))$, where $\varepsilon_i(\boldsymbol{k})$ are band energies measured in units of t_1.

One can use also an alternative expression (6.34) for susceptibility obtaining shorter expression

$$\chi_{\mathrm{orb}}(\mu, T) = -\frac{\mu_0 e^2 t_1}{2\hbar^2}\frac{\mathrm{Im}}{\pi}\int_{-\infty}^{+\infty}d\varepsilon\, n_F(t_1\varepsilon)\int_{BZ}\frac{d^2k}{4\pi^2}\,\mathrm{tr}\left\{GH^x GH^y GH^x GH^y\right\}. \tag{6.37}$$

Evaluating the trace, we find

$$\mathrm{tr}\left\{GH^x GH^y GH^x GH^y\right\} = \left(\frac{2\alpha a(\varepsilon^2 - 1)}{\det[\varepsilon - \frac{1}{t_1}H(\boldsymbol{k})]}\right)^4 \sin^2(k_x a)\sin^2(k_y a). \tag{6.38}$$

The advantage of this formula is that the numerator is much simpler comparing to Eqs.(6.59)-(6.60). However, the larger power of denominator

makes it harder to perform numerical calculation, since the behavior at band-touching point is more singular.

The integrals over energy can be evaluated analytically using Cauchy formula with residues. Next, we need to calculate the integrals over wavevector in full BZ. They are cumbersome and can be performed only numerically.

The numerical evaluation can be performed by sampling many points in BZ, and replacing integral by a quadrature sum. For this purpose we use Monte Carlo approach - it converges very fast with increasing number of sample points for multidimensional integrals. Taking N sample points in BZ, the integral over d^2k is replaced by the sum $\int_{BZ} \frac{d^2k}{(2\pi)^2} f(\boldsymbol{k}) = \frac{1}{N} \sum_j f(\boldsymbol{k}_j)$. Then, the final formula used in evaluation is

$$\chi_{\mathrm{orb}}\left(\mu, T\right) = \frac{\chi_0}{N} \sum_{j=1}^{N} \left[\sum_i \operatorname*{res}_{\varepsilon = \varepsilon_i} n_F(t_1 \varepsilon) f^R(\varepsilon) \right]_{\boldsymbol{k} = \boldsymbol{k}_j}. \qquad (6.39)$$

The residues were evaluated analytically using expressions (6.59)-(6.60), and the band energy solutions of spectral equation (6.3) were substituted numerically into final expressions. Here we introduced the scale factor for susceptibility $\chi_0 = \mu_0 e^2 a^2 t_1 / 12\hbar^2$.

The results of evaluation for χ as a function of chemical potential are shown in Fig.6.4. We have checked that good convergence is reached for $N = 10^5$ and $N = 5 \times 10^5$ for the terms (6.59) and (6.60), respectively. The errors of integration become in this case several orders less than the absolute values of susceptibility. As a test, we checked that the sum rule, which is given by Eq.(6.35), holds true with the same precision.

The orbital susceptibility exhibits standard weak diamagnetic peaks near the edges of the spectrum, which can be easily understood from the Landau-Peierls (LP) formula [227, 232, 234, 235],

$$\chi_{\mathrm{LP}}(\mu, T) = \frac{\mu_0 e^2}{12\hbar^2} \sum_{i=1}^{4} \int \frac{d^2k}{4\pi^2} n_F'(\varepsilon_i) \left(\partial_x^2 \varepsilon_i \partial_y^2 \varepsilon_i - \partial_{xy}^2 \varepsilon_i \partial_{xy}^2 \varepsilon_i \right), \qquad (6.40)$$

which takes into account only intraband contributions. Here $n_F'(\varepsilon)$ is a derivative of the Fermi distribution function. We note that the LP contribution in total susceptibility comes from the first two terms in Eq.(6.31) which contain second derivatives.

In the case of T-graphene only the lower (upper) band gives strong contribution to the orbital susceptibility at the lower (upper) edge of the

spectrum. This can be clearly seen from Figs.6.2 and 6.3, since at lower (upper) edge the corresponding band in Γ (M) point is separated by a large gap from other three bands. The dispersion of this band is quadratic in momenta, see Eq.(6.9), and both derivatives in first term of LP formula are positive. The second term exactly vanishes, and thus the LP susceptibility is negative because $n'_F(\varepsilon) < 0$. These peaks are clearly visible in susceptibility described by the red line (term 1) in panels a) - c) of Fig.6.4 (leftmost and rightmost negative peaks). At the same time, the Landau-Peierls formula does not capture the contribution of high-order saddle points. This is because the large contribution from a Fermi function derivative $n'_F(\varepsilon_i)$ is compensated by vanishing determinant of Hessian matrix that is present in round brackets.

At the ordinary van Hove points, which are placed on upper and lower bands at X-points at the energy levels $\varepsilon^X_{1,4} = \mp\sqrt{1 + 4\alpha^2}$, one finds strong paramagnetic peaks. These peaks are also well-described by the Landau-Peierls formula (6.40). Substituting series expansion (6.19) or (6.20), one finds that only the first term in Landau-Peierls formula is nonzero, and have positive sign due to opposite signs of ∂^2_x and ∂^2_y derivatives. Moreover, due to the divergent DOS at this energy level, the contribution of this band dominates and leads to strong paramagnetism. This is also related to famous magnetic breakdown phenomena [234], where the quasiclassical approximation in terms of electronic orbits fails in the vicinity of saddle points due to effects of tunneling from one trajectory to the neighboring one that leads to rotation of the electron in a direction opposite to the direction of classical rotation (see Ref.[50] for physical picture of this phenomenon). Large paramagnetic peaks coming from the Landau-Peierls formula are well seen in the red line (term 1) in the left panel of Fig.6.4 ($\alpha = 1/3$). Due to the sum rule (6.35) they are almost compensated by diamagnetic contribution in the green line (term 2). The competition of two terms in Eq.(6.36) leads to several dia- to paramagnetic transitions when we continuously change the chemical potential μ (see Fig.6.4). The susceptibility for $\alpha = 3/2$ behaves qualitatively similar to the case with $\alpha = 1/3$.

The behavior of the susceptibility is more interesting when the hopping parameter α is close to unity. At the Fermi level $\mu = 0$ the orbital susceptibility does not exhibit any peculiar properties. However, when the doping is tuned to band-touching point $\mu = t_1$, one can expect nontrivial behavior of susceptibility due to presence of massless fermions forming a

Dirac cone and flat lines with high-order VHS of DOS. Near the energy levels $\mu = \pm t_1$ (see the panels b) and d) in Fig.6.4) we find strong diamagnetic and paramagnetic peaks. Since the contribution of high-order VHS is suppressed in the LP formula (term 1) we are left with diamagnetic contribution from the term 2 due to Dirac excitations when $|\mu| \gtrsim t_1$. On the other hand, when $|\mu| \lesssim t_1$ there is a strong paramagnetic contribution in the term 2 from high-order VHS. The existence of the orbital paramagnetism is a necessary condition to cancel the diamagnetic contribution in order to satisfy the sum rule (6.35). The competition of these two contributions leads to a sharp dia- to paramagnetic transition at $|\mu| \approx t_1$ (see panels b), d) in Fig.6.4). This transition manifests itself in Fig.6.5 where the susceptibility at $\mu = t_1$ is plotted as a function of α (blue line).

Below we analyze the orbital susceptibility for effective linear and quadratic Hamiltonians given by Eqs.(6.24) and (6.29) to obtain some insights into the physics of these peculiar features.

6.4.2 Analytical results in effective pseudospin-1 model around band-touching

Let us firstly use the linear effective Hamiltonian around band-touching point to find an analytical approximation for the susceptibility. It is given by Eq.(6.24), and we omit the dimensional parameter t_1, restoring it in the final expressions for susceptibility,

$$H_3 \equiv \frac{H_{SU(3)}}{t_1} = \begin{pmatrix} 1 & 0 & -\frac{iak_x}{\sqrt{2}} \\ 0 & 1 & \frac{iak_y}{\sqrt{2}} \\ \frac{iak_x}{\sqrt{2}} & -\frac{iak_y}{\sqrt{2}} & 2\alpha - 1 \end{pmatrix}. \tag{6.41}$$

The corresponding Green's function is

$$G_{SU(3)} = \frac{1}{\det[\varepsilon - H_3]} \times$$

$$\begin{pmatrix} \varepsilon^2 - \frac{a^2 k_y^2}{2} - 2\alpha(\varepsilon - 1) - 1 & -\frac{1}{2}a^2 k_x k_y & -\frac{ia(\varepsilon-1)k_x}{\sqrt{2}} \\ -\frac{a^2 k_x k_y}{2} & \varepsilon^2 - \frac{a^2 k_x^2}{2} - 2\alpha(\varepsilon - 1) - 1 & \frac{ia(\varepsilon-1)k_y}{\sqrt{2}} \\ \frac{ia(\varepsilon-1)k_x}{\sqrt{2}} & -\frac{ia(\varepsilon-1)k_y}{\sqrt{2}} & (\varepsilon - 1)^2 \end{pmatrix}. \tag{6.42}$$
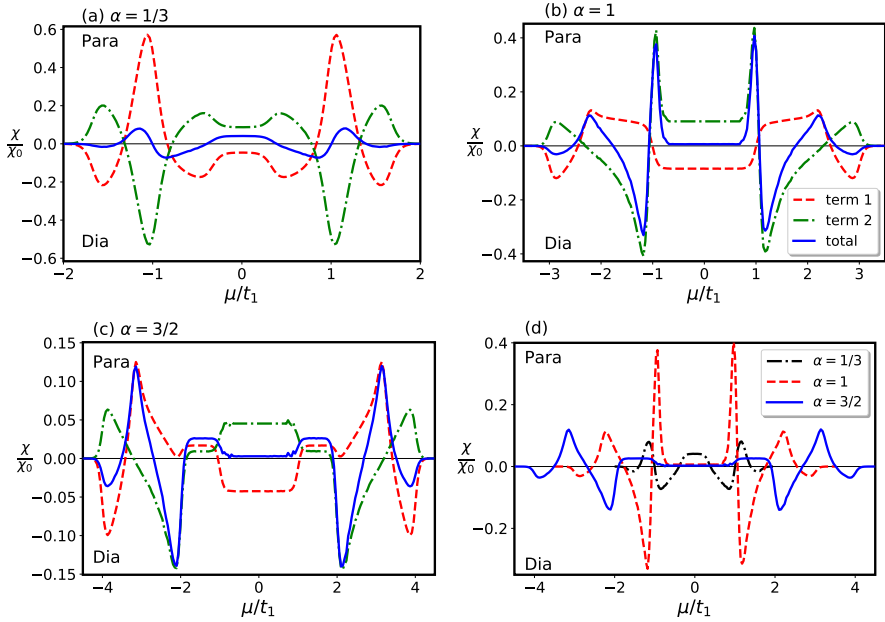
Figure 6.4. The dependence of susceptibility χ on chemical potential μ, measured in units of t_1 hopping parameter, for three values of α: a) $1/3$, b) 1, c) $3/2$. The susceptibility is normalized to scale factor $\chi_0 = \mu_0 e^2 a^2 t_1 / 12\hbar^2$. The legend on panel (b) shows the lines definitions in panels a) - c): dashed and dash-dotted lines correspond to first and second term contributions in $\hat{X}$ (see Eq.(6.36)), while the solid line describes the total susceptibility (the different ranges in y-axis are taken for better visibility). Panel d) shows the total susceptibility for three values of α.

The determinant in denominator is simple

$$\det[\varepsilon - H_3] = \frac{1-\varepsilon}{2}\left(a^2\boldsymbol{k}^2 + 2(\varepsilon-1)(2\alpha-\varepsilon-1)\right) \qquad (6.43)$$

and gives two Dirac cones and the flat band at $\varepsilon = 1$. The first derivatives of Hamiltonian are,

$$H_3^x = \frac{a}{\sqrt{2}}\begin{pmatrix} 0 & 0 & -i \\ 0 & 0 & 0 \\ i & 0 & 0 \end{pmatrix}, \quad H_3^y = \frac{a}{\sqrt{2}}\begin{pmatrix} 0 & 0 & 0 \\ 0 & 0 & i \\ 0 & -i & 0 \end{pmatrix}, \qquad (6.44)$$

while all second derivatives are zero. Then, we can apply the formula (6.34), which in our case reduces to

$$\chi_{\mathrm{orb}}(\mu, T) = -\frac{\mu_0 e^2 t_1}{2\hbar^2}\frac{\mathrm{Im}}{\pi S}\int\limits_{-\infty}^{+\infty} n_F(\varepsilon)\,\mathrm{Tr}\left\{GH^xGH^yGH^xGH^y\right\}\mathrm{d}\varepsilon. \quad (6.45)$$

Calculating the matrix trace we come at the orbital susceptibility given by the triple integral,

$$\chi_{\mathrm{orb}}(\mu, T) = -\frac{\mu_0 e^2 t_1}{2\hbar^2}\frac{\mathrm{Im}}{\pi}\int_{-\infty}^{+\infty} n_F(t_1\varepsilon)d\varepsilon$$

$$\times \int \frac{d^2k}{4\pi^2}\frac{16a^8 k_x^2 k_y^2}{\left(a^2\left(k_x^2 + k_y^2\right) + 2(\varepsilon-1)(2\alpha-\varepsilon-1)\right)^4}. \qquad (6.46)$$

The integration over momenta is easily performed using polar coordinates

$$\int \frac{d^2k}{4\pi^2}\frac{16a^8 k_x^2 k_y^2}{\left(a^2\left(k_x^2 + k_y^2\right) + 2(\varepsilon-1)(2\alpha-\varepsilon-1)\right)^4}$$

$$= \frac{a^2}{12\pi} \times \begin{cases} \frac{1}{2(\alpha-1)}\left(\frac{1}{\varepsilon-1} - \frac{1}{\varepsilon+1-2\alpha}\right), & \alpha \neq 1, \\ -\frac{1}{(\varepsilon-1)^2}, & \alpha = 1. \end{cases} \qquad (6.47)$$

Then, using the formula

$$\mathrm{Im}\int_{-\infty}^{+\infty}\frac{f(E)}{(E-\alpha)^j}\mathrm{d}E = -\frac{\pi}{(j-1)!}f^{(j-1)}(\alpha), \qquad (6.48)$$

for susceptibility we finally obtain:

$$\chi_{\mathrm{orb}}(\mu, T) = -\frac{\chi_0}{2\pi}\begin{cases} \frac{1}{2(\alpha-1)}\left(n_F(t_1(2\alpha-1)) - n_F(t_1)\right), & \alpha \neq 1, \\ t_1 n_F'(t_1), & \alpha = 1. \end{cases} \qquad (6.49)$$

Note that the case $\alpha = 1$ is the limit of the upper case with $\alpha \neq 1$. The result for $\alpha = 1$ has the same functional structure as the susceptibility for low-energy model of graphene [227], but differs in numerical factor and sign. The latter difference is connected with the presence of flat band in spectrum. In such a case the flat band plays the crucial role giving strong delta-like paramagnetic response of the system at $\mu = t_1$ instead of diamagnetic, which was a result of two Dirac cones in graphene. Note however, that the linear effective Hamiltonian does not capture the correct dispersion of the middle band. The model contains completely flat band and the spectrum (6.25) is similar to a gapped dice model where the paramagnetic contribution from flat band exceeds diamagnetic contribution from Dirac cones (see Ref.[196])

The plot of effective susceptibility defined by Eq.(6.49) is shown in Fig.6.5 as a function of a hopping parameter α. On the plot it is denoted as "Eq.(24)" effective theory. We compare its dependence on α with total susceptibility of actual model evaluated numerically. The doping level $\mu = t_1$ coincides with the band touching point at which the high-order VHS and Dirac point are present for $\alpha = 1$. The numerical calculations demonstrate the presence of dia- to paramagnetic transition at $\alpha \approx 0.94$, which is absent in the low-energy result (6.49). Thus, we should analyze more precise effective model, which is given by the second-order Hamiltonian Eq.(6.29).

6.4.3 Paramagnetic-diamagnetic phase transition at band-touching point and second-order effective Hamiltonian

The calculation of orbital susceptibility for the second-order effective Hamiltonian (6.29) involves all terms in $\hat{X}$ operator (6.31), because all first and second derivatives of Hamiltonian (6.29) over k_i are nonzero. The corresponding Green's function is presented in Appendix, see Eq.(6.61). Since the calculations quickly become cumbersome, we present only numerical results here. For the integrals over wave number $\boldsymbol{k}$ we use Monte-Carlo method. The energies for each point in k-space are found from Eq.(6.63) and then we use the integration formula (6.39) multiplied by volume factor $\Lambda^2 a^2 / \pi^2$. Here Λ is a cut-off parameter, that defines the region of applicability of second-order effective Hamiltonian (6.29). We estimated it as $\Lambda \approx 0.8 \frac{1}{a}$ by comparing exact spectrum with one obtained from Eq.(6.63).

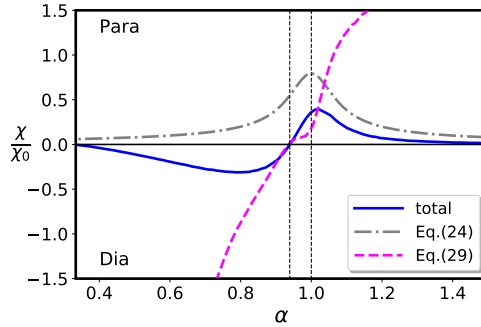The orbital susceptibility for the effective Hamiltonian (6.29) at the

Figure 6.5. The dependence of orbital susceptibility on relative strength of tight-binding parameters $\alpha = t_2/t_1$ for $\mu = 1.0t_1$ and $T = 0.05t_1$. The numerically-evaluated total susceptibility (solid blue line) is compared with susceptibility obtained from effective pseudospin-1 Hamiltonians (6.24) (gray dashdotted line) and (6.29) (magenta dashed line).

band-touching point $\mu = 1.0t_1$ as a function of a hopping parameter α is presented in Fig.6.5. It is clearly seen that this Hamiltonian exhibits dia- to paramagnetic transition at $\alpha = 0.94$ in agreement with tight-binding Hamiltonian and in contrast to the linear effective Hamiltonian (6.24). Qualitatively, one can expect that such a transition occurs due to the presence of Dirac cones, which give strong diamagnetism in graphene [197, 227], and the proximity of a high-order VHS that should result in strong paramagnetism. The competition between these two opposite responses together with the weak role of fourth band leads to a dia- to paramagnetic transition.

6.4.4   The role of van Hove singularities

Let us discuss the role of van Hove singularities in T-graphene. For the ordinary VHS the orbital susceptibility exhibits paramagnetic peak [50]. This can be understood using the standard Landau-Peierls formula for contribution of single band [227]. In T-graphene, at the doping level $\mu = \pm t_1$, one meets the three-band-touching points, at which two Dirac cones and middle band with flat lines intersect. In a single-layer graphene the presence of Dirac cones leads to singular diamagnetic contribution into orbital susceptibility $\chi \sim -\chi_0 \delta(\mu)$ at zero temperature [197]. In the gapped dice model, spectrum of which is similar to (6.25), the paramagnetic contribution due to a flat band exceeds diamagnetic contribution

from Dirac cones (see Ref.[196]). In the case of T-graphene, the presence of middle band, which is not flat anymore but contains flat lines with high-order VH singularities on it, leads to strong paramagnetic contribution competing with diamagnetic contribution from Dirac cones, thus resulting in sign change of the orbital susceptibility.

High-order Van Hove singularities manifest themselves in many physical quantities as was reported in, e.g., Refs. [27, 28, 216–224]. In the present paper we focused on the magnetic susceptibility of non-interacting electrons in square-octagon lattice. However, one should expect the manifestation of high-order VHS of T-graphene also in other physical quantities besides orbital susceptibility which is a subject for future studies. We note that the accessibility of doping levels beyond the van Hove singularity was demonstrated in recent experiment for single-layer graphene [236].

6.5   Conclusions

In this paper we have studied the spectrum structure of tight-binding model for square-octagon lattice and analyzed the emergence of Dirac cones and van Hove singularities of different type. Firstly, we found that the singularities in DOS, that correspond to the flat lines in spectrum of T-graphene, represent VHS of high-order. Their benchmarks are large divergence exponent $\kappa = 1/2$ (instead of logarithmic divergence for ordinary VHS) and asymmetry of DOS near corresponding energy level. Such high-order saddle points in spectrum are intermediate between the ordinary saddle points and completely flat bands. Also, using the Löwdin partitioning, we derived an effective second-order Hamiltonian that correctly captures dispersions of three bands near the high-order saddle point.

Secondly, we have studied the orbital susceptibility of electrons on square-octagon lattice. We have found that while for ordinary VHS there are standard paramagnetic peaks predicted long ago by Vignale [50], the recently introduced high-order VHS [25] manifest themselves in a more complicated way. The tight-binding magnetic susceptibility exhibits several dia- to paramagnetic transitions when a chemical potential runs the whole zone.

Studying the orbital susceptibility at band-touching point $(\mu = t_1)$ as a function of the tight-binding hoppings ratio α, we found a dia- to paramagnetic transition at $\alpha \approx 0.94$. Its existence can be qualitatively understood due to competitions of contributions from Dirac cones, which

give strong diamagnetism, and high-order VHS that result in strong paramagnetism. The effective low-energy pseudospin-1 Hamiltonian near the Γ point (6.24) correctly describes paramagnetic contribution but does not capture the dia- to paramagnetic transition. On the other hand, the effective Hamiltonian (6.29), which keeps second-order terms in a wavevector expansion, correctly reproduces the dia- to paramagnetic transition at $\alpha = 0.94$ given by the tight-binding Hamiltonian.

The tight-binding parameter α can be varied due to in-plane deformations keeping C_4 symmetry, thus allowing to verify the dia- to paramagnetic transition in experiment. Though it is not probably easy to fine-tune the hopping parameters experimentally, one can observe the different phases by analyzing different materials that are based on square-octagon lattice (see Refs. [53, 211]). Also, the T-graphene model can be realized experimentally with cold fermionic atoms in an optical lattice, or in phononic crystals [237]. In these cases it could be possible to test directly the sign change of the susceptibility as a function of α. In further studies of the T-graphene model it would be interesting to include impurities and interactions. In the recent publication [238] the role of high-order VHS in the orbital magnetic susceptibility was studied for twisted bilayer graphene. These studies complement the analysis in the present work.

6.6 Appendix: Flat lines in dispersion of middle bands and lattice symmetry

In this Appendix we show that the flat lines in spectrum are related to the C_4 point symmetry group. Also we show, that every point of flat line represents a high-order saddle point. Firstly, one can check that setting $k_x = 0$ (or $k_y = 0$) in spectral equation (6.3), it can be factorized:

$$(\varepsilon - 1)\left(-\left(4\alpha^2 + 1\right)\varepsilon + 4\alpha^2 \cos(ak_y) + \varepsilon^3 + \varepsilon^2 - 1\right) = 0. \qquad (6.50)$$

Here we used scaled energy parameter ε, measured in units of t_1. Thus, we find the middle band dispersion $\varepsilon = 1$, which describes a flat line. The same property of spectral equation holds true for $k_x a = \pm\pi$ and $k_y a = \pm\pi$ lines, with $\varepsilon = -1$.

The wavevector in tight-binding Hamiltonian (6.2) is measured from Γ point. Performing the rotation to the basis of C_4 symmetry group via the

unitary matrix given in Eq.(6.23), we find the transformed Hamiltonian $U_{C_{4v}}^{\dagger} H U_{C_{4v}}$. Along flat line direction $k_x = 0$ (and similarly for $k_y = 0$) the Hamiltonian reduces to the matrix

$$
U_{C_{4v}}^{\dagger} H U_{C_{4v}}(k_x = 0, k_y) = \frac{t_1}{2} \times
$$
$$
\begin{pmatrix}
-1 - 4\alpha - \cos(ak_y) & 0 & i\sqrt{2}\sin(ak_y) & -1 + \cos(ak_y) \\
0 & 2 & 0 & 0 \\
-i\sqrt{2}\sin(ak_y) & 0 & 2\cos(ak_y) & i\sqrt{2}\sin(ak_y) \\
-1 + \cos(ak_y) & 0 & -i\sqrt{2}\sin(ak_y) & -1 + 4\alpha - \cos(ak_y)
\end{pmatrix}.
$$
$$(6.51)$$

Thus, one can conclude that the presence of flat lines is protected not only by C_4 symmetry, but also by the geometry of tight-binding model. As was noted in Ref.[206], at the Γ point the flat lines represent nearly flat band (two lines intersect at the angle $\frac{\pi}{2}$). When the two hopping parameters are equal, $\alpha = 1$, the corresponding linear low-energy model (6.24) treats the middle band as completely flat and is similar to a pseudospin-1 model. However, in the second order approximation (see Eq.(6.29)) the middle band becomes dispersive. This fact distinguishes this pseudospin-1 model from other models, such as Lieb [21], Kagome [75] or $\alpha - T_3$ [13, 14, 89] models, where the presence of exactly flat band is supported by the lattice geometry in tight-binding approximation.

Finally, expanding the spectral equation (6.3) near the flat line $k_x = 0$ up to second order in $k_x a$, we find

$$
\delta^4 - 4\delta^3 + 4\left(1 - \alpha^2\right)\delta^2 + 2\alpha^2\delta\left((k_x a)^2 - 2\cos(k_y a) + 2\right)
$$
$$
+ 2\alpha^2 (k_x a)^2 (\cos(k_y a) - 1) = 0. \tag{6.52}
$$

Here $\delta = 1 - \varepsilon$ measures the deviation of energy from flat line value. In this equation we can omit the third and fourth order corrections (δ^3 and δ^4), and obtain simple quadratic equation. The solution, that corresponds to the flat line, has the following approximate behavior

$$
\delta \approx \frac{k_x^2 a^2}{2} - \frac{k_x^4 a^4}{4\alpha^2 \left(\cos(k_y a) - 1\right)}. \tag{6.53}
$$

The determinant of Hessian matrix for such a solution is always zero. Thus we conclude, that every point on a flat line is a high-order saddle point.

6.7 Appendix: Green's function of tight-binding and Löwdin Hamiltonians

In this Appendix we calculate the Green function of the tight-binding Hamiltonian (6.2). Standardly it is defined as

$$G(\boldsymbol{k}, \varepsilon) = \frac{1}{t_1} \left(\varepsilon - \frac{1}{t_1} H(\boldsymbol{k}) \right)^{-1} \tag{6.54}$$

for energy ε measured in units of t_1. Using the formula for adjoint matrix, we find the simple but long expression. For the clarity, we write the Green's function in block form:

$$G(\boldsymbol{k}, \varepsilon) = \frac{1}{t_1 \det[\varepsilon - \frac{1}{t_1} H(\boldsymbol{k})]} \begin{pmatrix} G_{11} & G_{12} \\ G_{12}^\dagger & G_{22} \end{pmatrix}. \tag{6.55}$$

The corresponding blocks are given by the following expressions:

$$G_{11}(\boldsymbol{k}, \varepsilon) = \tag{6.56}$$
$$\begin{bmatrix} \varepsilon(-2\alpha^2 + \varepsilon^2 - 1) + 2\alpha^2 \cos k_y a & \alpha e^{-ik_y a}(-\varepsilon + e^{ik_x a})(-1 + \varepsilon e^{ik_y a}) \\ \alpha e^{-ik_x a}(-1 + \varepsilon e^{ik_x a})(-\varepsilon + e^{ik_y a}) & \varepsilon(-2\alpha^2 + \varepsilon^2 - 1) + 2\alpha^2 \cos k_x a \end{bmatrix},$$

$$G_{12}(\boldsymbol{k}, \varepsilon) = \tag{6.57}$$
$$\begin{bmatrix} 2\alpha^2(\varepsilon - \cos k_y a) - (\varepsilon^2 - 1)e^{ik_x a} & \alpha(-\varepsilon + e^{ik_x a})(\varepsilon - e^{ik_y a}) \\ \alpha(-\varepsilon + e^{ik_x a})(\varepsilon - e^{ik_y a}) & 2\alpha^2(\varepsilon - \cos k_x a) - (\varepsilon^2 - 1)e^{ik_y a} \end{bmatrix},$$

$$G_{22}(\boldsymbol{k}, \varepsilon) = \tag{6.58}$$
$$\begin{bmatrix} \varepsilon(-2\alpha^2 + \varepsilon^2 - 1) + 2\alpha^2 \cos k_y a & \alpha e^{-ik_x a}(-1 + \varepsilon e^{ik_x a})(-\varepsilon + e^{ik_y a}) \\ \alpha e^{-ik_y a}(-\varepsilon + e^{ik_x a})(-1 + \varepsilon e^{ik_y a}) & \varepsilon(-2\alpha^2 + \varepsilon^2 - 1) + 2\alpha^2 \cos k_x a \end{bmatrix}.$$

These expressions are used to evaluate the traces for "*term 1*" and "*term 2*" (first and second terms in Eq.(6.36)):

$$\mathrm{tr}\,[\text{term 1}] = \frac{a^4}{\det[\varepsilon - \frac{1}{t_1} H(\boldsymbol{k})]^2} \times$$
$$\left[4\alpha^2 \left(\left(\varepsilon^2 + 1 \right) \cos(k_x a) - 2\varepsilon \right) \left(\left(\varepsilon^2 + 1 \right) \cos(k_y a) - 2\varepsilon \right) \right], \tag{6.59}$$

$$\text{tr}\,[\text{term 2}] = \frac{16\alpha^2 a^4}{\det[\varepsilon - \frac{1}{t_1}H(\boldsymbol{k})]^3} \times$$

$$\left[t_1^2 \alpha^2 \left(\varepsilon^2 + 2 \right)^2 + 2\alpha^2 \varepsilon^2 \cos(2k_y a)(\varepsilon \cos(k_x a) - 1)^2 + \right.$$

$$+ \varepsilon \left(\alpha^2 \varepsilon \left(\varepsilon^2 + 2 \right) \cos(2k_x a) + \left((\varepsilon^2 - 1)^2 - 4\varepsilon^2 \alpha^2 \left(\varepsilon^2 + 2 \right) \right) \cos(k_x a) \right)$$

$$+ \cos(k_y a) \left(-2 \left(2\alpha^2 + 1 \right) \varepsilon^3 - 8\alpha^2 \varepsilon - 4\alpha^2 \varepsilon^3 \cos(2k_x a) \right.$$

$$\left. + \left(4\alpha\varepsilon - \varepsilon^2 + 1 \right) \left(4\alpha\varepsilon + \varepsilon^2 - 1 \right) \cos(k_x a) + \varepsilon^5 + \varepsilon \right) - \varepsilon^2 \left(\varepsilon^2 - 1 \right)^2 \right].$$

$$(6.60)$$

For the second-order effective Hamiltonian (6.29), which is obtained with the help of Löwdin partitioning method, the Green's function is (we set $a = 1$ to simplify the notation)

$$G = \frac{1}{t_1 \det \left[\varepsilon - \frac{H_{SU(3)}^{(2)}(\boldsymbol{k})}{t_1} \right]} \times \qquad\qquad (6.61)$$

$$\begin{pmatrix} G_{11} & -\frac{k_x k_y \left(\boldsymbol{k}^2 + 16\alpha - 4\varepsilon + 4 \right)}{16(\alpha+1)} & -\frac{ik_x \left(2(\varepsilon-1) + \alpha \left(k_y^2 + 2\varepsilon - 2 \right) \right)}{2\sqrt{2}(\alpha+1)} \\ -\frac{k_x k_y \left(\boldsymbol{k}^2 + 16\alpha - 4\varepsilon + 4 \right)}{16(\alpha+1)} & G_{22} & \frac{i \left(2(\varepsilon-1) + \alpha \left(k_x^2 + 2\varepsilon - 2 \right) \right) k_y}{2\sqrt{2}(\alpha+1)} \\ \frac{ik_x \left(2(\varepsilon-1) + \alpha \left(k_y^2 + 2\varepsilon - 2 \right) \right)}{2\sqrt{2}(\alpha+1)} & -\frac{i \left(2(\varepsilon-1) + \alpha \left(k_x^2 + 2\varepsilon - 2 \right) \right) k_y}{2\sqrt{2}(\alpha+1)} & G_{33} \end{pmatrix}$$

$$(6.62)$$

where

$$G_{11} = \left[1 - \frac{\boldsymbol{k}^2}{4} - 2\alpha + \varepsilon \right] \left[\frac{(2\alpha + 1)k_y^2}{4(\alpha + 1)} + \varepsilon - 1 \right] - \frac{k_y^2}{2},$$

$$G_{22} = \left[\frac{(2\alpha + 1)k_x^2}{4(\alpha + 1)} + \varepsilon - 1 \right] \left[1 - \frac{\boldsymbol{k}^2}{4} - 2\alpha + \varepsilon \right] - \frac{k_x^2}{2},$$

$$G_{33} = (\varepsilon - 1)^2 + \frac{(2\alpha + 1)\boldsymbol{k}^2(\varepsilon - 1) + \alpha k_x^2 k_y^2}{4(\alpha + 1)}.$$

and the determinant is given by the following third-order polynomial:

$$
\det \left[\varepsilon - \frac{H^{(2)}_{SU(3)}(\boldsymbol{k})}{t_1} \right] = \varepsilon^3 - \frac{\varepsilon^2 \left(\alpha \left(8\alpha - k^2 + 12 \right) + 4 \right)}{4(\alpha + 1)}
$$

$$
- \frac{\varepsilon \left(-32(\alpha + 1)(4\alpha - 1) + \alpha k^4 \cos(4\phi) + (3\alpha + 2)k^4 + 16\alpha(2\alpha + 1)k^2 \right)}{32(\alpha + 1)}
$$

$$
- \frac{128 \left(2\alpha^2 + \alpha - 1 \right) + \alpha k^6 + 4(\alpha - 2)(2\alpha + 1)k^4}{128(\alpha + 1)}
$$

$$
+ \frac{32\alpha(4\alpha + 1)k^2 + \alpha k^4 \left(8\alpha + k^2 + 4 \right) \cos(4\phi)}{128(\alpha + 1)}. \tag{6.63}
$$

These expressions were used above for the calculation of orbital suscepti-
bility from the effective second-order model.

Chapter 7

Shot noise distinguishes Majorana fermions from vortices injected in the edge mode of a chiral *p*-wave superconductor

7.1 Introduction

A chiral *p*-wave superconductor is the superconducting counterpart to a quantum Hall insulator [239]: Both are two-dimensional materials with a gapped bulk and gapless modes that circulate unidirectionally (chirally) along the boundary. Backscattering is suppressed when the counterpropagating edge modes are widely separated. The resulting unit transmission probability for quasiparticles injected into an edge mode implies a quantized thermal conductance for both systems — half as large in the superconductor because the quasiparticles are Majorana fermions [240–242] (coherent superpositions of electrons and holes) rather than the Dirac fermions (independent electrons and holes) of an integer quantum Hall edge mode.

This close correspondence [243] between topological insulators, as in the integer quantum Hall effect, and topological superconductors, as in chiral *p*-wave superconductivity, refers to their fermionic quasiparticle ex-

citations. The superconducting phase allows for an additional collective degree of freedom, a winding of the phase field forming a vortex, with non-Abelian rather than fermionic exchange statistics [241, 244]. Vortices are typically immobile, pinned to defects in the bulk, but they may also be mobile phase boundaries in the edge mode. The 2π winding of the superconducting phase around a bulk vortex corresponds on the edge to a π-phase domain wall for Majorana fermions [245].

It is the purpose of this chapter to identify electrical signatures of edge vortices, and to distinguish these from the familiar electronic transport properties of Majorana fermions [246–254]. For that purpose we contrast the two injection geometries shown in Fig. 7.1. Majorana fermions are injected by a voltage source, contacted via a tunnel junction to an edge mode. The analogous edge vortex injector is a flux-biased Josephson junction. A 2π increment of the superconducting phase difference ϕ injects one vortex into each of the opposite edges [255].

If the edge modes would propagate in the same direction, the vortices could fuse in a metal contact [256]. This fusion process is associated with a noiseless charge transport of $\pm e/2$ [257, 258]. (The sign depends on how the world lines of the vortices are braided.) For counterpropagating edge modes as in Fig. 7.1 the vortices cannot fuse, they will enter different contacts to the left and to the right of the Josephson junction. The charge transfer into each contact is zero on average, but it is not noiseless: The injection process produces shot noise, in the case of edge vortices as well in the case of Majorana fermions.

The equal-weight electron-hole superposition that is characteristic of a
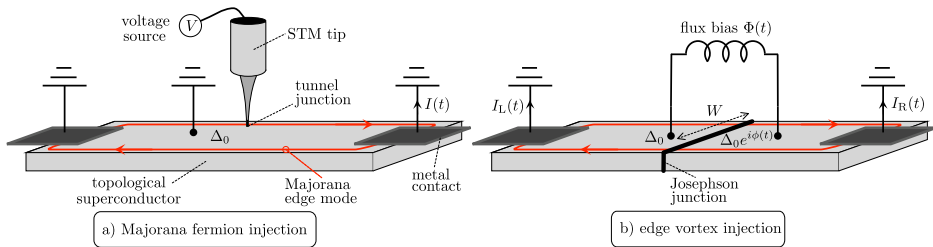

Figure 7.1. Topological superconductor with chiral Majorana edge modes. In panel a) a voltage bias across a tunnel junction injects Majorana fermions into the right-moving edge mode. In panel b) a flux bias across a Josephson junction injects edge vortices in the counter-propagating edge modes. The two injection processes can be detected and distinguished by shot noise measurements.

Majorana fermion results in a charge variance of e^2 per injected fermion, producing a quantized shot noise power [54]. We find that the charge variance per edge vortex is nonlocal, it depends logarithmically on the separation L between pairs of vortices on the same edge:

$$\text{Var}\, Q_{\text{vortex}} = \frac{e^2}{\pi^2} \ln(L/\lambda), \;\; \text{for} \;\; L \gg \lambda. \tag{7.1}$$

Here λ is the width of the π-phase domain wall, which sets the size of the edge vortex core. The dependence on the ratio L/λ persists when $L \gg \lambda$, so when the domain walls do not overlap. This nonlocality signals the long-range correlation that exists between vortices in a topological superconductor.

The outline of this paper is as follows. In the next section we formulate the general scattering theory on which our analysis is based. The Majorana nature of the quasiparticle excitations implies that expectation values of pairs of creation operators do not vanish — as they would for Dirac fermions. This technical complication plays no role for DC transport, but needs to be accounted for in the case of time dependent perturbations, when inelastic scattering plays a role [259]. In Sec. 7.3 we generalize a relationship between the charge variance and the average particle current derived in Ref. [54] for DC transport to the time dependent setting. The charge noise of the edge vortices is calculated in Sec. 7.4 and compared with the known result [260] for Majorana fermions in Sec. 7.5. We propose a voltage-biased geometry in which the edge vortices produce a shot noise power that increases $\propto V \ln V$ — in contrast to the linear voltage dependence of the Majorana fermion noise power.

7.2 Trace formula for the variance of the transferred charge

We start with a general inelastic scattering formulation, in terms of a set of fermionic quasiparticle operators $a_n(E)$ for the incoming modes and $b_n(E)$ for the outgoing modes, related by the energy dependent scattering matrix,

$$b_n(E) = \int_{-\infty}^{\infty} \frac{dE'}{2\pi} \sum_m S_{nm}(E, E') a_m(E'). \tag{7.2}$$

Each mode index $n = 1, 2, \ldots N$ contains an electron and hole component in a Nambu spinor. Pauli matrices $\sigma_x, \sigma_y, \sigma_z$ act on the spinor degree of

freedom (with σ_0 the 2×2 unit matrix). The scattering matrix is unitary and constrained by particle-hole symmetry,

$$S(E, E') = \sigma_x S^*(-E, -E')\sigma_x. \tag{7.3}$$

We seek the charge transferred by quasiparticle excitations at $E > 0$ into a subset M of the N electron-hole modes. The projector $\mathcal{D}_M$ selects these M modes and the projector $\mathcal{P}_+$ selects positive energies. The charge operator for the outgoing modes is

$$Q = e \int_0^\infty \frac{dE}{2\pi} \sum_{n=1}^M b_n^\dagger(E)\sigma_z b_n(E) \equiv e b^\dagger \sigma_z \mathcal{D}\mathcal{P}_+ b. \tag{7.4}$$

The scattering matrix converts this into an expression in terms of the incoming mode operators,

$$Q = e a^\dagger \cdot S^\dagger \sigma_z \mathcal{D}\mathcal{P}_+ S \cdot a. \tag{7.5}$$

In these equations the Pauli matrix σ_z accounts for the opposite charge $\pm e$ of the electron and hole components of the Nambu spinor. (For ease of notation we will set $e \equiv 1$ in many of the equations.)

Moments of Q are evaluated by taking pairwise contractions of $a, a^\dagger$, each of which are given by the Fermi function $f(E)$,

$$\langle a_n^\dagger(E)a_m(E')\rangle = f(E)\sigma_0\delta_{nm}\delta(E - E'),$$
$$\langle a_n^\dagger(E)a_m^\dagger(E')\rangle = f(E)\sigma_x\delta_{nm}\delta(E + E'). \tag{7.6}$$

The second contraction is anomalous [259], it does not vanish because of the particle-hole symmetry relation $a(E) = \sigma_x a^\dagger(-E)$. If the scattering is elastic the anomalous contraction which couples $+E$ to $-E$ does not contribute — but in the more general case of inelastic scattering it cannot be ignored for any moment higher than the first.

In the zero-temperature limit the Fermi function $f(E) = (1 + e^{E/k_B T})^{-1}$ becomes a projector $\mathcal{P}_-$ onto negative energies. We will take that limit in what follows. This also means that thermal noise from the incoming modes need not be considered.

Carrying out the contractions we find the average $\langle Q \rangle$ and the variance $\operatorname{Var} Q = \langle Q^2 \rangle - \langle Q \rangle^2$ of the transferred charge,

$$\langle Q \rangle = \operatorname{Tr} \mathcal{P}_- S^\dagger \sigma_z \mathcal{D}\mathcal{P}_+ S, \tag{7.7}$$

$$\operatorname{Var} Q = \operatorname{Tr} \mathcal{P}_- S^\dagger \mathcal{D}\mathcal{P}_+ S - \operatorname{Tr} \mathcal{P}_- S^\dagger \sigma_z \mathcal{D}\mathcal{P}_+ S \mathcal{P}_- S^\dagger \sigma_z \mathcal{D}\mathcal{P}_+ S$$
$$- \operatorname{Tr} \mathcal{P}_- S^\dagger \sigma_z \mathcal{D}\mathcal{P}_+ S \mathcal{P}_- S^\dagger \sigma_z \mathcal{D}\mathcal{P}_- S. \tag{7.8}$$

The third term in Eq. (7.8) originates from the anomalous contraction in combination with the particle-hole symmetry relation (7.3). The third term combines with the second term to remove one energy projector,

$$\operatorname{Var} Q = \operatorname{Tr} \mathcal{P}_- S^\dagger \mathcal{D} \mathcal{P}_+ S - \operatorname{Tr} \mathcal{P}_- S^\dagger \sigma_z \mathcal{D} \mathcal{P}_+ S \mathcal{P}_- S^\dagger \sigma_z \mathcal{D} S. \qquad (7.9)$$

While Eq. 7.7 for the average charge has an intuitive interpretation of scattering from filled states at $E < 0$ to empty states at $E > 0$, the formula (7.9) for the charge noise is less intuitive. As a check, we show in App. 7.6 that it agrees with the more general Klich formula of full counting statistics [261].

7.3 Correspondence between charge variance and average particle number

We apply the general scattering theory to the setting of Fig. 7.1b. There are M electron-hole modes in each metal contact, $N = 2M$ in total, coupled via a pair of counterpropagating Majorana edge modes. The coupling is inelastic because of a time dependent phase difference $\phi(t)$ across the Josephson junction that separates the two contacts. The 2π increment of ϕ imposed by a flux bias injects an edge vortex into each contact, and we wish to determine the charge noise associated with that injection process.

The scattering matrix decomposes into transmission blocks t, t' and reflection blocks r, r', each of dimension $M \times M$,

$$S(E, E') = \begin{pmatrix} r(E, E') & t(E, E') \\ t'(E, E') & r'(E, E') \end{pmatrix}. \qquad (7.10)$$

The projector

$$\mathcal{D} = \begin{pmatrix} 1 & 0 \\ 0 & 0 \end{pmatrix} \qquad (7.11)$$

selects the matrices t and r in the expressions (7.7) and (7.9) for the mean and variance of the charge transferred into the right contact,

$$\langle Q \rangle = \operatorname{Tr} \mathcal{P}_- \big(t^\dagger \sigma_z \mathcal{P}_+ t + r^\dagger \sigma_z \mathcal{P}_+ r \big), \qquad (7.12)$$

$$\operatorname{Var} Q = \operatorname{Tr} \mathcal{P}_- \big(t^\dagger \mathcal{P}_+ t + r^\dagger \mathcal{P}_+ r \big) - 2 \operatorname{Re} \operatorname{Tr} \mathcal{P}_- r^\dagger \sigma_z \mathcal{P}_+ t \mathcal{P}_- t^\dagger \sigma_z r$$
$$- \operatorname{Tr} \mathcal{P}_- \big(r^\dagger \sigma_z \mathcal{P}_+ r \mathcal{P}_- r^\dagger \sigma_z r + t^\dagger \mathcal{P}_+ \sigma_z t \mathcal{P}_- t^\dagger \sigma_z t \big). \qquad (7.13)$$

We consider the structure of the matrices t and r in more detail.

The $M \times M$ transmission matrix $t(E, E')$ describes propagation from the left contact into the right contact via the right-moving Majorana mode. It can be decomposed as

$$t_{nm}(E, E') = u_n(E)v_m(E')\tau(E, E'), \qquad (7.14)$$

in terms of the inelastic transmission amplitude $\tau(E, E')$ of the Majorana mode. The $n = 1, 2, \ldots M$ spinors $u_n(E)$ and $v_n(E)$, normalized to unity,

$$\sum_{n=1}^{M} |u_n(E)|^2 = 1 = \sum_{n=1}^{M} |v_n(E)|^2, \qquad (7.15)$$

describe the elastic coupling between the Majorana mode and the electron-hole modes at the interface with the right contact (u_n) and the left contact (v_n).

The $M \times M$ reflection matrix $r(E, E')$ for reflection of an electron-hole mode incident from the right contact can be decomposed as

$$r_{nm}(E, E') = d_{nm}(E)\delta(E - E') + u_n(E)w_m(E')\rho(E, E'). \qquad (7.16)$$

The first term d_{nm} describes direct elastic reflection at the interface between the superconductor and the right contact. The second term describes inelastic reflection at the Josephson junction, decomposed as the product of the transmission amplitude w_m from the right contact into the left-moving Majorana mode, the reflection amplitude ρ from the Josephson junction, and the transmission amplitude u_n from the right-moving Majorana mode into the right contact. Both u_n and w_m are normalized to unity. Note that u_n appears also in the decomposition (7.14) of t_{nm}.

We make the key assumption that the elastic scattering at the superconductor - contact interface is only weakly energy dependent near the Fermi level, $E = 0$, so that we may approximate $u_n(E) \approx u_n(0)$.

To justify this approximation, we note, on the one hand, that the characteristic energy dependence of the elastic scattering amplitudes is on the scale of $E_{\text{elastic}} \simeq \hbar v_{\text{F}}/\xi_0$, where v_{F} is the Fermi velocity and the superconducting coherence length ξ_0 sets the effective width of the interface. On the other hand, the characteristic energy dependence of the inelastic scattering by the Josephson junction is on the scale $E_{\text{inelastic}} = \hbar(W/\xi_0)\dot{\phi}$, where W is the junction width and $\dot{\phi}$ the rate of change of the superconducting phase [255]. It is consistent to neglect the energy

dependence of $u_n(E)$ while retaining the energy dependence of $\tau(E, E')$ and $\rho(E, E')$ if $E_{\text{inelastic}} \ll E_{\text{elastic}}$, hence if the junction is sufficiently narrow:

$$E_{\text{inelastic}} \ll E_{\text{elastic}} \Rightarrow W \ll v_{\text{F}}/\dot{\phi}. \tag{7.17}$$

As we show in App. 7.7, this single assumption combined with particle-hole symmetry implies that the following matrix products vanish:

$$\mathcal{P}_- t^\dagger \sigma_z \mathcal{P}_+ t \mathcal{P}_- = 0, \ \mathcal{P}_- r^\dagger \sigma_z \mathcal{P}_+ r \mathcal{P}_- = 0, \ \mathcal{P}_- r^\dagger \sigma_z \mathcal{P}_+ t \mathcal{P}_- = 0. \tag{7.18}$$

What underlies these three identities is that the inelastic contributions to the transmission and reflection matrices are rank-one matrices in the mode index.

It follows upon combination of Eqs. (7.12) and (7.18), and noting that $\text{Tr} \, \mathcal{P}_-(\cdots) = \text{Tr} \, \mathcal{P}_-(\cdots)\mathcal{P}_-$, that there is no charge transfer into the right contact on average,

$$\langle Q \rangle = 0. \tag{7.19}$$

For the charge noise (7.13), Eq. (7.18) implies that the second and third trace vanish, only the first trace remains:

$$\text{Var} \, Q = e^2 \, \text{Tr} \, \mathcal{P}_- \big(t^\dagger \mathcal{P}_+ t + r^\dagger \mathcal{P}_+ r \big) \mathcal{P}_-$$
$$= e^2 \int_0^\infty \frac{dE}{2\pi} \int_{-\infty}^0 \frac{dE'}{2\pi} \big(|\tau(E, E')|^2 + |\rho(E, E')|^2 \big). \tag{7.20}$$

Eq. (7.20) states that the charge variance (divided by e^2) equals the average number of quasiparticles injected into the right contact by the time dependent phase difference across the Josephson junction. This relationship is analogous to the known relationship between electrical shot noise and thermal conductance in a setting without time-dependent driving [54, 260, 262].

7.4   Evaluation of the charge noise

We evaluate Eq. (7.20) for the case that the phase difference ϕ across the junction is advanced at a constant rate $\dot{\phi} = 2\pi/T$, via a linearly increasing flux bias $\Phi(t) = (h/2e)t/T$. We work in the adiabatic regime that the propagation time $\tau_W = W/v_{\text{F}}$ along the Josephson junction is small compared to the inelastic scattering time,

$$\tau_W \ll \hbar/E_{\text{inelastic}} \Rightarrow W \ll (\xi_0/W)v_{\text{F}}/\dot{\phi}. \tag{7.21}$$

The adiabaticity condition is stronger than the earlier assumption (7.17) for $W > \xi_0$.

The adiabatic scattering matrix depends only on the energy difference,

$$S(E, E') = \int_{-\infty}^{\infty} dt \, e^{i(E-E')t} S(t), \qquad (7.22)$$

it is the Fourier transform of the "frozen" scattering matrix $S(t)$ — evaluated for fixed value $\phi(t)$ of the superconducting phase difference. The transmission and reflection amplitudes $\tau(E, E') = \tau(E-E')$ and $\rho(E, E') = \rho(E - E')$ are likewise the Fourier transform of the "frozen" counterparts $\tau(t)$ and $\rho(t)$.

The adiabatic scattering matrix of a Josephson junction between counterpropagating edge modes is given by [246]

$$S(t) = \begin{pmatrix} 1/\cosh \beta(t) & \tanh \beta(t) \\ \tanh \beta(t) & -1/\cosh \beta(t) \end{pmatrix}, \quad \beta(t) = \frac{W}{\xi_0} \cos(\pi t/T). \quad (7.23)$$

The corresponding transmission and reflection amplitudes

$$\tau(t) = \tanh \beta(t), \quad \rho(t) = 1/\cosh \beta(t) \qquad (7.24)$$

are plotted in Fig. 7.2. The transmission amplitude is periodic with period $2T$, twice the period of the superconducting phase $\phi(t)$ because a 2π increment of ϕ is a π increment of the fermionic phase.

We write the charge noise formula (7.20) in the time domain, with a detection window $(0, 2\mathcal{N}T)$ that is a multiple of the periodicity $2T$,

$$\text{Var}\, Q = -\frac{e^2}{4\pi^2} \int_0^{2\mathcal{N}T} dt \int_0^{2\mathcal{N}T} dt' \, \frac{\tau(t)\tau(t') + \rho(t)\rho(t')}{(t - t' + i\varepsilon)^2}. \qquad (7.25)$$

The singularity at $t = t'$ is regularized by the infinitesimal $\varepsilon > 0$. The charge noise per vortex is

$$\text{Var}\, Q_{\text{vortex}} = \frac{1}{2} \lim_{\mathcal{N} \to \infty} \frac{1}{\mathcal{N}} \text{Var}\, Q, \qquad (7.26)$$

the factor of $1/2$ is there because two vortices are injected into each edge in a time $2T$.
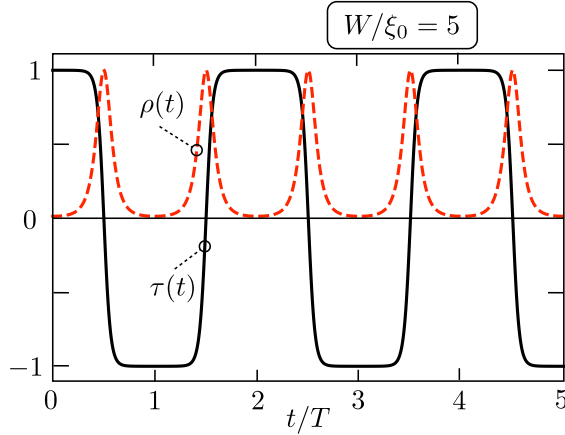
Figure 7.2. Plot of the transmission and reflection amplitudes (7.24), calculated for a linearly increasing phase difference $\phi(t) = 2\pi t/T$ across the Josephson junction. The junction fully reflects the counterpropagating Majorana edge modes when $\phi = \pi$ modulo 2π.

In view of the periodicity $\tau(t + 2T) = \tau(t)$, $\rho(t + 2T) = \rho(t)$ we have

$$\operatorname{Var} Q_{\text{vortex}} = -\lim_{\mathcal{N}\to\infty} \frac{e^2}{8\mathcal{N}\pi^2} \sum_{n=0}^{\mathcal{N}} \sum_{m=0}^{\mathcal{N}} \int_0^{2T} dt \int_0^{2T} dt' \frac{\tau(t)\tau(t') + \rho(t)\rho(t')}{(t - t' + 2T(n - m) + i\varepsilon)^2}$$

$$= -\frac{e^2}{32T^2} \int_0^{2T} dt \int_0^{2T} dt' \frac{\tau(t)\tau(t') + \rho(t)\rho(t')}{\sin^2[\frac{1}{2}(\pi/T)(t - t' + i\varepsilon)]}$$

$$= -\frac{e^2}{32\pi^2} \int_0^{2\pi} dt \int_0^{2\pi} dt' \frac{\sinh\left(\frac{W}{\xi_0}\cos t\right)\sinh\left(\frac{W}{\xi_0}\cos t'\right) + 1}{\sin^2[\frac{1}{2}(t - t' + i\varepsilon)]\cosh\left(\frac{W}{\xi_0}\cos t\right)\cosh\left(\frac{W}{\xi_0}\cos t'\right)}.$$

$$(7.27)$$

Because of the identity

$$\int_0^{2\pi} dt \int_0^{2\pi} dt' \frac{1}{\sin^2[\frac{1}{2}(t - t' + i\varepsilon)]} = 0, \qquad (7.28)$$

we may rewrite the integral (7.27) as

$$\operatorname{Var} Q_{\text{vortex}} = -\frac{e^2}{32\pi^2} \int_0^{2\pi}\int_0^{2\pi} \frac{dt\,dt'\left[1 - \cosh\left(\frac{W}{\xi_0}(\cos t - \cos t')\right)\right]}{\sin^2[\frac{1}{2}(t - t')]\cosh\left(\frac{W}{\xi_0}\cos t\right)\cosh\left(\frac{W}{\xi_0}\cos t'\right)}.$$
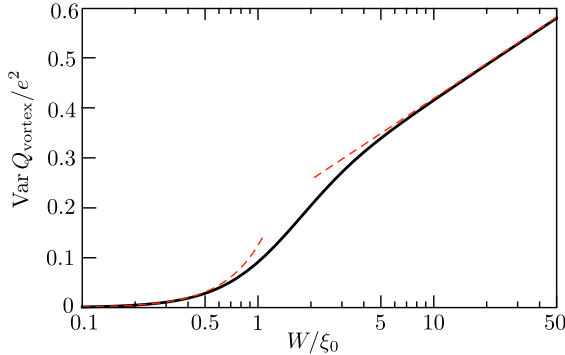
$$(7.29)$$

Figure 7.3. Plot of the charge noise per vortex as a function of the ratio W/ξ_0 (logarithmic scale). The solid curve is computed from Eq. (7.29), the dashed curves are the asymptotes (7.30).

The infinitesimal ε may now be set to zero, the integral remains finite.

The W-dependence of $\mathrm{Var}\,Q_{\mathrm{vortex}}$ is plotted in Fig. 7.3. The asymptotics for small and for large W/ξ_0 are[1]

$$\mathrm{Var}\,Q_{\mathrm{vortex}} = \frac{e^2}{8}(W/\xi_0)^2 \ \ \text{for}\ \ W/\xi_0 \ll 1,$$

$$\mathrm{Var}\,Q_{\mathrm{vortex}} = \frac{e^2}{\pi^2}\ln(2\pi W/\xi_0) \ \ \text{for}\ \ W/\xi_0 \gg 1.$$

(7.30)

The large-W asymptotics can be written equivalently as Eq. (7.1), with a logarithmic dependence on the ratio of the separation $L = 2\pi v_{\mathrm{F}}/\dot{\phi}$ between subsequent edge vortices and the width $\lambda = (v_{\mathrm{F}}/\dot{\phi})(\xi_0/W)$ of the phase boundary which represents the core of the edge vortex.[2]

7.5 Discussion

The experimental observable in a shot noise measurement is the noise power P, being the correlator of the time dependent current fluctuations $\delta I(t)$:

$$P = \int_{-\infty}^{\infty} dt\, \langle \delta I(0)\delta I(t)\rangle = \lim_{t\to\infty} \frac{1}{t}\left(\langle Q(t)^2\rangle - \langle Q(t)\rangle^2\right). \qquad (7.31)$$

---

[1]For the small-W asymptotics, expansion of the integrand in Eq. (7.29) to second order in W/ξ_0 gives $(W/\xi_0)^2[\cos(t+t')-1]$, which is then readily integrated. For the large-W asymptotics, see App. 7.8.

[2]The time $\lambda/v_{\mathrm{F}} = \hbar/E_{\mathrm{inelastic}}$ is the width of the peaks in $\rho(t)$ in Fig. 7.2.
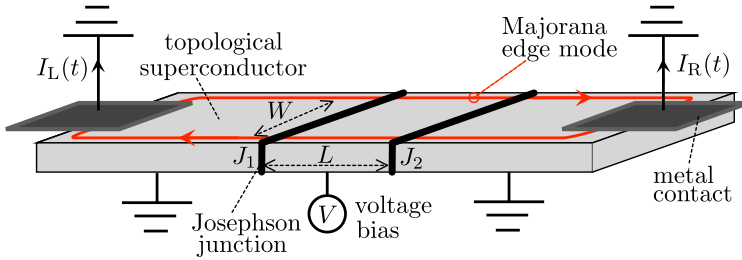
Figure 7.4. Variation on the geometry of Fig. 7.1b, with two Josephson junctions instead of a single junction, and a voltage bias instead of a flux bias. The shot noise power increases as $V \ln V$ with the applied voltage.

Here $Q(t)$ is the transferred charge in a time t.

For the flux-biased vortex injector of Fig. 7.1b the result (7.1) implies that

$$P_{\text{vortex}} = \frac{1}{T} \operatorname{Var} Q_{\text{vortex}} = \frac{e^2}{h} \frac{2e\dot{\Phi}}{\pi^2} \ln(L/\lambda), \ \ \text{for} \ \ L \gg \lambda. \tag{7.32}$$

We contrast this with the shot noise power of the fermion injector of Fig. 7.1a, given by [260]

$$P_{\text{fermion}} = \frac{e^2}{h} \frac{eV}{2}. \tag{7.33}$$

A flux rate of change $\dot{\Phi}$ is equivalent to a voltage bias V, so the replacement $\dot{\Phi} \leftrightarrow V$ in the two formulas is expected. The key difference is the appearance of a logarithmic dependence of the vortex shot noise on the separation of subsequent vortices. There is no such dependence on the Majorana fermion separation. This nonlocality suggests that an unpaired edge vortex has a divergent charge noise, which indeed it does (see App. 7.9).

To observe the anomalous dependence of P_{vortex} on the edge vortex separation, one would need to be able to vary the ratio L/λ. In the geometry of Fig. 7.1b one has $L/\lambda = 2\pi W/\xi_0$, so this ratio is fixed by the parameters of the Josephson junction. Since it might be problematic to engineer a junction with adjustable width, we show in Fig. 7.4 an alternative double-junction geometry where the ratio L/λ can be varied at a fixed geometry by a voltage bias.

A 2π increment of ϕ injects two vortices on each edge, one for each Josephson junction. The separation L of the edge vortices now equals the spacing between the two Josephson junctions, so this length is fixed

by the geometry. However, the vortex core size $\lambda = (v_F/\dot{\phi})(\xi_0/W) = (hv_F/2eV)(\xi_0/W)$ can be adjusted by varying the voltage bias V, allowing for a measurement of the anomalous L/λ dependence of the shot noise power in a fixed geometry. The resulting logarithmic voltage dependence of the shot noise power,[3]

$$P_{\text{vortex}} = \frac{e^2}{h} \frac{4eV}{\pi^2} \ln(V/V_c), \quad V_c = \frac{\hbar v_F \xi_0}{2eLW}, \tag{7.34}$$

holds over wide voltage range $V_c \ll V \ll (W/\xi_0)V_c$ for $W \gg \xi_0$. This $V \ln V$ increase of P_{vortex} contrasts with the purely linear voltage dependence of P_{fermion} and serves as a distinguishing signature between these two types of excitations of a Majorana edge mode, a signature that is accessible by a purely electrical transport measurement.

7.6 Appendix: Consistency of Eq. (7.9) with the Klich formula for the cumulant generating function

In the main text we derived the formula (7.9) for the variance of the transmitted charge directly from the contractions (7.6). We showed that the anomalous contraction of two creation operators has the effect of eliminating one of the projectors onto positive energies. As a check, we show here how the same result follows from the Klich formula [261] in the theory of full counting statistics.

We note the sequence of equalities

$$\begin{aligned}
\text{Var}\,Q &= \text{Tr}\,\mathcal{P}_-S^\dagger\mathcal{D}\mathcal{P}_+S - \text{Tr}\,\mathcal{P}_-S^\dagger\sigma_z\mathcal{D}\mathcal{P}_+S\mathcal{P}_-S^\dagger\sigma_z\mathcal{D}S \\
&= \text{Tr}\,\mathcal{P}_-S^\dagger\sigma_z\mathcal{D}\mathcal{P}_+S\mathcal{P}_+S^\dagger\sigma_z\mathcal{D}S \\
&= \text{Tr}\,\mathcal{P}_-S^\dagger\sigma_z\mathcal{D}\mathcal{P}_-S\mathcal{P}_+S^\dagger\sigma_z\mathcal{D}S. \tag{7.35}
\end{aligned}$$

For the second equality we substituted $S\mathcal{P}_-S^\dagger = 1 - S\mathcal{P}_+S^\dagger$ and used $(\sigma_z\mathcal{D})^2 = \mathcal{D}$. The third equality follows from particle-hole symmetry.[4]

---

[3]The calculation of the charge variance for the geometry of Fig. 7.4 is worked out in App. 7.10.

[4]The particle-hole symmetry relation (7.3) of the scattering matrix implies that traces of the form (7.35) are invariant upon the replacements: $\text{Tr}\,M \mapsto \text{Tr}\,M^\dagger$, $\sigma_z \mapsto -\sigma_z$, $\mathcal{P}_\pm \mapsto \mathcal{P}_\mp$.

Hence, by adding the second and third equality we arrive at

$$\operatorname{Var} Q = \tfrac{1}{2} \operatorname{Tr} \mathcal{P}_- S^\dagger \sigma_z \mathcal{D} S \mathcal{P}_+ S^\dagger \sigma_z \mathcal{D} S. \tag{7.36}$$

Each factor $\sigma_z \mathcal{D}$ now appears without an energy projector. Similarly, the expression (7.7) for the average charge can be rewritten identically as[5]

$$\langle Q \rangle = \tfrac{1}{2} \operatorname{Tr} \mathcal{P}_- S^\dagger \sigma_z \mathcal{D} S, \tag{7.37}$$

without the energy projector multiplying $\sigma_z \mathcal{D}$.

Eqs. (7.36) and (7.37) agree with the Klich formula for the cumulant generating function[6] [258]

$$\ln\langle e^{i\xi Q} \rangle = \tfrac{1}{2} \ln \operatorname{Det} \left[1 - \mathcal{P}_- + \mathcal{P}_- S^\dagger e^{i\xi \sigma_z \mathcal{D}} S \right]$$
$$= \tfrac{1}{2} i\xi \operatorname{Tr} \mathcal{P}_- S^\dagger \sigma_z \mathcal{D} S - \tfrac{1}{4} \xi^2 \operatorname{Tr} \mathcal{P}_- S^\dagger \sigma_z \mathcal{D} S \mathcal{P}_+ S^\dagger \sigma_z \mathcal{D} S + \mathcal{O}(\xi^3). \tag{7.38}$$

7.7   Appendix: Proof of Eq. (7.18)

To show that the three matrix products (7.18) all vanish, we substitute the decompositions (7.14) and (7.16) of the transmission and reflection matrices. Because the reflection matrix in Eq. (7.18) is sandwiched between projectors $\mathcal{P}_+$ and $\mathcal{P}_-$, the elastic contribution d_{nm} in Eq. (7.16) drops out. The inelastic contributions to each matrix product contain the same factor

$$\sum_{n=1}^{M} u_n^\dagger(E) \sigma_z u_n(E) = \sum_{n=1}^{M} u_n^{\mathrm{T}}(-E)(\sigma_x \cdot \sigma_z) u_n(E) = -i \sum_{n=1}^{M} u_n^{\mathrm{T}}(-E)\sigma_y u_n(E), \tag{7.39}$$

where in the second equality we used particle-hole symmetry.

We now make the assumption, valid for $W \ll v_{\mathrm{F}}/\dot{\phi}$, that we can neglect the energy dependence of the elastic coupling amplitude $u_n(E) \approx u_n(0)$ between the right-moving Majorana mode and the right contact. Then Eq. (7.39) reduces to zero because σ_y is an antisymmetric matrix, hence $u_n^T \sigma_y u_n = 0$.

---

[5]Eq. (7.37) follows from Eq. (7.7) in view of equalities $\operatorname{Tr} \mathcal{P}_- S^\dagger \sigma_z \mathcal{D} \mathcal{P}_+ S = -\operatorname{Tr} \mathcal{P}_+ S^\dagger \sigma_z \mathcal{D} \mathcal{P}_+ S = \operatorname{Tr} \mathcal{P}_+ S^\dagger \sigma_z \mathcal{D} \mathcal{P}_- S$. The first equality holds because $\operatorname{Tr} S^\dagger \sigma_z \mathcal{D} \mathcal{P}_+ S = 0$, the second equality follows from particle-hole symmetry.

[6]In Eq. (3.12) of Ref. [258] the generating function contains a σ_y instead of a σ_z Pauli matrix, because there the Majorana basis instead of the electron-hole basis is chosen for the Nambu spinors.

7.8 Appendix: Computation of the logarithmic asymptote of the charge noise

To derive the logarithmic large-W asymptotics of Eq. 7.30, we note that for $W \gg \xi_0$ the scattering amplitude profile (7.23) is well described by the approximation [255]

$$\tau(t) = \begin{cases} -\tanh[\frac{1}{2}(t - T/2)/t_0] & \text{for } 0 < t < T, \\ \tanh[\frac{1}{2}(t - 3T/2)/t_0] & \text{for } T < t < 2T, \end{cases} \quad (7.40a)$$

$$\rho(t) = \begin{cases} 1/\cosh[\frac{1}{2}(t - T/2)/t_0] & \text{for } 0 < t < T, \\ 1/\cosh[\frac{1}{2}(t - 3T/2)/t_0] & \text{for } T < t < 2T, \end{cases} \quad (7.40b)$$

$$t_0 = (\xi_0/W)(T/2\pi), \quad (7.40c)$$

repeated periodically with period $2T$. On the scale of Fig. 7.2, with $W/\xi_0 = 5$, the approximation is nearly indistinguishable from the full result.

The Fourier coefficients

$$\tau(\omega_n) = \int_0^{2T} dt\, e^{i\omega_n t}\tau(t), \quad \rho(\omega_n) = \int_0^{2T} dt\, e^{i\omega_n t}\rho(t), \quad \omega_n = \pi n/T, \quad (7.41)$$

in the large-W/ξ_0 regime can be calculated from the integrals

$$\begin{aligned} \int_{-\infty}^{\infty} dt\, e^{i\omega t}\tanh(\tfrac{1}{2}t/t_0) &= \frac{2\pi i t_0}{\sinh(\pi\omega t_0)}, \\ \int_{-\infty}^{\infty} dt\, e^{i\omega t}\frac{1}{\cosh(\tfrac{1}{2}t/t_0)} &= \frac{2\pi t_0}{\cosh(\pi\omega t_0)}, \end{aligned} \quad (7.42)$$

with the result

$$\tau(\omega_n) = \left(e^{i\omega_n \frac{T}{2}} - e^{i\omega_n \frac{3T}{2}}\right)\frac{2\pi i t_0}{\sinh(\pi\omega_n t_0)} \Rightarrow |\tau(\omega_n)|^2 = \delta_{n,\text{odd}}\frac{(4\pi t_0)^2}{\sinh^2(\pi\omega_n t_0)},$$

$$\rho(\omega_n) = \left(e^{i\omega_n \frac{T}{2}} + e^{i\omega_n \frac{3T}{2}}\right)\frac{2\pi t_0}{\cosh(\pi\omega_n t_0)} \Rightarrow |\rho(\omega_n)|^2 = \delta_{n,\text{even}}\frac{(4\pi t_0)^2}{\cosh^2(\pi\omega_n t_0)}.$$
$$(7.43)$$

The charge noise per vortex then follows by writing Eq. (7.20) as a Fourier series,

$$\text{Var}\, Q_{\text{vortex}} = \frac{e^2}{4\pi^2}\frac{\pi}{2T}\sum_{n=0}^{\infty}\omega_n\left(|\tau(\omega_n)|^2 + |\rho(\omega_n)|^2\right). \quad (7.44)$$

For $T/t_0 = 2\pi W/\xi_0 \gg 1$ the sum may be approximated by an integral and produces the logarithmic growth

$$\operatorname{Var} Q_{\mathrm{vortex}} \to \frac{e^2}{\pi^2} \ln(T/t_0), \ \ \text{for} \ \ T \gg t_0. \tag{7.45}$$

7.9 Appendix: Divergent charge noise for an unpaired edge vortex

If a single vortex is injected into each edge, the scattering amplitudes (7.40) in the time interval $(0, T)$ hold for all times,

$$
\begin{aligned}
\tau(t) &= -\tanh(\tfrac{1}{2}t/t_0) \Rightarrow \tau(E, E') = -\frac{2\pi i t_0}{\sinh[\pi(E - E')t_0]}, \\
\rho(t) &= 1/\cosh(\tfrac{1}{2}t/t_0) \Rightarrow \rho(E, E') = \frac{2\pi t_0}{\cosh[\pi(E - E')t_0]}.
\end{aligned}
\tag{7.46}
$$

Substitution into Eq. (7.20) gives an expression for the charge noise,

$$\operatorname{Var} Q = e^2 t_0^2 \int_0^\infty dE\, E \left(\frac{1}{\sinh^2 \pi E t_0} + \frac{1}{\cosh^2 \pi E t_0} \right), \tag{7.47}$$

with a logarithmic divergence at $E = 0$.

For a finite answer we may introduce a finite detection time t_{det}, cutting off the integral for $E \lesssim 1/t_{\mathrm{det}}$, which gives

$$\operatorname{Var} Q = \frac{e^2}{\pi^2} \ln(t_{\mathrm{det}}/t_0), \ \ \text{for} \ \ t_{\mathrm{det}} \gg t_0. \tag{7.48}$$

In the case of a periodic sequence of edge vortices considered in the main text, the spacing T between subsequent vortices takes over from t_{det} to provide a finite charge variance.

7.10 Appendix: Charge noise in a double - Josephson junction geometry

In Fig. 7.4 we have modified the geometry of Fig. 7.1b to include a second Josephson junction next to the first. A flux bias, or equivalently a voltage bias as in the figure, will then inject two edge vortices on each edge.

The scattering matrix of the pair of Josephson junctions is composed from the scattering matrices S_{J_1}, S_{J_2} of the individual junctions, for which we take the adiabatic approximation,

$$S_{J_n}(E, E') = \int_{-\infty}^{\infty} dt\, e^{i(E-E')t} S_{J_n}(t),$$

$$S_{J_n}(t) = \begin{pmatrix} \sin\alpha_n(t) & \cos\alpha_n(t) \\ \cos\alpha_n(t) & -\sin\alpha_n(t) \end{pmatrix}, \quad \alpha_n(t) = \arccos\tanh\beta(t). \tag{7.49}$$

Adiabaticity requires that the time W/v_{F} to move from one edge to the opposite edge along a junction is short compared to the vortex injection time $t_0 = (\xi_0/W)\dot{\phi}^{-1}$. The time L/v_{F} to move from one junction to the next may be large compared to t_0.

The phase fields $\alpha_1(t)$ and $\alpha_2(t)$ of the two Josephson junctions both switch from 0 to π on a time scale t_0 around $t = 0$.[7] If $\lambda = v_{\mathrm{F}}t_0 \ll L$ the two edge vortices injected by these switching events do not overlap. We consider that regime in what follows and for ease of notation set $v_{\mathrm{F}} \equiv 1$.

The transmission amplitude $\tau(E, E')$ from left to right and the reflection amplitude $\rho(E, E')$ from the right are given in the time domain by

$$\tau(t, t') = \delta(t - t' - L)\cos\alpha_2(t' + L)\cos\alpha_1(t'),$$
$$\rho(t, t') = \delta(t - t')\sin\alpha_2(t) +$$
$$+ \delta(t - t' - 2L)\cos\alpha_2(t' + 2L)\sin\alpha_1(t' + L)\cos\alpha_2(t'). \tag{7.50}$$

The assumption $L \gg \lambda$ prevents the appearance of terms delayed by more than $2L$, or equivalently, there are no multiple reflections at the junctions.

Using again that $L \gg \lambda$ we note that $\cos\alpha_2(t' + 2L)\cos\alpha_2(t') \approx -1$ whenever $\sin\alpha_1(t' + L)$ is nonzero, hence we may simplify the expression for ρ into

$$\rho(t, t') = \delta(t - t')\sin\alpha_2(t) - \delta(t - t' - 2L)\sin\alpha_1(t' + L). \tag{7.51}$$

At the same level of approximation, we have

$$\tau(t, t') = \delta(t - t' - L)[\cos\alpha_2(t' + L) - \cos\alpha_1(t') + 1]. \tag{7.52}$$

---

[7]For counterpropagating edge modes the phase α is an *even* function of the phase difference ϕ across the Josephson junction [246]. For co-propagating edge modes, in contrast, α is an *odd* function of ϕ and in that case α_1 and α_2 would have opposite sign [255].

Transformation to the energy domain gives

$$
\tau(E, E') = e^{iE'L} \left[c_2(E - E') - e^{i(E-E')L} c_1(E - E') + 2\pi\delta(E - E') \right],
$$
$$
\rho(E, E') = s_2(E - E') - e^{i(E+E')L} s_1(E - E'),
$$

$$(7.53)$$

with the definitions

$$
c_n(E) = \int_{-\infty}^{\infty} dt \, e^{iEt} \cos\alpha_n(t), \quad s_n(E) = \int_{-\infty}^{\infty} dt \, e^{iEt} \sin\alpha_n(t). \quad (7.54)
$$

The dominant contribution to the charge noise in Eq. (7.20) comes from the transmission amplitude, because of the $1/E$ singularity of $c_1(E)$ and $c_2(E)$ according to Eq. (7.46). For the single-vortex noise we needed a finite detection time to cut off the singularity, here the spacing L of the vortices is an effective cut-off in the case $c_1 = c_2$ of two identical tunnel junctions. Then we find

$$
\operatorname{Var} Q \approx e^2 \lambda^2 \int_0^{\infty} dE \, E \, \frac{|1 - e^{iEL}|^2}{\sinh^2 \pi E\lambda} \rightarrow \frac{2e^2}{\pi^2} \ln(L/\lambda), \text{ for } L \gg \lambda. \quad (7.55)
$$

This is twice the result (7.1) because it refers to two vortices.

A constant applied voltage V cause the superconducting phase to increase linearly in time, $\dot\phi = 2eV/\hbar$, hence $\lambda = v_{\mathrm{F}}(\xi_0/W)(\hbar/2eV)$. If $V \ll \hbar v_{\mathrm{F}}/eL$ the injected edge vortices from subsequent periods do not overlap. The resulting shot noise power $P = (\dot\phi/2\pi)\operatorname{Var} Q$ takes the form

$$
P = \frac{e^2}{h} \frac{4eV}{\pi^2} \ln\left(\frac{2eV LW}{\hbar v_{\mathrm{F}} \xi_0}\right), \text{ for } \frac{\hbar v_{\mathrm{F}}}{L} \frac{\xi_0}{W} \ll eV \ll \frac{\hbar v_{\mathrm{F}}}{L}. \quad (7.56)
$$

Chapter 8

Voltage staircase

8.1 Introduction

A single-mode weak link between superconductors supports a two-level system with a spacing that is adjustable via the superconducting phase difference [263, 264]. Because Andreev reflection is at the origin of the phase sensitivity, the levels are called Andreev levels. Although their existence was implicit in early studies of the Josephson effect [265], the characteristic dependence $\propto \sqrt{1 - \tau \sin^2(\phi/2)}$ of the level spacing on the phase ϕ, with τ the transmission probability, was only identified [266] with the advent of nanostructures. The present interest in quantum information processing is driving theoretical [267, 268] and experimental [269–272] studies of Andreev levels as qubits.

To assess the coherence of the qubit one would use AC microwave radiation of the two-level system and perform a time-resolved detection of the Rabi oscillations of the wave function [273]. In this work we will show how a DC current I_{DC} and measurement of the time-averaged voltage $\bar{V}$ can be used to detect Rabi oscillations of an Andreev qubit: The staircase dependence of $\bar{V}$ on I_{DC} counts the number of Rabi oscillations per 2π increment of ϕ.

Our study is motivated by Choi, Calzona, and Trauzettel's report [55] of such a remarkable effect (dubbed "DC Shapiro steps") in a Majorana qubit — which is the building block of a topological quantum computer. As we will see, neither the unique topological properties of a Majorana qubit (its non-Abelian braiding and fusion rules) nor its specific symmetry class (class D, with broken time-reversal and spin-rotation symmetry)
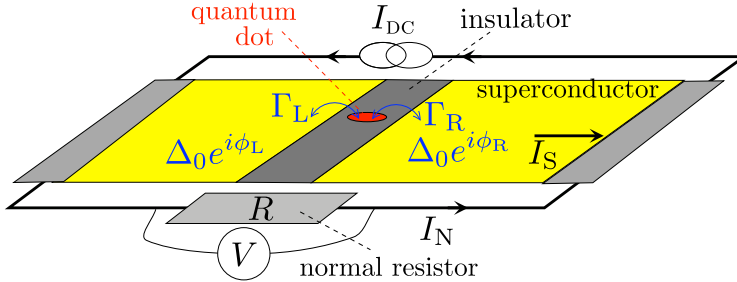
Figure 8.1. Current-biased, resistively-shunted Josephson junction, formed out
of two superconductors (phases ϕ_L and ϕ_R) separated by an insulator containing
a quantum dot (tunnel rates Γ_L and Γ_R from the left and from the right). The
superconducting phases become time dependent when a voltage difference V
develops in response to a DC current I_{DC}.

are needed, a similar phenomenology can be found in a non-topological
Andreev qubit with preserved symmetries (class CI).

The outline of this paper is as follows. In the next section 8.2 we
present the model of the weak link that we will consider: a quantum
dot connecting two superconductors with a tunnel rate Γ small compared
to the superconducting gap Δ_0. Such a Josephson junction has been
extensively studied [274–276] in the regime where Coulomb charging and
the Kondo effect govern the charge transfer [277–279]. We will assume the
charging energy is small and treat the quasiparticles as noninteracting.

The dynamics of a current-biased, resistively shunted quantum-dot
Josephson junction is studied in Secs. 8.3 and 8.4. The voltage staircase
is shown in Fig. 8.3 and the one-to-one relationship with the number of
Rabi oscillations is in Fig. 8.6. In the concluding section 7.5 we will explain
why the substitution of the quantum dot by a quantum point contact will
remove the voltage staircase.

8.2   Andreev level Hamiltonian

We consider the Josephson junction shown in Fig. 8.1, consisting of a
quantum dot in the normal state (N) coupled via a tunnel barrier to
superconductors (S) at the left and right, with pair potentials $\Delta_0 e^{i\phi_L}$ and
$\Delta_0 e^{i\phi_R}$. We focus on the weakly coupled regime, when the tunnel rates
Γ_L and Γ_R through the barrier are small compared to Δ_0.

We assume that the fully isolated quantum dot has a single electronic

energy level E_0 within an energy range $\Gamma = \Gamma_L + \Gamma_R$ from the Fermi energy μ. The normal-state conductance G_N is then given by the Breit-Wigner formula

$$G_N = \frac{2e^2}{h}\tau_{BW}, \quad \tau_{BW} = \frac{\Gamma_L \Gamma_R}{(E_0 - \mu)^2 + \frac{1}{4}\Gamma^2}. \tag{8.1}$$

Coupling of electrons and holes by Andreev reflection from the superconductor produces a pair of Andreev levels at energies $\pm E_A(\phi)$, dependent on the phase difference $\phi = \phi_L - \phi_R$ between the left and right superconductors.

A simplifying assumption of our analysis is that the Coulomb charging energy U is small compared to Γ and can be neglected. If U is larger than Γ but still smaller than Δ_0, the main effect of the charging energy is a shift of the energy level of the dot, $E_0 \mapsto E_0 + U/2$. Provided $E_0 > 0$ the ground state remains a spin-singlet [280], and we do not expect a qualitative change in our results. If U becomes larger than Δ_0 the supercurrent is reduced by a factor Γ/Δ_0 because tunneling of a Cooper pair into the quantum dot is suppressed [277–279].

To describe the non-equilibrium dynamics of the junction we seek the effective low-energy Hamiltonian of time-dependent Andreev levels. This requires information not only on the eigenvalues but also on the eigenfunctions. In subsections 8.2.1 and 8.2.2 we summarize results from Refs. [280–283] for the time-independent situation, which we need as input for the dynamical study starting from subsection 8.2.3.

8.2.1   Andreev levels

For arbitrary ratio of Γ and Δ_0 the energies of the Andreev levels are equal to the two real solutions $\pm E_A$ of the equation [281, 282]

$$\Omega(E, \phi) + \Gamma E^2 \sqrt{\Delta_0^2 - E^2} = 0, \tag{8.2}$$

with

$$\begin{aligned} \Omega(E, \phi) &= (\Delta_0^2 - E^2)\left[E^2 - (E_0 - \mu)^2 - \tfrac{1}{4}\Gamma^2\right] \\ &\quad + \Delta_0^2 \Gamma_L \Gamma_R \sin^2(\phi/2). \end{aligned} \tag{8.3}$$

In the weak-coupling regime $\Gamma \ll \Delta_0$, assuming also $|E_0 - \mu| \ll \Delta_0$, this reduces to

$$\begin{aligned} E_A &= \Delta_{eff}\sqrt{1 - \tau_{BW}\sin^2(\phi/2)}, \\ \Delta_{eff} &= \sqrt{(E_0 - \mu)^2 + \tfrac{1}{4}\Gamma^2}, \end{aligned} \tag{8.4}$$
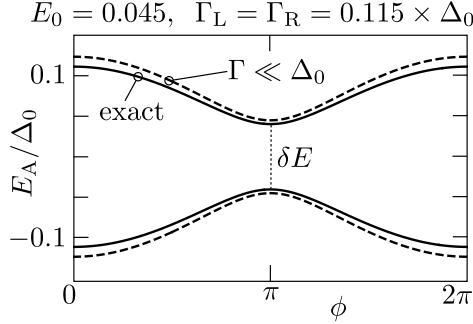
Figure 8.2. Andreev levels $\pm E_A(\phi)$ according to the full expression (8.2) (solid curve) and in the weak-coupling approximation (8.4) (dashed curve, parameters $E_0 = 0.045$, $\mu = 0$, $\Gamma_L = \Gamma_R = 0.115$, all in units of Δ_0).

no longer dependent on Δ_0. The two Andreev levels have an avoided crossing at $\phi = \pi$, separated by an energy

$$\delta E = \sqrt{4(E_0 - \mu)^2 + (\Gamma_L - \Gamma_R)^2}, \tag{8.5}$$

see Fig. 8.2.

The equilibrium supercurrent, at temperatures $k_B T \ll \Gamma$, is given by

$$I_{eq}(\phi) = -\frac{2e}{\hbar}\frac{dE_A}{d\phi} = \frac{e\Gamma_L\Gamma_R \sin\phi}{2\hbar E_A(\phi)}, \tag{8.6}$$

with critical current (maximal supercurrent)

$$I_c = \frac{e}{\hbar}\left(\sqrt{(E_0 - \mu)^2 + \tfrac{1}{4}\Gamma^2} - \sqrt{(E_0 - \mu)^2 + \tfrac{1}{4}\Gamma^2 - \Gamma_L\Gamma_R}\right). \tag{8.7}$$

There is no contribution from the continuous spectrum in the weak-coupling regime [281].

8.2.2   Effective Hamiltonian: time-independent phase

For time-independent phases the effective low-energy Hamiltonian in the weak-coupling regime $\Gamma \ll \Delta_0$ follows from second-order perturbation theory [280, 283],

$$H = -\tfrac{1}{2}\big(e^{i\phi_L}\Gamma_L + e^{i\phi_R}\Gamma_R\big)a_\uparrow^\dagger a_\downarrow^\dagger + \text{H.c.} + (E_0 - \mu)(a_\uparrow^\dagger a_\uparrow + a_\downarrow^\dagger a_\downarrow). \tag{8.8}$$

Here $a_\uparrow$ and $a_\downarrow$ are the fermionic annihilation operators of a spin-up or spin-down electron in the quantum dot.

The corresponding Bogoliubov-De Gennes (BdG) Hamiltonian $\mathcal{H}$ is a 4×4 matrix contracted with the spinors $\Psi = (a_\uparrow, -a_\downarrow^\dagger, a_\downarrow, -a_\uparrow^\dagger)$ and $\Psi^\dagger$,

$$H = \tfrac{1}{2}\Psi^\dagger \cdot \mathcal{H} \cdot \Psi + E_0 - \mu. \tag{8.9}$$

It is block-diagonal, so we only need to consider one 2×2 block, given by

$$\mathcal{H} = \begin{pmatrix} E_0 - \mu & \tfrac{1}{2}e^{i\phi_\mathrm{L}}\Gamma_\mathrm{L} + \tfrac{1}{2}e^{i\phi_\mathrm{R}}\Gamma_\mathrm{R} \\ \tfrac{1}{2}e^{-i\phi_\mathrm{L}}\Gamma_\mathrm{L} + \tfrac{1}{2}e^{-i\phi_\mathrm{R}}\Gamma_\mathrm{R} & \mu - E_0 \end{pmatrix}. \tag{8.10}$$

One readily checks that the eigenvalues $\pm E_\mathrm{A}$ of $\mathcal{H}$ are given by Eq. (8.4).

8.2.3   Effective Hamiltonian: time-dependent phase

When the left and right superconductors are at different voltages $\pm V/2$, the superconducting phase becomes time dependent. We choose a gauge such that $\phi_\mathrm{L}(t) = \phi(t)/2$, $\phi_\mathrm{R}(t) = -\phi(t)/2$, evolving in time according to the Josephson relation

$$\dot\phi \equiv d\phi/dt = (2e/\hbar)V. \tag{8.11}$$

The voltage bias imposes an electrical potential on the quantum dot, which shifts μ by an amount $\tfrac{1}{2}\gamma eV$ with $\gamma = (\Gamma_\mathrm{L} - \Gamma_\mathrm{R})/\Gamma$. The time dependent BdG Hamiltonian then becomes

$$\mathcal{H}(t) = \begin{pmatrix} E_0 - \mu - \tfrac{1}{4}\hbar\gamma\dot\phi(t) & \tfrac{1}{2}e^{i\phi(t)/2}\Gamma_\mathrm{L} + \tfrac{1}{2}e^{-i\phi(t)/2}\Gamma_\mathrm{R} \\ \tfrac{1}{2}e^{-i\phi(t)/2}\Gamma_\mathrm{L} + \tfrac{1}{2}e^{i\phi(t)/2}\Gamma_\mathrm{R} & \mu - E_0 + \tfrac{1}{4}\hbar\gamma\dot\phi(t) \end{pmatrix}$$
$$= [E_0 - \mu - \tfrac{1}{4}\hbar\gamma\dot\phi(t)]\sigma_z + \tfrac{1}{2}\Gamma[\sigma_x \cos\tfrac{1}{2}\phi(t) - \gamma\sigma_y \sin\tfrac{1}{2}\phi(t)]. \tag{8.12}$$

The Pauli matrices act on the electron-hole degree of freedom. The corresponding current operator is given by

$$I(t) = \frac{2e}{\hbar}\frac{\partial}{\partial\phi}\mathcal{H}(t) = -\frac{e\Gamma}{2\hbar}[\sigma_x \sin\tfrac{1}{2}\phi(t) + \gamma\sigma_y \cos\tfrac{1}{2}\phi(t)]. \tag{8.13}$$

Notice that the Hamiltonian (8.12) depends both on $\phi(t)$ and on $\dot\phi(t)$, unless $\Gamma_\mathrm{L} = \Gamma_\mathrm{R}$. It is possible to remove the $\dot\phi$-dependence by a time-dependent unitary transformation [1], but since this does not simplify our subsequent calculations we will keep the form (8.12).

---

[1] The time-dependent unitary transformation $\Psi \mapsto U^\dagger\Psi$, $\mathcal{H} \mapsto U^\dagger\mathcal{H}U - i\hbar U^\dagger dU/dt$ with $U(t) = e^{i\sigma_z\gamma\phi(t)/4}$ removes the $\dot\phi$-term from the Hamiltonian (8.12). The γ-parameter then appears in the superconducting phases, $\phi_\mathrm{L} = \tfrac{1}{2}(1 - \gamma)\phi$, $\phi_\mathrm{R} = -\tfrac{1}{2}(1 + \gamma)\phi$.

8.3   Voltage staircase

As shown in Fig. 8.1, a time-independent current bias I_{DC} is driven partially through the Josephson junction, as a supercurrent $I_{\mathrm{S}}(t)$, and partially through a parallel resistor R as a normal current $I_{\mathrm{N}}(t) = V(t)/R$. Substitution of the Josephson relation (8.11) gives the differential equation

$$d\phi(t)/dt = (2eR/\hbar)[I_{\mathrm{DC}} - I_{\mathrm{S}}(t)]. \tag{8.14}$$

Here we neglect the junction capacitance (overdamped regime of a resistively shunted Josephson junction) [284]. We work in the low-temperature regime, $k_{\mathrm{B}}T \ll \Delta_0$, so that we may ignore thermal fluctuations of the phase due to the voltage noise over the external resistance [285].

The supercurrent is obtained from the expectation value

$$I_{\mathrm{S}}(t) = \langle\Psi(t)|I(t)|\Psi(t)\rangle, \tag{8.15}$$

where the current operator is given by Eq. (8.13) and the wave function evolves according to the Schrödinger equation

$$i\hbar\frac{d}{dt}|\Psi(t)\rangle = \mathcal{H}(t)|\Psi(t)\rangle. \tag{8.16}$$

As initial condition we take $\phi(0) = 0$ and $|\Psi(0)\rangle$ the eigenstate of the Andreev level at $-E_{\mathrm{A}}$ for $\phi = 0$. The DC current I_{DC} is increased slowly from zero to some maximal value and then slowly decreased back to zero. The I–V characteristic is obtained by averaging $V(t)$ over a moving time window in which I_{DC} is approximately constant. [2]

Results of this numerical integration are shown in Fig. 8.3. We observe a staircase dependence of $\bar{V}$ on I_{DC}. The nonzero voltage appears at the critical current (8.7) for the up-sweep and disappears at a slightly lower current for the down sweep. (A similar difference between switching current and retrapping current was found for the Majorana qubit [286].) The voltage steps at $I_{\mathrm{DC}} > I_c$ also show hysteresis: the voltage jump up happens at larger DC current than the voltage jump down. (This hysteresis also appears in the Majorana qubit, see App. 8.6.)

---

[2]The parameters $E_0, \Gamma_{\mathrm{L}}, \Gamma_{\mathrm{R}}$ used in Fig. 8.3 are listed in each panel; additional parameters: $\mu = 0$ in both panels, $R = 0.20$ and $0.25\,\hbar/e^2$ in panels a) and b), respectively. The voltage $\bar{V}$ is averaged over a time window δt such that $\delta t \times dI_{\mathrm{DC}}/dt = 6.3 \cdot 10^{-4}\,e\Delta_0/\hbar$. To check that we are sweeping slowly enough, we reduced dI_{DC}/dt by a factor of two and found little difference.
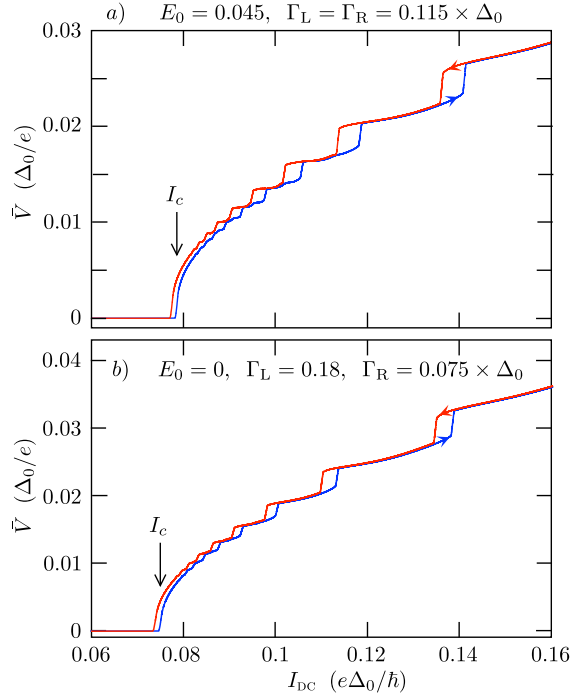
Figure 8.3. Current-voltage characteristic of the quantum-dot Josephson junction, for two different parameter sets2. The blue curve is for increasing DC current, the red curve for decreasing current. The Andreev levels in Fig. 8.2 correspond to the parameters in panel a). The critical current (8.7) is indicated by the black arrow.

8.4 Andreev qubit dynamics

The voltage staircase of Fig. 8.3 is a signature of Rabi oscillations of the Andreev qubit formed by the two Andreev levels in the Josephson junction, in much the same way that the voltage steps of Ref. [55] were driven by Rabi oscillations of a Majorana qubit. Let us investigate the Andreev qubit dynamics.

8.4.1 Adiabatic evolution

In the adiabatic regime of a slow driving, $\hbar\dot{\phi} \ll \delta E$, transitions between the Andreev levels can be neglected and the phase evolves in time as an
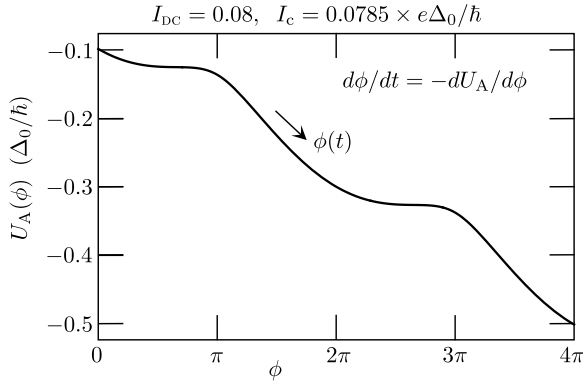
Figure 8.4. Washboard potential (8.18) that governs the time dependence of
the superconducting phase in the adiabatic limit. The curve is plotted for the
junction parameters of Figs. 8.2 and 8.3a, at a value of I_{DC} slightly above the
critical current I_{c}.

overdamped classical particle,

$$\dot{\phi} + dU_{\mathrm{A}}/d\phi = 0, \tag{8.17}$$

moving in the "washboard potential" [284]

$$U_{\mathrm{A}}(\phi) = -(2eR/\hbar)\big[\phi I_{\mathrm{DC}} + (2e/\hbar)E_{\mathrm{A}}(\phi)\big], \tag{8.18}$$

plotted in Fig. 8.4.

The time dependence of the phase resulting from integration of Eq.
(8.17) is shown in panel a) of Fig. 8.5. Panel b) tracks the adiabatic
dynamics of the Andreev qubit, by plotting the Bloch sphere coordinates
$\boldsymbol{R} = (X, Y, Z)$, with $R_\alpha(t) = \langle\Psi(t)|\sigma_\alpha|\Psi(t)\rangle$. The qubit dynamics is
4π-periodic in ϕ, because the Hamiltonian (8.12) is 4π-periodic: When
ϕ is increased by 2π one has $\mathcal{H} \mapsto \sigma_z\mathcal{H}\sigma_z$, so on the Bloch sphere the
qubit is rotated by π around the z-axis ($X \mapsto -X,\ Y \mapsto -Y$). The
full spectrum is a 2π-periodic function of ϕ, in particular the Josephson
current (8.6) is 2π-periodic — this nontopological Josephson junction does
not exhibit the 4π-periodic Josephson effect that is the hallmark of a
topological superconductor.

8.4.2 Pulsed Rabi oscillations

Panels c) and d) of Fig. 8.5 show the full non-adiabatic dynamics, obtained
by integration of Eq. (8.16) for the same parameter set as in panels a) and
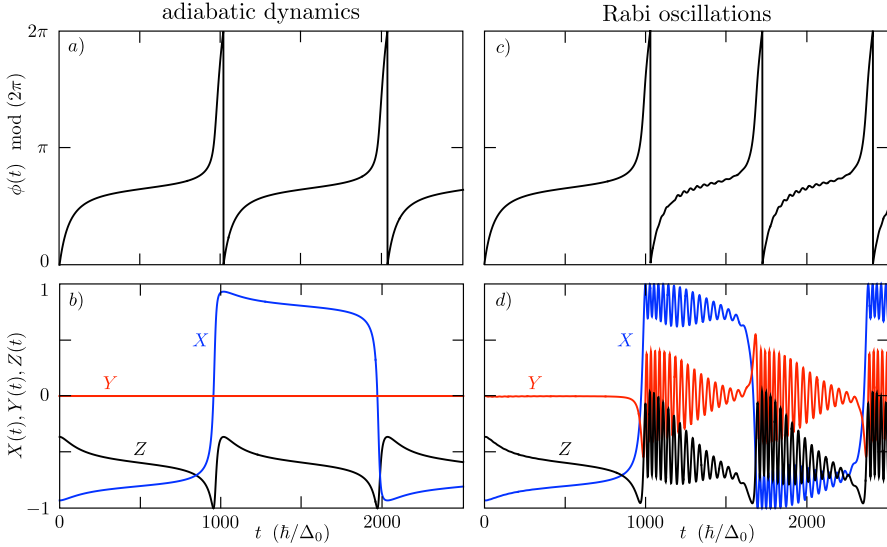
Figure 8.5. Time dependence of the superconducting phase (top row) and of the Bloch sphere coordinates of the Andreev qubit (bottom row), in the adiabatic limit (left column) and in the non-adiabatic regime in which transitions between the Andreev levels produce Rabi oscillations of the qubit (right column). The junction parameters are those of Fig. 8.3a, at $I_{\mathrm{DC}} = 0.08\,e\Delta_0/\hbar$. The wave function was initialized as an eigenstate of the lowest Andreev level $-E_{\mathrm{A}}(0)$ at $t = 0$.

b). Transitions between the Andreev levels produce pronounced Rabi oscillations of the qubit, also visible as small oscillations in $\phi(t)$.

Because the supercurrent carried by the two Andreev levels $\pm E_{\mathrm{A}}$ has the opposite sign, the inter-level transitions reduce I_{S}, thereby increasing $I_{\mathrm{N}} = I_{\mathrm{DC}} - I_{\mathrm{S}}$ and hence $\bar{V}$. This is evident from Fig. 8.5c, which shows that the first 2π increment of ϕ, without interlevel transitions, takes a time $\delta t \approx 1000\,\hbar/\Delta_0$, while the second 2π increment, with Rabi oscillations, only takes a time $\delta t = 700$. The average voltage $\bar{V} \simeq 2\pi/\delta t$ is therefore increased by a factor $10/7$ because of the interlevel transitions.

The Rabi oscillations are pulsed: they appear abruptly when ϕ crosses $(2n - 1)\pi$ and increases rapidly to $2n\pi$, which is the steepest part of the washboard potential (see Fig. 8.4).

To estimate the Rabi frequency we substitute

$$\Psi(t) = \left(u(t)e^{i\phi(t)/4}, v(t)e^{-i\phi(t)/4}\right)$$

in the Schrödinger equation (8.16) and make the rotating wave approximation, discarding rapidly oscillating terms $\propto e^{i\phi(t)}$:

$$
\begin{aligned}
i\hbar\dot{u}(t) &= [E_0 - \mu + \tfrac{1}{2}eV(t)]u(t) + \tfrac{1}{4}\Gamma v(t),\\
i\hbar\dot{v}(t) &= -[E_0 - \mu + \tfrac{1}{2}eV(t)]v(t) + \tfrac{1}{4}\Gamma u(t).
\end{aligned}
\tag{8.19}
$$

(We have set $\Gamma_{\mathrm{L}} = \Gamma_{\mathrm{R}}$ for simplicity.) If we further neglect the slow time dependence of the voltage, we obtain oscillations $\propto \sin^2 \omega_{\mathrm{R}} t$ of the Bloch vector components X, Y, Z with Rabi frequency

$$
\hbar\omega_{\mathrm{R}} = \sqrt{(E_0 - \mu + \tfrac{1}{2}eV)^2 + (\Gamma/4)^2}.
\tag{8.20}
$$

The oscillations in Fig. 8.5d near $t = 1000 \times \hbar/\Delta_0$ have a period of $35\,\hbar/\Delta_0$, while $T_{\mathrm{R}} = \pi/\omega_{\mathrm{R}} = 40\,\hbar/\Delta_0$ if we set $V = RI_{\mathrm{DC}}$, in reasonable agreement.

8.4.3   Voltage steps count Rabi oscillations

The key discovery of Ref. [55] is that steps in the time-averaged voltage track the change in the number of Rabi oscillations of the Majorana qubit per 2π increment of the superconducting phase. Fig. 8.6 shows the same correspondence for the Andreev qubit.

If we estimate the duration δt of a 2π phase increment by the product of the number N of Rabi oscillations and the Rabi period T_{R}, we obtain the estimate $(2e/\hbar)\bar{V} = 2\pi/\delta t \simeq 2\omega_{\mathrm{R}}/N$. A stepwise decrease of N with increasing I_{DC} would then produce a stepwise increase of $\bar{V}$. This argument is suggestive, but does not explain the sharpness of the steps. We have no quantitative analytical derivation for why the steps are as sharp as they appear in the numerics.

8.5   Discussion

Two lessons learned from this study are: 1) Rabi oscillations of an Andreev qubit can be counted "one-by-one" without either requiring time-resolved detection or AC driving; 2) The voltage staircase phenomenology of Ref. [55] does not need a topological Majorana qubit — it exists in a conventional Andreev qubit.

We worked in the weak-coupling regime $\Gamma \ll \Delta_0$ because it simplifies the calculations, but also for a physics reason: The voltage staircase is suppressed when Γ becomes larger than Δ_0, due to a well-known decoherence
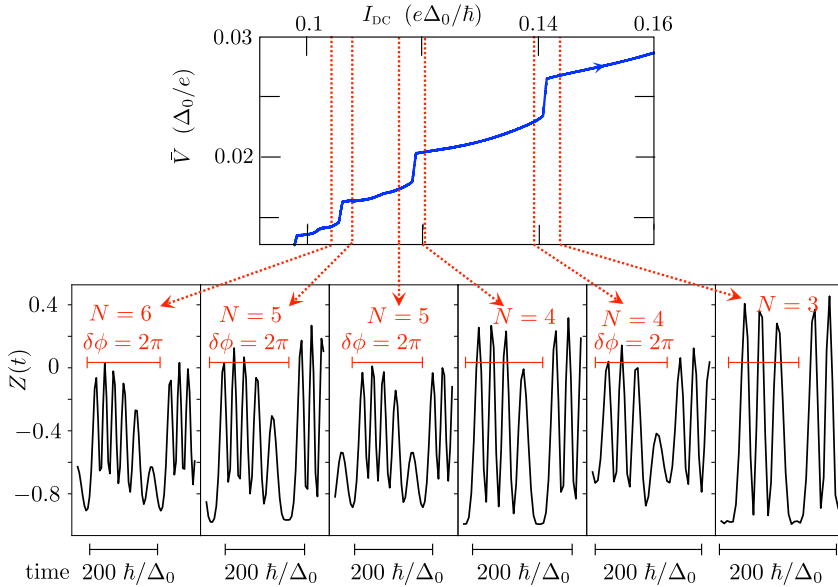
Figure 8.6. Top panel: portion of the I–V characteristic from Fig. 8.3a, with red dotted lines into the the bottom panels to show how the voltage steps line up with the change in the number N of Rabi oscillations of the qubit in a 2π phase increment $\delta\phi$.

mechanism [285, 287]: Equilibration of the Andreev levels $\pm E_{\mathrm{A}}(\phi)$ with the continuous spectrum at $|E| > \Delta_0$ when ϕ crosses an integer multiple of 2π. Let us discuss this in a bit more detail.

For $\Gamma \gg \Delta_0$ the Andreev levels are given by

$$E_{\mathrm{A}} = \Delta_0 \sqrt{1 - \tau_{\mathrm{BW}} \sin^2(\phi/2)}, \qquad (8.21)$$

according to Eq. (8.2), with τ_{BW} the Breit-Wigner transmission probability (8.1). The difference with the weak-coupling result (8.4) is that the reduced gap Δ_{eff} has been replaced by the true gap Δ_0. This means the Andreev level merges with the superconducting continuum whenever $\phi = 0$ modulo 2π. As the phase evolves in time in response to the current bias, each 2π phase increment will restart from an equilibrium distribution.

Now if we examine Fig. 8.5, panels c) and d), we see that the Rabi oscillations are pulsed by the rapid increase of the phase in the $(\pi, 2\pi)$ interval, and only fully develop in the $(2\pi, 3\pi)$ interval. Equilibration at

$\phi = 2\pi$ will restart the cycle from $t = 0$, suppressing the Rabi oscillations and hence the voltage staircase.

For the same reason a superconducting quantum point contact will not show the voltage staircase: its Andreev levels also reconnect with the superconducting continuum at $\phi = 0$ modulo 2π.

This argument points to one difference in the Majorana versus Andreev phenomenology of the voltage staircase: A topological Josephson junction needs to be magnetic in order to prevent the equilibration of the Majorana modes with the continuum at $\phi = 0$ modulo 2π [246]. In a non-topological quantum-dot Josephson junction this can achieved without breaking time-reversal symmetry.

As a topic for further research, it would be worthwhile to see if the voltage staircase can be used to count the number of Rabi oscillations over multiple 2π phase increments, since that would provide additional information on the coherence time of the qubit. This could involve the constructive interference of Landau-Zener transitions at $\phi = \pi, 3\pi, \ldots$ [288].

8.6 Appendix: Hysteresis of the voltage staircase for the Majorana qubit

The voltage staircase of the Andreev qubit is hysteretic, the steps appear at higher current for the up-sweep than for the down-sweep. No hysteresis was reported in Ref. [55], here we show that it is present for the Majorana qubit as well.

Instead of Eqs. (8.12) and (8.13) one has for the Majorana qubit the time dependent Hamiltonian

$$\mathcal{H}(t) = E_x \sigma_x + E_z \sigma_z \cos \tfrac{1}{2}\phi(t), \qquad (8.22)$$

and current operator

$$I(t) = \frac{2e}{\hbar} \frac{\partial}{\partial \phi} \mathcal{H}(t) = -\frac{eE_z}{\hbar} \sigma_z \sin \tfrac{1}{2}\phi(t). \qquad (8.23)$$

The Pauli matrices act on the fermion parity of two pairs of Majorana zero-modes, such that σ_x flips the even–even parity state into the odd–odd parity state, while σ_z changes the sign of the odd–odd parity state. While the physical origin of the Majorana coupling terms is different from the
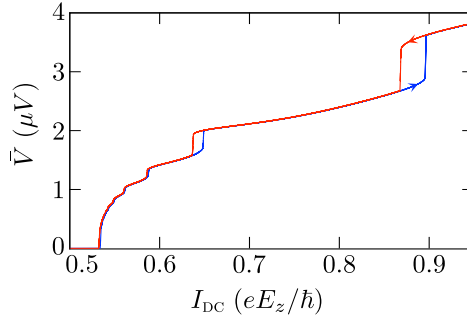
Figure 8.7. Hysteretic voltage staircase of the Majorana Josephson junction, for the parameters of Ref. [55], Fig. 3. The blue curve is for increasing DC current, the red curve for decreasing current. (The voltage $\bar{V}$ is averaged over a time window δt such that $\delta t \times dI_{\mathrm{DC}}/dt = 10^{-3}\, eE_z/\hbar$.)

Andreev qubit, mathematically the Hamiltonian (8.22) is equivalent to Eq. (8.12) in the symmetric case $\Gamma_{\mathrm{L}} = \Gamma_{\mathrm{R}}$. (Switch $\sigma_x \leftrightarrow \sigma_z$ by a unitary transformation and replace $E_x \mapsto E_0 - \mu$ and $E_z \mapsto \Gamma/2$.)

In Fig. 8.7 we show the hysteretic voltage staircase, for the same parameters $E_z = 5\,\mu\mathrm{eV}$, $E_x/E_z = 0.67$, $R = 0.827\,\hbar/e^2$ as in Ref. [55].

Bibliography

[1] Y. Cao, V. Fatemi, S. Fang, K. Watanabe, T. Taniguchi, E. Kaxiras, and P. Jarillo-Herrero. *Unconventional superconductivity in magic-angle graphene superlattices.* Nature **556**, 43 (2018).

[2] J. M. Park, Y. Cao, K. Watanabe, T. Taniguchi, and P. Jarillo-Herrero. *Tunable strongly coupled superconductivity in magic-angle twisted trilayer graphene.* Nature **590**, 249 (2021).

[3] H. Zhou, L. Holleis, Y. Saito, L. Cohen, W. Huynh, C. L. Patterson, F. Yang, T. Taniguchi, K. Watanabe, and A. F. Young. *Isospin magnetism and spin-polarized superconductivity in bernal bilayer graphene.* Science **375**, 774 (2022).

[4] H. Zhou, T. Xie, T. Taniguchi, K. Watanabe, and A. F. Young. *Superconductivity in rhombohedral trilayer graphene.* Nature **598**, 434 (2021).

[5] B. R. Ortiz, S. M. L. Teicher, Y. Hu, J. L. Zuo, P. M. Sarte, E. C. Schueller, A. M. M. Abeykoon, M. J. Krogstad, S. Rosenkranz, R. Osborn, R. Seshadri, L. Balents, J. He, and S. D. Wilson. CsV_3Sb_5*: a $\mathbb{Z}_2$ topological kagome metal with a superconducting ground state.* Phys. Rev. Lett. **125**, 247002 (2020).

[6] Y. Cao, D. Rodan-Legrain, J. M. Park, F. N. Yuan, K. Watanabe, T. Taniguchi, R. M. Fernandes, L. Fu, and P. Jarillo-Herrero. *Nematicity and Competing Orders in Superconducting Magic-Angle Graphene.* Science **372**, 264 (2020).

[7] M. R. Slot, T. S. Gardenier, P. H. Jacobse, G. C. P. van Miert, S. N. Kempkes, S. J. M. Zevenhuizen, C. M. Smith, D. Vanmaekelbergh, and I. Swart. *Experimental realization and characterization of an electronic Lieb lattice.* Nature Phys. **13**, 672 (2017).

[8]   S. Mukherjee, A. Spracklen, D. Choudhury, N. Goldman, P. Öh-berg, E. Andersson, and R. R. Thomson. *Observation of a localized flat-band state in a photonic Lieb lattice.* Phys. Rev. Lett. **114**, 245504 (2015).

[9]   W. Jiang, H. Huang, and F. Liu. *A Lieb-like lattice in a covalent-organic framework and its Stoner ferromagnetism.* Nature Comm. **10**, 2207 (2019).

[10] B. Cui, X. Zheng, J. Wang, D. Liu, S. Xie, and B. Huang. *Realization of Lieb lattice in covalent-organic frameworks with tunable topology and magnetism.* Nature Comm. **11**, 66 (2020).

[11] B. Sutherland. *Localization of electronic wave functions due to local topology.* Phys. Rev. B **34**, 5208 (1986).

[12] D. Bercioux, D. F. Urban, H. Grabert, and W. Häusler. *Massless Dirac-Weyl fermions in a T_3 optical lattice.* Phys. Rev. A **80**, 063603 (2009).

[13] A. Raoux, M. Morigi, J.-N. Fuchs, F. Piéchon, and G. Montambaux. *From dia- to paramagnetic orbital susceptibility of massless fermions.* Phys. Rev. Lett. **112**, 026402 (2014).

[14] E. V. Gorbar, V. P. Gusynin, and D. O. Oriekhov. *Electron states for gapped pseudospin-1 fermions in the field of a charged impurity.* Phys. Rev. B **99**, 155124 (2019).

[15] B. Bradlyn, J. Cano, Z. Wang, M. G. Vergniory, C. Felser, R. J. Cava, and B. A. Bernevig. *Beyond Dirac and Weyl fermions: unconventional quasiparticles in conventional crystals.* Science **353**, aaf5037 (2016).

[16] C. C. Abilio, P. Butaud, T. Fournier, B. Pannetier, J. Vidal, S. Tedesco, and B. Dalzotto. *Magnetic field induced localization in a two-dimensional superconducting wire network.* Phys. Rev. Lett. **83**, 5102 (1999).

[17] E Serret, P Butaud, and B Pannetier. *Vortex correlations in a fully frustrated two-dimensional superconducting network.* Europhys. Lett. **59**, 225 (2002).

[18] C. Naud, G. Faini, and D. Mailly. *Aharonov-Bohm cages in 2d normal metal networks.* Phys. Rev. Lett. **86**, 5104 (2001).

[19] M. Rizzi, V. Cataudella, and R. Fazio. *Phase diagram of the Bose-Hubbard model with $\mathcal{T}_3$ symmetry.* Phys. Rev. B **73**, 144511 (2006).

[20]   E. H. Lieb. *Two theorems on the Hubbard model*. Phys. Rev. Lett. **62**, 1201 (1989).

[21]   R. Shen, L. B. Shao, B. Wang, and D. Y. Xing. *Single Dirac cone with a flat band touching on line-centered-square optical lattices*. Phys. Rev. B **81**, 041410(R) (2010).

[22]   K. S. Novoselov, A. K. Geim, S. V. Morozov, D. Jiang, Y. Zhang, S. V. Dubonos, I. V. Grigorieva, and A. A. Firsov. *Electric field effect in atomically thin carbon films*. Science **306**, 666 (2004).

[23]   M. Kang, L. Ye, S. Fang, J.-S. You, A. Levitan, M. Han, J. I. Facio, C. Jozwiak, A. Bostwick, E. Rotenberg, M. K. Chan, R. D. McDonald, D. Graf, K. Kaznatcheev, E. Vescovo, D. C. Bell, E. Kaxiras, J. van den Brink, M. Richter, M. P. Ghimire, J. G. Checkelsky, and R. Comin. *Dirac fermions and flat bands in the ideal kagome metal FeSn*. Nature Mat. **19**, 163 (2019).

[24]   L. Van Hove. *The occurrence of singularities in the elastic frequency distribution of a crystal*. Phys. Rev. **89**, 1189 (1953).

[25]   N. F. Q. Yuan, H. Isobe, and L. Fu. *Magic of high-order van Hove singularity*. Nature Comm. **10**, 5769 (2019).

[26]   R. Nandkishore, L. S. Levitov, and A. V. Chubukov. *Chiral superconductivity from repulsive interactions in doped graphene*. Nature Phys. **8**, 158 (2012).

[27]   L. Classen, A. V. Chubukov, C. Honerkamp, and M. M. Scherer. *Competing orders at higher-order van hove points*. Phys. Rev. B **102**, 125141 (2020).

[28]   Y.-P. Lin. *Chiral flat band superconductivity from symmetry-protected three-band crossings*. Phys. Rev. Res. **2**, 043209 (2020).

[29]   N. F. Q. Yuan and L. Fu. *Classification of critical points in energy bands based on topology, scaling, and symmetry*. Phys Rev. B **101**, 125120 (2020).

[30]   A. Chandrasekaran, A. Shtyk, J. J. Betouras, and C. Chamon. *Catastrophe theory classification of Fermi surface topological transitions in two dimensions*. Phys. Rev. Res. **2**, 013355 (2020).

[31]   M. Aghaee and et.al. *InAs-Al hybrid devices passing the topological gap protocol*. (2022) arXiv:`2207.02472`.

[32] M. A. Ruderman and C. Kittel. *Indirect exchange coupling of nuclear magnetic moments by conduction electrons*. Phys. Rev. **96**, 99 (1954).

[33] T. Kasuya. *A theory of metallic ferro- and antiferromagnetism on Zener's model*. Prog. Theor. Phys. **16**, 45 (1956).

[34] K. Yosida. *Magnetic properties of cu-mn alloys*. Phys. Rev. **106**, 893 (1957).

[35] F. Zhang, H. Min, M. Polini, and A. H. MacDonald. *Spontaneous inversion symmetry breaking in graphene bilayers*. Phys. Rev. B **81**, 041402 (2010).

[36] K. Sun and E. Fradkin. *Time-reversal symmetry breaking and spontaneous anomalous Hall effect in Fermi fluids*. Phys. Rev. B **78**, 245122 (2008).

[37] K. Sun, H. Yao, E. Fradkin, and S. A. Kivelson. *Topological insulators and nematic phases from spontaneous symmetry breaking in 2D Fermi systems with a quadratic band crossing*. Phys. Rev. Lett. **103**, 046811 (2009).

[38] J. Martin, B. E. Feldman, R. T. Weitz, M. T. Allen, and A. Yacoby. *Local compressibility measurements of correlated states in suspended bilayer graphene*. Phys. Rev. Lett. **105**, 256806 (2010).

[39] R. T. Weitz, M. T. Allen, B. E. Feldman, J. Martin, and A. Yacoby. *Broken-symmetry states in doubly gated suspended bilayer graphene*. Science **330**, 812 (2010).

[40] F. Freitag, J. Trbovic, M. Weiss, and C. Schönenberger. *Spontaneously gapped ground state in suspended bilayer graphene*. Phys. Rev. Lett. **108**, 076602 (2012).

[41] J. Velasco, L. Jing, W. Bao, Y. Lee, P. Kratz, V. Aji, M. Bockrath, C. N. Lau, C. Varma, R. Stillwell, D. Smirnov, F. Zhang, J. Jung, and A. H. MacDonald. *Transport spectroscopy of symmetry-broken insulating states in bilayer graphene*. Nature Nanotech. **7**, 156 (2012).

[42] Y. Lee, K. Myhro, D. Tran, N. Gilgren, J. Velasco, W. Bao, M. Deo, and C. N. Lau, *Band gap and correlated phenomena in bilayer and trilayer graphene*, in SPIE proceedings, edited by T. George, M. S. Islam, and A. K. Dutta (2013).

[43] M. Yankowitz, F. Wang, C. N. Lau, and B. J. LeRoy. *Local spectroscopy of the electrically tunable band gap in trilayer graphene.* Phys. Rev. B **87**, 165102 (2013).

[44] K. Myhro, S. Che, Y. Shi, Y. Lee, K. Thilahar, K. Bleich, D. Smirnov, and C. N. Lau. *Large tunable intrinsic gap in rhombohedral-stacked tetralayer graphene at half filling.* 2D Mat. **5**, 045013 (2018).

[45] Y. H. Kwan, G. Wagner, T. Soejima, M. P. Zaletel, S. H. Simon, S. A. Parameswaran, and N. Bultinck. *Kekulé spiral order at all nonzero integer fillings in twisted bilayer graphene.* Phys. Rev. X **11**, 041063 (2021).

[46] T. Cea. *Superconductivity induced by the intervalley coulomb scattering in a few layers of graphene.* Phys. Rev. B **107**, l041111 (2023).

[47] J. Cserti and G. Dávid. *Unified description of Zitterbewegung for spintronic, graphene, and superconducting systems.* Phys. Rev. B **74**, 172305 (2006).

[48] E. Schrödinger. *Über die kräftefreie bewegung in der relativistischen quantenmechanik.* Sitzungsber. Preuss. Akad. Wiss., Phys. Math. Kl. **24**, 418 (1930).

[49] E. Illes, J. P. Carbotte, and E. J. Nicol. *Hall quantization and optical conductivity evolution with variable Berry phase in the $\alpha - T_3$ model.* Phys. Rev. B **92**, 245410 (2015).

[50] G. Vignale. *Orbital paramagnetism of electrons in a two-dimensional lattice.* Phys. Rev. Lett. **67**, 358 (1991).

[51] J. Vallejo-Bustamante, N. J. Wu, C. Fermon, M. Pannetier-Lecoeur, T. Wakamura, K. Watanabe, T. Taniguchi, T. Pellegrin, A. Bernard, S. Daddinounou, V. Bouchiat, S. Guéron, M. Ferrier, G. Montambaux, and H. Bouchiat. *Detection of graphene's divergent orbital diamagnetism at the dirac point.* Science **374**, 1399 (2021).

[52] Y. Liu, G. Wang, Q. Huang, L. Guo, and X. Chen. *Structural and electronic properties of T graphene: a two-dimensional carbon allotrope with tetrarings.* Phys. Rev. Lett. **108**, 225505 (2012).

[53] P. V. Gaikwad and A. Kshirsagar. *Octagonal family of monolayers, bulk and nanotubes.* arXiv:2003.00158.

[54] A. R. Akhmerov, J. P. Dahlhaus, F. Hassler, M. Wimmer, and C. W. J. Beenakker. *Quantized conductance at the Majorana phase transition in a disordered superconducting wire*. Phys. Rev. Lett. **106**, 057001 (2011).

[55] S.-J. Choi, A. Calzona, and B. Trauzettel. *Majorana-induced dc shapiro steps in topological josephson junctions*. Phys. Rev. B **102**, 140501 (2020).

[56] Y. Yafet. *Ruderman-kittel-kasuya-yosida range function of a one-dimensional free-electron gas*. Phys. Rev. B **36**, 3948 (1987).

[57] B. Fischer and M. W. Klein. *Magnetic and nonmagnetic impurities in two-dimensional metals*. Phys. Rev. B **11**, 2025 (1975).

[58] L. Brey, H. A. Fertig, and S. D. Sarma. *Diluted graphene antiferromagnet*. Phys. Rev. Lett. **99**, 116802 (2007).

[59] S. Saremi. *RKKY in half-filled bipartite lattices: graphene as an example*. Phys. Rev. B **76**, 184430 (2007).

[60] E. Kogan. *RKKY interaction in gapped or doped graphene*. Graphene **02**, 8 (2013).

[61] M. Sherafati and S. Satpathy. *Analytical expression for the RKKY interaction in doped graphene*. Phys. Rev. B **84**, 125416 (2011).

[62] O. Roslyak, G. Gumbs, and D. Huang. *Gap-modulated doping effects on indirect exchange interaction between magnetic impurities in graphene*. J. Appl. Phys. **113**, 123702 (2013).

[63] J. Cao, H. A. Fertig, and S. Zhang. *RKKY interactions in graphene Landau levels*. Phys. Rev. B **99**, 205430 (2019).

[64] E. Kogan. *RKKY interaction in graphene at finite temperature*. C J. of Carb. Res. **5**, 14 (2019).

[65] E. Kogan. *RKKY interaction in graphene*. Phys. Rev. B **84**, 115119 (2011).

[66] A. M. Black-Schaffer. *RKKY coupling in graphene*. Phys. Rev. B **81**, 205416 (2010).

[67] M. Sherafati and S. Satpathy. *RKKY interaction in graphene from the lattice Green's function*. Phys. Rev. B **83**, 165425 (2011).

[68] N. Klier, S. Shallcross, S. Sharma, and O. Pankratov. *Ruderman-kittel-kasuya-yosida interaction at finite temperature: graphene and bilayer graphene*. Phys. Rev. B **92**, 205414 (2015).

[69] P. D. Gorman, J. M. Duffy, M. S. Ferreira, and S. R. Power. *RKKY interaction between adsorbed magnetic impurities in graphene: symmetry and strain effects*. Phys. Rev. B **88**, 085405 (2013).

[70] F. Parhizgar, M. Sherafati, R. Asgari, and S. Satpathy. *Ruderman-Kittel-Kasuya-Yosida interaction in biased bilayer graphene*. Phys. Rev. B **87**, 165429 (2013).

[71] N. Klier, S. Shallcross, and O. Pankratov. *Asymptotic discontinuities in the RKKY interaction in the graphene Bernal bilayer*. Phys. Rev. B **90**, 245118 (2014).

[72] M. Zare. *RKKY interaction in biased single-layer silicene*. Phys. Rev. B **100**, 085434 (2019).

[73] G. C. Paul, S. F. Islam, and A. Saha. *Fingerprints of tilted Dirac cones on the RKKY exchange interaction in 8-Pmmn borophene*. Phys. Rev. B **99**, 155418 (2019).

[74] V. Kaladzhyan, A. A. Zyuzin, and P. Simon. *RKKY interaction on the surface of three-dimensional Dirac semimetals*. Phys. Rev. B **99**, 165302 (2019).

[75] D. Green, L. Santos, and C. Chamon. *Isolated flat bands and spin-1 conical bands in two-dimensional lattices*. Phys. Rev. B **82**, 075104 (2010).

[76] J. D. Malcolm and E. J. Nicol. *Magneto-optics of massless Kane fermions: role of the flat band and unusual Berry phase*. Phys. Rev. B **92**, 035118 (2015).

[77] Z. Lan, N. Goldman, and P. Öhberg. *Coexistence of spin-1/2 and spin-1 Dirac-Weyl fermions in the edgecentered honeycomb lattice*. Phys. Rev. B **85**, 155451 (2012).

[78] L. Wang and D.-X. Yao. *Coexistence of spin-1 fermion and Dirac fermion on the triangular kagome lattice*. Phys. Rev. B **98**, 161403 (2018).

[79] P. Tang, Q. Zhou, and S.-C. Zhang. *Multiple types of topological fermions in transition metal silicides*. Phys. Rev. Lett. **119**, 206402 (2017).

[80] J. Vidal, R. Mosseri, and B. Douçot. *Aharonov-Bohm cages in two-dimensional structures*. Phys. Rev. Lett. **81**, 5888 (1998).

[81] J. D. Malcolm and E. J. Nicol. *Magneto-optics of general pseudospin-s two-dimensional Dirac-Weyl fermions.* Phys. Rev. B **90**, 035405 (2014).

[82] E. Illes and E. J. Nicol. *Magnetic properties of the α-T_3 model: magneto-optical conductivity and the Hofstadter butterfly.* Phys. Rev. B **94**, 125435 (2016).

[83] Á. D. Kovács, G. Dávid, B. Dóra, and J. Cserti. *Frequency-dependent magneto-optical conductivity in the generalized α-T_3 model.* Phys. Rev. B **95**, 035414 (2017).

[84] T. Biswas and T. K. Ghosh. *Magnetotransport properties of the α-T_3 model.* J. Phys.: Condens. Matter **28**, 495302 (2016).

[85] Y. Xu and L.-M. Duan. *Unconventional quantum hall effects in two-dimensional massive spin-1 fermion systems.* Phys. Rev. B **96**, 155301 (2017).

[86] M. W. Alam, B. Souayeh, and S. F. Islam. *Enhancement of thermoelectric performance of a nanoribbon made of α- T_3 lattice.* J. Phys.: Condens. Matter **31**, 485303 (2019).

[87] T. Biswas and T. K. Ghosh. *Dynamics of a quasiparticle in the α-t3 model: role of pseudospin polarization and transverse magnetic field on zitterbewegung.* J. Phys.: Condens. Matter **30**, 075301 (2018).

[88] S. F. Islam and P. Dutta. *Valley-polarized magnetoconductivity and particle-hole symmetry breaking in a periodically modulated $\alpha - T_3$ lattice.* Phys. Rev. B **96**, 045418 (2017).

[89] D. O. Oriekhov, E. V. Gorbar, and V. P. Gusynin. *Electronic states of pseudospin-1 fermions in dice lattice ribbon.* Low Temp. Phys. **44**, 1313 (2018).

[90] O. V. Bugaiko and D. O. Oriekhov. *Electronic states of pseudospin-1 fermions in $\alpha - T_3$ lattice ribbons in a magnetic field.* J. Phys.: Condens. Matter **31**, 325501 (2019).

[91] V. A. Khodel. *Theory of Fermi liquid with flat bands.* Journal of Low Temperature Physics **191**, 14–34 (2017).

[92] D. Leykam, A. Andreanov, and S. Flach. *Artificial flat band systems: from lattice models to experiments.* Adv. Phys.: X **3**, 1473052 (2018).

[93] P. Delplace, J. B. Marston, and A. Venaille. *Topological origin of equatorial waves.* Science **358**, 1075–1077 (2017).

[94] H. Zheng and M. Z. Hasan. *Quasiparticle interference on type-i and type-II Weyl semimetal surfaces: a review.* Adv. Phys.: X **3**, 1466661 (2018).

[95] A. P. Prudnikov, Y. A. Brychkov, and O. I. Marichev. *Vol. ii: Integrals and Series. Special Functions.* (Nauka, Moskow, 1983).

[96] A. P. Prudnikov, Y. A. Brychkov, and O. I. Marichev. *Vol. iii: Integrals and Series. Special Functions.* (Nauka, Moskow, 1983).

[97] E. T. Whittaker and A. Watson. *Course of modern analysis,4th ed.* (Cambridge University Press, Cambridge, 1927).

[98] H. Bateman and A. Erdelyi. *Higher transcendental functions, vol. 1.* (MC Graw-Hill Book, New York, 1953).

[99] Y. N. Demkov and G. F. Drukarev. *Particle of low binding energy in a magnetic field.* Sov. Phys. JETP **22**, 182 (1965).

[100] T. T. Heikkilä and G. E. Volovik. *Dimensional crossover in topological matter: evolution of the multiple Dirac point in the layered system to the flat band on the surface.* JETP Lett. **93**, 59–65 (2011).

[101] T. T. Heikkilä, N. B. Kopnin, and G. E. Volovik. *Flat bands in topological media.* JETP Lett. **94**, 233–239 (2011).

[102] F. C. de Lima and G. J. Ferreira. *High-degeneracy points protected by site-permutation symmetries.* Phys. Rev. B **101**, 041107(R) (2020).

[103] F. C. de Lima and A. Fazzio. *Emergent quasiparticles in Euclidean tilings.* Nanoscale **13**, 5270–5274 (2021).

[104] B. Dey and T. K. Ghosh. *Photoinduced valley and electron-hole symmetry breaking in $\alpha - T_3$ lattice: the role of a variable Berry phase.* Phys. Rev. B **98**, 075422 (2018).

[105] A. Iurov, G. Gumbs, D. Huang, C. for High Technology Materials, and U. of New Mexico. *Peculiar electronic states, symmetries and Berry phases in irradiated $\alpha - T_3$ materials.* Phys. Rev. B **99**, 205135 (2019).

[106] S. D. Sarma, S. Adam, E. H. Hwang, and E. Rossi. *Electronic transport in two-dimensional graphene.* Rev. Mod. Phys. **83**, 407–470 (2011).

[107] T. Cea and F. Guinea. *Band structure and insulating states driven by coulomb interaction in twisted bilayer graphene*. Phys. Rev. B **102**, 045107 (2020).

[108] M. I. Katsnelson. *Graphene: Carbon in Two Dimensions*. (Cambridge University Press, Cambridge, 2012).

[109] G. Baym and L. P. Kadanoff. *Conservation laws and correlation functions*. Phys. Rev. **124**, 287 (1961).

[110] G. Baym. *Self-consistent approximations in many-body systems*. Phys. Rev. **127**, 1391 (1962).

[111] J. M. Cornwall, R. Jackiw, and E. Tomboulis. *Effective action for composite operators*. Phys. Rev. D **10**, 2428 (1974).

[112] E. V. Gorbar, V. P. Gusynin, V. A. Miransky, and I. A. Shovkovy. *Dynamics in the quantum Hall effect and the phase diagram of graphene*. Phys. Rev. B **78**, 085437 (2008).

[113] J. L. Garcia-Pomar, A. Cortijo, and M. Nieto-Vesperinas. *Fully valley-polarized electron beams in graphene*. Phys. Rev. Lett. **100**, 236801 (2008).

[114] D. S. L. Abergel and T. Chakraborty. *Generation of valley polarized current in bilayer graphene*. Appl. Phys. Lett. **95**, 062107 (2009).

[115] M. O. Goerbig. *Electronic properties of graphene in a strong magnetic field*. Rev. Mod. Phys. **83**, 1193 (2011).

[116] C. T. Kelley. *Iterative methods for linear and nonlinear equations*. (Society for Industrial and Applied Mathematics, Philadelphia, 1995).

[117] V. P. Gusynin, V. A. Miransky, and I. A. Shovkovy. *Dynamical flavor symmetry breaking by a magnetic field in 2+1 dimensions*. Phys. Rev. D **52**, 4718–4735 (1995).

[118] I. F. Herbut. *Interactions and phase transitions on graphene's honeycomb lattice*. Phys. Rev. Lett. **97**, 146401 (2006).

[119] V. A. Khodel and V. R. Shaginyan. *Superfluidity in system with fermion condensate*. JETP Lett. **51**, 553 (1990).

[120] G. E. Volovik. *A new class of normal Fermi liquids*. JETP Lett. **53**, 222 (1991).

[121] G. E. Volovik. *The Fermi condensate near the saddle point and in the vortex core.* JETP Lett. **59**, 830 (1994).

[122] G. E. Volovik. *Flat band and Planckian metal.* JETP Lett. **110**, 352–353 (2019).

[123] D. N. Basov and T. Timusk. *Electrodynamics of high-T_c superconductors.* Rev. Mod. Phys. **77**, 721–779 (2005).

[124] J. P. Carbotte, T. Timusk, and J. Hwang. *Bosons in high-temperature superconductors: an experimental survey.* Rep. Prog. Phys. **74**, 066501 (2011).

[125] T. Ando. *Dynamical conductivity and zero-mode anomaly in honeycomb lattices.* Journal of the Physical Society of Japan **71**, 1318–1324 (2002).

[126] V. P. Gusynin and S. G. Sharapov. *Transport of Dirac quasiparticles in graphene: Hall and optical conductivities.* Phys. Rev. B **73**, 245411 (2006).

[127] V. P. Gusynin, S. G. Sharapov, and J. P. Carbotte. *Unusual microwave response of Dirac quasiparticles in graphene.* Phys. Rev. Lett. **96**, 256802 (2006).

[128] R. R. Nair, P. Blake, A. N. Grigorenko, K. S. Novoselov, T. J. Booth, T. Stauber, N. M. R. Peres, and A. K. Geim. *Fine structure constant defines visual transparency of graphene.* Science **320**, 1308 (2008).

[129] Z. Q. Li, E. A. Henriksen, Z. Jiang, Z. Hao, M. C. Martin, P. Kim, H. L. Stormer, and D. N. Basov. *Dirac charge dynamics in graphene by infrared spectroscopy.* Nature Phys. **4**, 532–535 (2008).

[130] T. Stauber, N. M. R. Peres, and A. K. Geim. *Optical conductivity of graphene in the visible region of the spectrum.* Phys. Rev. B **78**, 085432 (2008).

[131] A. A. Schafgans, K. W. Post, A. A. Taskin, Y. Ando, X.-L. Qi, B. C. Chapler, and D. N. Basov. *Landau level spectroscopy of surface states in the topological insulator $Bi_{0.91}Sb_{0.09}$ via magneto-optics.* Phys. Rev. B **85**, 195440 (2012).

[132] R. Y. Chen, S. J. Zhang, J. A. Schneeloch, C. Zhang, Q. Li, G. D. Gu, and N. L. Wang. *Optical spectroscopy study of the three-dimensional Dirac semimetal $ZrTe_5$.* Phys. Rev. B **92**, 075107 (2015).

[133] B. Xu, Y. M. Dai, L. X. Zhao, K. Wang, R. Yang, W. Zhang, J. Y. Liu, H. Xiao, G. F. Chen, A. J. Taylor, D. A. Yarotski, R. P. Prasankumar, and X. G. Qiu. *Optical spectroscopy of the Weyl semimetal TaAs*. Phys. Rev. B **93**, 121110(R) (2016).

[134] D. Neubauer, J. P. Carbotte, A. A. Nateprov, A. Löhle, M. Dressel, and A. V. Pronin. *Interband optical conductivity of the [001]-oriented Dirac semimetal Cd_3As_2*. Phys. Rev. B **93**, 121202(R) (2016).

[135] M. I. Katsnelson. *Zitterbewegung, chirality, and minimal conductivity in graphene*. Euro. Phys. J. B **51**, 157–160 (2006).

[136] J. Schwinger. *On gauge invariance and vacuum polarization*. Physical Review **82**, 664–679 (1951).

[137] V. P. Gusynin, S. G. Sharapov, and J. P. Carbotte. *Sum rules for the optical and Hall conductivity in graphene*. Phys. Rev. B **75**, 165407 (2007).

[138] S. Yuan, H. De Raedt, and M. I. Katsnelson. *Modeling electronic structure and transport properties of graphene with resonant scattering centers*. Phys. Rev. B **82**, 115448 (2010).

[139] Y. Hasegawa, R. Konno, H. Nakano, and M. Kohmoto. *Zero modes of tight-binding electrons on the honeycomb lattice*. Phys. Rev. B **74**, 033413 (2006).

[140] G. Montambaux, F. Piéchon, J.-N. Fuchs, and M. O. Goerbig. *A universal Hamiltonian for motion and merging of Dirac points in a two-dimensional crystal*. Euro. Phys. J. B **72**, 509–520 (2009).

[141] G. Montambaux, F. Piéchon, J.-N. Fuchs, and M. O. Goerbig. *Merging of Dirac points in a two-dimensional crystal*. Phys. Rev. B **80**, 153412 (2009).

[142] L. Tarruell, D. Greif, T. Uehlinger, G. Jotzu, and T. Esslinger. *Creating, moving and merging Dirac points with a Fermi gas in a tunable honeycomb lattice*. Nature **483**, 302–305 (2012).

[143] M. Bellec, U. Kuhl, G. Montambaux, and F. Mortessagne. *Topological transition of Dirac points in a microwave experiment*. Phys. Rev. Lett. **110**, 033902 (2013).

[144] P. Adroguer, D. Carpentier, G. Montambaux, and E. Orignac. *Diffusion of Dirac fermions across a topological merging transition in two dimensions*. Phys. Rev. B **93**, 125113 (2016).

[145] K. Ziegler and A. Sinner. *Lattice symmetries, spectral topology and opto-electronic properties of graphene-like materials.* Europhys. Lett. **119**, 27001 (2017).

[146] A. Mawrie and B. Muralidharan. *Direction-dependent giant optical conductivity in two-dimensional semi-Dirac materials.* Phys. Rev. B **99**, 075415 (2019).

[147] J. P. Carbotte and E. J. Nicol. *Signatures of merging Dirac points in optics and transport.* Phys. Rev. B **100**, 035441 (2019).

[148] J. Jang, S. Ahn, and H. Min. *Optical conductivity of black phosphorus with a tunable electronic structure.* 2D Mat. **6**, 025029 (2019).

[149] X. Zhou, W. Chen, and X. Zhu. *Anisotropic magneto-optical absorption and linear dichroism in two-dimensional semi-Dirac electron systems.* Phys. Rev. B **104**, 235403 (2021).

[150] Y.-R. Chen, Y. Xu, J. Wang, J.-F. Liu, and Z. Ma. *Enhanced magneto-optical response due to the flat band in nanoribbons made from the $\alpha - T_3$ lattice.* Phys. Rev. B **99**, 045420 (2019).

[151] B. Dey, P. Kapri, O. Pal, and T. K. Ghosh. *Unconventional phases in Haldane model of dice lattice.* Phys. Rev. B **101**, 235406 (2020).

[152] C.-D. Han and Y.-C. Lai. *Optical response of two-dimensional Dirac materials with a flat band.* Phys. Rev. B **105**, 155405 (2022).

[153] V. Apaja, M. Hyrkäs, and M. Manninen. *Flat bands, Dirac cones, and atom dynamics in an optical lattice.* Phys. Rev. A **82**, 041402(R) (2010).

[154] N. Goldman, D. F. Urban, and D. Bercioux. *Topological phases for fermionic cold atoms on the Lieb lattice.* Phys. Rev. A **83**, 063601 (2011).

[155] H. Tasaki. *From Nagaoka's ferromagnetism to flat-band ferromagnetism and beyond: an introduction to ferromagnetism in the Hubbard model.* Progress of Theoretical Physics **99**, 489–548 (1998).

[156] N. B. Kopnin, T. T. Heikkilä, and G. E. Volovik. *High-temperature surface superconductivity in topological flat-band systems.* Phys. Rev. B **83**, 220503(R) (2011).

[157] A. Julku, S. Peotta, T. I. Vanhala, D.-H. Kim, and P. Törmä. *Geometric origin of superfluidity in the Lieb-lattice flat band.* Phys. Rev. Lett. **117**, 045303 (2016).

[158] R. A. Vicencio, C. Cantillano, L. Morales-Inostroza, B. Real, C. Mejía-Cortés, S. Weimann, A. Szameit, and M. I. Molina. *Observation of localized states in Lieb photonic lattices.* Phys. Rev. Lett. **114**, 245503 (2015).

[159] R. Drost, T. Ojanen, A. Harju, and P. Liljeroth. *Topological states in engineered atomic lattices.* Nature Phys. **13**, 668 (2017).

[160] D. Mayou. *Generalized Drude formula for the optical conductivity of quasicrystals.* Phys. Rev. Lett. **85**, 1290 (2000).

[161] M. Ezawa. *Highly anisotropic physics in phosphorene.* J. Phys.: Conf. Series **603**, 012006 (2015).

[162] P. K. Pyatkovskiy and T. Chakraborty. *Dynamical polarization and plasmons in a two-dimensional system with merging Dirac points.* Phys. Rev. B **93**, 085145 (2016).

[163] H. Feshbach and F. Villars. *Elementary relativistic wave mechanics of spin 0 and spin 1/2 particles.* Rev. Mod. Phys. **30**, 24 (1958).

[164] J. Schliemann, D. Loss, and R. M. Westervelt. *Zitterbewegung of electronic wave packets in III-V zinc-blende semiconductor quantum wells.* Phys. Rev. Lett. **94**, 206801 (2005).

[165] L. J. LeBlanc, M. C. Beeler, K Jiménez-García, A. R. Perry, S Sugawa, R. A. Williams, and I. B. Spielman. *Direct observation of zitterbewegung in a bose–einstein condensate.* New Journal of Physics **15**, 073011 (2013).

[166] E. V. Gorbar, V. P. Gusynin, and D. O. Oriekhov. *Gap generation and flat band catalysis in dice model with local interaction.* Phys. Rev. B **103**, 155155 (2021).

[167] B. Dey and T. K. Ghosh. *Floquet topological phase transition in the $\alpha-\mathcal{T}_3$ lattice.* Phys. Rev. B **99**, 205429 (2019).

[168] A. Iurov, L. Zhemchuzhna, D. Dahal, G. Gumbs, and D. Huang. *Quantum-statistical theory for laser-tuned transport and optical conductivities of dressed electrons in $\alpha - \mathcal{T}_3$ materials.* Phys. Rev. B **101**, 035129 (2020).

[169] B. Dóra, J. Kailasvuori, and R. Moessner. *Lattice generalization of the Dirac equation to general spin and the role of the flat band.* Phys. Rev. B **84**, 195422 (2011).

[170] Z. Li and J. P. Carbotte. *Longitudinal and spin-valley Hall optical conductivity in single layer MoS_2*. Phys. Rev. B **86**, 205425 (2012).

[171] C. J. Tabert and E. J. Nicol. *AC/DC spin and valley Hall effects in silicene and germanene*. Phys. Rev. B **87**, 235426 (2013).

[172] N. A. Sinitsyn, J. E. Hill, H. Min, J. Sinova, and A. H. MacDonald. *Charge and spin Hall conductivity in metallic graphene*. Phys. Rev. Lett. **97**, 106804 (2006).

[173] T. M. Radchenko, A. A. Shylau, and I. V. Zozoulenko. *Influence of correlated impurities on conductivity of graphene sheets: Time-dependent real-space Kubo approach*. Phys. Rev. B **86**, 035418 (2012).

[174] I. S. Gradstein and I. M. Ryzhik. *Table of Integrals, Series, and Products*. (Academic Press, New York, 1965).

[175] A. K. Geim and K. S. Novoselov. *The rise of graphene*. Nat. Mater. **6**, 183 (2007).

[176] D Hsieh, D Qian, L Wray, Y Xia, Y. S. Hor, R. J. Cava, and M. Z. Hasan. *A topological Dirac insulator in a quantum spin Hall phase*. Nature **452**, 970 (2008).

[177] M. Z. Hasan and C. L. Kane. *Colloquium : topological insulators*. Rev. Mod. Phys. **82**, 3045 (2010).

[178] B. A. Bernevig and T. L. Hughes. *Topological Insulators and Topological Superconductors*. (Princeton University Press, 2013).

[179] H.-J. Kim, K.-S. Kim, J.-F. Wang, M. Sasaki, N. Satoh, A. Ohnishi, M. Kitaura, M. Yang, and L. Li. *Dirac versus Weyl fermions in topological insulators: Adler-Bell-Jackiw anomaly in transport phenomena*. Phys. Rev. Lett. **111**, 246603 (2013).

[180] X. Huang, L. Zhao, Y. Long, P. Wang, D. Chen, Z. Yang, H. Liang, M. Xue, H. Weng, Z. Fang, X. Dai, and G. Chen. *Observation of the chiral-anomaly-induced negative magnetoresistance in 3D Weyl semimetal TaAs*. Phys. Rev. X **5**, 031023 (2015).

[181] Y. Li, Z. Wang, P. Li, X. Yang, Z. Shen, F. Sheng, X. Li, Y. Lu, Y. Zheng, and Z.-A. Xu. *Negative magnetoresistance in weyl semimetals NbAs and NbP: intrinsic chiral anomaly and extrinsic effects*. Front. Phys. **12**, 127205 (2017).

[182]   N. P. Armitage, E. J. Mele, and A. Vishwanath. *Weyl and Dirac semimetals in three-dimensional solids.* Rev. Mod. Phys. **90**, 015001 (2018).

[183]   E. V. Gorbar, V. A. Miransky, I. A. Shovkovy, and P. O. Sukhachov. *Electronic Properties of Dirac and Weyl Semimetals.* (World Scientific, Singapore, Jan. 2021).

[184]   K. S. Novoselov, E. McCann, S. V. Morozov, V. I. Fal'ko, M. I. Katsnelson, U. Zeitler, D. Jiang, F. Schedin, and A. K. Geim. *Unconventional quantum Hall effect and Berry's phase of 2π in bilayer graphene.* Nat. Phys. **2**, 177–180 (2006).

[185]   E. McCann and M. Koshino. *The electronic properties of bilayer graphene.* Rep. Prog. Phys. **76**, 056503 (2013).

[186]   E. McCann and V. I. Fal'ko. *Landau-Level Degeneracy and Quantum Hall Effect in a Graphite Bilayer.* Phys. Rev. Lett. **96**, 086805 (2006).

[187]   D. S. L. Abergel and V. I. Fal'ko. *Optical and magneto-optical far-infrared properties of bilayer graphene.* Phys. Rev. B **75**, 155430 (2007).

[188]   J. M. B. Lopes dos Santos, N. M. R. Peres, and A. H. Castro Neto. *Graphene Bilayer with a Twist: Electronic Structure.* Phys. Rev. Lett. **99**, 256802 (2007).

[189]   E. Suárez Morell, J. D. Correa, P. Vargas, M. Pacheco, and Z. Barticevic. *Flat bands in slightly twisted bilayer graphene: Tight-binding calculations.* Phys. Rev. B **82**, 121407 (2010) arXiv:1012.4320.

[190]   R. Bistritzer and A. H. MacDonald. *Moire bands in twisted double-layer graphene.* Proc. Natl. Acad. Sci. U. S. A. **108**, 12233–12237 (2010).

[191]   M. Yankowitz, S. Chen, H. Polshyn, K. Watanabe, T. Taniguchi, D. Graf, A. F. Young, and C. R. Dean. *Tuning superconductivity in twisted bilayer graphene.* Science **363**, 1059 (2018).

[192]   X. Lu, P. Stepanov, W. Yang, M. Xie, M. A. Aamir, I. Das, C. Urgell, K. Watanabe, T. Taniguchi, G. Zhang, A. Bachtold, A. H. MacDonald, and D. K. Efetov. *Superconductors, Orbital Magnets, and Correlated States in Magic Angle Bilayer Graphene.* Nature **574**, 653657 (2019).

[193] E. Y. Andrei and A. H. MacDonald. *Graphene Bilayers with a Twist.* Nat. Mater. **19**, 1265 (2020).

[194] M. Oh, K. P. Nuckolls, D. Wong, R. L. Lee, X. Liu, K. Watanabe, T. Taniguchi, and A. Yazdani. *Evidence for unconventional superconductivity in twisted bilayer graphene.* Nature **600**, 240–245 (2021) arXiv:2109.13944.

[195] I. Syozi. *Statistics of Kagome Lattice.* Prog. Theor. Phys. **6**, 306–308 (1951).

[196] F Piéchon, J.-N. Fuchs, A Raoux, and G Montambaux. *Tunable orbital susceptibility in α-T_3 tight-binding models.* J. Phys.: Conf. Series **603**, 012001 (2015).

[197] J. W. McClure. *Diamagnetism of Graphite.* Phys. Rev. **104**, 666–671 (1956).

[198] A. Iurov, G. Gumbs, and D. Huang. *Many-body effects and optical properties of single and double layer $\alpha - \mathcal{T}_3$ lattices.* J. Phys. Condens. Matter **32**, 415303 (2020) arXiv:2004.05681.

[199] P. O. Sukhachov, D. O. Oriekhov, and E. V. Gorbar. *Optical conductivity of bilayer dice lattices.* (2023) arXiv:2303.08258.

[200] E. Mostaani, N. D. Drummond, and V. I. Fal'ko. *Quantum Monte Carlo Calculation of the Binding Energy of Bilayer Graphene.* Phys. Rev. Lett. **115**, 115501 (2015).

[201] H. Terrones, M. Terrones, E. Hernández, N. Grobert, J.-C. Charlier, and P. M. Ajayan. *New metallic allotropes of planar and tubular carbon.* Phys. Rev. Lett. **84**, 1716–1719 (2000).

[202] A. N. Enyashin and A. L. Ivanovskii. *Graphene allotropes.* Physica Status Solidi (b) **248**, 1879–1883 (2011).

[203] Q. Gu, D. Xing, and J. Sun. *Superconducting single-layer T-graphene and novel synthesis routes.* Chin. Phys. Lett. **36**, 097401, 097401 (2019).

[204] X.-L. Sheng, H.-J. Cui, F. Ye, Q.-B. Yan, Q.-R. Zheng, and G. Su. *Octagraphene as a versatile carbon atomic sheet for novel nanotubes, unconventional fullerenes, and hydrogen storage.* J. Appl. Phys. **112**, 074315 (2012).

[205]   A. Bao, H.-S. Tao, H.-D. Liu, X. Zhang, and W.-M. Liu. *Quantum magnetic phase transition in square-octagon lattice*. Sci. Rep. **4**, 6918 (2014).

[206]   Y. Yamashita, M. Tomura, Y. Yanagi, and K. Ueda. *SU(3) Dirac electrons in the $\frac{1}{5}$-depleted square-lattice Hubbard model at $\frac{1}{4}$ filling*. Phys. Rev. B **88**, 195104 (2013).

[207]   W. Li, M. Guo, G. Zhang, and Y.-W. Zhang. *Gapless MoS_2 allotrope possessing both massless Dirac and heavy fermions*. Phys. Rev. B **89**, 205402 (2014).

[208]   N. Pomata and T.-C. Wei. *Demonstrating the affleck-kennedy-lieb-tasaki spectral gap on 2d degree-3 lattices*. Phys. Rev. Lett. **124**, 177203 (2020).

[209]   Y. Sun, C. Felser, and B. Yan. *Graphene-like Dirac states and quantum spin Hall insulators in square-octagonal MX_2 (M = Mo, W; X = S, Se, Te) isomers*. Phys. Rev. B **92**, 165421 (2015).

[210]   K. Umemoto, R. M. Wentzcovitch, S. Saito, and T. Miyake. *Body-Centered Tetragonal $\mathbf{C}_4$: A Viable sp^3 Carbon Allotrope*. Phys. Rev. Lett. **104**, 125504 (2010).

[211]   R. Majidi. *Electronic properties of T graphene-like C–BN sheets: A density functional theory study*. Phys. E: Low-dim. Sys. and Nanostr. **74**, 371–376 (2015).

[212]   R. Majidi. *Density functional theory study on structural and mechanical properties of graphene, T-graphene, and R-graphyne*. Theor. Chem. Acc. **136**, 109 (2017).

[213]   W.-J. Yin, Y.-E. Xie, L.-M. Liu, R.-Z. Wang, X.-L. Wei, L. Lau, J.-X. Zhong, and Y.-P. Chen. *R-graphyne: a new two-dimensional carbon allotrope with versatile Dirac-like point in nanoribbons*. J. Mat. Chem. A **1**, 5341 (2013).

[214]   A. I. Podlivaev and L. A. Openov. *Kinetic stability of octagraphene*. Phys. Sol. State **55**, 2592 (2013).

[215]   H. Isobe and L. Fu. *Supermetal*. Physical Review Research **1**, 033206 (2019).

[216]   A. Shtyk, G. Goldstein, and C. Chamon. *Electrons at the monkey saddle: A multicritical Lifshitz point*. Phys. Rev. B **95**, 035137 (2017).

[217] D. V. Efremov, A. Shtyk, A. W. Rost, C. Chamon, A. P. Mackenzie, and J. J. Betouras. *Multicritical Fermi Surface Topological Transitions*. Phys. Rev. Lett. **123**, 207202 (2019).

[218] A. Ramires, P. Coleman, A. H. Nevidomskyy, and A. M. Tsvelik. *β-YbAlB4: a critical nodal metal*. Phys. Rev. Lett. **109**, 176404 (2012).

[219] Y.-P. Lin and R. M. Nandkishore. *Parquet renormalization group analysis of weak-coupling instabilities with multiple high-order van hove points inside the brillouin zone*. Phys. Rev. B **102**, 245122 (2020).

[220] Y. Sherkunov and J. J. Betouras. *Electronic phases in twisted bilayer graphene at magic angles as a result of van hove singularities and interactions*. Phys. Rev. B **98**, 205151 (2018).

[221] D. V. Chichinadze, L. Classen, and A. V. Chubukov. *Valley magnetism, nematicity, and density wave orders in twisted bilayer graphene*. Phys. Rev. B **102**, 125120 (2020).

[222] H. Isobe, N. F. Q. Yuan, and L. Fu. *Unconventional superconductivity and density waves in twisted bilayer graphene*. Phys. Rev. X **8**, 041041 (2018).

[223] Y. Wang, J. Kang, and R. M. Fernandes. *Topological and nematic superconductivity mediated by ferro-su(4) fluctuations in twisted bilayer graphene*. Phys. Rev. B **103**, 024506 (2021).

[224] J. González and T. Stauber. *Kohn-Luttinger superconductivity in twisted bilayer graphene*. Phys. Rev. Lett. **122**, 026801 (2019).

[225] N. W. Ashcroft and N. D. Mermin. *Solid state physics*. (Saunders College Publishing, Fort Worth, 1976).

[226] G. Gómez-Santos and T. Stauber. *Measurable lattice effects on the charge and magnetic response in graphene*. Phys. Rev. Lett. **106**, 045504 (2011).

[227] A. Raoux, F. Piéchon, J.-N. Fuchs, and G. Montambaux. *Orbital magnetism in coupled-bands models*. Phys. Rev. B **91**, 085120 (2015).

[228] J. Li, T. Datta, and D.-X. Yao. *Einstein-de haas effect of topological magnons*. Phys. Rev. Res. **3**, 023248 (2021).

[229] T. Louvet, P. Delplace, A. A. Fedorenko, and D. Carpentier. *On the origin of minimal conductivity at a band crossing.* Phys. Rev. B **92**, 155116 (2015).

[230] P.-O. Löwdin. *A note on the quantum-mechanical perturbation theory.* The Journal of Chemical Physics **19**, 1396–1401 (1951).

[231] L.-K. Lim, J.-N. Fuchs, F. Piéchon, and G. Montambaux. *Dirac points emerging from flat bands in Lieb-kagome lattices.* Phys. Rev. B **101**, 045131 (2020).

[232] F. Piéchon, A. Raoux, J.-N. Fuchs, and G. Montambaux. *Geometric orbital susceptibility: quantum metric without Berry curvature.* Phys. Rev. B **94**, 134423 (2016).

[233] H. Fukuyama. *Theory of orbital magnetism of Bloch electrons: coulomb interactions.* Prog. Theor. Phys. **45**, 704–729 (1971).

[234] L. Landau. *Diamagnetismus der metalle.* Zeitschrift für Physik **64**, 629–637 (1930).

[235] R. Peierls. *Zur theorie des diamagnetismus von leitungselektronen.* Zeitschrift für Physik **80**, 763–791 (1933).

[236] P. Rosenzweig, H. Karakachian, D. Marchenko, K. Küster, and U. Starke. *Overdoping graphene beyond the van hove singularity.* Phys. Rev. Lett. **125**, 176403 (2020).

[237] U. Choudhry, S. Yue, and B. Liao. *Origins of significant reduction of lattice thermal conductivity in graphene allotropes.* Phys. Rev. B **100**, 165401 (2019).

[238] D. Guerci, P. Simon, and C. Mora. *Moiré lattice effects on the orbital magnetic response of twisted bilayer graphene and Condon instability.* Phys. Rev. B **103**, 224436 (2021).

[239] C. Kallin and J. Berlinsky. *Chiral superconductors.* Rep. Prog. Phys. **79**, 054502 (2016).

[240] T. Senthil and M. P. A. Fisher. *Quasiparticle localization in superconductors with spin-orbit scattering.* Phys. Rev. B **61**, 9690 (2000).

[241] N. Read and D. Green. *Paired states of fermions in two dimensions with breaking of parity and time-reversal symmetries and the fractional quantum hall effect.* Phys. Rev. B **61**, 10267 (2000).

[242] M. Banerjee, M. Heiblum, V. Umansky, D. E. Feldman, Y. Oreg, and A. Stern. *Observation of half-integer thermal hall conductance.* Nature **559**, 205–210 (2018).

[243] X.-L. Qi and S.-C. Zhang. *Topological insulators and superconductors.* Rev. Mod. Phys. **83**, 1057 (2011).

[244] D. A. Ivanov. *Non-abelian statistics of half-quantum vortices in p-wave superconductors.* Phys. Rev. Lett. **86**, 268 (2001).

[245] P. Fendley, M. P. A. Fisher, and C. Nayak. *Edge states and tunneling of non-abelian quasiparticles in the $p + ip$ superconductors.* Phys. Rev. B **75**, 045317 (2007).

[246] L. Fu and C. L. Kane. *Probing neutral majorana fermion edge modes with charge transport.* Phys. Rev. Lett. **102**, 216403 (2009).

[247] A. R. Akhmerov, J. Nilsson, and C. W. J. Beenakker. *Electrically detected interferometry of majorana fermions in a topological insulator.* Phys. Rev. Lett. **102**, 216404 (2009).

[248] G. Strübi, W. Belzig, M.-S. Choi, and C. Bruder. *Interferometric and noise signatures of majorana fermion edge states in transport experiments.* Phys. Rev. Lett. **107**, 136403 (2011).

[249] J. Li, G. Fleury, and M. Büttiker. *Scattering theory of chiral majorana fermion interferometry.* Phys. Rev. B **85**, 125440 (2012).

[250] M. Alos-Palop, R. P. Tiwari, and M. Blaauboer. *Adiabatic quantum pumping of chiral majorana fermions.* Phys. Rev. B **89**, 045307 (2014).

[251] D. S. Shapiro, A. Shnirman, and A. D. Mirlin. *Current-phase relation and h/e-periodic critical current of a chiral josephson contact between one-dimensional majorana modes.* Phys. Rev. B **93**, 155411 (2016).

[252] L. Chirolli, J. P. Baltanás, and D. Frustaglia. *Chiral majorana interference as a source of quantum entanglement.* Phys. Rev. B **97**, 155416 (2018).

[253] B. Lian, X.-Q. Sun, A. Vaezi, X.-L. Qi, and S.-C. Zhang. *Topological quantum computation based on chiral majorana fermions.* Proceedings of the National Academy of Sciences **115**, 10938–10942 (2018).

[254] Y.-H. Li, J. Liu, H. Liu, H. Jiang, Q.-F. Sun, and X. C. Xie. *Noise signatures for determining chiral majorana fermion modes.* Phys. Rev. B **98**, 045141 (2018).

[255] C. Beenakker, P. Baireuther, Y. Herasymenko, I. Adagideli, L. Wang, and A. Akhmerov. *Deterministic creation and braiding of chiral edge vortices.* Phys. Rev. Lett. **122**, 146803 (2019).

[256] C. Beenakker, A. Grabsch, and Y. Herasymenko. *Electrical detection of the majorana fusion rule for chiral edge vortices in a topological superconductor.* SciPost Physics **6**, 022 (2019).

[257] I. Adagideli, F. Hassler, A. Grabsch, M. Pacholski, and C. Beenakker. *Time-resolved electrical detection of chiral edge vortex braiding.* SciPost Physics **8**, 013 (2020).

[258] F. Hassler, A. Grabsch, M. J. Pacholski, D. O. Oriekhov, O. Ovdat, I. Adagideli, and C. W. J. Beenakker. *Half-integer charge injection by a josephson junction without excess noise.* Phys. Rev. B **102**, 045431 (2020).

[259] C. Beenakker. *Annihilation of colliding bogoliubov quasiparticles reveals their majorana nature.* Phys. Rev. Lett. **112**, 070604 (2014).

[260] N. V. Gnezdilov, B. van Heck, M. Diez, J. A. Hutasoit, and C. W. J. Beenakker. *Topologically protected charge transfer along the edge of a chiral p-wave superconductor.* Phys. Rev. B **92**, 121406 (2015).

[261] I. Klich. *A note on the full counting statistics of paired fermions.* J. Stat. Mech.: Theory and Experiment **2014**, P11006 (2014).

[262] N. V. Gnezdilov, M. Diez, M. J. Pacholski, and C. W. J. Beenakker. *Wiedemann-franz-type relation between shot noise and thermal conduction of majorana surface states in a three-dimensional topological superconductor.* Phys. Rev. B **94**, 115415 (2016).

[263] A. Furusaki and M. Tsukada. *Current-carrying states in josephson junctions.* Phys. Rev. B **43**, 10164 (1991).

[264] C. W. J. Beenakker and H. van Houten. *Josephson current through a superconducting quantum point contact shorter than the coherence length.* Phys. Rev. Lett. **66**, 3056 (1991).

[265] I. O. Kulik and A. N. Omel´yanchuk. *Properties of superconducting microbridges in the pure limit.* Sov. J. Low Temp. Phys. **3**, 459 (1977).

[266] C. W. J. Beenakker. *Universal limit of critical-current fluctuations in mesoscopic josephson junctions.* Phys. Rev. Lett. **67**, 3836 (1991).

[267] A. Zazunov, V. S. Shumeiko, E. N. Bratus', J. Lantz, and G. Wendin. *Andreev level qubit.* Phys. Rev. Lett. **90**, 087003 (2003).

[268] N. M. Chtchelkatchev and Y. V. Nazarov. *Andreev quantum dots for spin manipulation.* Phys. Rev. Lett. **90**, 226806 (2003).

[269] L. Bretheau, Ç. Girit, H. Pothier, D. Esteve, and C. Urbina. *Exciting andreev pairs in a superconducting atomic contact.* Nature **499**, 312–315 (2013).

[270] C. Janvier, L. Tosi, L. Bretheau, Ç. Girit, M. Stern, P. Bertet, P. Joyez, D. Vion, D. Esteve, M. F. Goffman, H. Pothier, and C. Urbina. *Coherent manipulation of andreev states in superconducting atomic contacts.* Science **349**, 1199 (2015).

[271] M. Hays, G. de Lange, K. Serniak, D. van Woerkom, D. Bouman, P. Krogstrup, J. Nygård, A. Geresdi, and M. Devoret. *Direct microwave measurement of andreev-bound-state dynamics in a semiconductor-nanowire josephson junction.* Phys. Rev. Lett. **121**, 047001 (2018).

[272] M. Hays, V. Fatemi, D. Bouman, J. Cerrillo, S. Diamond, K. Serniak, T. Connolly, P. Krogstrup, J. Nygård, A. L. Yeyati, A. Geresdi, and M. H. Devoret. *Coherent manipulation of an andreev spin qubit.* Science **373**, 430 (2021).

[273] F. S. Bergeret, P. Virtanen, A. Ozaeta, T. T. Heikkilä, and J. C. Cuevas. *Supercurrent and andreev bound state dynamics in superconducting quantum point contacts under microwave irradiation.* Phys. Rev. B **84**, 054504 (2011).

[274] A. Martín-Rodero and A. L. Yeyati. *Josephson and andreev transport through quantum dots.* Adv. Phys. **60**, 899 (2011).

[275] V Meden. *The anderson-josephson quantum dot - a theory perspective.* J. Phys.: Condens. Matter **31**, 163001 (2019).

[276] A. L. Yeyati, A. Martín-Rodero, and E. Vecino. *Nonequilibrium dynamics of andreev states in the kondo regime.* Phys. Rev. Lett. **91**, 266802 (2003).

[277] L. I. Glazman and K. A. Matveev. *Resonant Josephson current through Kondo impurities in a tunnel barrier.* JETP Lett. **49**, 659 (1989).

[278] B. I. Spivak and S. A. Kivelson. *Negative local superfluid densities: the difference between dirty superconductors and dirty bose liquids.* Phys. Rev. B **43**, 3740–3743 (1991).

[279] T. Novotný, A. Rossini, and K. Flensberg. *Josephson current through a molecular transistor in a dissipative environment.* Phys. Rev. B **72**, 224502 (2005).

[280] T. Meng, S. Florens, and P. Simon. *Self-consistent description of andreev bound states in josephson quantum dot devices.* Phys. Rev. B **79**, 224521 (2009).

[281] C. W. J. Beenakker and H. van Houten, *Resonant josephson current through a quantum dot*, in *Springer series in electronics and photonics* (Springer Berlin Heidelberg, 1992), pp. 175–179.

[282] I. A. Devyatov and M. Y. Kupriyanov. *Resonant josephson tunneling through s-i-s junctions of arbitrary size.* Journal of Experimental and Theoretical Physics **85**, 189–194 (1997).

[283] P. Recher, Y. V. Nazarov, and L. P. Kouwenhoven. *Josephson light-emitting diode.* Phys. Rev. Lett. **104**, 156802 (2010).

[284] M. Tinkham. *Introduction to superconductivity.* (Dover, 2004).

[285] D. V. Averin, A. Bardas, and H. T. Imam. *Resistively shunted superconducting quantum point contacts.* Phys. Rev. B **58**, 11165 (1998).

[286] J.-J. Feng, Z. Huang, Z. Wang, and Q. Niu. *Hysteresis from nonlinear dynamics of majorana modes in topological josephson junctions.* Phys. Rev. B **98**, 134515 (2018).

[287] D. Averin and A. Bardas. *Adiabatic dynamics of superconducting quantum point contacts.* Phys. Rev. B **53**, R1705 (1996).

[288] S. Shevchenko, S. Ashhab, and F. Nori. *Landau-Zener-Stückelberg interferometry.* Physics Reports **492**, 1–30 (2010).

Summary

The flat bands in a spectrum are defined as regions of momentum space in which the quasiparticle dispersion is nearly constant. The states composing a flat band can be viewed as quasiparticles with very large effective mass, thus being localized in real space. The two-dimensional crystals hosting flat bands were studied theoretically two decades before the first atomically-thin material – graphene – appeared. The field of studying and building new flat band materials is still growing.

Nowadays, with the appearance of experimental realizations of flat band materials, the interest in their physical properties has grown enormously. The present thesis is dedicated to studying the quantum transport phenomena and correlated effects that appear in flat band materials. Its main contribution lies in the description of spin-spin exchange interactions, excitonic gap generations, magnetic and optical properties in such materials.

The Chapters 2, 3 and 4 contain calculation for a single-layer 2D flat band crystals. In Chapter 2 we derive spin-spin exchange interaction between two impurities placed on a dice lattice. The results show that interaction is enhanced only for a specific geometric position of impurities, which is related to the structure of flat band wave functions. In this Chapter we derived analytic expressions for the chemical potential and temperature dependence of the interaction strength, which generalize results known in the graphene literature. In Chapter 3 we analyze the role of electron-hole interactions in the dynamical formation of the excitonic gap. It is found that the flat band plays the role of a catalyst and enhances only specific order parameters, which leaves the flat band undeformed. In Chapter 4 we extend an application of the zitterbewegung approach to a number of flat band materials, which allows us to derive exact analytic results and understand the role of different optical interband transitions in the transport properties of these materials.

Chapter 5 extends the study to bilayer crystals composed out of two flat band single layer crystals. It contains the derivation of effective models describing three-band-crossing points, the analysis of deformations of flat bands as an effect of interlayer hopping, and the calculation of spectral functions of such systems.

Chapter 6 contains a calculation of the orbital susceptibility for a model of a possible graphene allotrope called T-graphene. The dia-to-paramagnetic transition is predicted as a result of the interplay between Dirac cones and nearly-flat bands, producing Van Hove singularities.

The last two Chapters, 7 and 8, are focused on the transport properties of superconductors hosting Majorana zero modes or Andreev bound states. The results in Chapter 7 show how one might distinguish Majorana zero modes from Majorana fermions by measuring the shot noise. Chapter 8 describes how Andreev bound states placed nearly at zero energy can create the same effect which is expected for a qubit built from Majorana modes: a staircase in the voltage-current characteristic of a Josephson junction containing a quantum dot.

Samenvatting

De vlakke banden in een spectrum worden gedefinieerd als gebieden van de impulsruimte waarin de quasideeltjesdispersie bijna constant is. De toestanden die een vlakke band vormen kunnen gezien worden als quasideeltjes met een zeer grote effectieve massa en zijn dus ruimtelijk gelokaliseerd. Twee decennia voordat het eerste atomair dunne materiaal - grafeen - verscheen, werden tweedimensionale kristallen met vlakke banden theoretisch bestudeerd. Het bestuderen en bouwen van nieuwe materialen met vlakke banden is nog steeds een actief onderwerp.

Tegenwoordig, met het verschijnen van experimentele realisaties van vlakke bandmaterialen, is de interesse in hun fysische eigenschappen enorm gegroeid. Dit proefschrift is gewijd aan de studie van quantumtransportverschijnselen en gecorreleerde effecten die optreden in vlakbandmaterialen. De belangrijkste bijdrage ligt in de beschrijving van magnetische en optische eigenschappen in dergelijke materialen.

De hoofdstukken 2, 3 en 4 bevatten berekeningen voor éénlaagse 2D vlakbandkristallen. In hoofdstuk 2 leiden we de spin-spin interactie af tussen twee onzuiverheden op een dobbelsteenrooster. De resultaten tonen aan dat de interactie alleen wordt versterkt voor een specifieke geometrische positie van onzuiverheden, die gerelateerd is aan de structuur van de golffuncties van de vlakke band. In dit hoofdstuk hebben we analytische uitdrukkingen afgeleid voor de chemische potentiaal en de temperatuurafhankelijkheid van de interactiesterkte, die resultaten veralgemenen die bekend zijn in de grafeenliteratuur.

In hoofdstuk 3 analyseren we de rol van elektron-gat interacties in de dynamische vorming van de excitonische "gap". Het blijkt dat de vlakke band de rol van katalysator speelt en alleen specifieke ordeparameters versterkt, waardoor de vlakke band onvervormd blijft.

In hoofdstuk 4 breiden we een toepassing van de zitterbewegung-benadering uit naar een aantal materialen met een vlakke band, waar-

door we exacte analytische resultaten kunnen afleiden en de rol van verschillende optische interbandovergangen in de transporteigenschappen van deze materialen kunnen begrijpen.

Hoofdstuk 5 breidt de studie uit naar tweelaagskristallen die zijn opgebouwd uit twee vlakband enkellaags kristallen. Het bevat de analyse van vervormingen van vlakke banden als effect van interlaags hoppen, en de berekening van spectrale functies van dergelijke systemen.

Hoofdstuk 6 bevat een berekening van de orbitale susceptibiliteit voor een model van een mogelijk grafeenallotroop, T-grafeen genaamd. De dia-naar-paramagnetische overgang wordt voorspeld als gevolg van de wisselwerking tussen Dirac-kegels en bijna-vlakke banden, waardoor Van Hove-singulariteiten ontstaan.

De laatste twee hoofdstukken, 7 en 8, richten zich op de transporteigenschappen van supergeleiders met Majorana nulpunten of Andreev gebonden toestanden. De resultaten in hoofdstuk 7 laten zien hoe je Majorana nulmodes kunt onderscheiden van Majorana fermionen door de hagelruis te meten. Hoofdstuk 8 beschrijft hoe Andreev-gebonden toestanden die bijna op nulenergie zijn geplaatst hetzelfde effect kunnen veroorzaken dat verwacht wordt voor een qubit opgebouwd uit Majorana-modes: een laddervormige spanning-stroomkarakteristiek van een Josephson-junctie die een quantumdot bevat.

Curriculum Vitæ

I was born on the 19th of June 1996 in Kyiv, Ukraine. During my school years, I was participating in the math, physics and chemistry olympiads. In 2010 I started my high-school studies in the natural-scientific lyceum 145. During these years, I clearly realized that my main talent is in physics. In the last year I joined the Ukrainian team on the International Physics Olympiad held in Kazakhstan, and won a silver medal there.

In 2014 I began my Bachelor studies in Physics at Taras Schevchenko national university of Kyiv, where later I also continued as a master student at the Quantum Field Theory department of the Physics Faculty. During these times, I discovered my interest in the broad range of topics of condensed matter physics and I liked to apply there the methods which I learned from quantum field theory and the Standard Model. Together with my supervisors Prof. dr. Eduard Gorbar and Prof. dr. Valery Gusynin from the Bogoliubov Institute of Theoretical Physics, we published a number of papers on graphene and new flat band materials. In 2017 I met Prof. Leonid Levitov from MIT at a student event, and we started studies of relativistic plasmons that are close in speed to light.

During the last year of my master course, in February 2020, I visited the group of Prof. dr. Carlo Beenakker in Leiden for an internship, to start studies of Majorana zero modes. Notably, it was the last month before all subsequent lockdowns. In June 2020 I started my PhD studies in Leiden under the supervision of Carlo Beenakker, continuing the work on Majorana zero modes and related phenomena such as Andreev bound states. Later, I expanded the scope of my research to novel twisted bilayer materials as well as continued the studies of flat band materials, building on my knowledge from my master study. In parallel, I liked working with bachelor and master students on scientific projects, the results of which were published in several papers during the last years. Throughout my PhD, I participated in a number of conferences and summer schools, expanding my knowledge and presenting my research. I also worked as

a teaching assistant for the course of physics of quantum and classical information.

As a next step after completing my PhD, I will join the quantum matter and AI group of Prof. Eliska Greplova at the Kavli Institute of Nanoscience in the Technical University of Delft. There I will focus on the study of the connections between novel atomically-thin materials and quantum devices.

List of Publications

[1] D. O. Oriekhov, O. O. Sobol, E. V. Gorbar, and V. P. Gusynin. *Coulomb center instability in bilayer graphene.* Phys. Rev. B **96**, 165403 (2017).

[2] D. O. Oriekhov, E. V. Gorbar, and V. P. Gusynin. *Electronic states of pseudospin-1 fermions in dice lattice ribbon.* Low Temp. Phys. **44**, 1313–1324 (2018).

[3] O. V. Bugaiko and D. O. Oriekhov. *Electronic states of pseudospin-1 fermions in $\alpha - \mathcal{T}_3$ lattice ribbons in a magnetic field.* J. Phys.: Condens. Matter **31** 325501 (2019).

[4] E. V. Gorbar, V. P. Gusynin, and D. O. Oriekhov. *Electron states for gapped pseudospin-1 fermions in the field of a charged impurity.* Phys. Rev. B **99**, 155124 (2019).

[5] D. O. Oriekhov and V. P. Gusynin. *RKKY interaction in a doped pseudospin-1 fermion system at finite temperature.* Phys. Rev. B **101**, 235162 (2020) [Chapter 2].

[6] D. O. Oriekhov and L. S. Levitov. *Plasmon resonances and tachyon ghost modes in highly conducting sheets.* Phys. Rev. B **101**, 245136 (2020).

[7] F. Hassler, A. Grabsch, M. J. Pacholski, D. O. Oriekhov, O. Ovdat, I. Adagideli, and C. W. J. Beenakker. *Half-integer charge injection by a Josephson junction without excess noise.* Phys. Rev. B **102**, 045431 (2020).

[8] C. W. J. Beenakker and D. O. Oriekhov. *Shot noise distinguishes Majorana fermions from vortices injected in the edge mode of a chiral p-wave superconductor.* SciPost Phys. **9**, 080 (2020) [Chapter 7].

[9] D. O. Oriekhov, Y. Cheipesh, and C. W. J. Beenakker. *Voltage staircase in a current-biased quantum-dot Josephson junction*. Phys. Rev. B **103**, 094518 (2021) [Chapter 8].

[10] E. V. Gorbar, V. P. Gusynin, and D. O. Oriekhov. *Gap generation and flat band catalysis in dice model with local interaction*. Phys. Rev. B **103**, 155155 (2021) [Chapter 3].

[11] D. O. Oriekhov, V. P. Gusynin, and V. M. Loktev. *Orbital susceptibility of T-graphene: Interplay of high-order van Hove singularities and Dirac cones*. Phys. Rev. B **103**, 195104 (2021) [Chapter 6].

[12] D. O. Oriekhov and S. Voronov. *Current distribution and group velocities for electronic states on $\alpha - \mathcal{T}_3$ lattice ribbons in a magnetic field*. J. Phys.: Condens. Matter **33** 285503 (2021).

[13] T. Vakhtel, D. O. Oriekhov, and C. W. J. Beenakker. *Bloch oscillations in the magnetoconductance of twisted bilayer graphene*. Phys. Rev. B **105**, L241408 (2022).

[14] Y. Kulynych and D. O. Oriekhov. *Differential entropy per particle as a probe of van Hove singularities and flat bands*. Phys. Rev. B **106**, 045115 (2022).

[15] D. O. Oriekhov and V. P. Gusynin. *Optical conductivity of semi-Dirac and pseudospin-1 models: Zitterbewegung approach*. Phys. Rev. B **106**, 115143 (2022) [Chapter 4].

[16] D. O. Oriekhov, T. T. Osterholt, T. Vakhtel, A. R. Akhmerov, and C. W. J. Beenakker. *Breathing mode in open-orbit magnetotransport: A magnetic lens with a quantum mechanical focal length*. Phys. Rev. B **106**, 235413 (2022)

[17] P. O. Sukhachov, D. O. Oriekhov, and E. V. Gorbar. *Stackings and effective models of bilayer dice lattices*. arXiv:2303.01452 [Chapter 5]

[18] A. S. Shankar, D. O. Oriekhov, A. K. Mitchell, and L. Fritz. *Kondo effect in twisted bilayer graphene*. arXiv:2303.02492.

[19] V. A. Zakharov, A. Mert Bozkurt, A. R. Akhmerov, and D. O. Oriekhov. *Landau quantization near generalized van Hove singularities: magnetic breakdown and orbit networks*. arXiv:2303.07447.

[20] P. O. Sukhachov, D. O. Oriekhov, and E. V. Gorbar. *Optical conductivity of bilayer dice lattices.* arXiv:2303.08258.